FINAL REPORT, Initially submitted January 27, 2023, Modified and resubmitted May 17, 2023

Project Title: Mineral Alteration of Shales by $C0_2$ and Brine Containing Surfactants

Federal Award Identification Number: DE-SC0017328

Agency Code: 8900, **Organization:** Office of Basic Energy Sciences

PI: Charles J Werth, University of Texas at Austin

1. What are the major goals of the project?

The overall goal of the proposed research is to determine the effect of surfactants on shale mineral reactivity with CO_2 and brine. The specific objectives of the proposed work are to 1) Determine the effect of shale mineralogy and surfactant properties on surfactant adsorption and wettability alteration, 2) Determine the effects of surfactant adsorption and wettability alteration on mineral reactivity with CO_2 and brine for varying hydrodynamic conditions, and 3) Develop a modified mineral reaction model with CO_2 and brine that considers the effects of surfactant adsorption. Four tasks are planned to address the project objectives. These are 1) Select and characterize shale samples, 2) Evaluate the effects of surfactant and reservoir properties on adsorption and mineral reactivity, 3) Determine the effects of surfactant adsorption, wettability alteration, and hydrodynamics on mineral reaction kinetics, and 4) Quantify how surfactant sorption and mineral wettability alteration affect mineral reaction modeling.

2. What was accomplished under these goals?

The major accomplishments from project efforts are documented below.

1) We published a paper in *ACS Energy and Fuels* regarding sorption of different surfactants to different shales and shale mineral/organic matter components.

Zeng, T., K.T. Kim, C.J. Werth, L.E. Katz, K.K. Mohanty, Surfactant Adsorption on Shale Samples: Experiments and an Additive Model, Energy and Fuels, ef-2019-04016z (10.1021/acs.energyfuels.9b04016), 2020.

The major findings are summarized in a document presented in Section A of this report. This work addresses Tasks 1 and 2.

2) We published a paper in *Colloids and Surfaces A: Physicochemical and Engineering Aspects*, regarding mechanisms of surfactant inhibition on dissolution of shale and associated calcite mineral components.

Kim, K.T., T. Zeng, S.P.J. Mantha, K.K. Mohanty, G. Henkelman, L.E. Katz, Charles J. Werth, Surfactant Inhibition Mechanisms of Carbonate Mineral Dissolution in Shale, Colloids and Surfaces A: Physicochemical and Engineering Aspects, 625, 126857, 2021.

The major findings are summarized in a document presented in Section B of this report. This work addresses Tasks 2, 3, and 4.

3) We published a paper in *ACS Sustainable Chemistry and Engineering*, regarding environmental and economic impacts of replacing slickwater with CO2-based fracturing fluid.

Lin, W., A.M. Bergquist, K. Mohanty, C.J. Werth, Environmental impacts of replacing slickwater with low-no-water fracturing fluids for shale gas recovery, ACS Sustainable Chemistry & Engineering, 6(6), 7515-7524, 2018.

The major findings are summarized in a document presented in Section C of this report. This work allowed us to compile data for different shale reservoirs, and the suitability of using CO_2-based fluids in shale reservoirs. Consequently, it partially addressed Task 1.

4) We are almost ready to submit a manuscript regarding mechanisms of surfactant inhibition on calcite mineral components at reservoir temperature and pressure. A document summarizing this work is presented in Section D of this report. This work addresses Tasks 2, 3, and 4.

5) We submitted a manuscript regarding mechanisms of reaction of simulated reservoir brine with shale components, and effects on shear slip at reservoir pressure. The major findings are presented in Section E of this report. This work addresses Tasks 2 and 3.

6) We performed initial experiments that evaluate the effects of flow and reactive transport on surfactant inhibition of calcite mineral dissolution in a microfluidic reactor. The results are still in the process of being collected and analyzed and are not presented in this report. This work addresses Tasks 2, 3, and 4.

3. What opportunities for training and professional development has the project provided?

The former student Dr. Tongzhou Zeng worked on the project from May 2017-2021. He had the opportunity to learn a number of characterization methods, including XRD, SEM, EDS, AFM, ICP-OES, and HPLC. He presented at a conference, and he is the first author of the paper published in *ACS Energy and Fuels*. Dr. Zeng graduated and is now a Research Scientist at Meta in Austin, TX.

The student David Kyungtae Kim has been working on the project since January 2018. He’s had the opportunity to learn the aforementioned characterization methods in addition to laser profilometry and time of flight – secondary ion mass spectrometry (ToF-SIMS), he’s learned how to perform calcite dissolution experiments at reservoir temperature and pressure, including taking aqueous sampling from these systems over time, and he’s learned how to run density functional theory calculations for interpreting his data. David is the first author of the paper published in *Colloids and Surfaces A: Physicochemical and Engineering Aspects*. Although project funding ended, David continues to work on this project with support from a teaching assistantship and discretionary funds allocated to Werth as part of his endowed chair. David will be the lead author on the manuscript in preparation that presents the effects of surfactant adsorption on calcite dissolution at reservoir pressure and temperature (Section D), and on a future manuscript that will present the effects of flow and reactive transport on surfactant inhibition of calcite mineral dissolution. It is anticipated that David will graduate in August of 2023.

The former student Dr. Samantha Fuchs contributed to his project from 2020-2021. Prior to 2020, she was supported for three years by the DOE EFRC on Geological Carbon Sequestration led by the University of Illinois, where her work focused on the effect of CO2-saturated brine on chemical reactions and geomechanical integrity of storage (i.e., sandstone) reservoirs. After this EFRC ended, she shifted her work to complement this project, and evaluated the effect of acidic brines on chemical reactions and geomechanical integrity of shales. Dr. Fuchs is first author on the submitted manuscript (Section E). As part of this effort, she gained skills characterizing the chemical and geomechanical properties of shale in these efforts, using methods such as laser profilometry, SEM, thin section preparation, optical microscopy, and triaxial core flooding. Dr. Fuchs graduated in summer 2021, and is now employed by Geosyntec.

4. How have the results been disseminated to the communities of interest?

Three papers regarding this project have been published, one has been submitted, and one is almost ready for submittal. Data (microfluidics) is being collected for a six manuscript. Results were presented at a petroleum engineering conference by Tongzhou Zeng, at the DOE BES annual meeting in 2019 by Werth, at AGU in 2019 by Werth, at AGU in 2022 by David Kim, and at ACS in 2023 by David Kim.

5. Is there additional project work to perform now that the project has ended?

The project funding was depleted in early 2021. However, David Kyungtae Kim continued working on the project with his support covered by either a teaching assistantship or discretionary funds from Werth's endowed chair. David led the writing of one paper, led the writing of the manuscript about to be submitted (Section D), and is leading the microfluidic effort that will result in a third first-author manuscript. Dr. Samantha Fuchs graduated with her PhD from the University of Texas at Austin in 2021. During her last year as a PhD student, she worked on this project with support from a DOE fellowship and from discretionary funds provided from Werth's endowed chair. She prepared and submitted a manuscript on the effects of acidic brine on geochemical and geomechanical properties of a shale fracture surface under shear (Section E).

6. How is the remainder of the report organized?

The remainder of the report is presented as follows:

Section A) Presentation of major findings published in *ACS Energy and Fuels.*

Section B) Presentation of major findings published in *Colloids and Surfaces A: Physicochemical and Engineering Aspects.*

Section C) Presentation of major findings published in *ACS Sustainable Chemistry and Engineering*.

Section D) Presentation of major findings on the effects of surfactant adsorption on calcite dissolution at reservoir pressure and temperature.

Section E) Presentation of major findings on mechanisms of reaction of simulated reservoir brine with shale components, and effects on shear slip at reservoir pressure.

Section A: Presentation of major findings published in *ACS Energy and Fuels*

Surfactant Adsorption on Shale: Experiments and an Additive Model

Introduction

Shales are cap rocks for aquifers and hydrocarbon reservoirs. Shales are multi-mineral (clays, quartz, carbonates, and sometimes organics) substrates with nanometer scale pores and ultralow permeability (< 1 μD). There are plans and field tests to store CO_2 in underground reservoirs. For long-term sequestration (e.g., thousands of years), shales must act as barriers to upward CO_2 migration. By some estimates, the United States has the capacity to store CO_2 generated at stationary power plants for more than 40 years in deep saline aquifers and conventional oil reservoirs (IEA, 2019). In the latter, surfactants are being used with CO_2 to enhance production. Organic shales are also sources for hydrocarbons. According to the Energy Institute of America (EIA, 2019b), shale oil production in 2019 from the seven major plays reached 8.45 million barrels per day, including the "big three" US shale oil formations: Bakken, Eagle Ford, and Permian basin. Profitable shale oil production has been possible because of horizontal wells with multi-stage hydraulic fracturing. Hydraulic fracturing techniques have improved significantly in recent years, but the estimated oil production from these unconventional reservoirs is still less than 10%. Typically, oil production rates fall sharply in the first year (more than 75%), so new wells must be continually drilled to maintain production rates; this comes with high capital costs and environmental impacts. Hence, injection of surfactants and/or CO_2 is being considered to increase oil production from existing conventional and unconventional wells.

Surfactants have been studied for enhanced oil recovery in conventional reservoirs for many decades (Nelson and Pope, 1978). They reduce interfacial tension between oil and water and help mobilize trapped oil after waterflooding. Surfactant flooding has shown promising results in both lab and field-scale efforts (Seethepalli et al., 2004; Abalkhail et al., 2020; Barnes et al., 2018). The use of surfactants in shale reservoirs is relatively new. Kim et al. (2016) reported that oil recovery from surfactant-treated Eagle Ford shale cores improved significantly compared to cores treated with a baseline fluid containing no surfactants. Multiple experiments have shown that adding surfactant to shale can improve the efficiency of water imbibition by altering wettability (Wang et al., 2011; Wang et al., 2012; Neog and Schechter, 2016; Zeng et al., 2018). Wettability can be altered by either adding some molecules (or ions) on the solid surface or removing some molecules from the solid surface. If the first mechanism is followed, then the surfactants are adsorbed. If the second mechanism is followed, then adsorption is minimized.

A major concern of surfactant treatment is the loss of injected chemicals, mainly due to adsorption onto reservoir rock surfaces. The mechanisms of adsorption include a number of forces: e.g., electrostatic attraction, covalent bonding, hydrogen bonding, entropic interactions between hydrophobic chains on surfactants and organic matter on solids (Zhang and Somasundaran, 2006). Reducing surfactant adsorption is essential in designing a chemical-flood treatment. Wang et al. (2015) showed that the adsorption of a surfactant in carbonate cores was reduced by 30%~50% in the presence of a polymer, either pre-flushed or co-injected. Adding alkali can also reduce the adsorption of anionic surfactants by reducing the positive surface charge on calcites by increasing the pH (Hirasaki et al., 2008; Ghosh et al., 2017). For sandstone reservoirs, because the rock surface is mainly negatively charged, anionic surfactants are commonly used to avoid excessive adsorption.

The adsorption of surfactants onto mineral surfaces has been investigated in many prior studies; **Table 1** summarizes recent efforts. Different adsorbents and substrates are noted, as well as the main techniques for quantifying adsorption. Results from prior work indicate that at low surfactant concentrations, adsorption is dominated by electrostatic interactions between surfactant head groups and charged sites on mineral surfaces; at higher surfactant concentrations, physical interactions between hydrophobic chains and solid surfaces become important (Zhang and Somasundaran, 2006; Martínez-Luévanos et al., 1999; Mihajlović et al., 2013; Young and Miller, 2000). Typical isotherms for surfactant adsorption to minerals rise sharply at low concentrations, and reach a plateau value at the surfactant's critical micelle concentration (Gao et al., 2015). Different minerals have different affinity for different surfactants (Jian et al., 2016; Ma et al., 2013). Generally, surfactants and minerals with opposite charge and/or with more hydrogen bonding interactions enhance sorption. An important question in this chapter is what components of shale dominate surfactant sorption.

There are very few surfactant adsorption investigations on shales; studies discussed above were conducted on porous rocks of permeability 1 mD or larger. Shales are composed of many minerals, e.g., calcites, dolomites, clays, quartz and kerogen. Mirchi et al. (2014) measured adsorption of a non-ionic surfactant on a preserved shale; they measured a Langmuir isotherm which plateaued at 2.5 mg/g of adsorption just above the critical micelle concentration (CMC). J. Zhang et al. (2016) measured adsorption of an anionic, nonionic and blended surfactant onto the Middle Bakken shale, and observed

Langmuir adsorption with maximum capacities between 0.62 and 33 mg/g. Alvarez et al. (2017) showed that anionic surfactant adsorption onto different Bakken shale samples has capacities ranging from 6.2 to 8.9 mg/g at 0.2 wt% concentration. Missing in these studies is an understanding of how different shale components contribute to surfactant adsorption.

Table 1 - Summary of surfactant-mineral adsorption studies

Author and Year	Adsorbent	Substrate	Main Quantification Method
Duran-Alvarez et al. (2016)	DTAB, SDS, and CAPB	Calcite	Zeta-potential
Gao et al. (2015)	Dodecylamine(DDZ)	Scheelite, calcite	AFM
Grigg and Bai (2005)	Surfactant CD 1045 (CD)	5 minerals and 3 cores	Static & dynamic adsorption (HPLC)
Jian et al. (2016)	$C_{12-14}E_{22}$ (non-ionic)	dolomite, silica, kaolin	Static experiment (HPLC)
Ma et al. (2013)	CPC and SDS	Dolomite, limestone, calcite, silica, kaolin	Static experiment (titration)
Martinez-luevanaos et al. (1999)	Sodium dodecyl sulfate	Celestite and calcite	Static experiment (UV-vis)
Mihajlovic et al. (2013)	Stearic acid	Calcite	Active ratio from floating test
ShamsiJazeyi et al. (2014a & 2014b)	Anionic surfactant blend, polyacrylate	Calcite, dolomite	Static and dynamic adsorption (titration)
Somasundaran and Zhang (2006)	Dodecylbenzensulfonate, n-dodecyl-β-D-maltoside	Alumina and silica	Various
Young and Miller (1999)	Oleate	Calcite	In situ FT-IR/IRS
Zhou et al. (2016)	OTAC and ADS	Calcite, quartz, and shales	Contact angle

The objective of this chapter is to study and understand the mechanisms of surfactant adsorption onto shale surfaces. Adsorption of three different surfactants onto a single shale sample was first investigated, i.e., cationic, anionic, and neutral. The anionic surfactant was selected for further study because of its relatively low (i.e., favorable) adsorption. Mineral and organic matter contents of six shales were determined, and anionic surfactant adsorptions onto the shales and two common mineral components were investigated. This data was used to develop and parameterize a multi-component shale adsorption model in order to understand surfactant adsorption onto the shales.

Methodologies

Materials

Three different surfactants with varying head group charge were selected for adsorption experiments. They are shown in **Table 2** and consist of one anionic surfactant, one cationic surfactant, and one nonionic surfactant. The chemical structures of the three surfactants are shown in **Figure 1**.

Table 2 - List of surfactants selected used

Surfactant	Trade Name and Source	Description	Molecular Weight (g/mol)
C15-18 Internal Olefin Sulfonate (IOS)	Enordet 0332 (Shell)	Anionic, Foaming agent, High T tolerant	332
Nonyl Phenol Ethoxylate	Tergitol NP-40s (Sigma Aldrich)	Nonionic, High T and salinity tolerant	1980
Cetyltrimethylammonium bromide (CTAB)	CTAB (Millipore Sigma)	Cationic, High T and salinity tolerant	364

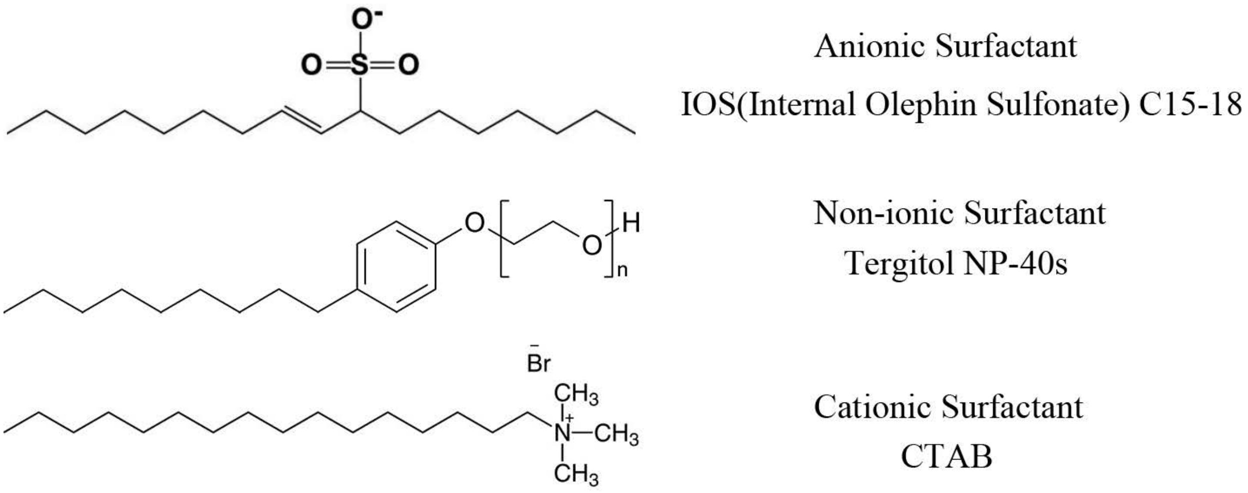

Figure 1 - Chemical structures of selected surfactants.

The CMC of the surfactants were determined by measuring the surface tension of water at different surfactant concentrations. The surface tension is a decreasing function of surfactant concentration below the CMC, and is a constant above the CMC.

Shale samples were obtained from the Eagle Ford reservoir (EF-Res) and four outcrop (OC) cores of several shale formations (from Kocurek Industries, Inc.), including Eagle Ford (EF-OC), Wolfcamp-OC, Mancos-OC, and Marcellus-OC. Calcite, quartz, and Green Shale were purchased from Ward's Science. Calcite and quartz samples were pure minerals, and Green Shale which contains approximately 70% illite was used as a representative clay-rich shale. The rock samples were mostly dry and were used as received.

Rock sample characterization

The specific surface area (SSA) of rock samples was measured using N_2 adsorption by Micromeritics 3-Flex surface analyzer. Samples were analyzed over the pressure range from 0.73mmHg to 748 mmHg, and analyzed using the Brunauer-Emmett-Teller (BET) isotherm. Mineralogy of the rock samples was measured by a commercial laboratory (Premier Oilfield Group), and Bruker D8 XRD was used. The total organic content (TOC) was also measured by Premier Oilfield Group using Leco-carbon analyzer. TOC represents all organic forms of carbon in the sample. TOC was measured at 1100 °C in the presence of oxygen. All samples were treated with HCl to remove carbonates (inorganic carbon) before TOC measurements.

Surfactant adsorption

All shale and mineral samples were broken into fine particles to create a powder, and all particles that passed through a #170 sieve (90 μm) were collected. Samples were prepared by mixing the desired amount of a dry sample powder with a 3 wt% KCl solution in bottles, and allowing it to fully hydrate for 5 days. The KCl solution was used to represent subsurface formation water, and to prevent clay swelling that occurs upon exposure to fresh water. After hydration, the test surfactant was added to the shale-brine or mineral-brine solution. The pH of the solution was not adjusted. For IOS experiments, the equilibrium pH was around 8.7 for all experiments. The bottles were allowed to equilibrate for 5 days at 80 ^oC. After equilibration, brine from the top of the bottles was collected via a pipette, diluted and analyzed for the surfactant concentration. In initial experiments, the surfactant concentration in the brine was monitored and "equilibration" was defined as the time when this concentration stopped changing with time. An equilibration time of 5 days was found to be sufficient.

Analytical method for measuring surfactant concentration

An HPLC method was developed to measure the non-ionic NP-40s surfactant concentration. A Shimadzu HPLC Nexera-i LC-2040C with a Shimadzu RF-20A fluorescence detector was used. The mobile phase was 60% Acetonitrile and 40% water (isocratic). The flow rate was 1mL/min. The column used was a 50 mm x 4.6 mm Shimadzu C18 with 5 micron bead size. The fluorescence detection parameters were: λ_{ex}=222 nm, λ_{em}=305 nm. An example chromatogram is shown in **Figure 2**.

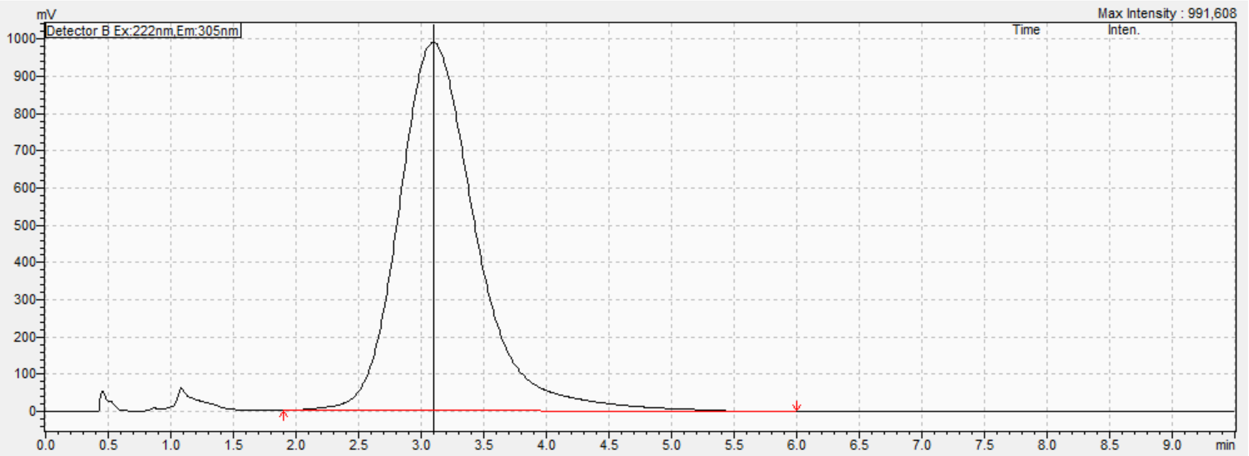

Figure 2 - HPLC response for NP-40s, the peak for the surfactant is between 1.8 min and 6 min

Both anionic and cationic surfactant concentrations were analyzed by UV-vis. The methods to detect anionic and cationic surfactants are very similar: the procedures are the same and the only difference is the chemical used. The principle of the methods is shown in **Eq. 1** and **Eq. 2**. The anionic surfactant (AS) reacts with methylene blue (MB) to form a 1:1 AS-MB complex (Jurado et al., 2006). Similarly, the cationic surfactant (CS) reacts with methyl orange (MO) to form a 1:1 CS-MO complex. Both of these complexes are organic; they were extracted by chloroform out of the water phase, and then analyzed by a Cary 50 UV-vis Spectrophotometer. Detailed steps for the analysis are listed in **Table 3.**

$$\text{Cationic Surf}^{+}(aq)+\text{MO}^{-}(aq) \leftrightarrow [\ \text{Cationic Surf-MO}\ ](org) \qquad (1)$$

$$\text{Anionic Surf}^{-}(aq)+\text{MB}^{+}(aq) \leftrightarrow [\ \text{Anionic Surf-MB}\ ](org) \qquad (2)$$

Table 3 - Steps to measure anionic and cationic surfactant concentrations

For anionic surfactant (IOS C15-18)	For cationic surfactant (CTAB)
1. Add 5 mL DI water into a cuvette 2. Add 100 µL Methylene blue solution (2g/L, pH 5~6 changed by H3BO3) 3. Add 200 µL sodium tetraborate buffer (50mM, pH 10.5) 4. Add surfactant to be analyzed, make sure excess amount of methylene blue. 5. Stir the solution a little bit 6. Add 4mL chloroform, close the cap and shake 1 min 7. Let solution settle down for 5 min 8. Extra 200 µL bottom chloroform phase and add it to 1800 µL chloroform (dilute 10 times), analyze by UV-Vis. The color is blue and the peak is at ~650 nm	1. Add 5 mL DI water into a cuvette 2. Add 100 µL Methyl orange solution (2g/L) 3. Add 200 µL buffer (0.5M citric acid + 0.2M Na2HPO4) 4. Add surfactant to be analyzed, make sure excess amount of methyl orange, 5. Stir the solution a little bit 6. Add 4mL chloroform, close the cap and shake 1 min 7. Let solution settle down for 5 min 8. Extra 200 µL bottom chloroform phase and add it to 1.8mL chloroform (dilute 10 times), analyze by UV-Vis. The color is yellow and the peak is at ~420 nm

Atomic Force Microscopy

Asylum MFP-3D atomic force microscope was used for this work. DNP-10 probes were used (Bruker) that are made of silicon nitride with triangular cantilevers with nominal spring constant 0.35 N/m. The scan was conducted in contact mode with a scan rate of 0.5 Hz.

Results

Mineralogy & TOC

Scanning electron microscope (SEM) images of Eagle Ford-Reservoir (EF-Res) shale samples were taken to evaluate surface morphology and heterogeneity (after a surface treatment with 2% HCl), and these were complemented by Energy dispersive spectroscopy (EDS) measurements at selected locations. Results are shown in **Figure 3**. The SEM images show that the shale is very heterogeneous at the scale of microns, with surface morphologies varying from flat sections, to angular features, mushroom shapes, or parallel stripes. The EDS results show high variability in elemental composition across the samples, and indicate regions on the order of tens of microns can be dominated by one mineral (e.g., silica) or another (e.g., calcite).

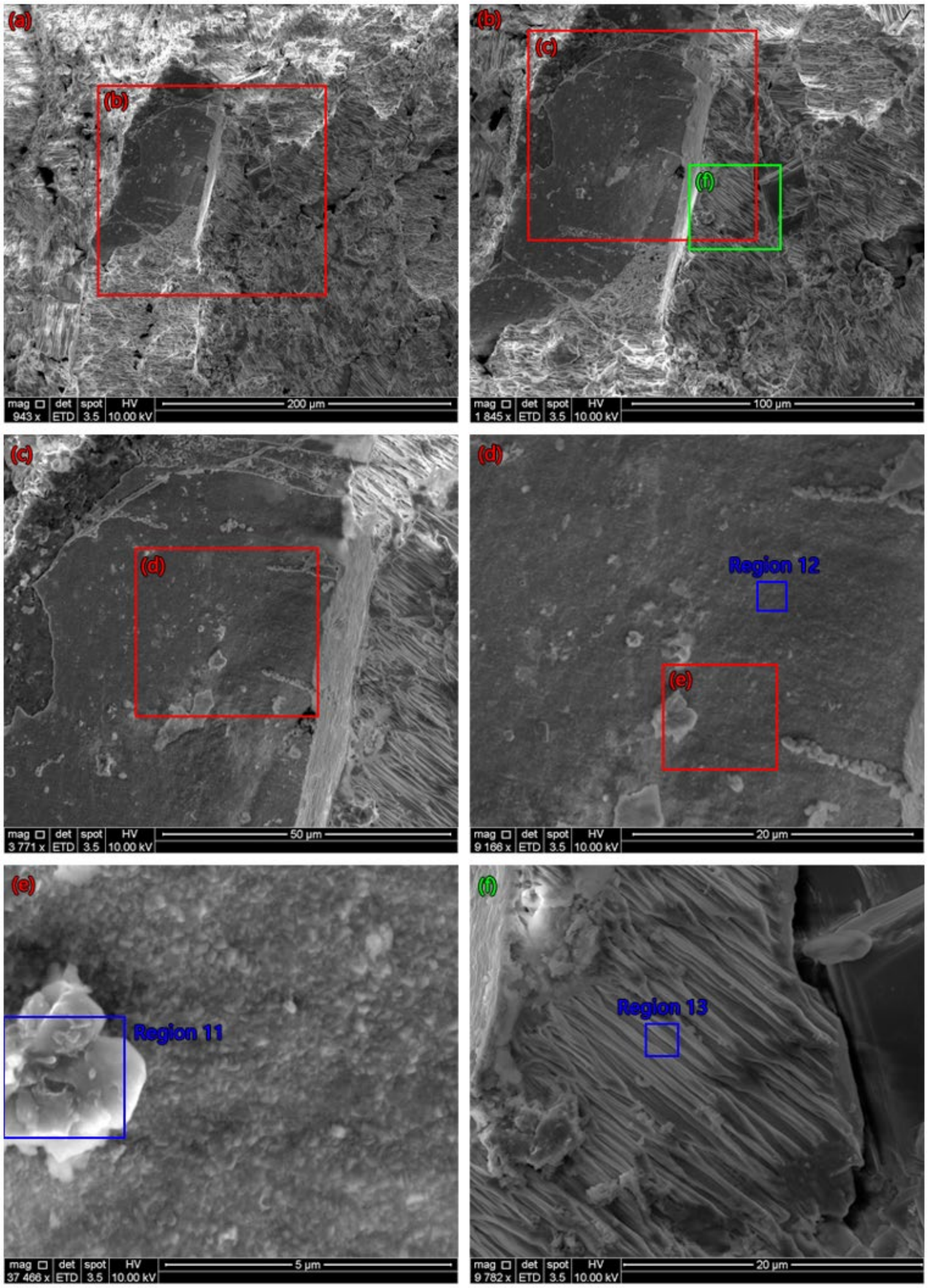

Region 11:
3.51% Ca
94.03% Si
2.46% Al

Region 12:
48.13% Ca
0.54% Si
0.35% Al
31.87% F

Region 13:
97.26% Ca
1.61% Si
1.12% Al

Figure 3 - SEM images and EDS results of Eagle Ford-Res shale

X-ray diffraction (XRD) and Total Organic Carbon Analysis (TOC) were performed to characterize the composition of the shale samples. The results are shown in **Table 4**. Each value is the average of 3 samples. Eagle Ford shales (both reservoir and outcrop) are dominated by calcite; Wolfcamp and Marcellus shales are also rich in calcite. Mancos shale and Green Shale are rich in clays and quartz. The TOC is the highest for the Eagle Ford reservoir shale, followed by Marcellus-OC shale. The Eagle Ford-OC shale has much lower TOC, silicate and alumino-silicate contents than Eagle Ford reservoir shale.

Table 4 - XRD and TOC for 6 shale samples in mass percentages.

Mineral	Chemical Formula	EF-Res sample	EF-OC sample	Wolfcamp –OC sample	Mancos –OC sample	Marcellus –OC sample	Green Shale sample
Calcite	$CaCO_3$	67.46	82.94	93.68	8.35	89.75	2.09
Dolomite	$CaMg(CO_3)_2$	0	3.55	0.20	10.78	0.22	3.89
Siderite	$FeCO_3$	0.15	0	0	0	0	0
Apatite	$Ca_5(PO_4)_3OH$	0.66	0	0	0	0	0
Pyrite	FeS_2	1.28	0	0	0.93	0	0
Quartz	SiO_2	8.72	4.38	2.54	47.29	4.43	25.35
K-Spar	$KAlSi_3O_8$	4.96	0	0	0.87	0	1.07
Plagioclase	$NaAlSi_3O_8$-$CaAl_2Si_2O_8$	4.09	1.27	1.14	4.33	1.09	0
Total Clays	-	11.60	7.04	1.86	27.18	3.14	67.60
Chlorite		0.49	0	0	1.39	0	0
Kaolinite		0.71	7.04	0	3.39	0	0
Illite/Mica		6.16	0	1.86	10.47	3.14	67.60
Mx I/S		4.24	0	0	11.93	0	0
TOC		**3.72**	**0.83**	**0.21**	**1.04**	**2.24**	**0.10**

BET Surface Area

BET surface area measurements were performed on all six shale samples and two pure minerals, which are calcite and quartz. The results are shown in **Table 5**. A typical BET surface area plot is shown in **Figure 4**. The region where relative pressure is between 0.05 and 0.35 in **Figure 4** was fitted with a straight line, and the slope and the intercept of the fitted line were used to calculate the specific area for the sample.

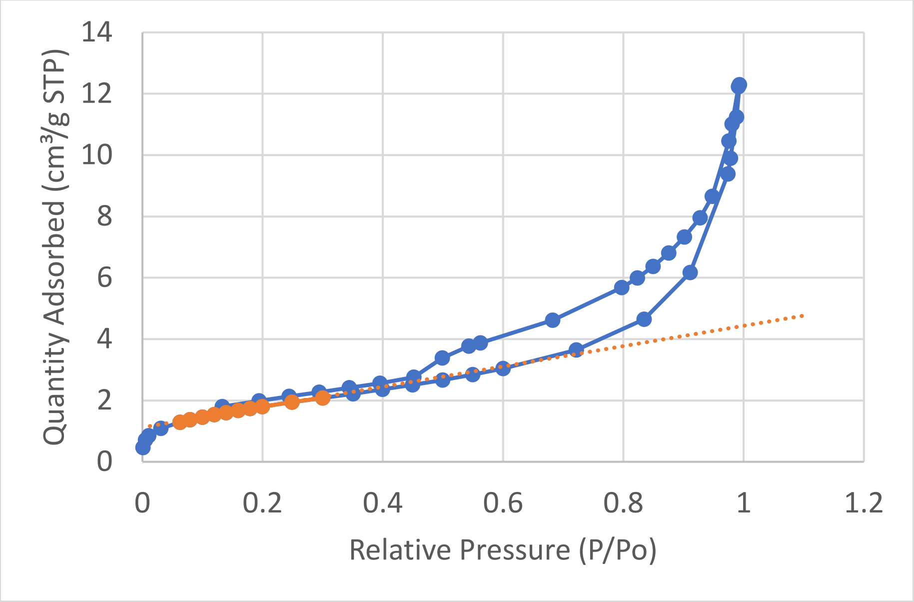

Figure 4 - Nitrogen adsorption as a function of pressure for EF-Res

The numbers listed in **Table 5** are the surface areas of powdered shale samples instead of shale blocks. Extra surface area was introduced because of the crushing of the rocks. However, these samples have both interparticle and intraparticle surface areas. We increase the interparticle area by crushing, but the interparticle area is much smaller than the intraparticle area. The adsorption reported in this draft could be a little bit higher than reservoir conditions due to the extra surface area introduced by crushing, but the main effect of powdering is decreasing the time required to reach adsorption equilibrium.

Table 5 - BET surface area of 2 minerals and 6 shale samples

Rock Type	Specific area (m^2/g)
Calcite	0.266 ± 0.006
Quartz	0.218 ± 0.003
EF-Res (reservoir rock) sample	6.651 ± 0.045
EF-OC (Outcrop) sample	0.580 ± 0.004
Wolfcamp-OC (Outcrop) sample	1.014 ± 0.002
Mancos-OC (Outcrop) sample	8.355 ± 0.026
Marcellus-OC (Outcrop) sample	1.333 ± 0.023
Green Shale (Outcrop) sample	19.258 ± 0.131

CMC of surfactants

The critical micelle concentrations (CMC) of the surfactants were determined by measuring the surface tension of water at different surfactant concentrations, as shown in **Figure 5**. The critical micelle concentration for the anionic IOS surfactant is 93 mg/L (0.28 mM), for the non-ionic NP-40s is 232 mg/L (0.12 mM), for the cationic CTAB is 248 mg/L (0.68 mM).

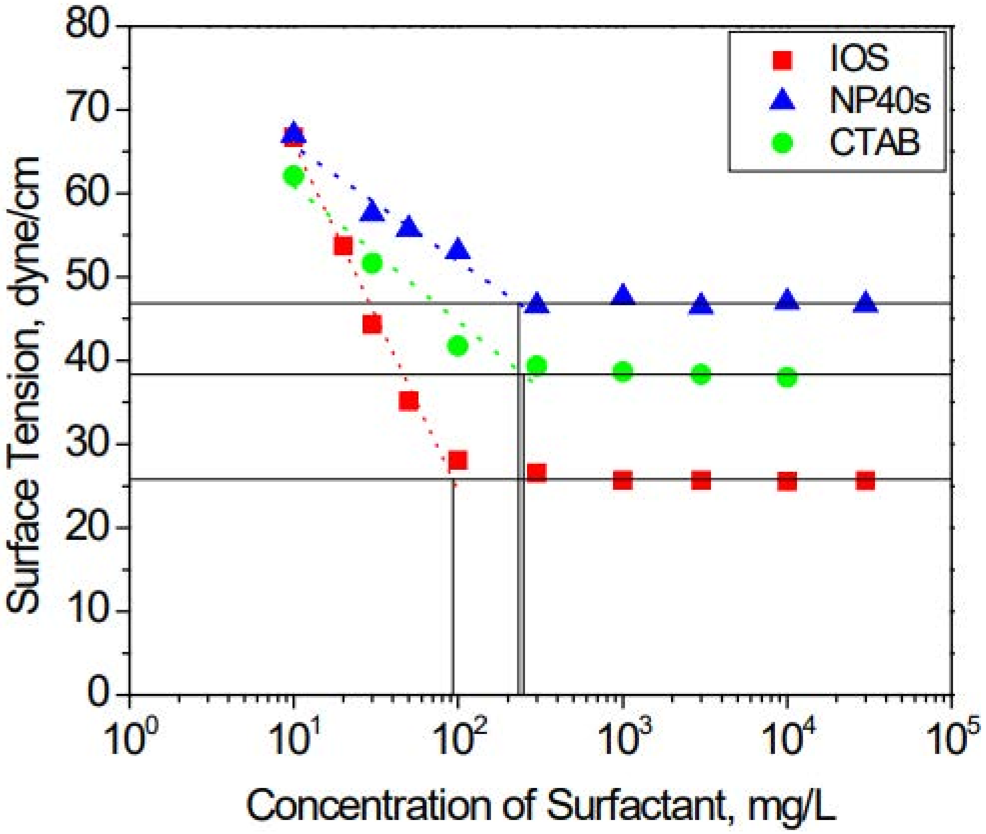

Figure 5 - Surface tension as a function of surfactant concentration; CMC values are indicated by the vertical lines

Adsorption on EF-Res

The adsorption coefficient, q, was calculated from the mass of shale powder in the adsorption experiment, the volume of surfactant solution, and the difference in surfactant concentration before and after sorption onto the shale, as shown in **Eq. 3**,

$$q = \frac{V_{sol} \times (C_0 - C_1)}{m_{rock}} \times 10^{-3} \qquad (3)$$

Where:

q is the surfactant adsorption coefficient, mg/g-rock;

V_{sol} is the total volume of the solution in original bulk solution, mL;

C_0 is the surfactant concentration in initial solution before equilibrated with rock, mg/L;

C_1 is the surfactant concentration in aqueous solution after equilibration with rock, mg/L;

and m_{rock} is the total mass of crushed rock, g.

The adsorption coefficient q for all 3 surfactants on EF-Res samples is plotted against the equilibrium concentration, as shown in **Figure 6**.

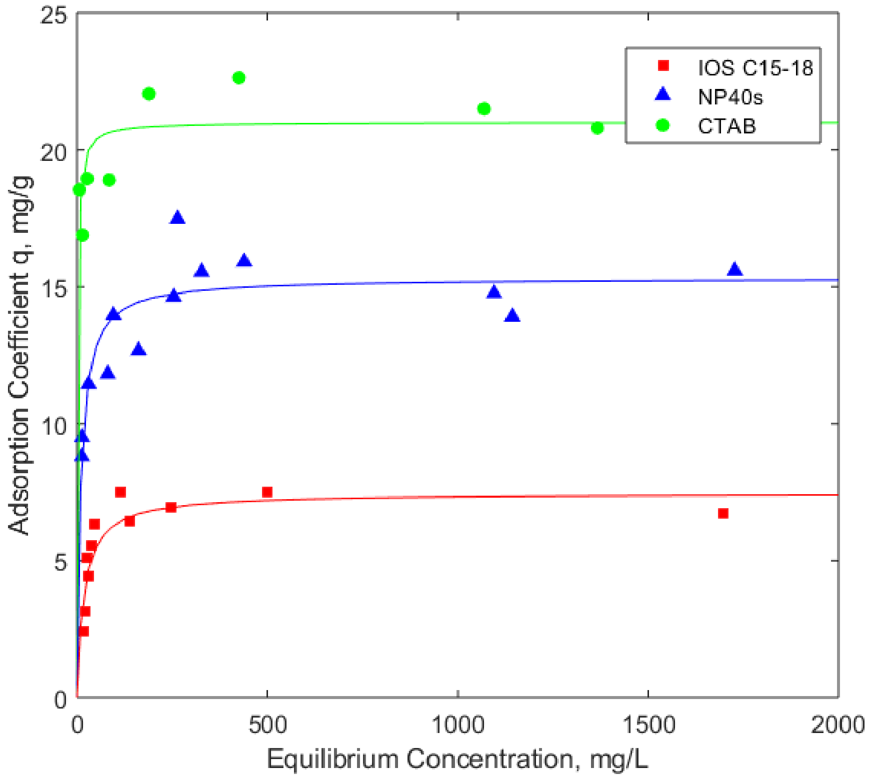

Figure 6 - Adsorption isotherm for three surfactants on EF-Res with Langmuir isotherm fits

Surfactant adsorption q increases as the surfactant concentration in water increases for concentrations below CMC. When the concentration goes beyond the CMC, q reaches a plateau. Langmuir isotherms were fit to the data using **Eq. 4**,

$$q = q_{\infty} \frac{KC}{1+KC} \tag{4}$$

where q_{∞} is the plateau (or maximum) adsorption coefficient (mg/g), K is an adsorption constant ($(\mathrm{mg/L})^{-1}$) related to the binding energy, and C is the equilibrium concentration (mg/L).

Table 6 - Maximum adsorption capacities.

Surfactant	IOS	NP-40s	CTAB
q_{∞}	6.81 mg/g	15.13 mg/g	21.67 mg/g
	20.51 mmol/kg	7.64 mmol/kg	59.53 mmol/kg
	1.02 mg/m^2	2.27 mg/m^2	3.26 mg/m^2

Maximum adsorption capacities, q_{∞}, are summarized in **Table 6**. CTAB shows the highest adsorption capacity in mg/g (or mg/m^2), followed by NP-40s, and then IOS. The strong CTAB sorption was expected, because this cationic surfactant likely binds to clay surfaces. Clays are typically negatively charged at neutral pH, and have a very high surface area compared to other shale minerals. The adsorption of CTAB on negatively charged solid surfaces have been studied in the literature in the presence of salt (Manne and Gaub, 1995; Pagac et al., 1998). Spherical micelles adsorbed on amorphous silica have been observed by AFM (Manne and Gaub, 1995). The positively charged micelles compete with the cations in the double layer, but adsorb on the negatively charged solid surfaces.

The preferential sorption of NP-40s over IOS was not expected, because shale surfaces are generally considered charged at neutral pH (Alvarez et al., 2018). However, shales also contain residual kerogen and oil, both hydrophobic components that can strongly adsorb NP-40s. Also, the molecular weight of NP-40s is more than 6 times greater than each of the other two surfactants. The non-ionic NP-40s has the lowest adsorption capacity in molar units. Sorption of IOS is expected to be dominated by binding to positively charged carbonate minerals (e.g., calcite, dolomite). These are the dominant minerals in the Eagle Ford shale, but they have a relatively small surface area compared to clays. This may explain why IOS is characterized by the weakest adsorption among the three surfactants. Since weak adsorption is a favorable quality when considering surfactant losses during injection, the IOS was selected for further study.

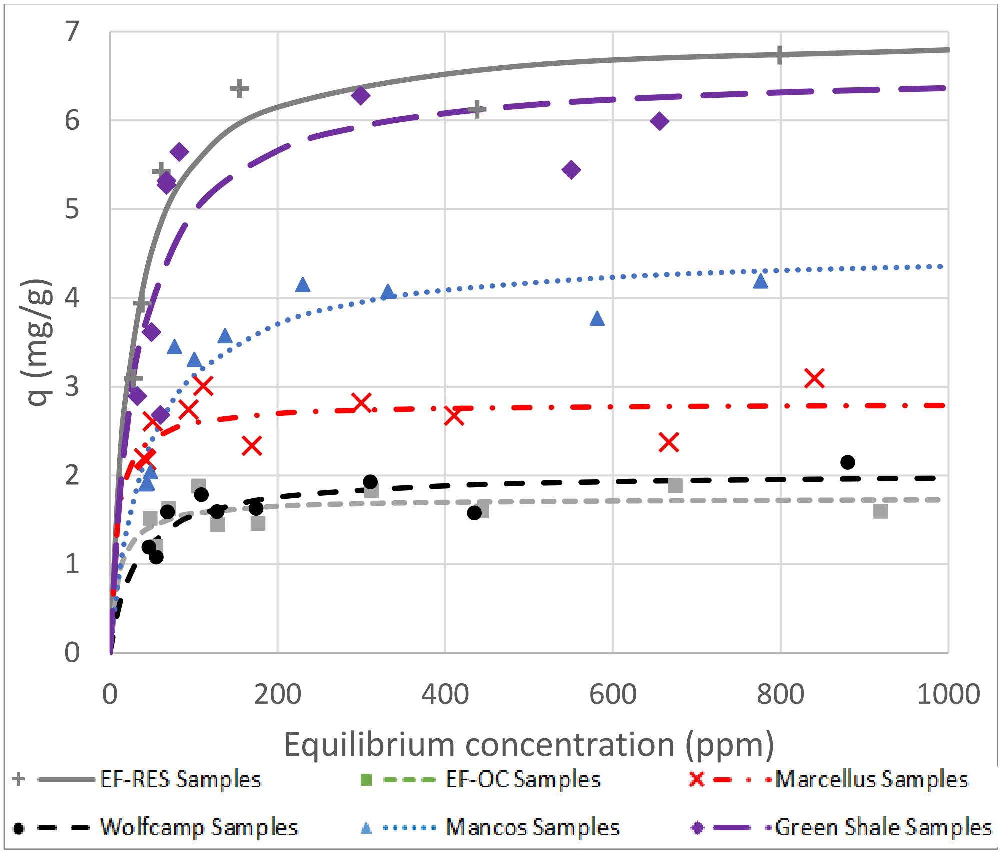

Figure 7 - Adsorption coefficient of IOS on 6 different shales and the fitted Langmuir isotherms

2.3.5 Effect of Shale Composition on Surfactant Adsorption

To understand the effect of shale composition on surfactant adsorption on shales, we measured the adsorption isotherms of the anionic IOS surfactant on 6 different shales and 2 pure minerals. Results are shown in **Figure 7** and **Figure 8**, respectively.

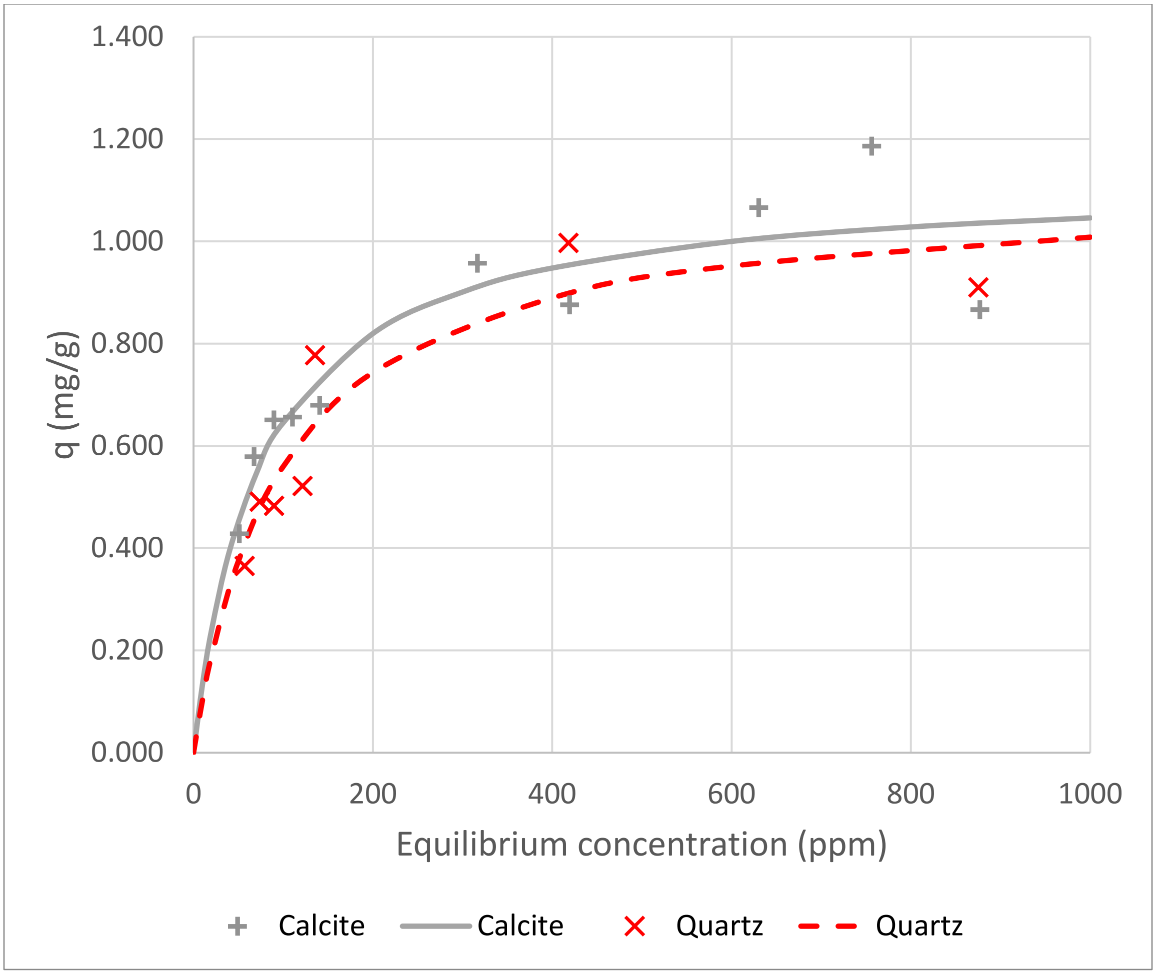

Figure 8 - Adsorption coefficient of IOS on two pure minerals and the fitted Langmuir isotherms

Per **Figure 7**, adsorption coefficients reach a plateau above the CMC for all shales. Eagle Ford reservoir rock shows the highest adsorption capacity, while the Eagle Ford outcrop shows the lowest adsorption capacity. This difference may result from the difference in organic and clay content. The reservoir rock had greater organic content, thus adsorbing more surfactant. The Green Shale and the Mancos outcrop show the next highest adsorption capacity, probably because they have more clay than other outcrops. The high surface area of clay provides more sites for adsorption. Per **Figure 8**, the adsorption capacity of calcite and quartz are much lower than that of the shales. Calcite and quartz samples have much less surface area than porous shale samples, and hence less adsorption capacity.

We performed AFM measurements of IOS adsorption on calcite to visualize the adsorption behavior. A single calcite sheet was cleaved from a calcite block, and immediately placed in water or 1000 mg/L surfactant solution. **Figure 9** shows the comparison between the calcite surface with and without surfactant adsorption. After 2.5 hours in DI water (**Figure 9** left), the calcite surface showed some etching as indicated by the dark color. However, when treated by surfactant solution (**Figure 9** right), the surfactant particles adsorbed onto the calcite surface in a hemi-micelle-like structure as indicated by the scattered light-colored hills. More AFM work can be conducted to have a better understanding of surfactant-mineral interaction in the nanometer-scale.

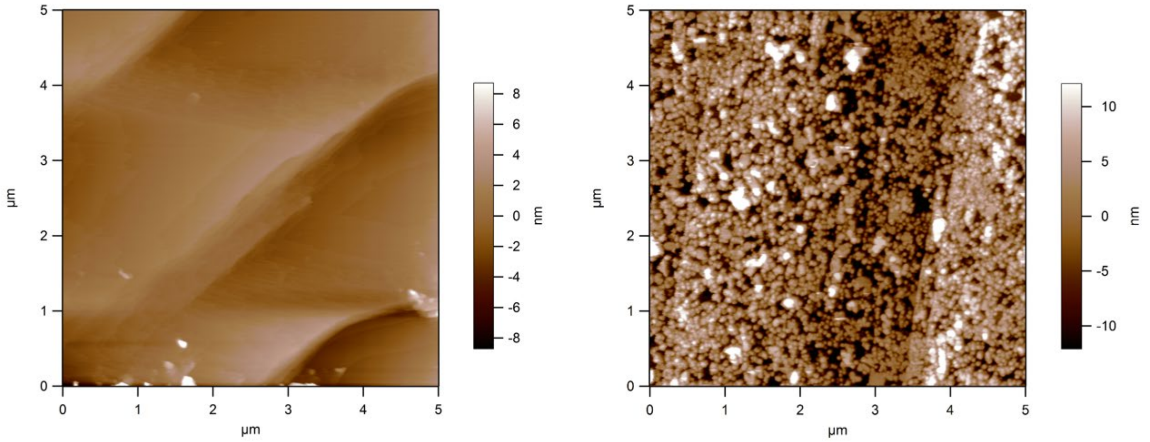

Figure 9 - 2D view of calcite surface after submerging in DI water (left) and DI water with 1,000 ppm IOS surfactant (right) for 2.5 hours

Adsorption model

Adsorption of IOS on the 2 pure minerals and all 6 shales showed Langmuir adsorption behavior. The Langmuir parameters q_∞ and K are listed in **Table 7**. The pure minerals have the lowest plateau adsorption coefficient, followed by the outcrop shales. The Green Shale and the Eagle Ford reservoir shale have the two highest adsorption coefficients.

Table 7 - Fitted parameters of the Langmuir model.

	q_∞ (mg/g)	K (ppm^{-1})
Calcite	1.12 ± 0.16	0.014
Quartz	1.11 ± 0.29	0.010
EF-Res sample	6.98 ± 1.05	0.037
EF-OC sample	1.74 ± 0.25	0.092
Wolfcamp-OC sample	2.03 ± 0.35	0.032
Mancos-OC sample	4.56 ± 0.61	0.022
Marcellus-OC sample	2.81 ± 0.35	0.119
Green Shale sample	6.59 ± 1.33	0.031

Assuming that all the minerals follow a Langmuir type adsorption, the adsorption of IOS on shales can be considered to be a combination of adsorption by minerals and organic matter. An additive model was constructed to predict the adsorption isotherm based on the composition of shales, as shown in **Eq. 5**.

$$q = \sum_{i=1}^{4} \frac{q_{\infty,i} * K_i C}{1 + K_i C} * f_i \qquad (5)$$

where

f_1 is the mass fraction of calcite in the rock (g/g),
f_2 is the mass fraction of quartz in the rock (g/g),
f_3 is the mass fraction of clay in the rock (g/g),
f_4 is the mass fraction of TOC in the rock (g/g),
$q_{\infty,1} = 1.12 \pm 0.16$ mg/g; $K_1 = 0.014$ (from calcite adsorption isotherm),
and $q_{\infty,2} = 1.11 \pm 0.29$ mg/g; $K_2 = 0.010$ (from quartz adsorption isotherm).

The parameters $q_{\infty,3}$, K_3, $q_{\infty,4}$, and K_4 are then fit by regression to minimize the error between the six predicted shale isotherms and the measured isotherms. Also, calcite and dolomite are lumped into "calcite" in this model, silicates (excluding clays) are lumped into "quartz", and clays are lumped together. The rationale is that these groupings have similar surface charge and/or surface area.

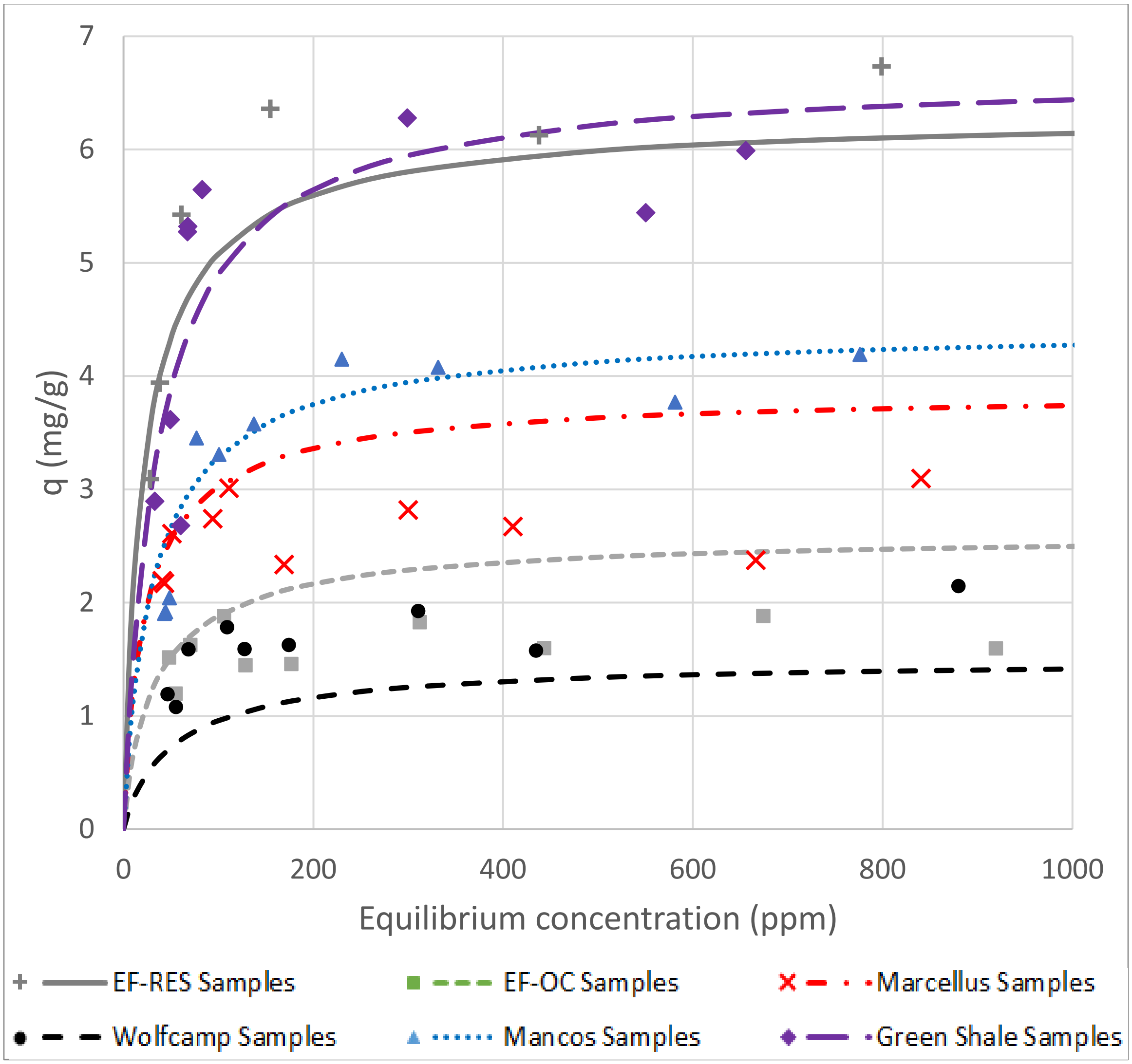

Figure 10 - Adsorption coefficient of IOS on 6 shale samples and the additive model predictions

Figure 10 shows the comparison of the additive model profiles to the experimental data. The best fits are obtained for Mancos and Green Shale, likely due to the way the additive model was built. Specifically, we fixed q_∞ and K for calcite and quartz, while using the regression to determine q_∞ and K for clay and organic matter. Therefore, for shales rich in carbonate minerals, like EF-OC, Wolfcamp-OC, and Marcellus-OC, which contain more than 80 wt% carbonate, running the regression does not cause much change in the additive model isotherms because the parameters for calcite were already fixed. However, for Mancos and Green Shale, which contain more clay minerals, running the regression on parameters for clay makes the additive model fit these two samples better.

An alternative way to interpret the fit is to plot q_∞ predicted from the additive model to q_∞ measured from the data; results are shown in **Figure 11**. The data points lie close to the y=x line, indicating adequate model quality. The deviation of predicted q_∞ originates from the heterogeneity of shale samples and the lumping within each mineral category.

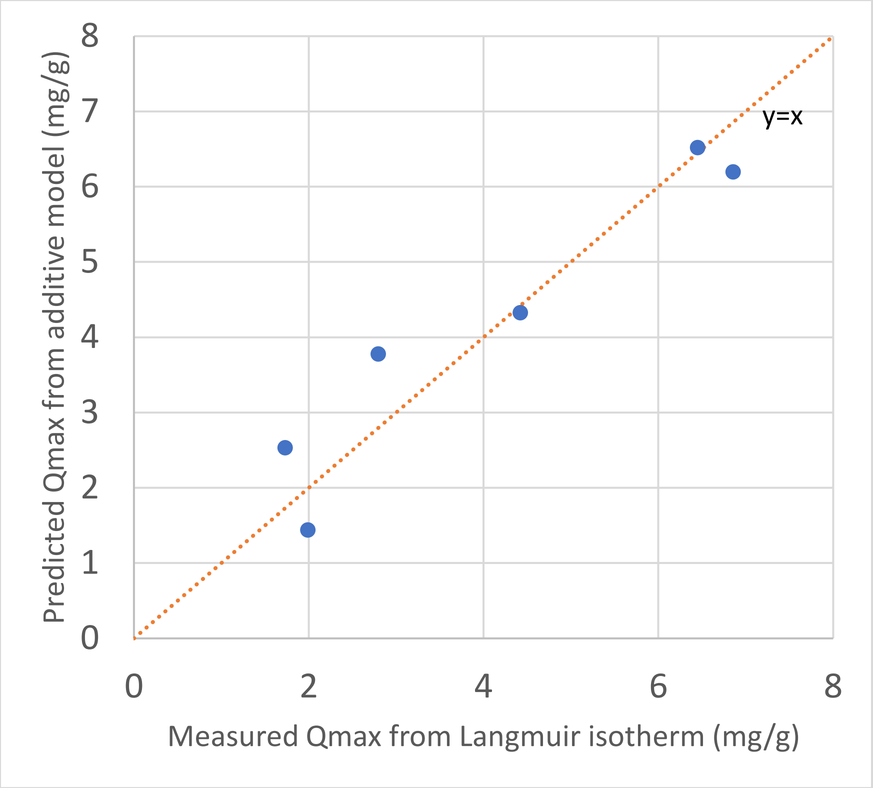

Figure 11 - Parity plot for measured q_∞ vs predicted q_∞

Best fit parameters from the model are

$q_{\infty,3} = 9.10 \pm 1.07$ mg/g, $K_3 = 0.030$,
$q_{\infty,4} = 104.6 \pm 19.3$ mg/g, and $K_4 = 0.080$.

These results show that calcite and quartz have the lowest adsorption capacities, and organic matter the highest. In fact, the $q_{\infty,4}$ for TOC exceeds others by one to two orders of magnitude. These results are reasonable, and the value of $q_{\infty,4}$ explains why the Eagle Ford reservoir rock has similar mineral composition as Eagle Ford outcrop, but a much higher adsorption capacity. This value and the relatively high TOC content also explain why IOS adsorption to Marcellus-OC is dominated by TOC.

The mass percentage of IOS on individual shale components is listed in **Table 8**. Despite the relatively high value of $q_{\infty,4}$, TOC does not completely dominate adsorption because its mass fraction (f_4) is always less 4%. In some cases (e.g., Green Shale), the TOC contribution to adsorption is small. For example, IOS adsorption in Mancos-OC and Green Shale are dominated by clay, while that in Wolfcamp-OC and EF-OC are controlled by calcite.

Table 8 - Mass percentages of IOS adsorption to shale components

	EF-Res sample	EF-OC sample	Wolfcamp-OC sample	Mancos-OC sample	Marcellus-OC sample	Green Shale sample
Calcite	12%	37%	70%	5%	26%	1%
Quartz	3%	2%	3%	13%	2%	4%
Clay	19%	25%	11%	56%	7%	93%
TOC	66%	36%	16%	26%	65%	2%
SUM	**100%**	**100%**	**100%**	**100%**	**100%**	**100%**

Conclusions

The adsorption capacity of three surfactants (cationic, nonionic and anionic) was measured on Eagle Ford reservoir shale samples. The cationic surfactant, CTAB, showed the highest adsorption capacity in molar units, followed by anionic IOS and then non-ionic NP-40s. CTAB also had the highest adsorption in mass units, followed by NP-40 and then IOS. Adsorption of anionic surfactant onto two pure minerals (calcite and quartz) and shale samples from six formations was investigated, and all of them showed Langmuir type isotherms. The adsorption capacity depends on the mineral composition of the rocks. The adsorption in Mancos-OC and Green Shale are dominated by clay, while that in Wolfcamp-OC and EF-OC are dominated by calcite. The adsorption in EF-Res sample and Marcellus-OC are dominated by the organic content. An additive model was built to estimate the adsorption capacity given the mineral composition and TOC. The model shows that organic matter and clay have the most significant impact per unit mass, but the contribution of each component on adsorption also depends on its corresponding mass fraction in the shales. The adsorption results are for the samples we tested and does not reflect the values for the whole shale formations, which are huge and heterogeneous.

References

Abalkhail, N. A., Liyanage, P. J., Upamali, K. A., Pope, G. A., & Mohanty, K. K. (2019). ASP Flood Application for a High-Temperature, High-Salinity Carbonate Reservoir. *SPE Middle East Oil and Gas Show and Conference*. https://doi.org/10.2118/194948-ms

Abalkhail, N., Liyanage, P. J., Upamali, K. A., Pope, G. A., & Mohanty, K. K. (2020). Alkaline-surfactant-polymer formulation development for a HTHS carbonate reservoir. *Journal of Petroleum Science and Engineering*, *191*, 107236. https://doi.org/10.1016/j.petrol.2020.107236

Afanasev, P., Scerbacova, A., Tsyshkova, A., Mukhina, E., Grishin, P., Grishaev, V., Cheremisin, A., Koltsov, I., Dvoretskaya, E., Kasyanenko, A., Demo, V., Prochukhan, K., & Cheremisin, A. (2019). Compositions of Anionic and Non-Ionic Surfactants within a Hybrid EOR Technology for Unconventional Hydrocarbon Reservoirs. *SPE Russian Petroleum Technology Conference*. https://doi.org/10.2118/196759-ms

Alfarge, D., Wei, M., & Bai, B. (2020). Introduction to shale and tight oil reservoirs. *Developments in Petroleum Science*, 1–13. https://doi.org/10.1016/b978-0-12-818343-4.00001-2

Alharthy, N., Teklu, T., Kazemi, H., Graves, R., Hawthorne, S., Braunberger, J., & Kurtoglu, B. (2017). Enhanced Oil Recovery in Liquid–Rich Shale Reservoirs: Laboratory to Field. *SPE Reservoir Evaluation & Engineering*, *21*(01), 137–159. https://doi.org/10.2118/175034-pa

Alkhaldi, M., Nasr-El-Din, H., & Sarma, H. (2009). Application of Citric Acid in Acid Stimulation Treatments. *Canadian International Petroleum Conference*. https://doi.org/10.2118/2009-015

Alvarez, J. O., & Schechter, D. S. (2016). Wettability Alteration and Spontaneous Imbibition in Unconventional Liquid Reservoirs by Surfactant Additives. *SPE Reservoir Evaluation & Engineering*, *20*(01), 107–117. https://doi.org/10.2118/177057-pa

Alvarez, J. O., Saputra, I. W. R., & Schechter, D. S. (2017). Potential of Improving Oil Recovery with Surfactant Additives to Completion Fluids for the Bakken. *Energy & Fuels*, *31*(6), 5982–5994. https://doi.org/10.1021/acs.energyfuels.7b00573

Alvarez, J. O., Saputra, I. W., & Schechter, D. S. (2018). The Impact of Surfactant Imbibition and Adsorption for Improving Oil Recovery in the Wolfcamp and Eagle Ford Reservoirs. *SPE Journal*, *23*(06), 2103–2117. https://doi.org/10.2118/187176-pa

Bardon, C., Corlay, P., Longeron, D., & Miller, B. (1994). CO2 Huff 'n' Puff Revives Shallow Light-Oil-Depleted Reservoirs. *SPE Reservoir Engineering*, *9*(02), 92–100. https://doi.org/10.2118/22650-pa

Barnes, J. R., van Batenburg, D. W., Faber, M. J., van Rijn, C. H., Geib, S., van Kuijk, S. R., Perez Regalado, D., King, T. E., Doll, M. J., & Crom, L. E. (2018). Quality Assurance and Quality Control of Surfactants for Field-Scale Enhanced-Oil-Recovery Pilot Projects. *SPE Reservoir Evaluation & Engineering*, *22*(02), 565–576. https://doi.org/10.2118/177613-pa

Bartz, S., Mach, J. M., Saeedi, J., Haskell, J., & Manrique, J. (1997). Let's get the most out of existing wells. *Oilfield review*, *9*(4), 2-21.

Bodini, S. A., Forni, L. P., Tuero, F., Crotti, M. A., & Labayen, I. L. (2018). Unconventional EOR: Field Tests Results in Vaca Muerta Shale Play: A Capillary Based Improved Oil Recovery Case Study for Shale/Tight Oil Scenarios. *SPE Argentina Exploration and Production of Unconventional Resources Symposium*. https://doi.org/10.2118/191877-ms

Cander, H. (2012). PS what are unconventional resources? A simple definition using viscosity and permeability. In *AAPG Annual Convention and Exhibition. Tulsa, US: American Association of Petroleum Geologists and Society for Sedimentary Geology*.

Carlisle, C., Al-Maraghi, E., Al-Saad, B., Britton, C., Fortenberry, R., & Pope, G. (2014). One-Spot Pilot Results in the Sabriyah-Mauddud Carbonate Formation in Kuwait Using a Novel Surfactant Formulation. *SPE Improved Oil Recovery Symposium*. https://doi.org/10.2118/169153-ms

Chen, C., Balhoff, M., & Mohanty, K. K. (2014). Effect of Reservoir Heterogeneity on Primary Recovery and CO2 Huff 'n' Puff Recovery in Shale-Oil Reservoirs. *SPE Reservoir Evaluation & Engineering*, *17*(03), 404–413. https://doi.org/10.2118/164553-pa

Das, A., Nguyen, N., & Nguyen, Q. P. (2020). Low tension gas flooding for secondary oil recovery in low-permeability, high-salinity reservoirs. *Fuel*, *264*, 116601. https://doi.org/10.1016/j.fuel.2019.116601

Durán-Álvarez, A., Maldonado-Domínguez, M., González-Antonio, O., Durán-Valencia, C., Romero-Ávila, M., Barragán-Aroche, F., & López-Ramírez, S. (2016). Experimental–Theoretical Approach to the Adsorption Mechanisms for Anionic, Cationic, and Zwitterionic Surfactants at the Calcite–Water Interface. *Langmuir*, *32*(11), 2608–2616. https://doi.org/10.1021/acs.langmuir.5b04151

Egboga, N. U., Mohanty, K. K., & Balhoff, M. T. (2017). A feasibility study of thermal stimulation in unconventional shale reservoirs. *Journal of Petroleum Science and Engineering*, *154*, 576–588. https://doi.org/10.1016/j.petrol.2016.10.041

EIA. (2019a). *Annual Energy Outlook 2019*. Eia.Gov. https://www.eia.gov/outlooks/archive/aeo19/

EIA. (2019b). *Drilling Productivity Report*. Eia.Gov. https://www.eia.gov/petroleum/drilling/archive/2019/06/

EIA. (2021). *Annual Energy Outlook 2021*. Eia.Gov. https://www.eia.gov/outlooks/aeo/

Falls, A., Thigpen, D., Nelson, R., Ciaston, J., Lawson, J., Good, P., Ueber, R., & Shahin, G. (1994). Field Test of Cosurfactant-Enhanced Alkaline Flooding. *SPE Reservoir Engineering*, *9*(03), 217–223. https://doi.org/10.2118/24117-pa

Gamadi, T. D., Sheng, J. J., & Soliman, M. Y. (2013). An Experimental Study of Cyclic Gas Injection to Improve Shale Oil Recovery. *SPE Annual Technical Conference and Exhibition*. https://doi.org/10.2118/166334-ms

Gao, Y., Zhao, M., Wang, J., & Zong, C. (2014). Performance and gas breakthrough during CO 2 immiscible flooding in ultra-low permeability reservoirs. *Petroleum Exploration and Development*, *41*(1), 88–95. https://doi.org/10.1016/s1876-3804(14)60010-0

Gao, Z., Sun, W., & Hu, Y. (2015). New insights into the dodecylamine adsorption on scheelite and calcite: An adsorption model. *Minerals Engineering*, *79*, 54–61. https://doi.org/10.1016/j.mineng.2015.05.011

Ghosh, P., Sharma, H., & Mohanty, K. K. (2017). Chemical Flooding in Low Permeability Carbonate Rocks. *SPE Annual Technical Conference and Exhibition*. https://doi.org/10.2118/187274-ms

Ghosh, P., Sharma, H., & Mohanty, K. K. (2019). ASP flooding in tight carbonate rocks. *Fuel*, *241*, 653–668. https://doi.org/10.1016/j.fuel.2018.12.041

Goral, J., Panja, P., Deo, M., Andrew, M., Linden, S., Schwarz, J. O., & Wiegmann, A. (2020). Confinement Effect on Porosity and Permeability of Shales. *Scientific Reports*, *10*(1). https://doi.org/10.1038/s41598-019-56885-y

Grigg, R., & Bai, B. (2005). Sorption of Surfactant Used in CO2 Flooding onto Five Minerals and Three Porous Media. *SPE International Symposium on Oilfield Chemistry*. https://doi.org/10.2118/93100-ms

Grinestaff, G., Barden, C., Miller, J., Franklin, W., Barden, C., & Ding, E. (2020). Evaluation of Eagle Ford Cyclic Gas Injection EOR: Field Results and Economics. *SPE Improved Oil Recovery Conference*. https://doi.org/10.2118/200427-ms

Habibi, A., Yassin, M. R., Dehghanpour, H., & Bryan, D. (2017). Experimental investigation of CO2-oil interactions in tight rocks: A Montney case study. *Fuel*, *203*, 853–867. https://doi.org/10.1016/j.fuel.2017.04.077

Hadlow, R. (1992). Update of Industry Experience With CO2 Injection. *SPE Annual Technical Conference and Exhibition*. https://doi.org/10.2118/24928-ms

He, K., & Xu, L. (2017). Unique Mixtures of Anionic/Cationic Surfactants: A New Approach to Enhance Surfactant Performance in Liquids-Rich Shale Reservoirs. *SPE International Conference on Oilfield Chemistry*. https://doi.org/10.2118/184515-ms

Healy, R. N., & Reed, R. L. (1977). Immiscible Microemulsion Flooding. *Society of Petroleum Engineers Journal*, *17*(02), 129–139. https://doi.org/10.2118/5817-pa

Hirasaki, G. J., Miller, C. A., & Puerto, M. (2008). Recent Advances in Surfactant EOR. *SPE Annual Technical Conference and Exhibition*. https://doi.org/10.2118/115386-ms

Ho, T. A., & Wang, Y. (2019). Enhancement of oil flow in shale nanopores by manipulating friction and viscosity. *Physical Chemistry Chemical Physics*, *21*(24), 12777–12786. https://doi.org/10.1039/c9cp01960j

Hoffman, B. T. (2012). Comparison of Various Gases for Enhanced Recovery from Shale Oil Reservoirs. *SPE Improved Oil Recovery Symposium*. https://doi.org/10.2118/154329-ms

Hoffman. B. T., & Evans, J. G. (2016). Improved Oil Recovery IOR Pilot Projects in the Bakken Formation. *SPE Low Perm Symposium*. https://doi.org/10.2118/180270-ms

Hoffman, B. T. (2018). Huff-N-Puff Gas Injection Pilot Projects in the Eagle Ford. *SPE Canada Unconventional Resources Conference*. https://doi.org/10.2118/189816-ms

IEA Greenhouse Gas R&D Programme. (2019). *A Brief History of CCS and Current Status*. https://ieaghg.org/docs/General_Docs/Publications/Information_Sheets_for_CCS_2.pdf

Jacobs, T. (2017). Optimism and Activity Rising in the Vaca Muerta. *Journal of Petroleum Technology*, *69*(05), 34–38. https://doi.org/10.2118/0517-0034-jpt

Jia, B., Tsau, J. S., & Barati, R. (2019). A review of the current progress of CO2 injection EOR and carbon storage in shale oil reservoirs. *Fuel*, *236*, 404–427. https://doi.org/10.1016/j.fuel.2018.08.103

Jian, G., Puerto, M. C., Wehowsky, A., Dong, P., Johnston, K. P., Hirasaki, G. J., & Biswal, S. L. (2016). Static Adsorption of an Ethoxylated Nonionic Surfactant on Carbonate Minerals. *Langmuir*, *32*(40), 10244–10252. https://doi.org/10.1021/acs.langmuir.6b01975

Jin, X. J., Pavia, M., Samuel, M., Shah, S., Zhang, R., & Thompson, J. (2019). Field Pilots of Unconventional Shale EOR in Permian Basin. *Unconventional Resources Technology Conference*. https://doi.org/10.15530/urtec-2019-506

Jurado, E., Fernández-Serrano, M., Núñez-Olea, J., Luzón, G., & Lechuga, M. (2006). Simplified spectrophotometric method using methylene blue for determining anionic surfactants: Applications to the study of primary biodegradation in aerobic screening tests. *Chemosphere*, *65*(2), 278–285. https://doi.org/10.1016/j.chemosphere.2006.02.044

Kiani, S., Rogers, S. E., Sagisaka, M., Alexander, S., & Barron, A. R. (2019). A New Class of Low Surface Energy Anionic Surfactant for Enhanced Oil Recovery. *Energy & Fuels*, *33*(4), 3162–3175. https://doi.org/10.1021/acs.energyfuels.9b00391

Kim, J., Zhang, H., Sun, H., Li, B., & Carman, P. (2016). Choosing Surfactants for the Eagle Ford Shale Formation: Guidelines for Maximizing Flowback and Initial Oil Recovery. *SPE Low Perm Symposium*. https://doi.org/10.2118/180227-ms

Kumar, K., Dao, E. K., & Mohanty, K. K. (2008). Atomic Force Microscopy Study of Wettability Alteration by Surfactants. *SPE Journal*, *13*(02), 137–145. https://doi.org/10.2118/93009-pa

Lee, J. H., & Lee, K. S. (2018). Effects of Aqueous Solubility and Diffusion of Multi-Components on Shale Reservoir Recovery during CO2 EOR. *SPE Argentina Exploration and Production of Unconventional Resources Symposium*. https://doi.org/10.2118/191859-ms

Li, L., Wang, C., Li, D., Fu, J., Su, Y., & Lv, Y. (2019). Experimental investigation of shale oil recovery from Qianjiang core samples by the CO2 huff-n-puff EOR method. *RSC Advances*, *9*(49), 28857–28869. https://doi.org/10.1039/c9ra05347f

Li, S., Li, Z., & Dong, Q. (2016). Diffusion coefficients of supercritical CO 2 in oil-saturated cores under low permeability reservoir conditions. *Journal of CO2 Utilization*, *14*, 47–60. https://doi.org/10.1016/j.jcou.2016.02.002

Liu, G., Sorensen, J. A., Braunberger, J. R., Klenner, R., Ge, J., Gorecki, C. D., Steadman, E. N., & Harju, J. A. (2014). CO2-Based Enhanced Oil Recovery from Unconventional Reservoirs: A Case Study of the Bakken Formation. *Day 2 Wed, April 02, 2014*. https://doi.org/10.2118/168979-ms

Lund, L. (2014). Decline curve analysis of shale oil production: The case of Eagle Ford.

Ma, K., Cui, L., Dong, Y., Wang, T., Da, C., Hirasaki, G. J., & Biswal, S. L. (2013). Adsorption of cationic and anionic surfactants on natural and synthetic carbonate materials. *Journal of Colloid and Interface Science*, *408*, 164–172. https://doi.org/10.1016/j.jcis.2013.07.006

Mahzari, P., Oelkers, E., Mitchell, T., & Jones, A. (2019). An Improved Understanding About CO2 EOR and CO2 Storage in Liquid-Rich Shale Reservoirs. *SPE Europec Featured at 81st EAGE Conference and Exhibition*. https://doi.org/10.2118/195532-ms

Manne, S., & Gaub, H. E. (1995). Molecular Organization of Surfactants at Solid-Liquid Interfaces. *Science*, *270*(5241), 1480–1482. https://doi.org/10.1126/science.270.5241.1480

Martínez-Luévanos, A., Uribe-Salas, A., & Lopez-Valdivieso, A. (1999). Mechanism of adsorption of sodium dodecylsulfonate on celestite and calcite. *Minerals Engineering*, *12*(8), 919–936. https://doi.org/10.1016/s0892-6875(99)00078-3

Mayerhofer, M. J., Lolon, E. P., Warpinski, N. R., Cipolla, C. L., Walser, D., & Rightmire, C. M. (2010). What Is Stimulated Reservoir Volume? *SPE Production & Operations*, *25*(01), 89–98. https://doi.org/10.2118/119890-pa

McGuire, P. L., Okuno, R., Gould, T. L., & Lake, L. W. (2016). Ethane-Based Enhanced Oil Recovery: An Innovative and Profitable Enhanced-Oil-Recovery Opportunity for a Low-Price Environment. *SPE Reservoir Evaluation & Engineering*, *20*(01), 042–058. https://doi.org/10.2118/179565-pa

Mihajlović, S. R., Vučinić, D. R., Sekulić, I. T., Milićević, S. Z., & Kolonja, B. M. (2013). Mechanism of stearic acid adsorption to calcite. *Powder Technology*, *245*, 208–216. https://doi.org/10.1016/j.powtec.2013.04.041

Miller, C., Tong, S., & Mohanty, K. K. (2018). A Chemical Blend for Stimulating Production in Oil-Shale Formations. *Unconventional Resources Technology Conference*. https://doi.org/10.15530/urtec-2018-2900955

Miller, C., Zeng, T., & Mohanty, K. (2019). Evaluation of Chemical Blends for Shale EOR. *SPE Annual Technical Conference and Exhibition*. https://doi.org/10.2118/195819-ms

Mirchi, V., Saraji, S., Goual, L., & Piri, M. (2014). Experimental Investigation of Surfactant Flooding in Shale Oil Reservoirs: Dynamic Interfacial Tension, Adsorption, and Wettability. *Unconventional Resources Technology Conference*. https://doi.org/10.15530/urtec-2014-1913287

Moghanloo, R. G., & Hosseinipoor, S. (2014). The Mechanistic Modeling of Fluid Flow in Shale. *Unconventional Resources Technology Conference*. https://doi.org/10.15530/urtec-2014-1921547

Mohanty, K. K., Tong, S., Miller, C., Zeng, T., Honarpour, M. M., Turek, E., & Peck, D. D. (2019). Improved Hydrocarbon Recovery Using Mixtures of Energizing Chemicals in Unconventional Reservoirs. *SPE Reservoir Evaluation & Engineering*, *22*(04), 1436–1448. https://doi.org/10.2118/187240-pa

Nelson, R., & Pope, G. (1978). Phase Relationships in Chemical Flooding. *Society of Petroleum Engineers Journal*, *18*(05), 325–338. https://doi.org/10.2118/6773-pa

Neog, A., & Schechter, D. S. (2016). Investigation of Surfactant Induced Wettability Alteration in Wolfcamp Shale for Hydraulic Fracturing and EOR Applications. *SPE Improved Oil Recovery Conference*. https://doi.org/10.2118/179600-ms

Nikolova, C., & Gutierrez, T. (2020). Use of Microorganisms in the Recovery of Oil From Recalcitrant Oil Reservoirs: Current State of Knowledge, Technological Advances and Future Perspectives. *Frontiers in Microbiology*, *10*. https://doi.org/10.3389/fmicb.2019.02996

Oakley, M. (2019). Flare Gas Monetization. *SPE Gas & Oil Technology Showcase and Conference*. https://doi.org/10.2118/198533-ms

Ozowe, W., Quintanilla, Z., Russell, R., & Sharma, M. (2020). Experimental Evaluation of Solvents for Improved Oil Recovery in Shale Oil Reservoirs. *SPE Annual Technical Conference and Exhibition*. https://doi.org/10.2118/201743-ms

Pagac, E. S., Prieve, D. C., & Tilton, R. D. (1998). Kinetics and Mechanism of Cationic Surfactant Adsorption and Coadsorption with Cationic Polyelectrolytes at the Silica−Water Interface. *Langmuir*, *14*(9), 2333–2342. https://doi.org/10.1021/la971308f

Pandey, A., Koduru, N., Stanley, M., Pope, G. A., & Weerasooriya, U. P. (2016). Results of ASP Pilot in Mangala Field: A Success Story. *SPE Improved Oil Recovery Conference*. https://doi.org/10.2118/179700-ms

Pankaj, P., Mukisa, H., Solovyeva, I., & Xue, H. (2018a). Boosting Oil Recovery in Naturally Fractured Shale Using CO2 Huff-n-Puff. *SPE/AAPG Eastern Regional Meeting*. https://doi.org/10.2118/191823-ms

Pankaj, P., Mukisa, H., Solovyeva, I., & Xue, H. (2018b). Enhanced Oil Recovery in Eagle Ford: Opportunities Using Huff-n-Puff Technique in Unconventional Reservoirs. *SPE Liquids-Rich Basins Conference*. https://doi.org/10.2118/191780-ms

Patil, P. D., Rohilla, N., Katiyar, A., Yu, W., Nelson, C., Falcone, S., & Rozowski, P. (2018). Surfactant Based EOR for Tight Oil Unconventional Reservoirs Through Wettability Alteration: Novel Surfactant Formulations and Their Efficacy to Induce Spontaneous Imbibition. *Unconventional Resources Technology Conference*. https://doi.org/10.15530/urtec-2018-2896289

Pu, H., & Li, Y. (2015). CO2 EOR Mechanisms in Bakken Shale Oil Reservoirs. *Carbon Management Technology Conference*. https://doi.org/10.7122/439769-ms

Reppert, T., Bragg, J., Wilkinson, J., Snow, T., Maer, N., & Gale, W. (1990). Second Ripley Surfactant Flood Pilot Test. *SPE/DOE Enhanced Oil Recovery Symposium*. https://doi.org/10.2118/20219-ms

Sanchez-Rivera, D., Mohanty, K., & Balhoff, M. (2015). Reservoir simulation and optimization of Huff-and-Puff operations in the Bakken Shale. *Fuel*, *147*, 82–94. https://doi.org/10.1016/j.fuel.2014.12.062

Seethepalli, A., Adibhatla, B., & Mohanty, K. (2004). Wettability Alteration During Surfactant Flooding of Carbonate Reservoirs. *SPE/DOE Symposium on Improved Oil Recovery*. https://doi.org/10.2118/89423-ms

ShamsiJazeyi, H., Verduzco, R., & Hirasaki, G. J. (2014a). Reducing adsorption of anionic surfactant for enhanced oil recovery: Part I. Competitive adsorption mechanism. *Colloids and Surfaces A: Physicochemical and Engineering Aspects*, *453*, 162–167. https://doi.org/10.1016/j.colsurfa.2013.10.042

ShamsiJazeyi, H., Verduzco, R., & Hirasaki, G. J. (2014b). Reducing adsorption of anionic surfactant for enhanced oil recovery: Part II. Applied aspects. *Colloids and Surfaces A: Physicochemical and Engineering Aspects*, *453*, 168–175. https://doi.org/10.1016/j.colsurfa.2014.02.021

Sharma, A., Azizi-Yarand, A., Clayton, B., Baker, G., McKinney, P., Britton, C., Delshad, M., & Pope, G. (2012). The Design and Execution of an Alkaline-Surfactant-Polymer Pilot Test. *SPE Improved Oil Recovery Symposium*. https://doi.org/10.2118/154318-ms

Shaw, J., Gatens, J., Lancaster, D., Lee, W., Avary, K., & Terry, D. (1989). Reservoir and Stimulation Analysis of a Devonian Shale Gas Field. *SPE Production Engineering*, *4*(04), 450–458. https://doi.org/10.2118/15938-pa

Sheng, J. J. (2015a). Enhanced oil recovery in shale reservoirs by gas injection. *Journal of Natural Gas Science and Engineering*, *22*, 252–259. https://doi.org/10.1016/j.jngse.2014.12.002

Sheng, J. J. (2015b). Increase liquid oil production by huff-n-puff of produced gas in shale gas condensate reservoirs. *Journal of Unconventional Oil and Gas Resources*, *11*, 19–26. https://doi.org/10.1016/j.juogr.2015.04.004

Shuler, P. J., Lu, Z., Ma, Q., & Tang, Y. (2016). Surfactant Huff-n-Puff Application Potentials for Unconventional Reservoirs. *SPE Improved Oil Recovery Conference*. https://doi.org/10.2118/179667-ms

Shutang, G., & Qiang, G. (2010). Recent Progress and Evaluation of ASP Flooding for EOR in Daqing Oil Field. *SPE EOR Conference at Oil & Gas West Asia*. https://doi.org/10.2118/127714-ms

Sigmund, P. M. (1976a). Prediction of Molecular Diffusion At Reservoir Conditions. Part 1- Measurement And Prediction of Binary Dense Gas Diffusion Coefficients. *Journal of Canadian Petroleum Technology*, *15*(02). https://doi.org/10.2118/76-02-05

Sigmund, P. M. (1976b). Prediction of Molecular Diffusion At Reservoir Conditions. Part II - Estimating the Effects Of Molecular Diffusion And Convective Mixing In

Multicomponent Systems. *Journal of Canadian Petroleum Technology*, *15*(03). https://doi.org/10.2118/76-03-07

Stalkup, F. I. (1983). *Miscible Displacement*. Henry L. Doherty Memorial Fund of AIME, Society of Petroleum Engineers of AIME.

Stegemeier, G. L. (1977). Mechanisms of entrapment and mobilization of oil in porous media. *Improved oil recovery by surfactant and polymer flooding*, 55-91.

Swami, V., Settari, A. T., & Javadpour, F. (2013). A Numerical Model for Multi-Mechanism Flow in Shale Gas Reservoirs with Application to Laboratory Scale Testing. *EAGE Annual Conference & Exhibition Incorporating SPE Europec*. https://doi.org/10.2118/164840-ms

Tovar, F. D., Barrufet, M. A., & Schechter, D. S. (2018a). Gas Injection for EOR in Organic Rich Shale. Part I: Operational Philosophy. *SPE Improved Oil Recovery Conference*. https://doi.org/10.2118/190323-ms

Tovar, F. D., Barrufet, M. A., & Schechter, D. S. (2018b). Gas Injection for EOR in Organic Rich Shales. Part II: Mechanisms of Recovery. *Unconventional Resources Technology Conference*. https://doi.org/10.15530/urtec-2018-2903026

Tovar, F. D., Barrufet, M. A., & Schechter, D. S. (2021). Enhanced Oil Recovery in the Wolfcamp Shale by Carbon Dioxide or Nitrogen Injection: An Experimental Investigation. *SPE Journal*, *26*(01), 515–537. https://doi.org/10.2118/204230-pa

Veedu, F. K., Thomas, D., Wang, P., Eskandaridalvand, K., Hornbrook, J., Pope, G., Al-maraghi, E., Singh, B., Al-Matar, B., Al-Saad, B., Al-Qahtani, M., & Tiwari, S. (2015). EOR Feasibility Study through an Integrated Laboratory Evaluation and Reservoir Simulation for a Large Carbonate Field in Kuwait. *SPE Reservoir Simulation Symposium*. https://doi.org/10.2118/173255-ms

Wang, D., Butler, R., Liu, H., & Ahmed, S. (2011). Surfactant Formulation Study for Bakken Shale Imbibition. *SPE Annual Technical Conference and Exhibition*. https://doi.org/10.2118/145510-ms

Wang, D., Butler, R., Zhang, J., & Seright, R. (2012). Wettability Survey in Bakken Shale With Surfactant-Formulation Imbibition. *SPE Reservoir Evaluation & Engineering*, *15*(06), 695–705. https://doi.org/10.2118/153853-pa

Wang, D., Wang, X., Ge, H., Sun, D., & Yu, B. (2020). Insights into the Effect of Spontaneous Fluid Imbibition on the Formation Mechanism of Fracture Networks in Brittle Shale: An Experimental Investigation. *ACS Omega*, *5*(15), 8847–8857. https://doi.org/10.1021/acsomega.0c00452

Wang, J., Han, M., Fuseni, A. B., & Cao, D. (2015). Surfactant Adsorption in Surfactant-Polymer Flooding for Carbonate Reservoirs. *SPE Middle East Oil & Gas Show and Conference*. https://doi.org/10.2118/172700-ms

Wang, T. S. (2001). Thermophysics Characterization of Kerosene Combustion. *Journal of Thermophysics and Heat Transfer*, *15*(2), 140–147. https://doi.org/10.2514/2.6602

Wu, W., & Sharma, M. M. (2016). Acid Fracturing in Shales: Effect of Dilute Acid on Properties and Pore Structure of Shale. *SPE Production & Operations*, *32*(01), 51–63. https://doi.org/10.2118/173390-pa

Yarveicy, H., Habibi, A., Pegov, S., Zolfaghari, A., & Dehghanpour, H. (2018). Enhancing Oil Recovery by Adding Surfactants in Fracturing Water: A Montney Case Study. *SPE Canada Unconventional Resources Conference*. https://doi.org/10.2118/189829-ms

Young, C., & Miller, J. (2000). Effect of temperature on oleate adsorption at a calcite surface: an FT-NIR/IRS study and review. *International Journal of Mineral Processing*, *58*(1–4), 331–350. https://doi.org/10.1016/s0301-7516(99)00057-5

Yu, W., Al-Shalabi, E. W., & Sepehrnoori, K. (2014a). A Sensitivity Study of Potential CO2 Injection for Enhanced Gas Recovery in Barnett Shale Reservoirs. *SPE Unconventional Resources Conference*. https://doi.org/10.2118/169012-ms

Yu, W., Lashgari, H., & Sepehrnoori, K. (2014b). Simulation Study of CO2 Huff-n-Puff Process in Bakken Tight Oil Reservoirs. *SPE Western North American and Rocky Mountain Joint Meeting*. https://doi.org/10.2118/169575-ms

Zeng, T., Miller, C. S., & Mohanty, K. K. (2020). Combination of a chemical blend with CO2 huff-n-puff for enhanced oil recovery in oil shales. *Journal of Petroleum Science and Engineering*, *194*, 107546. https://doi.org/10.1016/j.petrol.2020.107546

Zeng, T., S. Miller, C., & Mohanty, K. (2018). Application of Surfactants in Shale Chemical EOR at High Temperatures. *SPE Improved Oil Recovery Conference*. https://doi.org/10.2118/190318-ms

Zhang, F., Adel, I. A., Park, K. H., Saputra, I. W., & Schechter, D. S. (2018). Enhanced Oil Recovery in Unconventional Liquid Reservoir Using a Combination of CO2 Huff-n-Puff and Surfactant-Assisted Spontaneous Imbibition. *SPE Annual Technical Conference and Exhibition*. https://doi.org/10.2118/191502-ms

Zhang, F., Saputra, I. W., Adel, I. A., & Schechter, D. S. (2019). Numerical Investigation of EOR Applications in Unconventional Liquid Reservoirs through Surfactant-Assisted Spontaneous Imbibition SASI and Gas Injection Following Primary Depletion. *SPE Annual Technical Conference and Exhibition*. https://doi.org/10.2118/196055-ms

Zhang, J., Wang, D., & Olatunji, K. (2016). Surfactant Adsorption Investigation in Ultra-Lower Permeable Rocks. *SPE Low Perm Symposium*. https://doi.org/10.2118/180214-ms

Zhang, R., & Somasundaran, P. (2006). Advances in adsorption of surfactants and their mixtures at solid/solution interfaces. *Advances in Colloid and Interface Science*, *123–126*, 213–229. https://doi.org/10.1016/j.cis.2006.07.004

Zhang, Y., Gao, M., You, Q., Fan, H., Li, W., Liu, Y., Fang, J., Zhao, G., Jin, Z., & Dai, C. (2019). Smart mobility control agent for enhanced oil recovery during CO2 flooding in ultra-low permeability reservoirs. *Fuel*, *241*, 442–450. https://doi.org/10.1016/j.fuel.2018.12.069

Zhou, L., Das, S., & Ellis, B. R. (2016). Effect of Surfactant Adsorption on the Wettability Alteration of Gas-Bearing Shales. *Environmental Engineering Science*, *33*(10), 766–777. https://doi.org/10.1089/ees.2016.0003

Zhou, Z., Li, X., & Teklu, T. W. (2021). A Critical Review of Osmosis-Associated Imbibition in Unconventional Formations. *Energies*, *14*(4), 835. https://doi.org/10.3390/en14040835

Zhu, P., Balhoff, M. T., & Mohanty, K. K. (2015). Simulation of Fracture-to-Fracture Gas Injection in an Oil-Rich Shale. *SPE Annual Technical Conference and Exhibition*. https://doi.org/10.2118/175131-ms

Zou, A. (2015). *Compositional simulation of CO2 enhanced oil recovery in unconventional liquid reservoirs.* [Master thesis, Texas A&M University]. https://hdl.handle.net/1969.1/156374

Zou, C. (2017). Meaning of Unconventional Petroleum Geology. *Unconventional Petroleum Geology*, 49–95. https://doi.org/10.1016/b978-0-12-812234-1.00002-9

Section B: Presentation of major findings published in *Colloids and Surfaces A: Physicochemical and Engineering Aspects*

Surfactant Inhibition Mechanisms of Carbonate Mineral Dissolution in Shale

Abstract

Surfactants are common additives to hydraulic fracturing and enhanced oil recovery (EOR) fluids, and are under consideration for amendment to supercritical carbon dioxide for geological carbon sequestration (GCS). The effect of a common anionic surfactant, internal olefin sulfonate (IOS), on mineral dissolution from shale into brine was evaluated. When added to brine at concentrations exceeding the critical micelle concentration (94 mg/L), IOS inhibited carbonate mineral dissolution in an Eagle Ford shale, as well as dissolution of optical quality calcite (the dominant carbonate in the shale). Laser profilometry images provide spatial resolution across >3 orders of magnitude, and indicate that IOS addition to brine both enhances the formation of new etch pits in calcite, and impedes their further growth. Time-of-flight secondary ion mass spectrometry surface profiles show for the first time that IOS preferentially adsorbs at calcite pit edges versus flat calcite surfaces (i.e., terraces). Surface pressure calculations, sulfur K-edge near edge X-ray absorption fine structure (NEXAFS) spectroscopy results, and density functional theory (DFT) calculations support this observation; the DFT results indicate that the sulfonate head group of the IOS molecule binds strongly to the calcite step site as compared to the terrace site. The S K-edge NEXAFS results indicate that IOS adsorbed more to etched calcite surfaces compared to smooth calcite surfaces. Overall, the results indicate that weak adsorption on flat calcite surfaces (i.e., terraces) disrupts water structure and enhances mass transfer of dissolution, while strong adsorption on calcite pit edges displaces adsorbed water and inhibits further etch pit growth. This work provides the first direct evidence of preferential adsorption of IOS to etched calcite surfaces and links it to macroscopic dissolution kinetics. This work has implications for surfactant-containing fluids used in hydraulic fracturing, EOR and potentially GCS for subsurface injection into carbonate rich reservoirs.

Introduction

Shale formations have emerged as critical stratigraphic units in unconventional hydrocarbon recovery [1,2] and geological carbon sequestration [3,4]. In the former they are rich sources of oil and natural gas, and in the latter they serve as cap rock to prevent carbon dioxide escape. Shales are complex assemblages of fine mineral fragments and organic matter of varying reactivity [5], and in many cases are dominated by highly reactive carbonate minerals (e.g., Eagle Ford shale > 60% calcite [6–8], Wolfcamp and Marcellus shales >80% calcite+dolomite). Shales are exposed to injected fluids during hydraulic fracturing and geological carbon sequestration leading to dissolution and secondary mineral precipitation. Dissolution has been shown to open pore spaces and fractures in shale matrices and create conduits for fluid flow [9,10], and to decrease geomechanical integrity [10,11]. The latter can weaken rock, promoting collapse as rubble and the closure of propped fractures, or promote slippage along grain and fracture boundaries inducing seismicity. A number of researchers have investigated the effects of water with varying pH, carbon dioxide partial pressure (PCO_2), and temperature on shale mineral reactions [3,9,12]. The effects of various additives have also been evaluated [13,14]. However, the effects of surfactants on mineral reactivity have rarely been addressed.

Surfactants are commonly added to hydraulic fracturing and enhanced oil recovery (EOR) fluids to reduce interfacial tension and to alter reservoir wettability [16,17]. Anionic, cationic, zwitterionic, and nonionic surfactants are all used in practice, and the type selected for use in a reservoir depends on many factors including formation mineralogy, salinity, hardness, pH, and temperature [18]. Surfactant head groups bind to oppositely charged sites on mineral surfaces via electrostatic forces, and this is aided by weaker van der Waal forces [19,20]; this is also aided by favorable entropy changes that occur when hydrophobic surfactant tails partition from brine to neutrally charged mineral surfaces and natural organic matter. Near neutral pH, carbonates (e.g., points of zero charge$_{\text{calcite}}$=8-9.5 [21]) are positive and this aids anionic surfactant sorption [22]. At low concentrations on mineral surfaces, individual and non-interacting surfactant molecules adsorb at the most favorable sites (e.g., edges) [23,24]. As concentrations increase, hemimicelles can form at these same sites, and at less favorable sites, and surfactant molecules can interact with each other. Above the critical micelle concentration (CMC), adsorption is independent of surfactant concentration. Surfactants have been used to protect metal surfaces from corrosion in acidic solutions, with the assumption that they inhibit proton attack [25]. It follows that surfactants might protect shale mineral surfaces from dissolution, but this has not been examined.

The ubiquity of carbonates in shales and other human-impacted systems (e.g., conventional reservoirs, potable groundwater aquifers, soil, biological systems, and engineered structures) has motivated study of their reactivity under widely varying conditions [26,27]. Among the most studied carbonate is calcite, and its dissolution is of interest in this study. Broadly, calcite dissolution occurs by surface etching, where bound calcium and carbonate ions are solubilized on calcite surfaces preferentially at defect sites such as step edges and edge kinks [28–31]. Various rate laws and mechanisms have been proposed to describe calcite dissolution rates. In relatively pure water, dissolution rates have been related to proton (a_{H^+}), carbon dioxide ($a_{H_2CO_3^*}$), water (a_{H_2O}), calcium ($a_{Ca^{2+}}$), and bicarbonate ($a_{HCO_3^-}$) activities via eq 1 [32].

$$R = k_1 a_{H^+} + k_2 a_{H_2CO_3^*} + k_3 a_{H_2O} - k_4 a_{Ca^{2+}} a_{HCO_3^-} \qquad (1)$$

where $[H_2CO_3^*]=([CO_2(aq)] + [H_2CO_3^o])$. Below ~pH 3.5 the first term on the right hand side of eq 1 dominates. At higher pH, the forward reaction is governed by the second and/or third term depending on pCO_2 and pH. The reverse (precipitation) reaction (fourth term) becomes important as the solution approaches saturation with respect to calcite. When the third term dominates, dissolution is sufficiently slow such that mass transfer to the calcite surface can be ignored.

Many studies have evaluated the effects of aqueous constituents on calcite growth and dissolution, with the greater focus on inorganic ions. Both inhibition (e.g., organic acids, Fe^{2+}, Mg^{2+}, Sr^{2+}, PO_4^{3-}) and enhancement (e.g. chelators, Cl^-, I^-, F^-,) of dissolution kinetics have been observed [33–42], and in some cases enhancement changed to inhibition or vice versa as the concentration and/or molecular weight of structurally similar molecules changed (e.g., polyaspartate) [43,44]. Inhibition kinetic effects are often attributed to ion adsorption and pinning at step edges [33], as well as general competitive adsorption with Ca^{2+} and/or CO_3^{2-} [35]. Inhibition has also been related to incorporation of metal impurities into the carbonate mineral [36,45]. Enhancement of the kinetics is less common, but has been attributed to disruption of the adsorbed water layer at the calcite surface with possible lowering of the energy barrier for etch pit nucleation and enhanced mass transfer [43,44,46].

Aqueous constituents also affect calcite etch pit geometry. Rhombohedral etch pits ideally form on $\{10\bar{1}4\}$ surfaces in pure water. These pits primarily grow by dissolution of Ca^{2+} and CO_3^{2-} along acute and obtuse edges, and growth along obtuse steps is faster in pure water [28]. Inorganic ions have been shown to favorably adsorb at acute or obtuse edges, and thereby promote growth of etch pits in one or the other direction [33,36]. The effects of adsorbed organic ions appear even more complex and have been extensively studied in the field of biomineralization. Organic molecules containing amino acid or carboxyl groups bind with calcite surface and step edges by stereochemical recognition, resulting in macroscopic etch pit morphology modification or stabilization of different crystal facets [30,43,47–49]. Poly-n-aspartic acid, for example, was shown to preferentially adsorb to acute edges for n=1, 2, and obtuse edges for n=3, 4, 6 [43], thereby promoting growth in opposite directions. Also, different enantiomers of aspartic acid (i.e., D- and L-) adsorb at opposite acute edges of etch pits and yield different mirror image etch pit geometries [30]. The effects of surfactants, which have different hydrophilic functional groups (e.g. sulfonate) that can potentially interact with mineral surface and also hydrophobic chains that induce complex adsorption behavior by forming micelles, on calcite dissolution rates and etch pit morphologies have received little attention.

The objectives of this study are to determine which component(s) of shale are most reactive with a simplified model brine (0.4 M KCl) at circumneutral pH and low total carbonate (C_T) under ambient pCO_2, whether an anionic surfactant protects shale mineral component(s) from dissolution, and to identify the mechanisms of this protection. To address these objectives, dissolution kinetics of an Eagle Ford shale were measured under ambient conditions in brine without and with the anionic surfactant internal olefin sulfonate (IOS). Dissolution results and geochemical modeling were used to identify which mineral(s) reacted and were protected by IOS. Calcite was identified as the primary mineral protected by IOS from dissolution, and the dissolution kinetics of optical quality calcite were similarly measured and complemented with laser profilometry images of resulting etch pit geometries. Calcite-brine surface pressure values were determined from wettability measurements. Site specific distribution of IOS on calcite surfaces was evaluated with time-of-flight secondary ion mass spectrometry (ToF-SIMS), and further probed with near edge X-ray absorption fine structure (NEXAFS) spectroscopy and density functional theory (DFT) calculations. These different methods provided multiple lines of evidence to interpret the mechanisms affecting calcite dissolution inhibition by IOS.

Experimental

Materials

Most stock chemicals received were reagent grade. They include 1M HCl (Aldrich® 99.99%), HNO_3 (Fisher, Trace metal grade), 1N KOH (J.T.Backer, analytical grade), and solid KCl (Aldrich®, 99%). A 30.1 wt% anionic surfactant solution of internal olefin sulfonate (IOS C15-18) was obtained from Shell Oil Company (product number O332); the structure is shown in Figure 1a. A core sample of oil-wet shale from a burial depth of 3,400 m was obtained from the Eagle Ford reservoir in south Texas. Optical quality calcite crystals from Brazil and gypsum crystals were purchased from Ward's Scientific. Ultrapure water was prepared from a Thermo Scientific Barnstead Nanopure Model 7143, and it was characterized by a resistivity of 18.2 MΩ-cm.

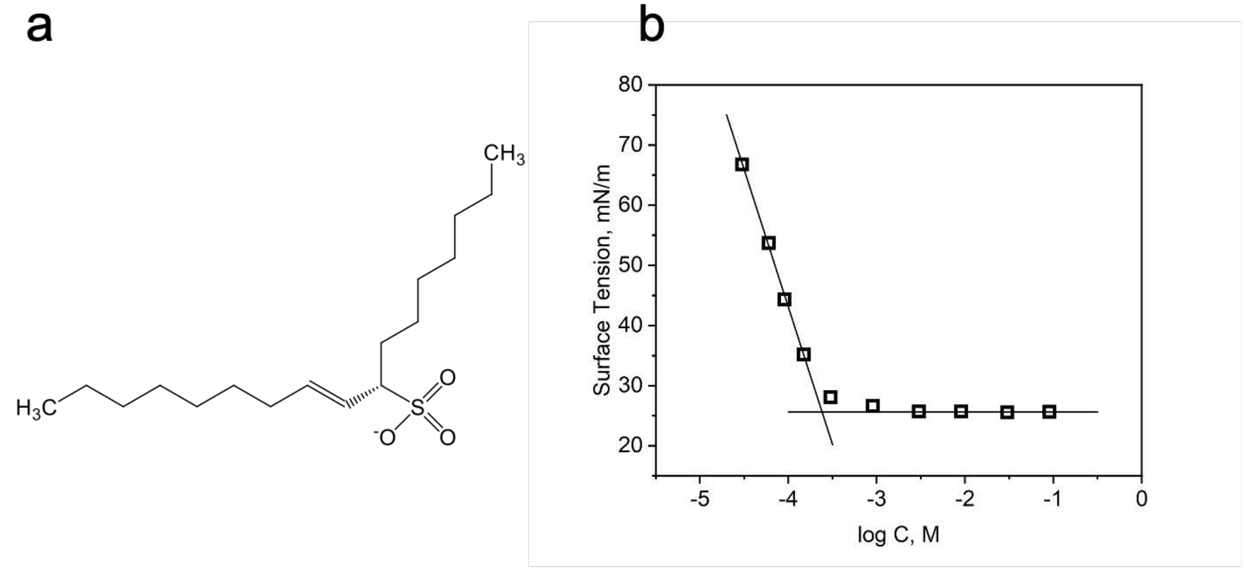

Figure 1. a) Representative structure of IOS (n=17), b) surface tension as a function of log molar concentration of IOS in brine (0.4 M KCl) at room temperature.

Brine and IOS Brine Solution Preparation

Ultrapure water and powdered KCl were combined to make a 0.401 M KCl solution, hereafter referred to as brine solution. This corresponds to an ionic strength of 0.401 M, which is similar to lower values identified in Eagle Ford shale formation water.[50] The anionic IOS surfactant was received and stored in a highly basic stock solution to maintain compound stability. It was chosen because it is a common additive to both enhanced oil recovery and hydraulic fracturing fluids [51,52]. The key roles of surfactants in hydraulic fracturing and EOR are interfacial tension reduction and reservoir wettability alteration to a more water-wet state [53]. Just before use, the required amount of IOS stock solution was diluted to 15,000 mg/L, then mixed with HCl to adjust the pH to 4.3. This pH reduction transformed all carbonate species into carbonic acid ($H_2CO_3^*$). Subsequently, sonication and vacuum were applied to degas dissolved CO_2 until no gas evolution was apparent. The pH of this solution was then adjusted upward to >6 by adding 0.1 M KOH. The CO_2 removal by sonication and vacuum was confirmed by acid titration with HCl. The pH-adjusted IOS stock solution was then diluted into brine to obtain desired IOS concentrations (e.g., 500 mg/L and 3000 mg/L). The pH values of all brine and combined IOS brine solutions were adjusted to 6.3 using 0.1 M HCl before use.

Eagle Ford Shale and Calcite Sample Preparation

The Eagle Ford shale was used in powder form. Larger chunks of Eagle Ford shale were turned into powder by grinding with a mortar and pestle. This powder was then rinsed in brine three times by sequential centrifugation at 6000 rpm and decanting; this was done to remove very fine mineral and organic matter particles that could pass through a syringe polyethersulfone (PES) filter during experimental sampling (see next section). The decanted brine was discarded, and the retained solids (>98%) were dried and then used in experiments.

The optical quality calcite was used as coarse grain particles, and in cleaved samples. Coarse grain particles were created by first rough grinding using a mortar and pestle. Next, these particles were passed through a #20 mesh sieve, and then collected on a #100 mesh sieve, to obtain the desired size fraction (150-850 μm). These calcite particles were then quickly (minutes) rinsed by sonicating in ultrapure water and decanted to remove very fine particles. Cleaved samples were prepared by cleaving 2 mm thick by ~1 cm^2 calcite specimens from larger blocks of optical quality calcite using a razor [54]. The cleaving exposed fresh $\{10\bar{1}4\}$ surfaces, and the cleaved samples were immediately immersed in experimental solution (details below) to prevent surface contamination and reaction with the atmosphere.

Eagle Ford Shale and Calcite Dissolution Experiments

Eagle Ford shale batch dissolution experiments were performed in 40 mL vials at 22 ± 1 °C by submerging ~0.5 g of powered samples in 10 mL of brine alone or IOS mixed brine solutions (hereafter referred to as IOS brine), and then sampling and analyzing for dissolved elements and ions over time. The vials were loosely covered so that CO_2 could exchange between brine and the atmosphere (open system), and then mixed with a stir bar. In most experiments, ~0.3 mL brine samples were collected at 1, 3, 6, 12, and 48 hours. All aqueous samples were collected through a 0.22 μm syringe filter.

Calcite batch dissolution experiments were performed in 40 mL vials at 22±1 °C by submerging ~0.5 g of particles or cleaved samples in 10 mL of brine alone or IOS brine, and then sampling and analyzing for Ca^{2+}, pH, and total carbonate over time. As before, the vials were loosely covered so that CO_2 could exchange between brine and the atmosphere, and for calcite particles the solution was continuously mixed. For all experiments, approximately 0.3 mL samples were collected after 1, 3, 6, 12, and 36 hours, again through 0.22 μm filters.

Calcite etch-pit experiments were performed using only cleaved calcite pieces. In one set of experiments, the cleaved calcite pieces were submerged in brine alone or IOS brine for 12 hours, removed from solution and gently rinsed with ethanol to remove salts and adsorbed IOS, dried with pure N_2, and then analyzed using laser profilometry. In another set of experiments, replicate calcite samples submerged in brine for 12 hours were then subsequently transferred to either a solution of only brine or a solution of IOS brine for another 12 hours. After this second aging period, the samples were again rinsed with ethanol, dried with N_2, and evaluated using laser profilometry.

All experiments were performed under ambient conditions, while reservoirs are typically under high pressure and elevated temperature. Hence, this work represents a first step toward mechanistic evaluation of surfactant effects on shale mineral dissolution, and further work under reservoir conditions is warranted.

Measurement of Ca^{2+} in Ion Exchange Sites

The cation exchange capacity was measured following method proposed by Amrhein and Suarez which is pertinent for calcite and/or gypsum rich soils [55]. Also, the amount of Ca^{2+} in ion exchange sites at the start of Eagle Ford shale dissolution experiments was evaluated to distinguish this contribution from dissolution of calcium-containing minerals. Briefly, powdered Eagle Ford shale samples were rinsed three times in brine and then placed into a 0.5 M aqueous solution of $MgCl_2$. The Ca^{2+} in solution was then measured. The Mg^{2+} will displace Ca^{2+} from cation exchange sites, as well as promote mineral dissolution because it is under-saturated in calcium. The Ca^{2+} displaced by Mg^{2+} is distinguished by subtracting the concentration of constituent ions (e.g., CO_3^{2-} for calcite, SO_4^{2-} for gypsum) from the measured total Ca^{2+} concentration.

Surface Tension and Contact Angle Measurements

A Ramé-hart Model 500 Goniometer was used for surface tension and contact angle measurements. Surface tension values were determined for brine and mixtures of IOS and brine using the pendant drop method. The CMC of IOS also was determined by calculating an inflection point from the surface tension vs log IOS concentration plot (Figure 1b). Contact angle values for brine and IOS brine were determined by placing a drop of these liquids onto a freshly cleaved calcite surface, and measuring contact angles from image analysis. The calcite surface was washed between measurements following Costa and Aquilano [56]. Each surface tension and contact angle value reported is the average of five different measurements.

Elemental and Ion Analyses

Elemental analysis was performed using a Varian 710-ES inductively coupled plasma – optical emissions spectroscopy (ICP-OES) instrument. Lower detection limits for Ca and Mg are 0.03 μg/L and 0.1 μg/L, respectively. 100 μL of each sample collected from experimental vials was diluted into 9.9 ml of Nanpure water mixed with 200 μL of concentrated nitric acid, and then analyzed for Ca and Mg. The oxyanion sulfate (SO_4^{2-}) was measured using a Thermo scientific Dionex ICS-2100 ion chromatograph (IC). 50 μL of each sample collected from experimental vials was diluted into 0.95 ml of ultrapure water and analyzed. Solution pH was measured using a Mettler Toledo pH electrode LE438. Carbonates were measured by acid titration using HCl.

Surface area, Mineralogy, and Total Organic Carbon

The specific surface area (SSA) of Eagle Ford shale was measured using N_2 adsorption with a Micromeritics 3Flex Surface Area analyzer. Samples were analyzed over the pressure range from 0.73 to 748 mm Hg at 77 K, and analyzed using the Brunauer-Emmett-Teller isotherm. Mineralogy and total organic carbon (TOC) of the Eagle Ford shale were measured by the commercial laboratory, Premier Oilfield Group. The former was measured by X-ray diffraction (XRD) using a Bruker D8 diffractometer, and the later by a total organic carbon analyzer using a Leco-carbon analyzer.

Laser Profilometer Analysis

A Keyence VK-1100 Laser Profilometer was used to characterize surface morphology and pit formation. Surface profiles were mainly collected with 50X lens to scan 211×281 μm^2. The vertical display resolution is 0.5 nm, and the precision of repeated scans in the laser confocal mode with the 20X lens is 40 nm. Depending on the size of the pits, higher magnification lenses were used. Surface profiles were processed with VK-X series Multi-file Analyzer software. The reference plain setting was first performed with a relatively flat surface, and then the depth and area of each pit were measured by referencing the adjacent flat surface. The arithmetic average areal roughness (S_a) was calculated over the scanned area.

IOS Surface Location and Coverage on Calcite

IOS surface location and coverage on calcite pieces was determined using Time-of-Flight Secondary Ion Mass spectrometry (ToF-SIMS). Freshly cleaved calcite samples were aged in brine for 12 hours to form etch pits. The brine was then mixed with IOS to reach 10 or 100 mg/L, and allowed to incubate for 1 hour. Samples were then removed from solution, gently dried by blowing ultrapure N_2, and placed in the ToF-SIMS instrument for analysis of the spatial distribution of IOS (i.e., SO_2^-) and calcite (i.e., Ca^-, CO_3^-) containing molecular fragments. A calcite sample aged in brine without IOS and in concentrated IOS on a silicon wafer were also analyzed as controls.

The specific instrument used was an ION-TOF (GmbH, Germany, 2010). During the sputtering/analysis process, a Cs^+ sputtering ion beam (beam energy 500 eV, current ~ 40 nA), and a pulsed Bi_3^+ cluster analysis ion beam (30 keV ion energy, 100 ns pulse duration) with either 3.7 pA (depth profiling) or 2.7 pA (high-resolution imaging) of measured sample current, were used. Additional details are in Supporting Information.

Relative amounts of IOS adsorbed on calcite with and without etch pits were determined using near edge X-ray absorption fine structure (NEXAFS) spectroscopy. A freshly cleaved gypsum ($CaSO_4 \cdot 2H_2O$) and concentrated IOS (30.1%) on a silicon wafer were prepared as controls to determine energy shift correction and type of sulfur functional groups in the IOS. A freshly cleaved calcite was also analyzed as a control to investigate sulfur impurities. Four additional samples with two different surface morphologies (i.e., etched or cleaved calcite) were prepared by first aging cleaved calcite in brine or calcite saturated brine, respectively for 12 hours. The brine or calcite-saturated brine was then mixed with IOS to reach 10 or 100 mg/L, and allowed to incubate with the calcite samples for 1 hour. The calcite-saturated brine was used to prevent etch pit formation and to hydrate calcite surface prior to adding IOS. Samples were then collected and dried following the procedure described with samples for ToF-SIMS. All calcite samples were prepared by cleaving a single crystal calcite.

NEXAFS measurements were performed at beamline 12-ID at the National Synchrotron Light Source II (NSLS-II). Fluorescence-yield (FY) NEXAFS data were collected near the sulfur K-edge (2449-2504 eV) and calcium K-edge (4030-4110 eV) using a Pilatus 300 KW detector positioned at 0.7° from the sample plane for both sulfur K-edge and calcium K-edge measurements. The total intensity from a region of the detector away from any scattering peaks was used as a fluorescence signal. Pre-edge subtraction and post-edge normalization was performed with Larch software [57]. Subsequently, normalized spectra were decomposed using multipeak fitting package 2 in Igor pro (WaveMetrics). Each spectrum was decomposed into 5 or less Gaussian functions and an arctangent function following the approach proposed by Manceau and Nagy [58].

Geochemical Modeling

Geochemical modeling was performed using PHREEQC. The *phreeqc.dat* database was used for thermodynamic data [59]. A list of reactions considered is in Table S1 (Supporting Information). The model was run by first defining the composition of brine in equilibrium with atmospheric CO_2 at 22 °C, and then equilibrating that solution with calcite and other Ca bearing minerals in the Eagle Ford shale (i.e., dolomite, gypsum). The moles of added minerals and the volume of solution were specified based on measured solution species and experimental conditions. Additional details are in section 3.3.

Density Functional Theory Calculations

Density Functional Theory (DFT) calculations based on the Generalized Gradient Approximation (GGA) were performed using the Vienna Ab initio Simulation Package (VASP). A plane wave basis set was used with an energy cutoff of 300 eV and a Gaussian smearing at the Fermi level with a width of 0.05 eV to improve convergence. The Perdew-Burke-Ernzerhof (PBE) [64] functional was used to describe electron exchange and correlation. The Brillouin zone was sampled at the Γ-point. The convergence criteria for electronic and geometric optimization were 10^{-6} eV and 0.01 eV/Å, respectively.

To mimic the experimental surfaces, slab models of calcite $\{10\bar{1}4\}$ were constructed with the atoms in the bottom layer fixed in bulk positions. The thickness of the vacuum layer was set to 14 Å to isolate the periodic slabs. Our model of the IOS molecule had 10 carbon atoms in the hydrocarbon side chains. The binding energy of the IOS molecule to the calcite substrate was calculated as

$$E_{binding} = E_{surface-IOS} - E_{surface} - E_{IOS} \qquad (2)$$

where $E_{surface}$ is the energy of the calcite surface, E_{IOS} is the energy of isolated IOS molecule and $E_{surface-IOS}$ is the energy of the system when IOS binds to the calcite surface. The VASPsol code [65] was used to consider (implicit) solvent interactions as a continuum dielectric with a relative permittivity set to 78.4 to mimic water.

Results and Discussion

Sample Characterization Results

The measured SSA of Eagle Ford shale is 6.65±0.05 m^2/g. These results are consistent with SSA measurements in the literature for Eagle Ford shale [7]. Mineralogical results for our Eagle Ford shale are shown in Table 1. They show that the sample is comprised of 67% calcite, 8.7% quartz, 6.2% Illite and Mica, 4.2% Illite/Smectite mixture, 5% K-feldspar, 4.1% plagioclase, and minor amounts of pyrite, kaolinite, chlorite, apatite, and siderite. This composition is similar to that measured by others [6–8], except for the lack of small amounts of gypsum and dolomite.

Table 1. Mineralogy and total organic matter content of Eagle Ford shale sample.

Mineral	Chemical Formula	Eagle Ford Shale
Calcite	$CaCO_3$	67.5%
Dolomite	$CaMg(CO_3)_2$	0%
Siderite	FeCO3	0.2%
Apatite	$Ca5(PO_4)_3OH$	0.7%
Pyrite	FeS_2	1.3%
Quartz	SiO_2	8.7%
K-Feldspar	$KAlSi_3O_8$	5.0%
Plagioclase	$NaAlSi_3O_8$-$CaAl_2Si_2O_8$	4.1%
Total Clays	Clay constituents below	11.6%
Chlorite		0.5%
Kaolinite		0.7%
Illte/Mica		6.2%
Mixed Illite/Smectite		4.2%
Total Organic Carbon		3.7 mg/g

The cation exchange capacity of the Eagle Ford shale is 89.1 meq/kg. The Ca and alkalinity (HCO_3^-) released into brine by Eagle Ford shale upon exposure to 0.5 M $MgCl_2$ after rinsing three times in brine were also measured. The difference between measured Ca and alkalinity was less than 0.01 mM. This indicates that at the start of Eagle Ford shale dissolution experiments (next section) there was no Ca^{2+} available for release from cation exchange sites. Any Ca^{2+} initially present at these sites was exchanged and removed during the triplicate KCl rinsing steps. Therefore, any Ca^{2+} released during Eagle Ford shale dissolution experiments is likely due to mineral dissolution.

Surface tension and contact angle results for calcite sample are presented in Table 2. The surface tension decreases when IOS is added to the brine, and there is no difference for the two IOS concentrations (which are both above the critical micelle concentration (CMC) of 94 mg/L). Contact angles on freshly cleaved calcite decrease with IOS addition to brine. The same measurements were taken on calcite after it was aged 12 hours in brine to create etch pits, and contact angles were lower for all cases. Calcite-brine interfacial tension values were calculated from Young's equation [60]; similar values were obtained for all setups (438 mJ/m^2 to 443 mJ/m^2) except a lower value was obtained for aged calcite with brine only (411 mJ/m^2) By comparison, Costa and Aquilano determined a comparable value of 409 mJ/m^2 for calcite and fresh water [56]. Aging calcite increases surface roughness (Section 3.5), which can further decrease interfacial tension [61,62]. Costa and Aquilano allowed their sample to "equilibrate in air", which may have increased surface roughness. Surface pressures (F) at the calcite-brine interface resulting from IOS addition were calculated from differences in interfacial tension ($F = \gamma_{SL(IOSBrine),i} - \gamma_{SL(Brine),i}$, where i is for fresh or aged calcite) following Fowkes and Harkins [63]. Values for fresh calcite were very small and not distinguishable from zero, while values for aged calcite were relatively large; the results indicate that the IOS preferentially adsorbs on aged versus fresh calcite-water interfaces.

Table 2. Contact angles, interfacial tensions, and adsorbed IOS

Parameter	Brine		IOS 500		IOS 3000	
	Fresh	Aged	Fresh	Aged	Fresh	Aged

Brine-Calcite Contact Angle*	72.9 ±5.4°	42.5 ±10.5	38.8 ±4.0°	22.5 ±3.8	20.5 ±1.9°	10.7 ±2.2
Brine-Air Surface Tension [mJ/m^2]**	71.9±0.4		28.1±0.9		26.6±0.01	
Brine-Calcite Interfacial Tension [mJ/m^2]#	443	411	442	438	439	438
Surface Pressure [mJ/m^2]##	NA	NA	-0.9‡	27	-0.2‡	27

*The left and right sides of five drops on calcite were evaluated for each measurements. **Pendant drop method. #Based on Young's relation ($\gamma_{LV}\cos\theta = \gamma_{SV} - \gamma_{SL}$). The surface tension of calcite with air is 464 mJ/m^2 from Bruno et al. [83]. ##From Fowkes and Harkins [63] ($F = \gamma_{LV,IOSBrine}\cos\theta_{IOSBrine} - \gamma_{LV,Brine}\cos\theta_{Brine}$). ‡These values result from subtracting one large number from another, and are not significantly different from zero. Therefore, these two surface pressures are too small for accurate quantification.

Dissolution of Eagle Ford Shale

Dissolution experiments were performed for Eagle Ford shale over a 48-hour period in brine and IOS brine. Results for the first 12 hours are shown in Figure 2, and for the entire 48 hours period in Figure S1 (Supporting Information). At the two IOS concentrations used (i.e., 500 and 3000 mg/L), approximately 61% (6.1 mg/g) and 12% (6.9 mg/g) of the IOS masses added to solution adsorbed to shale components, respectively, based on measured adsorption isotherms [64]. Total surface area covered by adsorbed molecules was estimated using the minimum surface area per molecule calculated from the Gibbs equation [65], i.e., 20.7 Å^2. Detailed calculations are in the Supporting Information. The total surface area covered by IOS at 500 and 3000 mg/L are 34.6% and 39.0% of the measured surface areas using N_2 adsorption, respectively. Also, IOS concentrations in solutions (i.e., 194 mg/L and 2655 mg/L) after sorption at both loadings exceed the CMC (94 mg/L). The elements Ca, Mg, Fe, S, Al, and Si were initially monitored in solution, and only Ca, Mg, and S appreciably changed. For S, the sulfate ion (SO_4^{2-}) was measured using ion chromatography and is reported in this form.

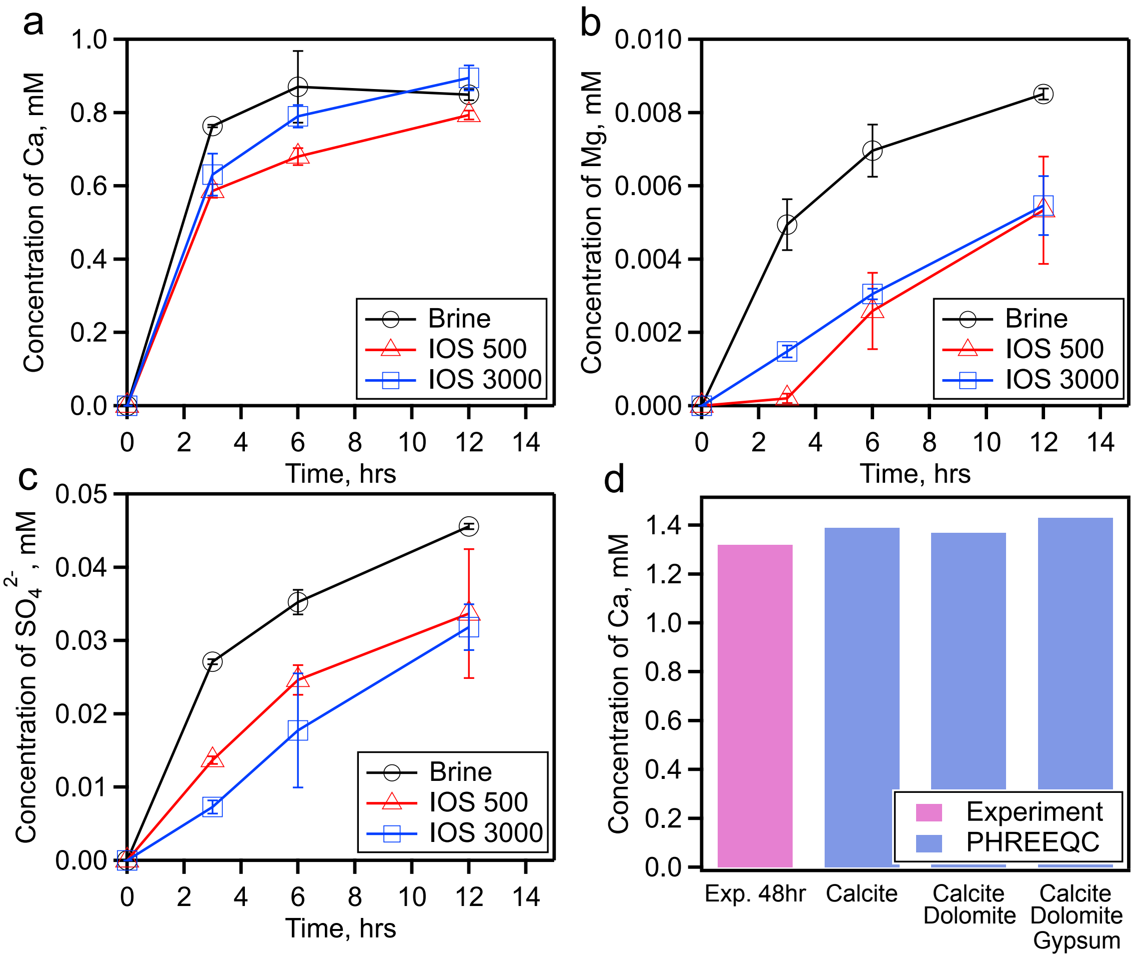

Figure 2. a) Ca, b) Mg, and c) SO_4^{2-} release into solution from Eagle Ford Shale after aging in brine or IOS brine for 12 hours. Initial pH of the solution is 6.3, and ionic strength of brine is 0.4 M. All experiments were run in triplicate, and error bar represents standard deviation. d) PHREEQC modeling results showing potential mineral contributions to Ca concentrations. IOS 500 and IOS 3000 refer to brine with either 500 or 3000 mg/L of IOS added.

Per Figure 2, the concentrations of Ca, Mg, and SO_4^{2-} all increased during the monitoring period, and an initial rapid rise is followed by a decreasing rate of increase; the pH during this time increases from 6.3 to approximately 8.0. This initial high rate of dissolution is expected, as fresh brine solution contains very few mineral species (e.g., no Ca, Mg, SO_4^{2-}, and only low CO_3^{2-}) and the driving force for dissolution is large. Over time, these species build up and mineral dissolution slows, but does not appear to reach steady state after 48 hours. The Ca concentrations at 48 hours are approximately 15 to 41 times greater than the SO_4^{2-} or Mg concentrations, respectively. Per

XRD, the only Ca containing mineral measured was calcite. However, the presence of Mg and SO_4^{2-} indicates minor amounts of dolomite and gypsum are present, and they have been identified in other samples of Eagle Ford shale [6–8].

Also per Figure 2, Ca, Mg, and SO_4^{2-} concentrations in brine and IOS brine are different. For Ca, this difference is only significant at 3 hours, and then it becomes indistinguishable with respect to the measurement error. However, for Mg and SO_4^{2-} the differences persist over 48 hours, but the magnitudes of these differences are small compared to those for Ca at 3 hours. Results for the different IOS concentrations are not as consistent. For example, less Ca dissolves for IOS 500 compared to IOS 3000, whereas for SO_4^{2-} the opposite is true. The reason for the conflicting trends is not clear, and may be due to transient uptake of IOS and/or inorganic ions onto ion exchange sites and/or hydrophobic domains in organic matter. Regardless, these results indicate that IOS protects shale minerals from dissolution. They also indicate that IOS primarily protects calcite from dissolution in the Eagle Ford shale but this effect is transient.

The pH and total carbonate were monitored during Eagle Ford shale dissolution and (along with ionic strength) used to calculate ion activities, (i.e., a_{H^+}, $a_{H_2CO_3^*}$, a_{H_2O}, $a_{Ca^{2+}}$, $a_{HCO_3^-}$). These were used with calculated rate constants from Plummer et al. [32] to approximate which terms in equation 1 dominate calcite dissolution from the shale. At all times after time zero, $k_3a_{H_2O}$ and $k_4a_{Ca^{2+}}a_{HCO_3^-}$ dominate equation 1 (Table S3). At 3 hours, $k_3a_{H_2O}$ slightly exceeds $k_4a_{Ca^{2+}}a_{HCO_3^-}$; after this time the opposite occurs, indicating precipitation is possible. However, the saturation index (SI) for calcite remains below 0 at all times, indicating only dissolution and not precipitation is active.

Ca^{2+} Mass Balance in Eagle Ford Shale

PHREEQC modeling was performed to determine if the Ca measured in brine solution during Eagle Ford shale dissolution at 48 hours was near equilibrium with calcite, and/or if other unaccounted sources of Ca were present. Modeling results are presented in Figure 2d; model equations are presented in Table S1 (Supporting Information). Only minerals containing Ca, Mg, CO_3^{2-}, and SO_4^{2-} were considered, since only these were identified in brine. Three different mineral phases were defined in modeling. Calcite was defined as an infinite mineral, since 67.5% of Eagle Ford shale is calcite. Dolomite and gypsum were also considered sources of Ca, and the moles of these minerals were set equal to the moles of Mg and SO_4^{2-} in solution at 48 hours, respectively. Alkalinity and pH were measured at 48 hours and were used to determine pCO_2. Finally, modeled pH, alkalinity, Mg, and SO_4^{2-} were compared with measured values for validation. The measured Ca concentration in solution after 48 hours represents the baseline for comparison.

Results in Figure 2d show that the measured Ca in solution is approximately 95.5% of the theoretical value at equilibrium. The contributions from dolomite and gypsum to modeled total Ca are 2.2% and 6.6% of total Ca, respectively, with the remaining contribution (91.2%) from calcite. Aqueous Ca complexes corresponding to three different modeling cases in Figure 2d are presented in Table S2. Speciation results for the case considering all three minerals (calcite, dolomite, and gypsum) show that the effect of $CaSO_4(aq)$, which can affect the free Ca^{2+} concentration, is negligible. Hence, PHREEQC model results show that (as expected) calcite is the major contributor of Ca in solution, and they uniquely suggest that IOS is primarily suppressing Ca release from this mineral at 3 hours. For this reason, the mechanisms of IOS inhibition on calcite were identified for further study.

Dissolution of Calcite

The effects of 500 and 3000 mg/L IOS addition to brine on calcite dissolution were evaluated over 36 hours using sieved calcite particles (150-850 µm); results are shown in Figure 3a. As with Eagle Ford shale, Ca concentrations in brine with only calcite increase during the monitoring period, and an initial rapid rise is followed by a decreasing rate of increase. This is expected because calcite constituent concentrations (i.e., Ca and CO_3^{2-}) in brine are initially very low, and they increase over time. Comparison of Ca concentrations in brine and IOS brine shows that IOS inhibits dissolution of the calcite particles, although differences at 1 and 36 hours are not significant (Figure 3a).

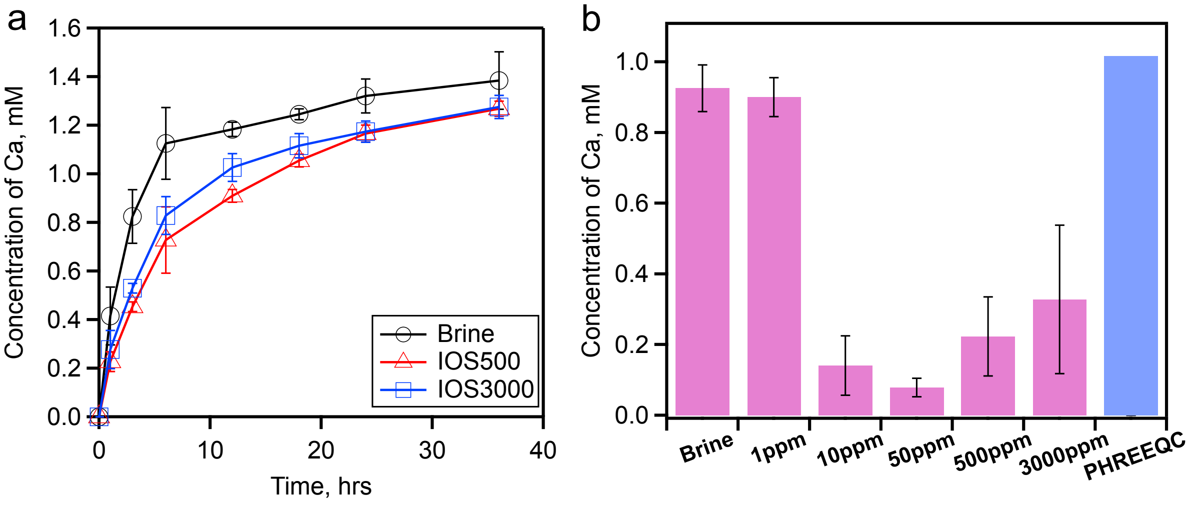

Figure 3. a) Transient Ca release into solution from calcite particles (150-850 μm) after aging in brine or IOS brine for 36 hours. b) Ca release into solution for cleaved calcite piece after aging in brine or IOS brine for 12 hours, along with PHREEQC model results showing simulated equilibrium Ca concentration. IOS 500 and IOS 3000 refer to brine with either 500 or 3000 mg/L of IOS added. Initial pH of the solution is 6.3, and ionic strength of brine is 0.4 M. All experiments were run in triplicate, and error bar represents standard deviation.

Results from the calcite particles motivated similar measurements on cleaved calcite at 12 hours, but over a wider concentration range; results are shown in Figure 3b. Measured concentrations of Ca decrease with increasing concentration of IOS from 1 mg/L to 50 mg/L (by up to 90% compared to brine only), and then increase as the IOS concentration exceeds the CMC (94 mg/L). The results show for the first time that a surfactant can substantially inhibit calcite dissolution, and that this inhibition is greatest at intermediate surfactant concentrations. Percent surface coverage at each concentration was calculated based on the same approach taken to calculate surface area coverage for Eagle Ford shale (Section 3.2), and values at 1, 10, 50, 500 and 3000 mg/L of IOS are 1.10, 9.78, 32.78, 69.66 and 77.76%, respectively. Interestingly, the minimum area per molecule calculated from the Gibbs equation (20.7 Å^2) is in good agreement with that calculated solely from the adsorption isotherm assuming bilayer adsorption (26.2 Å^2). Surface coverage calculations using either the minimum area per molecule from the Gibbs equation or the adsorption isotherm predict monolayer coverage is not exceeded, so results showing less inhibition above 50 mg/L were not expected.

The results suggest that above the CMC (i.e., 94 mg/L), the adsorption density decreases with increasing concentration and thus less inhibition occurs. This might be due to aggregation of IOS above the CMC. Several prior works evaluated surfactant sorption using AFM or molecular dynamics; they demonstrated that surfactants do not always form a continuous film (i.e., monolayer or bilayer). That can aggregate to form micelles, hemimicelles and/or rodlike aggregates on various surfaces at elevated concentrations [66–69]. We also determined via AFM that IOS can form micelles or hemimicelles on a calcite surface at 1000 mg/L (10xCMC). Thus, decreasing adsorption density of IOS with increasing concentration above the CMC appears reasonable.

The pH and total carbonate concentration were also monitored during calcite dissolution and (along with ionic strength) used to calculate ion activities, (i.e., a_{H^+}, $a_{H_2CO_3^*}$, a_{H_2O}, $a_{Ca^{2+}}$, $a_{HCO_3^-}$).

These were used with the aforementioned rate constants to determine which terms in equation 1 dominate dissolution [32]. At zero and 3 hours, $k_3 a_{H_2O}$ dominates (Table S4). For 6 hours and greater, values of $k_3 a_{H_2O}$ are similar to or less than$k_4 a_{Ca^{2+}} a_{HCO_3^-}$, indicating precipitation is also possible. The saturation index ($SI = \log(Q/K_{sp})$) was also calculated at each time point. It is negative up to and including 6 hours, and equal to only 0.06 and 0.21 at 12 and 36 hours, respectively. Hence, precipitation is less likely until greater than 36 hours.

PHREEQC modeling was also performed to determine if the Ca measured in brine solutions during calcite dissolution was near equilibrium. The simulated equilibrium value is approximately 1 mM (Figure 3b, blue bar). The simulated value is similar to the calcium concentration with cleaved calcite at 12 hours (0.95 mM), but below that for calcite particles at 36 hours (1.4 mM). The calcite particles after 36 hours are likely closer to equilibrium; the reason that the equilibrium Ca value is below the measured value may be due to a small error in the final pH measurement. An error of 0.1 near pH 8 will result in a modeled Ca concentration that is 0.5 mM different.

Calcite Etch Pit Progression and Morphology

Laser profilometry was used to probe etch pit development and identify dissolution mechanisms on freshly cleaved calcite surfaces (i.e., $\{10\bar{1}4\}$ face) placed in brine without and with IOS for 12 hours. Results shown in Figure 4 provide spatial resolution that spans more than three orders of magnitude. In brine only samples, relatively deep and large etch pits are created; etch pit depths are on the order of 5 μm, and etch pit side lengths are approximately 100 μm (Figure 4a). These etch pits vary in shape from classical rhombohedral to more triangular, where the latter are truncated across the obtuse side of the rhombus along the [010] direction. In IOS brine by contrast, only relatively shallow and small etch pits are created, with depths less than 0.15 μm; also, these etch pits are similar at the two IOS concentrations. Etch pits side lengths are less than 40 μm (Figure 4b and 4c). Hence, IOS addition to brine does not prevent initial dissolution but does appear to inhibit etch pit growth.

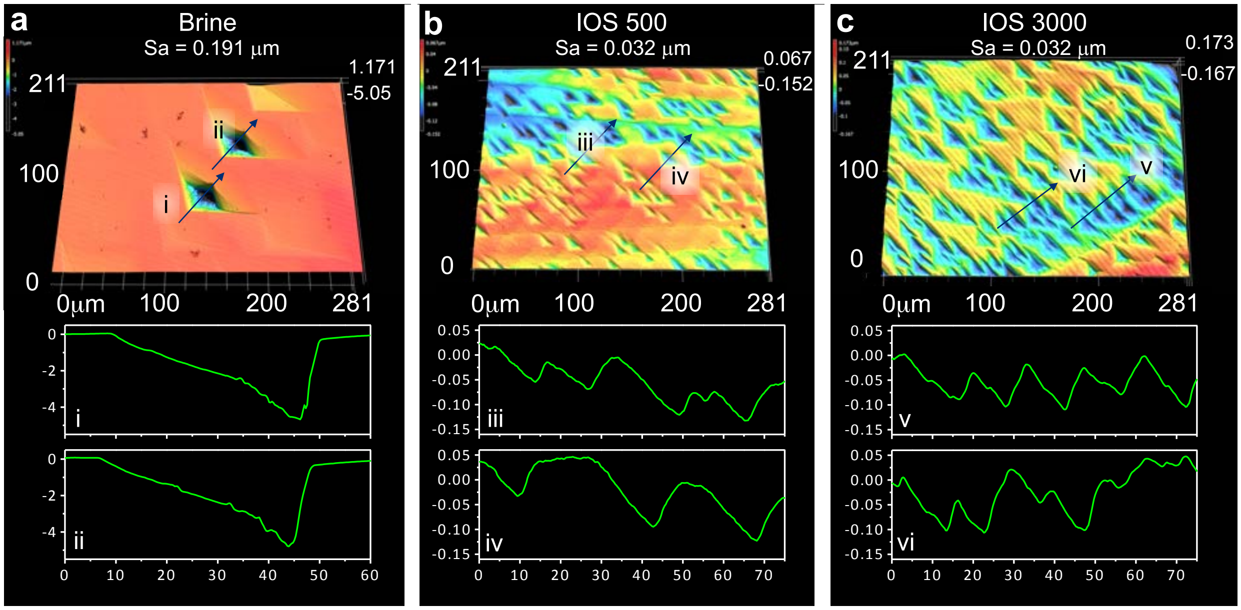

Figure 4. Laser profilometry results showing etch pits on freshly cleaved calcite surfaces aged in a) brine or b) IOS brine for 12 hours. IOS 500 and IOS 3000 refer to brine with either 500 or 3000 mg/L of IOS added. Arithmetic average areal surface roughness (S_a) is provided on top of each surface profile. All the numbers in this figure are in μm.

Cross-sectional profiles across etch pits are also shown in Figure 4. Etch pit angles were calculated, and are noted in Table 3. In the presence of only brine, the etch pit angle is smaller on the acute side of each rhombus, indicating that pit growth is faster on this edge. This is consistent with faster pit growth at this edge observed in the presence of Mg^{2+} by Arvidson et al. [33]. In the presence of pure water, others observed faster etch pit growth along obtuse edges [70]. In the presence of IOS brine, the shallow and small etch pits formed give rise to very small angles.

Table 3. Calcite pit angles.

Angle	Brine		IOS 500		IOS 3000	
	i	ii	iii	iv	v	vi
Pit Angle from Adjacent Horizontal at Acute Edge	6.2°	6.2°	0.5°	0.6°	0.6°	0.7°
Pit Angle from Adjacent Horizontal at Obtuse Edge	53.4°	55.6°	0.8°	0.9°	1.0°	1.9°

Etch pit densities were calculated (i.e., etch pit area divided by total area), and results are presented in Figure 5b. Surprisingly, a higher fraction of the calcite surface is covered with etch pits for calcite samples in IOS brine compared to only brine. This is also apparent by comparing Figure 4a with either Figure 4b or 4c. These results indicate a contrasting effect, namely that IOS promotes etch pit formation but restricts etch pit growth. These contrasting observations are possible because of the large spatial scale (0.05 to 200 µm) spanned by laser profilometry.

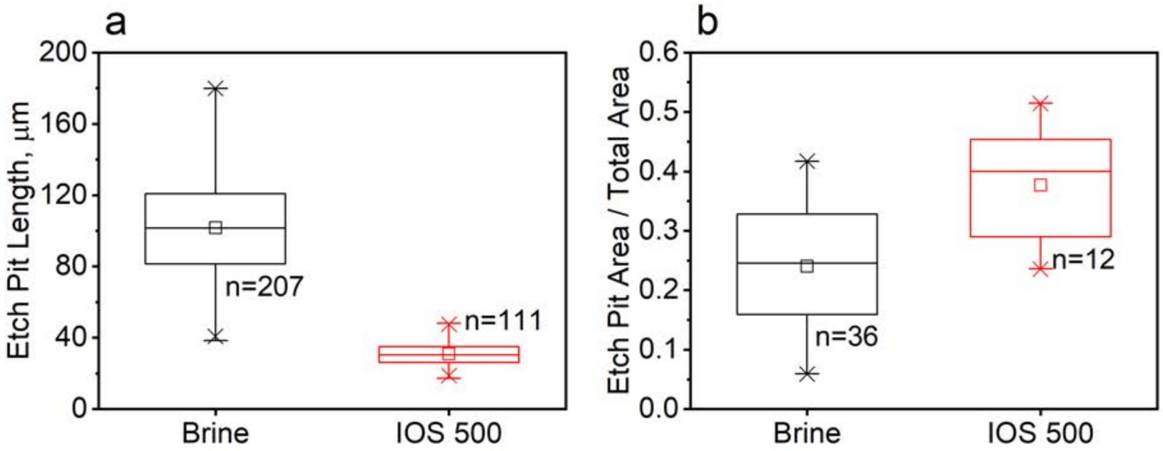

Figure 5. Box plots showing a) etch pit lengths and b) fraction of calcite surface area occupied by etch pits, both after 12 hours of aging in brine without (Brine) or with (IOS 500) IOS surfactant at 500 mg/L. Box plot lines represent median, 25th, and 75th percentile values plus outliers, with mean values shown by a square symbol.

In a second set of experiments, calcite surfaces reacted in only brine for 12 hours and then dried were re-submerged in either brine or IOS brine for another 12 hours. Results are shown in Figure 6. As expected, etch pits submerged in only brine for the second 12 hours continued to grow, and in some cases coalesced. However, etch pits submerged in IOS brine for the second 12 hours were almost completely arrested, i.e., they do not appear to have grown further. Examination of the line profiles drawn through etch pits grown in only brine the second 12 hours shows that the majority of etch pit growth was along the acute side of each rhombus (blue area in Figure 6), again indicating preferential growth on this edge.

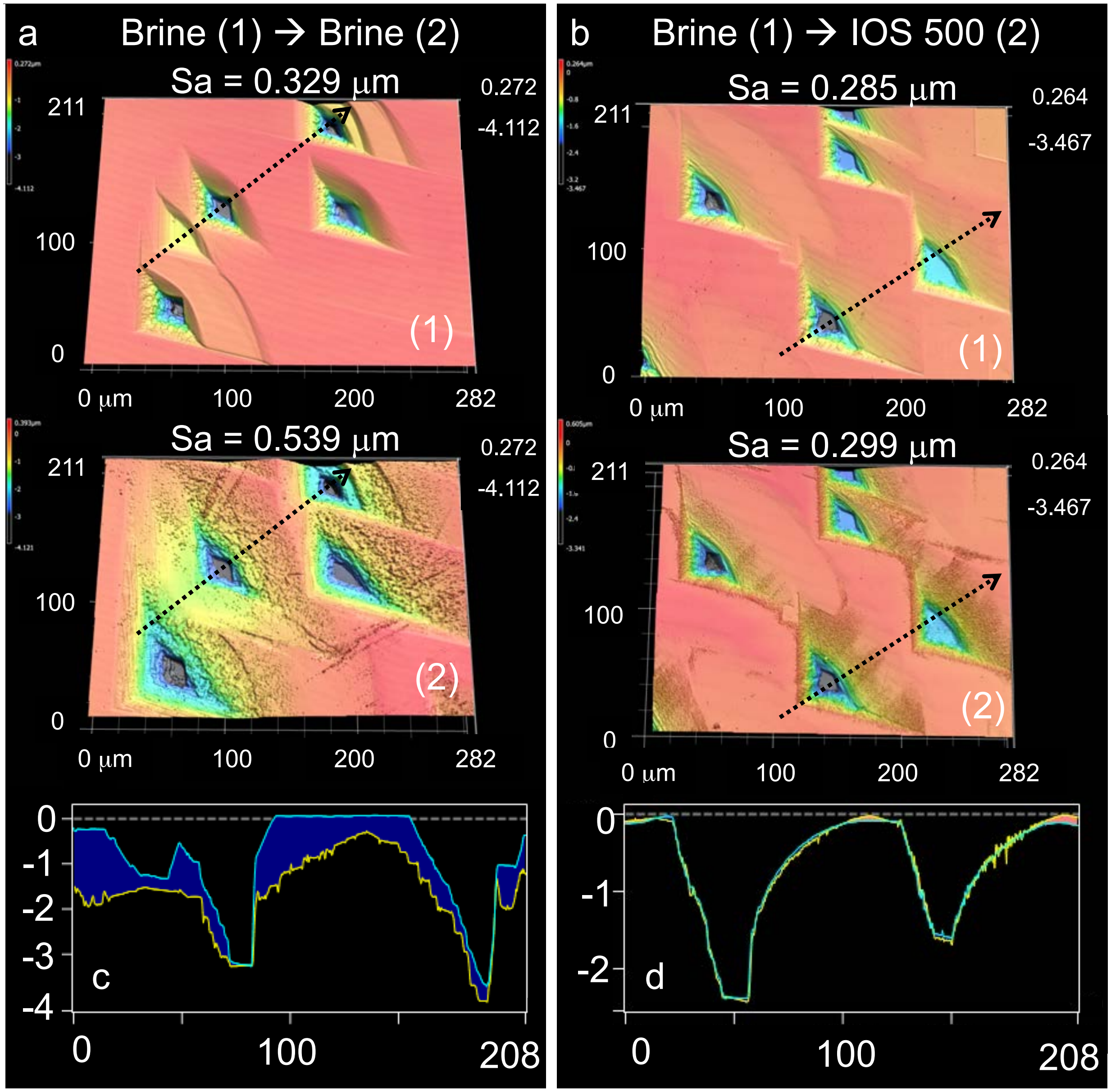

Figure 6. Laser profilometry results showing etch pits on freshly cleaved calcite surfaces a) aged for two sequential 12 hour periods in brine only, and b) aged for two sequential 12 hour periods with brine first, and then in IOS brine. IOS 500 refer to brine with 500 mg/L of IOS added. Arithmetic average areal surface roughness (S_a) is provided above each surface profile. All the numbers shown in this figure are in µm.

A surprising result from Figure 6 is that additional etch pits were not initiated when the sample initially aged in brine only was then aged for another 12 hours in IOS brine. From Figure 4, it is apparent that very high etch pit densities occur when freshly cleaved calcite is initially placed into

IOS brine. It is possible that initially formed µm-deep etch pits dominated surfactant sorption and reduce its concentration on flat $\{10\bar{1}4\}$ surfaces, thereby reducing the initiation of new etch pits.

Preferential Adsorption of IOS on Calcite Etch Pits

ToF-SIMS 2D(XY) profiles of SO_2^- for a control sample (calcite aged in brine) and samples aged in 10 or 100 mg/L IOS (calcite aged in brine and then incubated in IOS) are shown in Figure 8. The depth profile of SO_2^- in Figure 7 confirms that with IOS adsorption, SO_2^- accumulates on the top surface of calcite. When no IOS is added to brine, then SO_2^- is not detected on the sample surface (Figure 8a). At 10 mg/L (0.1xCMC), IOS appears to preferentially adsorb at acute edges, with distinct areas of high (yellow) and low (brown) coverage (Figure 8b). While at 100 mg/L, when the concentration is near the CMC, IOS coverage on the surface appears more uniform with intermediate (orange) coverage (Figure 8c). Preferential IOS adsorption at 10 mg/L to acute edges versus obtuse edges and terrace sites is facilitated by comparison of Figure 8b to Figure 8d, where in the latter the terrace, acute edge, and obtuse edge sites are color coded from the laser profilometry image for ease of comparison. Interestingly, surface coverage on the acute edges appears to be denser than that on the obtuse edges. Less dense coverage on the obtuse edge might be due a lower step density at obtuse edges compared to acute edges. A conceptual model of the surface profile along the line indicated by the double arrow in Figure 8d is presented in Figure 8e. It is based on the observation that the obtuse edge is much steeper than the acute edge, such that the latter has more steps that preferentially adsorb IOS. This could give rise to more IOS adsorption on the acute versus the obtuse sides of the pit.

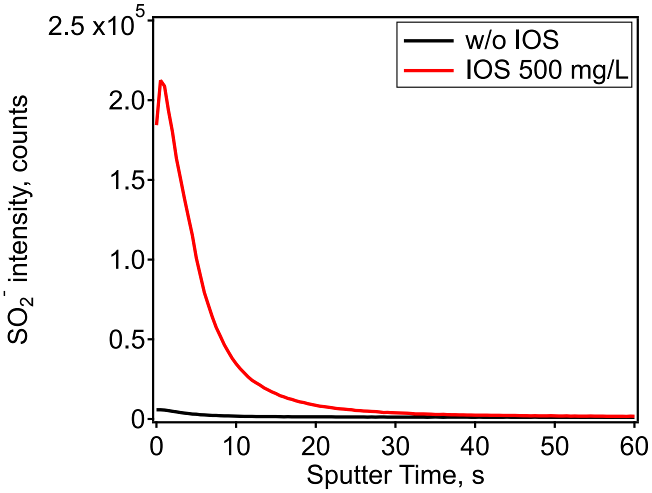

Figure 7. Background CO_3^- normalized SO_2^- ToF-SIMS profiles of calcite under two different conditions. Solid black line is a sample without IOS, whereas red line is a sample dried after exposure to IOS 500 for 1hr.

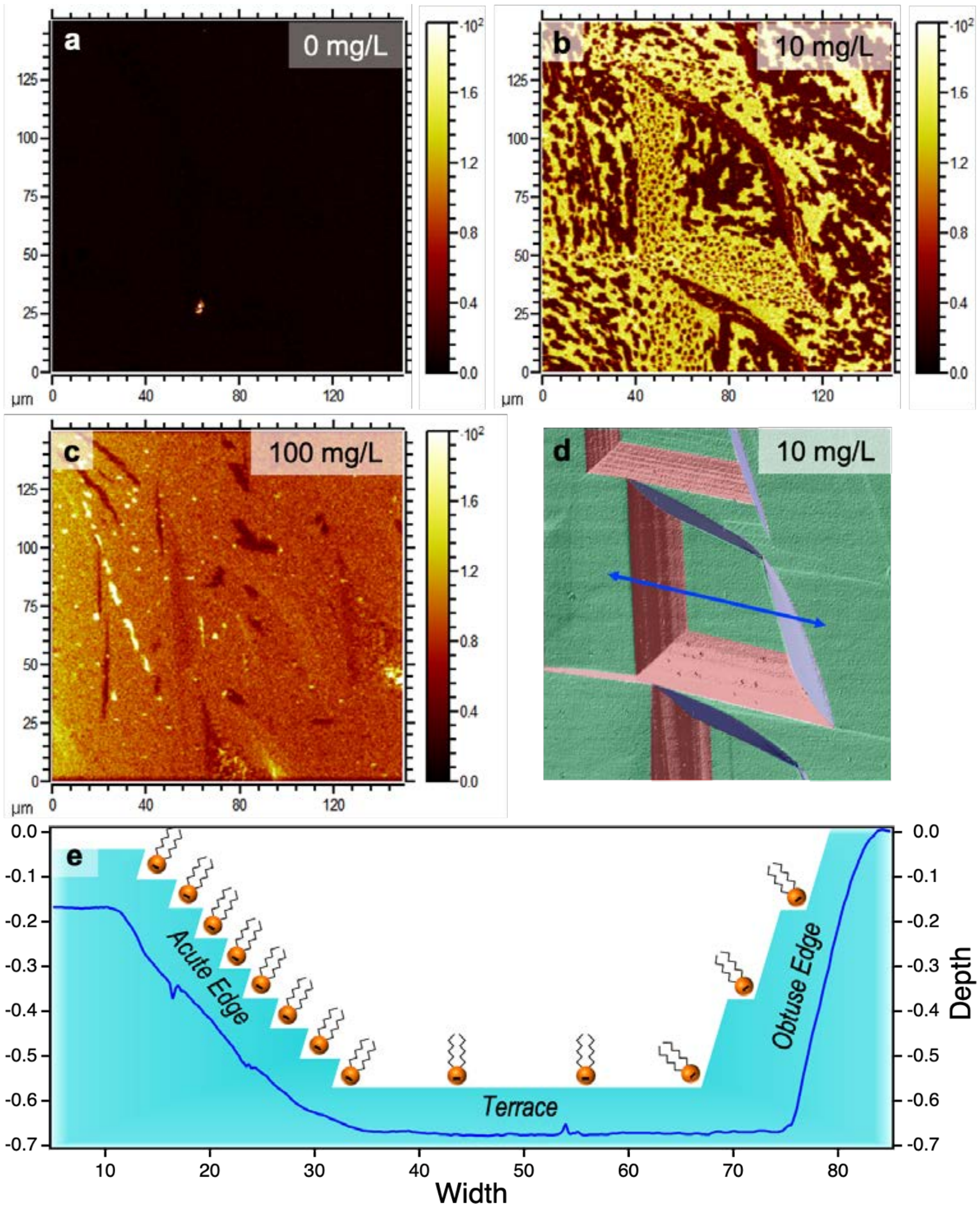

Figure 8. ToF-SIMS 2D(XY) images of SO_2^- distribution on calcite surfaces after a) aging in only brine for 12 hours and then drying, b-c) aging in only brine for 12 hours, followed by 10 and 100 mg/L IOS addition, respectively for an additional 1 hour, and then drying, d) comparison of laser profilometer result and corresponding b) ToF-SIMS 2D(XY) image of SO_2^-; green, red, and blue shades correspond to terrace, acute edges, and obtuse edges, respectively, e) schematic

representation of IOS adsorbed on the calcite surface; surface profile (blue line) shown in e) corresponds to the blue line in d).

Sulfur K-edge NEXAFS spectra of two calibrants (IOS and Gypsum), one control, and four experimental cases are shown in Figure 9. By decomposing the calibrants (Figure 9a-b), the energies of the s → p electron transitions of sulfonate and sulfate groups were identified and are approximately 2481($G_{sulfonate}$) and 2482.5 ($G_{sulfate}$) eV, respectively; these are in good agreement with reported values [58]. In addition, sulfate impurities in IOS were also identified ($G_{sulfate,\ IOS}$). The optical quality calcite crystals used in this study originated from nature, so the presence of sulfur impurities (i.e., sulfite, sulfonate, and sulfate) is reasonable (Figure 9c-e). For example, Pingitore et al. summarized different hypothetical modes of sulfur incorporation into carbonate minerals: i) anhydrite ($CaSO_4$) as mineral inclusions, ii) sulfite (SO_3^{2-}) and sulfate (SO_4^{2-}) substitution for carbonate, iii) sulfate as fluid inclusions, iv) organo-sulfur as organic matter [71]. Also, Perrin et al. experimentally observed the existence of sulfate in their optical quality calcite which contains S below 100 ppm, and sulfite in their synthetic S-MgCalcites using NEXAFS spectroscopy [72].

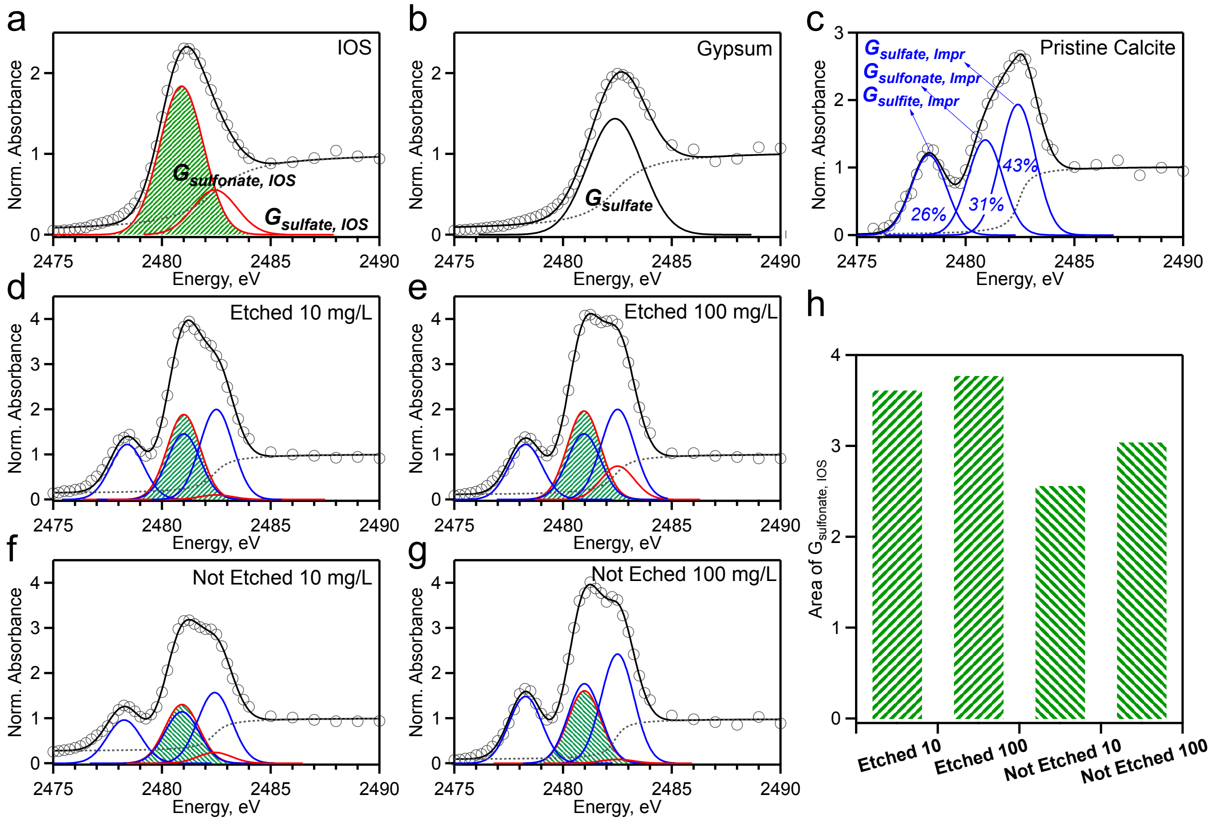

Figure 9. Sulfur K-edge NEXAFS spectra of: a) A drop of concentrated IOS solution (30.1 %) on a silicon wafer. b) Freshly cleaved gypsum without further treatment. c) Freshly cleaved calcite without further treatment. d-e) Freshly cleaved calcite aged in only brine for 12 hours, followed by aging for 1 more hour in brine mixed with either 10 and 100 mg/L IOS, and then dried. f-g) Freshly cleaved calcite aged in calcite-saturated brine for 12 hours to prevent pit formation, followed by aging for 1 more hour in brine mixed with either 10 and 100 mg/L IOS, and then dried. h) Decomposed peak areas of $G_{\text{sulfonate, IOS}}$ (green shaded area of d-g) showing relative amounts of IOS adsorbed to the calcite. Gaussian-Arctan fitting parameters are summarized in Table S5 (Supporting Information).

Due to the uncertainty in the sources of sulfur impurities, we first used three Gaussian functions that represent individual sulfur species with different oxidation states to decompose the spectra. The fractional contributions of three different sulfur functional groups ($G_{\text{sulfite, Impr}}$, $G_{\text{sulfonate, Impr}}$, and $G_{\text{sulfate, Impr}}$) to the measured spectrum were calculated based on the area of Gaussian functions as shown in Figure 9c. Subsequently, to distinguish the contributions of IOS and sulfur impurities in the prepared samples to sulfonate (2481 eV) and sulfate (2482.5 eV), two Gaussian functions (e.g., $G_{\text{sulfonate, IOS}}$ (red line) and $G_{\text{sulfonate, Impr}}$ (blue line)) were used to decompose each functional group contribution (Figure 9d-g). The ratio between impurities was fixed, assuming that ratios of sulfite to sulfonate and sulfite to sulfate for all calcite samples are identical, since all samples were prepared from one single calcite crystal. Ultimately, areas of $G_{\text{sulfonate, IOS}}$ (green) in Figure 9d-g were calculated and summarized in Figure 9h. Detailed Gaussian-Arctan fitting parameters are in Table S5.

Decomposed sulfur K-edge NEXAFS spectra for each of the IOS adsorbed calcite samples are in good agreement with findings in ToF-SIMS results. The existence of $G_{\text{sulfonate, IOS}}$, and differences in areas between samples, indicate that SO_2^- detected by ToF-SIMS originates from adsorbed IOS on calcite surfaces. The decomposed NEXAFS spectra enable semiquantitative comparison of the amount of IOS adsorbed on calcite surfaces. Overall, amounts of IOS adsorbed on etched calcite samples were greater than those on unetched (i.e., Not Etched) samples. In agreement with ToF-SIMS results, the NEXASF spectra indicate that IOS preferentially adsorb more to edges compared to terraces on calcite surfaces. Moreover, when samples were exposed to higher concentration of IOS, greater amounts of IOS partitioned onto calcite surfaces (i.e., Figure 9h Etched 10 vs Etched 100), as observed with ToF-SIMS (Figure 8a-c),

Calcium K-edge NEXAFS spectra were also measured to probe the effect of IOS adsorption to the surface Ca bonding environment and formation of polymorphs of calcium carbonate. No substantial difference in Ca K-edge NEXAFS spectra were observed between samples (Figure S2). This might be due to broad spectra peaks or the signal being dominated by bulk calcite. Meanwhile, polymorphs of $CaCO_3$ can form under different thermodynamic conditions and in the presence of surfactants. For example, Chen and Nan reported that precipitation of $CaCO_3$ polymorphs such as aragonite and vaterite can occur in the presence of anionic surfactants [74]. However, as shown in Figure S2, obtained Ca K-edge NEXAFS spectra of four samples and pristine calcite are similar with no clear signatures of other $CaCO_3$ polymorphs (i.e., amorphous calcium carbonate (ACC), aragonite and vaterite) emerging. Future studies to optimize the surface signal will be helpful to better probe calcite surface chemistry.

Prior efforts to identify preferential adsorption of solutes on edge or terrace sites have relied on less direct measures. Walker et al. treated cleaved calcite with a nonionic surfactant, hexamethyldisilazane (HMDS), to alter calcite wettability. They used Kelvin probe force microscopy (KPFM) to indicate preferential HMDS adsorption at existing step or edge sites [24]. Elhadj et al. and Sand et al. used AFM to image acute and obtuse step edge morphology changes during precipitation in the absence and presence of polyaspartic acid and polysaccharides, respectively [43,75]. They inferred binding location from these measurements, and supported their interpretation with theoretical binding energy calculations. The ToF-SIMS and S K-edge NEXAFS results in this study provide more direct evidence of preferential IOS adsorption at edge sites, thereby suggesting adsorbed IOS is inhibiting dissolution via step pinning at these locations.

DFT Simulation of IOS Adsorption on Calcite Surfaces

In order to better understand the experimental results, DFT was used to calculate binding energies of the IOS molecule on the calcite surface, and binding geometries of the IOS molecule at terrace, acute and obtuse step sites are shown in Figure 10. The calculated binding energies are shown in Table 4. Our most accurate calculations with implicit solvation indicate that IOS binding is strongest at the acute step (-1.02 eV) site followed closely by the obtuse step (-0.94 eV), and binding at the terrace site (-0.27 eV) is weakest. The same trend was observed for both vacuum and our implicit solvent model, as shown in Table 4. These calculations help to explain how preferential IOS adsorption at both acute and obtuse sites can disrupt and inhibit calcite dissolution. They also support the preferential adsorption of IOS at acuate versus obtuse sites as indicated by ToF-SIMS in subsection 3.6, and indicate this is at least partially due to preferential adsorption at acute edge versus obtuse edge sites.

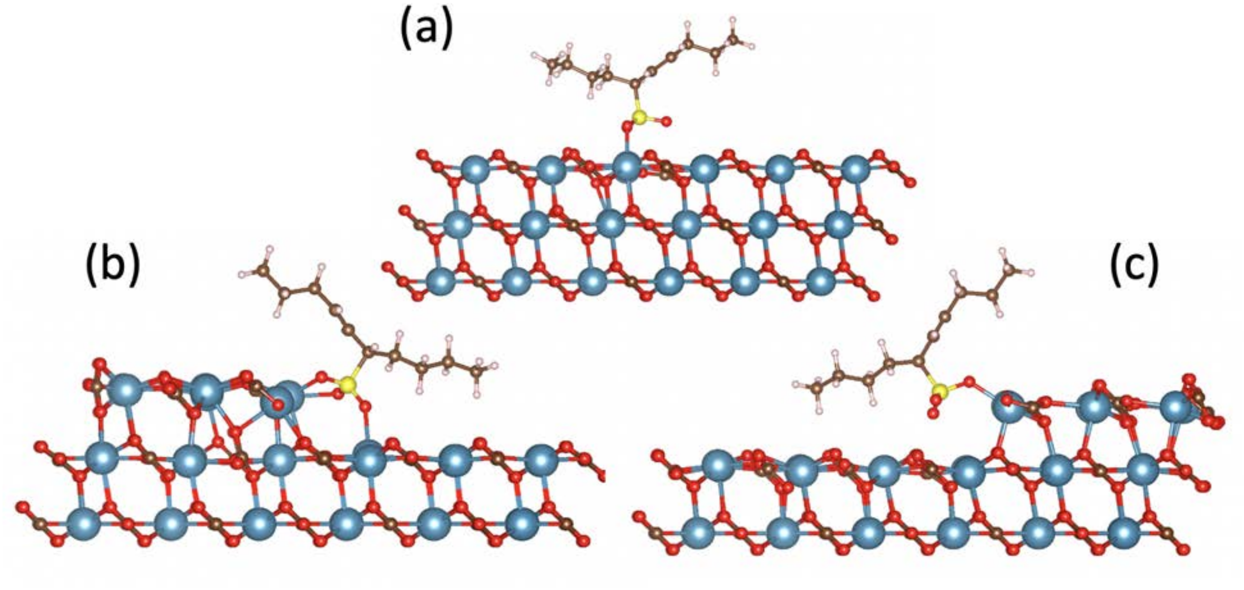

Figure 10. Side view of IOS adsorption at (a) terrace, (b) acute step and (c) obtuse step sites on the calcite $\{10\overline{1}4\}$ surface.

Table 4. Binding energies of the IOS molecule at different Calcite sites.

Binding energies (eV)	**Terrace site**	**Obtuse step**	**Acute step**
Vacuum	-0.78	-2.38	-3.51
Solvent	-0.28	-0.94	-1.02

Discussion

Results in this work highlight two apparently opposite effects of the IOS on calcite dissolution. The first is the formation of more etch pits (i.e., higher density) in the presence of IOS (e.g., 12 hours, Figure 3b), and the second is the inhibition of etch pit growth by IOS once they are created. Miyata et al. used molecular dynamics to interrogate mechanisms responsible for the growth of etch pits [76]. They simulated dissolution at a calcite edge site, and determined that dissolution starts when adsorbed water dissociates, and the proton is transferred to CO_3 and the hydroxyl ion to Ca. This allows bonds between the proton stabilized CO_3 and Ca to break, creating a separate bicarbonate ion (HCO_3^-) that desorbs from the calcite edge. The HCO_3^- then decomposes to a hydroxide ion and CO_2, the hydroxide ion adsorbs to Ca, and adsorbed $Ca(OH)_2$ is formed which can desorb into solution. The CO_2 released into solution then forms bicarbonate in bulk water at circumneutral pH. That study highlights the importance of adsorbed water in facilitating Ca and CO_3 hydration at the calcite surface and indicates that solutes that disrupt adsorbed water will affect calcite dissolution.

Nada and Shen et al. determined the binding conformation of aspartic acid and polystyrene sulfonate on a calcite $\{10\bar{1}4\}$ surface using molecular dynamics [48,77]. First, they showed that three layers of structured water molecules form on the calcite $\{10\bar{1}4\}$ surface. Adsorbed aspartic acid and polystyrene sulfonate are separated from calcite $\{10\bar{1}4\}$ surface by one or two intervening structured water molecules, and form a weak nonspecific bond with calcite $\{10\bar{1}4\}$ surface. In addition, Elhadj et al. studied the effect of polyaspartic acid concentration and chain length on calcite crystal growth, and observed growth enhancement at low concentrations and a transition to growth inhibition at high concentrations, where the transition occurred at lower concentrations for larger polyaspatic acids [43]. They attribute the transition to the number of calcite edge sites where polyaspartic acids displace water molecules. At low polyaspartic acid concentrations and low water displacement, sufficient restructuring of water occurs at the calcite surface to reduce the energy for diffusion of solvated ions across this boundary [44]. However, at high polyapsartic acid concentrations and high water displacement, there is sufficient dehydration of contiguous water molecules at the surface that solvation of Ca and CO_3 is inhibited. It follows that the strength and/or amount of IOS adsorption on flat versus edge sites may control contrasting patterns of rapid initial pit formation versus slow pit growth during dissolution.

Surface pressure values calculated from interfacial tensions (Table 2) indicate preferential IOS adsorption to etched versus smooth calcite surfaces, where the former have a higher density of edge sites. ToF-SIMS and S K-edge NEXAFS results support this interpretation, and the former shows IOS preferentially adsorbs to acute versus obtuse and terrace sites. Our DFT results also support this interpretation, and show slightly more favorable IOS adsorption at acute versus obtuse edge sites, both of which are much more favorable than adsorption at terrace sites (i.e., by 0.60-

1.66 eV). Similarly, Elhadj et al. found that polyaspartic acids adsorb more strongly to calcite edge versus terrace (flat) sites (by 1.3-6.5 eV) [43]. This leads us to postulate a conceptual model, where oxygen in the sulfonate head group of IOS interacts with Ca at calcite surfaces and displaces water. On calcite terraces, weaker adsorption energies indicates that fewer adsorbed IOS molecules per area displace less water, and they are characterized by faster attachment and detachment rates compared to edge sites. This disruption of water at flat surfaces could lower the energy barrier for diffusion of solvated molecules across the water hydration layer and promote faster pit formation (relative to brine only). However, at edge sites, where more strongly adsorbed IOS molecules are present, IOS molecules displace many more water molecules, and this inhibits CO_3 and Ca solvation and retards pit growth. Our calcite dissolution results with varying IOS concentrations show that as IOS concentrations exceed the CMC calcite dissolution rates increase, and this appears to be caused by IOS aggregation into micelles or hemimicelles on the calcite surface that reduces edge site adsorption coverage.

Surface complexation models (SCMs) for carbonates have been used to explain adsorption isotherms, surface charge, and to model dissolution and growth kinetics when inhibitors are present [78–82]. Defining reactions of surface species and their concentrations significantly affects the accuracy of modeling results. For example, Tagavifar et al. used the diffusion layer model (DLM), which assumes formation of inner sphere complexes, to model surfactant binding to a limestone surface without intervening water molecules [80]. They suggested two different surface reactions were needed based on the surfactant chemical structure: strong adsorption by charge regulated complexation with the surfactant head group; weak adsorption by hydrogen bonding between ethoxy or propoxy groups in the hydrocarbon chain. These proposed complexation reactions were not supported by spectroscopic or computational (i.e., molecular dynamics and DFT) evidence. However, binding energies from our DFT efforts, as well as ToF-SIM and S K-edge NEXAFS results, support stronger inner sphere complexation of IOS at defect sites (i.e., acute and obtuse edges). They also support weaker complexation at terrace sites, and the exact conformation of IOS at these sites requires further study via DFT and/or spectroscopic evaluation.

Conclusions

Primary findings in this work are the following:

- Adsorption of IOS to surfaces of minerals in Eagle Ford shale kinetically inhibited overall release of Ca into bulk solution, and this is attributed to inhibition of calcite dissolution.
- IOS adsorption from brine to calcite both enhances initial etch pit formation, and prevents further etch pit growth.
- ToF-SIMS, S K-edge NEXAFS and DFT results indicate that IOS preferentially adsorbs to edge sites compared to terrace sites.
- The weak binding of IOS to terrace sites observed in this work suggests that enhanced etch pit formation in IOS-containing brines is due to the disruption of structured water molecules at flat surfaces by IOS, resulting in relatively lower energy barriers for diffusion of solvated ions to and from the calcite surface.
- The strong preferential binding of IOS to edge sites suggests that inhibited etch pit growth in IOS-containing brines is due to displacement of water molecules at defect sites (i.e., obtuse and acute edges) by strongly adsorbed IOS molecules, resulting in limited solvation of calcite.

This work shows for the first time how surfactant adsorption amount and location to calcite surfaces can be probed over spatial scales approaching hundreds of microns using optical profilometry coupled with ToF-SIMS and NEXAFS spectroscopy. By comparison, AFM measurements of surfactant adsorption on calcite surfaces are limited to only a few microns. The implications of these results are that surfactants added to slick water, foams, and carbon dioxide injected into shale or conventional formations can inhibit dissolution of carbonate minerals. This may mitigate the formation of preferential flow paths, that could enhance oil and gas recovery from shales, or serve as conduits for upward fluid migration from deep reservoirs to potable groundwater. Further work is needed to determine if the observed effects extend to reservoir pressures and temperatures, and possible implications of these mechanisms in real reservoirs.

References

[1] EIA, EIA/ARI world shale gas and shale oil resource assessment technically recoverable shale gas and shale oil resources: an assessment of 137 shale formations in 41 countries outside the United States, 2013. www.adv-res.com.

[2] EIA, Annual energy outlook 2014 with projections to 2040, 2014. www.eia.gov/forecasts/aeo.

[3] F. Liu, P. Lu, C. Griffith, S.W. Hedges, Y. Soong, H. Hellevang, C. Zhu, CO2-brine-caprock interaction: Reactivity experiments on Eau Claire shale and a review of relevant literature, Int. J. Greenh. Gas Control. 7 (2012) 153–167. https://doi.org/10.1016/j.ijggc.2012.01.012.

[4] M.F. Irfan, T.M. Bisson, E. Bobicki, F. Arguelles-Vivas, Z. Xu, Q. Liu, T. Babadagli, CO2 storage in saline aquifers by dissolution and residual trapping under supercritical conditions: An experimental investigation, Colloids Surfaces A Physicochem. Eng. Asp. 548 (2018) 37–45. https://doi.org/10.1016/j.colsurfa.2018.03.062.

[5] J.A. Chermak, M.E. Schreiber, Mineralogy and trace element geochemistry of gas shales in the United States: Environmental implications, Int. J. Coal Geol. 126 (2014) 32–44.

[6] W.C. Dawson, Shale microfacies: Eagle Ford Group (Cenomanian-Turonian) north-central Texas outcrops and subsurface equivalents, Gulf Coast Assoc. Geol. Soc. Trans. 50 (2000) 607–621.

[7] D.S. Jennings, J. Antia, W.K. Camp, E. Diaz, B. Wawak, Petrographic characterization of the Eagle Ford Shale, South Texas: Mineralogy, common constituents, and distribution of nanometer-scale pore types, Electron Microsc. Shale Hydrocarb. Reserv. AAPG Mem. 102 (2013) 101–113.

[8] J. Schieber, R. Lazar, K. Bohacs, R. Klimentidis, M. Dumitrescu, J. Ottmann, An sem study of porosity in the eagle ford shale of Texas-pore types and porosity distribution in a depositional and sequence-stratigraphic context, AAPG Mem. 110 (2016) 167–186. https://doi.org/10.1306/13541961M1103589.

[9] F. Gherardi, T. Xu, K. Pruess, Numerical modeling of self-limiting and self-enhancing caprock alteration induced by CO2 storage in a depleted gas reservoir, Chem. Geol. 244 (2007) 103–129.

[10] R. Lahann, M. Mastalerz, J.A. Rupp, A. Drobniak, Influence of CO2 on New Albany

Shale composition and pore structure, Int. J. Coal Geol. 108 (2013) 2–9.

[11] J. Rohmer, A. Pluymakers, F. Renard, Mechano-chemical interactions in sedimentary rocks in the context of CO2 storage: Weak acid, weak effects?, Earth-Science Rev. 157 (2016) 86–110. https://doi.org/10.1016/j.earscirev.2016.03.009.

[12] J.P. Verdon, Significance for secure CO2 storage of earthquakes induced by fluid injection, Environ. Res. Lett. 9 (2014) 1–10. https://doi.org/10.1088/1748-9326/9/6/064022.

[13] S.A. Carroll, W.W. Mcnab, Z. Dai, S.C. Torres, Reactivity of Mount Simon Sandstone and the Eau Claire Shale Under CO2 Storage Conditions, Environ. Sci. Technol. 47 (2013) 252–261. https://doi.org/10.1021/es301269k.

[14] V. Marcon, C. Joseph, K.E. Carter, S.W. Hedges, C.L. Lopano, G.D. Guthrie, J.A. Hakala, Experimental insights into geochemical changes in hydraulically fractured Marcellus Shale, Appl. Geochemistry. 76 (2017) 36–50.

[15] A.N. Paukert Vankeuren, J.A. Hakala, K. Jarvis, J.E. Moore, Mineral Reactions in Shale Gas Reservoirs: Barite Scale Formation from Reusing Produced Water As Hydraulic Fracturing Fluid, Environ. Sci. Technol. 51 (2017) 9391–9402. https://doi.org/10.1021/acs.est.7b01979.

[16] J.J. Sheng, Status of surfactant EOR technology, Petroleum. 1 (2015) 97–105. https://doi.org/10.1016/j.petlm.2015.07.003.

[17] H.C. Tamayo, K.J. Lee, R.S. Taylor, Enhanced aqueous fracturing fluid recovery from tight gas formations: Foamed CO2 pre-pad fracturing fluid and more effective surfactant systems, J. Can. Pet. Technol. 47 (2008) 33–38. https://doi.org/10.2118/08-10-33.

[18] C. Negin, S. Ali, Q. Xie, Most common surfactants employed in chemical enhanced oil recovery, Petroleum. 3 (2017) 197–211. https://doi.org/10.1016/j.petlm.2016.11.007.

[19] S. Paria, K.C. Khilar, A review on experimental studies of surfactant adsorption at the hydrophilic solid-water interface, Adv. Colloid Interface Sci. 110 (2004) 75–95. https://doi.org/10.1016/j.cis.2004.03.001.

[20] B. Li, E. Ruckenstein, Adsorption of ionic surfactants on charged solid surfaces from aqueous solutions, Langmuir. 12 (1996) 5052–5063.

[21] P. Somasundaran, G.E. Agar, The zero point of charge of calcite, J. Colloid Interface Sci. 24 (1967) 433–440. https://doi.org/10.1016/0021-9797(67)90241-X.

[22] T. Ahmadall, M. V Gonzalez, J.H. Harwell, J.F. Scamehorn, Reducing Surfactant Adsorption in Carbonate Reservoirs, SPE Reserv. Eng. 8 (1993) 117–122. https://doi.org/10.2118/24105-PA.

[23] J.F. Scamehorn, R.S. Schechter, W.H. Wade, Adsorption of surfactants on mineral oxide surfaces from aqueous solutions. I: Isomerically pure anionic surfactants, J. Colloid Interface Sci. 85 (1982) 463–478. https://doi.org/10.1016/0021-9797(82)90013-3.

[24] S.M. Walker, M.C. Marcano, S. Kim, S.D. Taylor, U. Becker, Understanding Calcite Wettability Alteration through Surface Potential Measurements and Molecular Simulations, J. Phys. Chem. C. 121 (2017) 28017–28030. https://doi.org/10.1021/acs.jpcc.7b09565.

[25] H.M. Abd El-Lateef, V.M. Abbasov, L.I. Aliyeva, E.E. Qasimov, I.T. Ismayilov, Inhibition of carbon steel corrosion in CO2-saturated brine using some newly surfactants based on palm oil: Experimental and theoretical investigations, Mater. Chem. Phys. 142 (2013) 502–512. https://doi.org/10.1016/j.matchemphys.2013.07.044.

[26] U. Wehrmeister, D.E. Jacob, A.L. Soldati, N. Loges, T. Häger, W. Hofmeister, Amorphous, nanocrystalline and crystalline calcium carbonates in biological materials, J. Raman Spectrosc. 42 (2011) 926–935. https://doi.org/10.1002/jrs.2835.

[27] T. Matschei, B. Lothenbach, F.P. Glasser, The role of calcium carbonate in cement hydration, Cem. Concr. Res. 37 (2007) 551–558. https://doi.org/10.1016/j.cemconres.2006.10.013.

[28] N.H. De Leeuw, S.C. Parker, J.H. Harding, Molecular dynamics simulation of crystal dissolution from calcite steps, Phys. Rev. B. 60 (1999) 13792.

[29] I.N. MacInnis, S.L. Brantley, The role of dislocations and surface morphology in calcite dissolution, Geochim. Cosmochim. Acta. 56 (1992) 1113–1126. https://doi.org/10.1016/0016-7037(92)90049-O.

[30] C.A. Orme, A. Noy, A. Wierzbicki, M.T. Mcbride, M. Grantham, H.H. Teng, P.M. Dove, J.J. Deyoreo, Formation of chiral morphologies through selective binding of amino acids to calcite surface steps, Nature. 411 (2001) 775–779. https://doi.org/10.1038/35081034.

[31] W. Stumm, Reactivity at the mineral-water interface: Dissolution and inhibition, Colloids Surfaces A Physicochem. Eng. Asp. 120 (1997) 143–166. https://doi.org/10.1016/S0927-7757(96)03866-6.

[32] L.N. Plummer, Wigley T. M. L., D.L. Parkhurst, The Kinetics of Calcite Dissolution In CO2-Water systems at 5 degrees to 60 degrees C and 0.0 to 1.0 atm CO2, Am. J. Sci. 278 (1978) 179–216. https://doi.org/10.2475/ajs.278.2.179.

[33] R.S. Arvidson, M. Collier, K.J. Davis, M.D. Vinson, J.E. Amonette, A. Luttge, Magnesium inhibition of calcite dissolution kinetics, Geochim. Cosmochim. Acta. 70 (2006) 583–594.

[34] D.W. Britt, V. Hlady, In-situ atomic force microscope imaging of calcite etch pit morphology changes in undersaturated and 1-hydroxyethylidene-1, 1-diphosphonic acid poisoned solutions, Langmuir. 13 (1997) 1873–1876.

[35] R.G. Compton, C.A. Brown, The inhibition of calcite dissolution/precipitation: 1, 2-dicarboxylic acids, J. Colloid Interface Sci. 170 (1995) 586–590.

[36] N.H. De Leeuw, Molecular dynamics simulations of the growth inhibiting effect of Fe2+, Mg2+, Cd2+, and Sr2+ on calcite crystal growth, J. Phys. Chem. B. 106 (2002) 5241–5249.

[37] P.M. Dove, M.F. Hochella Jr, Calcite precipitation mechanisms and inhibition by orthophosphate: In situ observations by Scanning Force Microscopy, Geochim. Cosmochim. Acta. 57 (1993) 705–714.

[38] C.N. Fredd, H.S. Fogler, The influence of chelating agents on the kinetics of calcite dissolution, J. Colloid Interface Sci. 204 (1998) 187–197.

[39] A.R. Hoch, M.M. Reddy, G.R. Aiken, Calcite crystal growth inhibition by humic substances with emphasis on hydrophobic acids from the Florida Everglades, Geochim. Cosmochim. Acta. 64 (2000) 61–72.

[40] M. Ricci, J.J. Segura, B.W. Erickson, G. Fantner, F. Stellacci, K. Voïtchovsky, Growth and Dissolution of Calcite in the Presence of Adsorbed Stearic Acid, Langmuir. 31 (2015) 7563–7571. https://doi.org/10.1021/acs.langmuir.5b01732.

[41] E. Ruiz-Agudo, M. Urosevic, C. V. Putnis, C. Rodríguez-Navarro, C. Cardell, A. Putnis, Ion-specific effects on the kinetics of mineral dissolution, Chem. Geol. 281 (2011) 364–371. https://doi.org/10.1016/j.chemgeo.2011.01.003.

[42] T. Yang, W. Huh, J.Y. Jho, I.W. Kim, Effects of fluoride and polymeric additives on the dissolution of calcite and the subsequent formation of fluorite, Colloids Surfaces A Physicochem. Eng. Asp. 451 (2014) 75–84.

https://doi.org/10.1016/j.colsurfa.2014.03.040.

[43] S. Elhadj, E.A. Salter, A. Wierzbicki, J.J. De Yoreo, N. Han, P.M. Dove, Peptide controls on calcite mineralization: Polyaspartate chain length affects growth kinetics and acts as a stereochemical switch on morphology, Cryst. Growth Des. 6 (2006) 197–201.

[44] S. Elhadj, J.J. De Yoreo, J.R. Hoyer, P.M. Dove, Role of molecular charge and hydrophilicity in regulating the kinetics of crystal growth, Proc. Natl. Acad. Sci. 103 (2006) 19237–19242.

[45] K.J. Davis, P.M. Dove, J.J. De Yoreo, The role of Mg2+ as an impurity in calcite growth, Science (80-.). 290 (2000) 1134–1137.

[46] E. Ruiz-Agudo, M. Kowacz, C. V. Putnis, A. Putnis, The role of background electrolytes on the kinetics and mechanism of calcite dissolution, Geochim. Cosmochim. Acta. 74 (2010) 1256–1267. https://doi.org/10.1016/j.gca.2009.11.004.

[47] H.H. Teng, P.M. Dove, Surface site-specific interactions of aspartate with calcite during dissolution: Implications for biomineralization, Am. Mineral. 82 (1997) 878–887. https://doi.org/10.2138/am-1997-9-1005.

[48] H. Nada, Difference in the conformation and dynamics of aspartic acid on the flat regions, step edges, and kinks of a calcite surface: A molecular dynamics study, J. Phys. Chem. C. 118 (2014) 14335–14345. https://doi.org/10.1021/jp502332c.

[49] I. Choi, I.W. Kim, Molecular Dynamics Simulation to Understand the Ability of Anionic Polymers to Alter the Morphology of Calcite, (2017). https://doi.org/10.1155/2017/7594950.

[50] J.P. Nicot, A. Gherabati, R. Darvari, P. Mickler, Salinity Reversal and Water Freshening in the Eagle Ford Shale, Texas, USA, ACS Earth Sp. Chem. 2 (2018) 1087–1094. https://doi.org/10.1021/acsearthspacechem.8b00095.

[51] J.R. Barnes, H. Dirkzwager, J.R. Smit, J.P. Smit, R.C. Navarrete, B.H. Ellison, M.A. Buijse, Application of internal olefin sulfonates and other surfactants to EOR. Part 1: Structure - Performance relationships for selection at different reservoir conditions, in: SPE - DOE Improv. Oil Recover. Symp. Proc., OnePetro, 2010: pp. 663–678. https://doi.org/10.2118/129766-ms.

[52] H. Abdulelah, S. Mahmood, S. Al-Hajri, M. Hakimi, E. Padmanabhan, Retention of Hydraulic Fracturing Water in Shale: The Influence of Anionic Surfactant, Energies. 11

(2018) 3342. https://doi.org/10.3390/en11123342.

[53] M. Salehi, S.J. Johnson, J.T. Liang, Mechanistic study of wettability alteration using surfactants with applications in naturally fractured reservoirs, Langmuir. 24 (2008) 14099–14107. https://doi.org/10.1021/la802464u.

[54] H.H. Teng, Controls by saturation state on etch pit formation during calcite dissolution, Geochim. Cosmochim. Acta. 68 (2004) 253–262. https://doi.org/10.1016/S0016-7037(03)00423-X.

[55] C. Amrhein, D.L. Suarez, Procedure for determining sodium-calcium selectivity in calcareous and gypsiferous soils, Soil Sci. Soc. Am. J. 54 (1990) 999–1007. https://doi.org/10.2136/sssaj1990.03615995005400040011x.

[56] E. Costa, D. Aquilano, Experimental value of the specific surface energy of the cleavage {10.4} calcite rhombohedron in the presence of its saturated aqueous solution, Crystals. 8 (2018) 1–8. https://doi.org/10.3390/cryst8060238.

[57] X. Hong, M. Newville, T.S. Duffy, Larch: An Analysis Package for XAFS and Related Spectroscopies Related content High-pressure X-ray absorption fine structure in the diamond anvil cell and its applications in geological materials, J. Phys. Conf. Ser. 430 (2013) 12007. https://doi.org/10.1088/1742-6596/430/1/012007.

[58] A. Manceau, K.L. Nagy, Quantitative analysis of sulfur functional groups in natural organic matter by XANES spectroscopy, Geochim. Cosmochim. Acta. 99 (2012) 206–223. https://doi.org/10.1016/j.gca.2012.09.033.

[59] D.L. Parkhurst, C.A.J. Appelo, Description of input and examples for PHREEQC Version 3 — A computer program for speciation, batch-reaction, one-dimensional transport, and inverse geochemical calculations, 2013. https://doi.org/10.1016/0029-6554(94)90020-5.

[60] A.W. Adamson, A.P. Gast, Physical chemistry of surfaces, 5th ed., interscience, New York, 1990.

[61] J. Botto, S.J. Fuchs, B.W. Fouke, A.F. Clarens, J.T. Freiburg, P.M. Berger, C.J. Werth, Effects of Mineral Surface Properties on Supercritical CO2 Wettability in a Siliciclastic Reservoir, Energy and Fuels. 31 (2017) 5275–5285. https://doi.org/10.1021/acs.energyfuels.6b03336.

[62] J. Drelich, J.D. Miller, The effect of solid surface heterogeneity and roughness on the contact angle/drop (bubble) size relationship, J. Colloid Interface Sci. 164 (1994) 252–

259.

[63] F.M. Fowkes, W.D. Harkins, The state of monolayers adsorbed at the interface solid—aqueous solution, J. Am. Chem. Soc. 62 (1940) 3377–3386.

[64] T. Zeng, K.T. Kim, C.J. Werth, L.E. Katz, K.K. Mohanty, Surfactant Adsorption on Shale Samples: Experiments and an Additive Model, Energy and Fuels. 34 (2020) 5436–5443. https://doi.org/10.1021/acs.energyfuels.9b04016.

[65] M.J. Rosen, J.T. Kunjappu, Surfactants and interfacial phenomena, John Wiley & Sons, 2012.

[66] W.A. Ducker, E.J. Wanless, Surface-aggregate shape transformation, Langmuir. 12 (1996) 5915–5920. https://doi.org/10.1021/la9605448.

[67] E.J. Wanless, T.W. Davey, W.A. Ducker, Surface aggregate phase transition, Langmuir. 13 (1997) 4223–4228. https://doi.org/10.1021/la970146k.

[68] R.E. Lamont, W.A. Ducker, Surface-induced transformations for surfactant aggregates, J. Am. Chem. Soc. 120 (1998) 7602–7607. https://doi.org/10.1021/ja9742895.

[69] F. Jiménezjiménez-A ́ Ngeles, A. Khoshnood, A. Firoozabadi, Molecular Dynamics Simulation of the Adsorption and Aggregation of Ionic Surfactants at Liquid−Solid Interfaces, (2017). https://doi.org/10.1021/acs.jpcc.7b09466.

[70] A.S. Lea, J.E. Amonette, D.R. Baer, Y. Liang, N.G. Colton, Microscopic effects of carbonate, manganese, and strontium ions on calcite dissolution, Geochim. Cosmochim. Acta. 65 (2001) 369–379.

[71] N.E. Pingitore, G. Meitzner, K.M. Love, Identification of sulfate in natural carbonates by x-ray absorption spectroscopy, Geochim. Cosmochim. Acta. 59 (1995) 2477–2483. https://doi.org/10.1016/0016-7037(95)00142-5.

[72] J. Perrin, C. Rivard, D. Vielzeuf, D. Laporte, C. Fonquernie, A. Ricolleau, M. Cotte, N. Floquet, The coordination of sulfur in synthetic and biogenic Mg calcites: The red coral case, Geochim. Cosmochim. Acta. 197 (2017) 226–244. https://doi.org/10.1016/j.gca.2016.10.017.

[73] E. Chalmin, Y. Perrette, B. Fanget, J. Susini, Investigation of organic matter entrapped in synthetic carbonates - A multimethod approach, Microsc. Microanal. 19 (2013) 132–144. https://doi.org/10.1017/S1431927612013773.

[74] Z. Chen, Z. Nan, Controlling the polymorph and morphology of CaCO3 crystals using

surfactant mixtures, J. Colloid Interface Sci. 358 (2011) 416–422. https://doi.org/10.1016/j.jcis.2011.02.062.

[75] K.K. Sand, C.S. Pedersen, S. Sjöberg, J.W. Nielsen, E. Makovicky, S.L.S. Stipp, Biomineralization: Long-term effectiveness of polysaccharides on the growth and dissolution of calcite, Cryst. Growth Des. 14 (2014) 5486–5494. https://doi.org/10.1021/cg5006743.

[76] K. Miyata, J. Tracey, K. Miyazawa, V. Haapasilta, P. Spijker, Y. Kawagoe, A.S. Foster, K. Tsukamoto, T. Fukuma, Dissolution Processes at Step Edges of Calcite in Water Investigated by High-Speed Frequency Modulation Atomic Force Microscopy and Simulation, Nano Lett. 17 (2017) 4083–4089. https://doi.org/10.1021/acs.nanolett.7b00757.

[77] J.-W. Shen, C. Li, N.F.A. Van Der Vegt, C. Peter, Understanding the Control of Mineralization by Polyelectrolyte Additives: Simulation of Preferential Binding to Calcite Surfaces, (2013). https://doi.org/10.1021/jp402341w.

[78] P. Van Cappellen, L. Charlet, W. Stumm, P. Wersin, A surface complexation model of the carbonate mineral-aqueous solution interface, Geochim. Cosmochim. Acta. 57 (1993) 3505–3518. https://doi.org/10.1016/0016-7037(93)90135-J.

[79] J. Song, S. Rezaee, L. Zhang, Z. Zhang, M. Puerto, O.B. Wani, F. Vargas, S. Alhassan, S.L. Biswal, G.J. Hirasaki, Characterizing the Influence of Organic Carboxylic Acids and Inorganic Silica Impurities on the Surface Charge of Natural Carbonates Using an Extended Surface Complexation Model, (2019). https://doi.org/10.1021/acs.energyfuels.8b03896.

[80] M. Tagavifar, S.H. Jang, H. Sharma, D. Wang, L.Y. Chang, K. Mohanty, G.A. Pope, Effect of pH on adsorption of anionic surfactants on limestone: Experimental study and surface complexation modeling, Colloids Surfaces A Physicochem. Eng. Asp. 538 (2018) 549–558. https://doi.org/10.1016/j.colsurfa.2017.11.050.

[81] C. Geffroy, A. Foissy, J. Persello, B. Cabane, Surface complexation of calcite by carboxylates in water, J. Colloid Interface Sci. 211 (1999) 45–53. https://doi.org/10.1006/jcis.1998.5966.

[82] O.S. Pokrovsky, J. Schott, Processes at the magnesium-bearing carbonates/solution interface. II. Kinetics and mechanism of magnesite dissolution, Geochim. Cosmochim.

Acta. 63 (1999) 881–897. https://doi.org/10.1016/S0016-7037(99)00013-7.

[83] M. Bruno, F.R. Massaro, L. Pastero, E. Costa, M. Rubbo, M. Prencipe, D. Aquilano, New estimates of the free energy of calcite/water interfaces for evaluating the equilibrium shape and nucleation mechanisms, Cryst. Growth Des. 13 (2013) 1170–1179. https://doi.org/10.1021/cg3015817.

SUPPORTING INFORMATION

Surfactant Inhibition Mechanisms of Carbonate Mineral Dissolution in Shale

1. ToF-SIMS Analyses.

The Bi_3^+ was chosen to reduce the mixing induced by sputtering of Cs^+ and to enhance the yield of organic secondary ions. For depth profiling, a 300×300 μm^2 area was raster scanned with the sputtering beam while a 100×100 μm^2 area was raster scanned with the analysis beam within the regressing sputtered area. For higher-resolution imaging, a 500×500 μm^2 area was raster scanned with the sputtering beam while a 150×150 μm^2 area was raster scanned with burst-alignment mode. The high-resolution 2D (XY) images were obtained by overlapping 700 layers of scanning results (i.e., SO_2^-). All samples were degassed overnight under vacuum pressure of $<10^{-8}$ torr before analysis, and approximately 2×10^{-6} torr of Ar was used as a discharge medium during the ToF-SIMS analysis/sputtering process. All secondary ions had negative polarity.

2. Surface excess concentration and minimum area per molecule

Surface excess concentration of IOS (Γ) in mole/cm^2 at the interface of water and air was first calculated from following Equation S1. Surface excess concentration of IOS was calculated based on the surface tension measurement as a function of surfactant concentration in Figure S1b.

$$\Gamma = -\frac{1}{2.303yRT}\left(\frac{\partial\gamma}{\partial logC}\right)_T \qquad \text{(S1)}$$

Where $[\partial\gamma/(\partial \log C)]_T$ is the slope (Figure S1b), T is absolute temperature, R = 8.31 $J\cdot mol^{-1}\cdot K^{-1}$ and $y = 1 + C_{IOS}/(C_{IOS} + C_{KCl})$. To compensate for ionic strength of the brine (0.4 M KCl), $\partial logC$ was replaced by $\partial(logC + logf_{IOS})$, and f_{IOS} was calculated by using Debye-Hückel equation (Equation S2),

$$logf_{IOS} = -\frac{0.509{Z_{IOS}}^2\sqrt{I}}{1 + 0.33\alpha\sqrt{I}} \qquad \text{(S2)}$$

Where I is ionic strength of the solution, α is taken as 0.6 for IOS. Ionic strength of brine was calculated by PHREEQC. Concentration of IOS was not considered in ionic strength calculation because the maximum concentration of IOS used to calculate $[\partial\gamma/(\partial \log C)]_T$ was less than 10^{-3} M. Surface excess concentration was then converted to minimum area per molecule A_{min} in $Å^2$ by Equation S3.

$$A_{min} = \frac{10^{16}}{N\Gamma} \tag{S3}$$

Calculated excess surface concentration Γ and minimum area per molecule A_{min} are 8.01 mole/cm^2 and 20.7 $Å^2$, respectively.

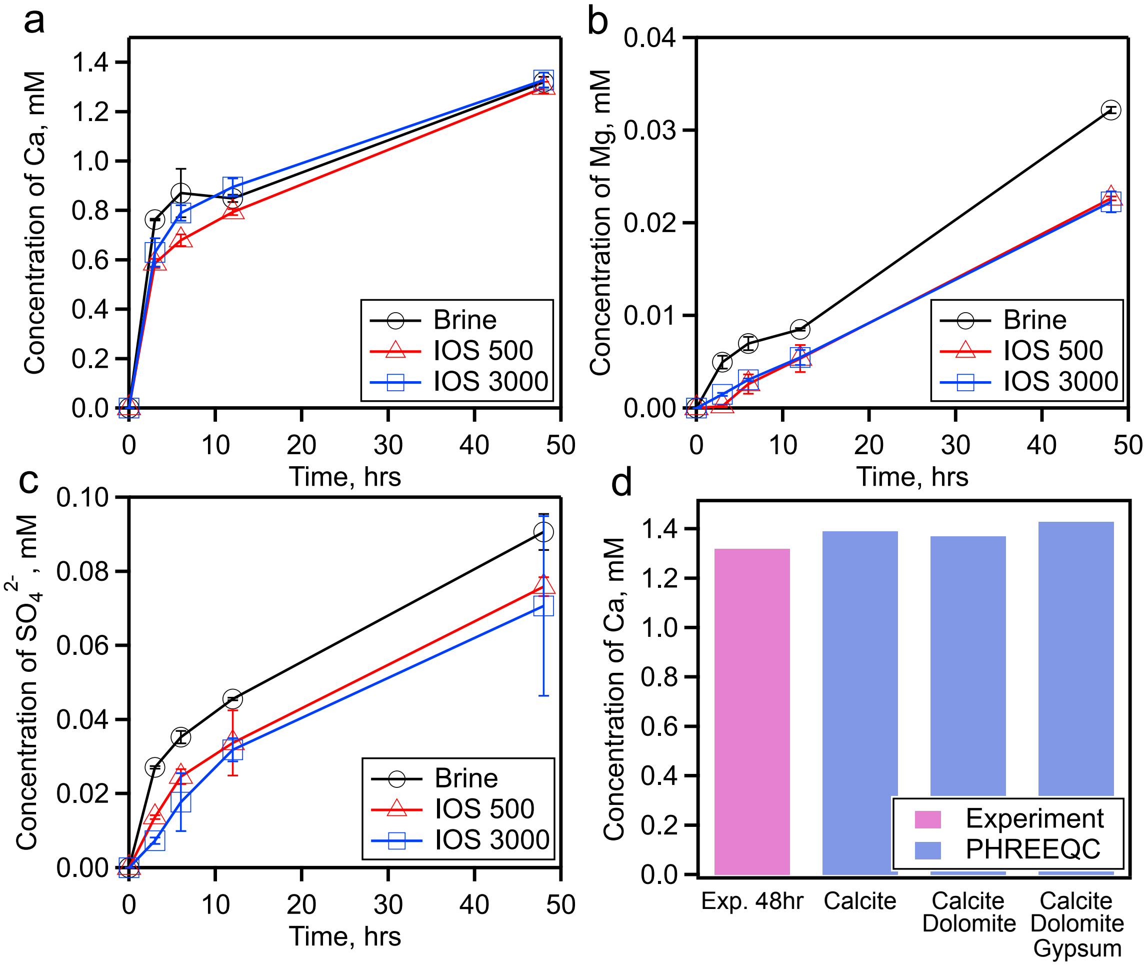

Figure S1. a) Ca, b) Mg, and c) SO_4^{2-} release into solution from Eagle Ford Shale after aging in brine or IOS brine for 48 hours. Initial pH of the solution is 6.3, and ionic strength of brine is 0.4 M. All experiments were run in triplicate, and error bar represents standard deviation. d) PHREEQC modeling results showing potential mineral contributions to Ca^{2+} concentrations. IOS 500 and IOS 3000 refer to brine with either 500 or 3000 mg/L of IOS added.

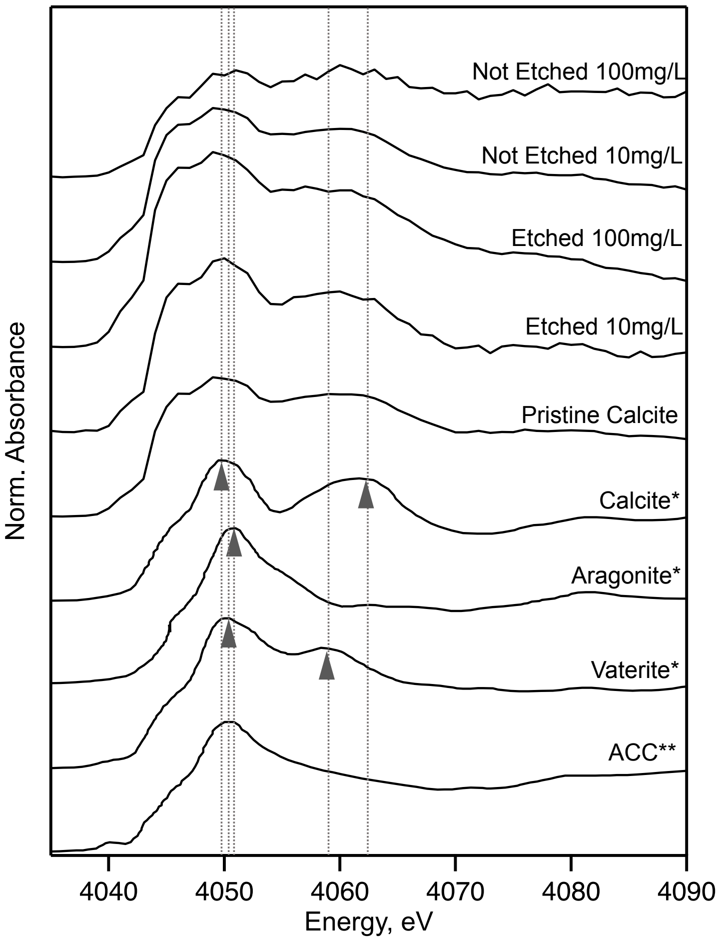

Figure S2. Calcium K-edge NEXAFS spectra of 5 samples in Figure 8 and reference spectra of calcite polymorphs. Reference spectra annotated with * and ** were reproduced from Hayakawa et al. and Politi et al., respectively [1,2].

Table S1. List of dissolution/precipitation and complexation reactions used in the PHREEQC.

Reaction (phreeqc.dat)			**Log K**
$CaCO_3(S)$	⇔	$Ca^{2+} + CO_3^{2-}$	-8.48
$CaMg(CO_3)_2(S)$	⇔	$Ca^{2+} + Mg^{2+} + 2CO_3^{2-}$	-17.09
$CaSO_4 \cdot 2H_2O(S)$	⇔	$Ca^{2+} + SO_4^{2-} + 2H_2O$	-4.58
$CO_2(g)$	⇔	$CO_2(aq)$	-1.468
$CO_3^{2-} + H^+$	⇔	HCO_3^-	10.329
$CO_3^{2-} + 2H^+$	⇔	$CO_2 + H_2O$	16.681
$Ca^{2+} + CO_3^{2-}$	⇔	$CaCO_3$	3.224
$Ca^{2+} + CO_3^{2-} + H^+$	⇔	$CaHCO_3^+$	11.435
$Ca^{2+} + SO_4^{2-}$	⇔	$CaSO_4$	2.25
$Ca^{2+} + HSO_4^-$	⇔	$CaHSO_4^+$	1.08
$Ca^{2+} + H_2O$	⇔	$CaOH^+ + H^+$	-12.78

Table S2. Ca speciation for Eagle Ford shale at 48 hours for three different modeling cases.

Calcite						
	Molality	Activity	Log Molality	Log Activity	Log γ	Fraction (%)
ToTCa	1.39×10^{-3}					
Ca^{2+}	1.37×10^{-3}	3.73×10^{-4}	-2.86	-3.43	-0.57	98.775
$CaHCO_3^+$	1.24×10^{-5}	8.88×10^{-6}	-4.91	-5.05	-0.14	0.890
$CaCO_3$	4.97×10^{-6}	5.46×10^{-6}	-5.30	-5.26	0.04	0.358
$CaOH^+$	8.92×10^{-9}	6.53×10^{-9}	-8.05	-8.19	-0.14	0.001
Calcite + Dolomite						
	Molality	Activity	Log Molality	Log Activity	Log g	Fraction (%)
ToTCa	1.37×10^{-3}					
Ca^{2+}	1.35×10^{-3}	3.68×10^{-4}	-2.87	-3.44	-0.57	98.757
$CaHCO_3^+$	1.23×10^{-5}	8.81×10^{-6}	-4.91	-5.06	-0.14	0.896
$CaCO_3$	4.97×10^{-6}	5.46×10^{-6}	-5.30	-5.26	0.04	0.363
$CaOH^+$	8.86×10^{-9}	6.48×10^{-9}	-8.05	-8.19	-0.14	0.001
Calcite + Dolomite + Gypsum						
	Molality	Activity	Log Molality	Log Activity	Log g	Fraction (%)
ToTCa	1.43×10^{-3}					
Ca^{2+}	1.41×10^{-3}	3.83×10^{-4}	-2.85	-3.42	-0.57	98.738
$CaHCO_3^+$	1.25×10^{-5}	8.99×10^{-6}	-4.90	-5.05	-0.14	0.877
$CaCO_3$	4.97×10^{-6}	5.46×10^{-6}	-5.30	-5.26	0.04	0.349
$CaSO_4$	7.61×10^{-7}	8.35×10^{-7}	-6.12	-6.08	0.04	0.053
$CaOH^+$	9.04×10^{-9}	6.62×10^{-9}	-8.04	-8.18	-0.14	0.001
$CaHSO_4^+$	6.82×10^{-14}	4.99×10^{-14}	-13.17	-13.30	-0.14	0.000

Table S3. Dissolution terms for Eagle Ford shale at various time points.

Parameter time=	0 hrs	3 hrs	6 hrs	12 hrs	48 hrs
pH	6.30	7.95	7.98	7.95	8.03
Alk [mequiv./kg]	0.10	2.63	2.73	2.71	2.88
a_{H^+} [M]	5.01×10^{-7}	1.69×10^{-8}	1.56×10^{-8}	1.71×10^{-8}	9.65×10^{-9}
$a_{Ca^{2+}}$ [M]		2.09×10^{-4}	2.40×10^{-4}	2.37×10^{-4}	3.76×10^{-4}
$a_{CO_3^{2-}}$ [M]	6.24×10^{-9}	2.89×10^{-6}	3.54×10^{-6}	3.18×10^{-6}	8.67×10^{-6}
$a_{HCO_3^-}$ [M]	7.10×10^{-5}	1.11×10^{-3}	1.26×10^{-3}	1.23×10^{-3}	1.90×10^{-3}
$a_{H_2CO_3^*}$ [M]	8.44×10^{-5}	4.45×10^{-5}	4.66×10^{-5}	4.99×10^{-5}	4.34×10^{-5}
SI (Log(Q/K_{SP}))		-0.76	-0.61	-0.66	-0.02
k_1 [cm/s]	4.93×10^{-2}	-	-	-	-
k_2 [cm/s]	2.89×10^{-5}	-	-	-	-
k_3 [cm/s]	1.16×10^{-7}	-	-	-	-
k_4 [cm^4/mmol·s]	3.05×10^{-1}	3.02×10^{-1}	3.02×10^{-1}	3.02×10^{-1}	3.02×10^{-1}
$k_1 a_{H^+}$ [mmol/cm^2·s]	2.47×10^{-8}	8.34×10^{-10}	7.71×10^{-10}	8.41×10^{-10}	4.76×10^{-10}
$k_2 a a_{H_2CO_3^*}$ [mmol/cm^2·s]	2.43×10^{-9}	1.28×10^{-9}	1.34×10^{-9}	1.44×10^{-9}	1.25×10^{-9}
$k_3 a_{H_2O}$ [mmol/cm^2·s]	1.15×10^{-7}	1.15×10^{-7}	1.15×10^{-7}	1.15×10^{-7}	1.15×10^{-7}
$k_4 a_{Ca^{2+}} a_{HCO_3^{2-}}$ [mmol/cm^2·s]	0	6.99×10^{-8}	9.08×10^{-8}	8.83×10^{-8}	2.16×10^{-7}

Table S4. Dissolution terms for calcite at various time points.

Parameter time=	0 hrs	3 hrs	6 hrs	12 hrs	36 hrs
pH	6.3	8	8.02	8.18	8.24
Alk [mequiv./kg]	0.10	1.71	2.43	2.74	2.89
a_{H^+} [M]	5.01×10^{-7}	1.02×10^{-8}	1.02×10^{-8}	7.46×10^{-9}	6.68×10^{-9}
$a_{Ca^{2+}}$ [M]	0	2.17×10^{-4}	2.95×10^{-4}	3.09×10^{-4}	3.16×10^{-4}
$a_{CO_3^{2-}}$ [M]	6.24×10^{-9}	5.05×10^{-6}	6.74×10^{-6}	9.58×10^{-6}	1.09×10^{-5}
$a_{HCO_3^-}$ [M]	7.10×10^{-5}	1.17×10^{-3}	1.56×10^{-3}	1.62×10^{-3}	1.65×10^{-3}
$a_{H_2CO_3^*}$ [M]	8.44×10^{-5}	2.81×10^{-5}	3.78×10^{-5}	2.87×10^{-5}	2.62×10^{-5}
SI (Log(Q/K_{SP}))		-0.5	-0.24	-0.06	0
k_1 [cm/s]	4.93×10^{-2}	-	-	-	-
k_2 [cm/s]	2.89×10^{-5}	-	-	-	-
k_3 [cm/s]	1.16×10^{-7}	-	-	-	-
k_4 [cm^4/mmol·s]	3.05×10^{-1}	3.01×10^{-1}	3.01×10^{-1}	3.01×10^{-1}	3.00×10^{-1}
$k_1 a_{H^+}$ [mmol/cm^2·s]	2.47×10^{-8}	5.00×10^{-10}	5.03×10^{-10}	3.68×10^{-10}	3.3×10^{-10}
$k_2 a a_{H_2CO_3^*}$ [mmol/cm^2·s]	2.43×10^{-9}	8.10×10^{-10}	1.09×10^{-9}	8.28×10^{-10}	7.56×10^{-10}
$k_3 a_{H_2O}$ [mmol/cm^2·s]	1.15×10^{-7}	1.15×10^{-7}	1.15×10^{-7}	1.15×10^{-7}	1.15×10^{-7}
$k_4 a_{Ca^{2+}} a_{HCO_3^{2-}}$ [mmol/cm^2·s]	0	7.58×10^{-8}	1.39×10^{-7}	1.51×10^{-7}	1.57×10^{-7}

Table S5. Summary of Gaussian-Arctan fitting parameters and atomic fraction (%) shown in Figure 9.

		IOS					**Gypsum**					**Pristine Calcite**				
		Energy	Width	Amp	Area	%	Energy	Width	Amp	Area	%	Energy	Width	Amp	Area	%
Arctan		2482.4	1.46	1			2482.4	1.17	1			2482.4	0.36	1.02		
Sulfite	$G_{\text{sulfite, Impr}}$											2478.3	**1.14**	1.18	2.40	26.1
Sulfonate	$G_{\text{sulfonate, Impr}}$											2480.9	**1.14**	1.41	2.86	31.1
	$G_{\text{Sulfonate, IOS}}$	2480.9	**1.42**	1.84	4.64	76.9										
Sulfate	$G_{\text{sulfate, Impr}}$						2482.4	1.78	1.44	4.53	100	2482.4	**1.14**	1.94	3.92	42.7
	$G_{\text{Sulfate, IOS}}$	2482.4	**1.42**	0.55	1.40	23.1										

		Etched 10 mg/L					**Etched 100 mg/L**				
		Energy	Width	Amp	Area	%	Energy	Width	Amp	Area	%
Arctan		2482.4	0.58	0.89			2482.4	0.57	0.92		
Sulfite	$G_{\text{sulfite, Impr}}$	2478.3	**1.08**	1.22	2.34	18.3	2478.3	**1.08**	1.22	2.35	16.6
Sulfonate	$G_{\text{sulfonate, Impr}}$	2481.0	**1.08**	1.45	2.78	21.8	2481.0	**1.08**	1.46	2.80	19.7
	$G_{\text{Sulfonate, IOS}}$	2481.0	**1.08**	1.89	3.61	28.3	2481.0	**1.08**	1.96	3.77	26.6
Sulfate	$G_{\text{sulfate, Impr}}$	2482.5	**1.08**	2.00	3.82	30.0	2482.5	**1.08**	2.00	3.84	27.1
	$G_{\text{Sulfate, IOS}}$	2482.5	**1.08**	0.10	0.19	1.5	2482.5	**1.08**	0.74	1.42	10.0

		Not Etched 10 mg/L					**Not Etched 100 mg/L**				
		Energy	Width	Amp	Area	%	Energy	Width	Amp	Area	%
Arctan		2482.4	0.50	0.74			2482.4	0.38	0.91		
Sulfite	$G_{\text{sulfite, Impr}}$	2478.3	**1.11**	0.96	1.88	18.4	2478.3	**1.07**	1.48	2.80	20.1
Sulfonate	$G_{\text{sulfonate, Impr}}$	2480.9	**1.11**	1.14	2.24	21.9	2481.0	**1.07**	1.76	3.33	24.0
	$G_{\text{Sulfonate, IOS}}$	2480.9	**1.11**	1.30	2.56	25.0	2481.0	**1.07**	1.61	3.04	21.8
Sulfate	$G_{\text{sulfate, Impr}}$	2482.4	**1.11**	1.57	3.08	30.1	2482.5	**1.07**	2.42	4.57	32.9
	$G_{\text{Sulfate, IOS}}$	2482.4	**1.11**	0.24	0.47	4.6	2482.5	**1.07**	0.09	0.16	1.2

References

[1] S. Hayakawa, Y. Hajima, S. Qiao, H. Namatame, T. Hirokawa, Characterization of calcium carbonate polymorphs with Ca K edge X-ray absorption fine structure spectroscopy, Anal. Sci. 24 (2008) 835-837.

[2] Y. Politi, Y. Levi-Kalisman, S. Raz, F. Wilt, L. Addadi, S. Weiner, I. Sagi, Structural characterization of the transient amorphous calcium carbonate precursor phase in sea urchin embryos, Adv. Funct. Mater. 16 (2006) 1289-1298.

Section C: Presentation of major findings published in *ACS Sustainable Chemistry and Engineering*

Environmental Impacts of Replacing Slickwater with Low/No-Water Fracturing Fluids for Shale Gas Recovery

ABSTRACT:

The environmental impacts of a typical hydraulic fracturing operation for shale gas recovery were evaluated using life cycle assessment, with energy demands for well drilling and fracturing determined from GHGfrack model. Dominant environmental impacts stem from well construction, which are >63% in all categories (e.g., global warming, eutrophication), and mainly due to diesel fuel combustion and steel production. The relative impacts related to water use (i.e., fracturing fluid components, water/wastewater transportation, wastewater disposal) are relatively small, ranging from 5-22% of total impacts in all categories; freshwater consumption for fracturing is a also small fraction of available water resources for the shale play considered. The impacts of replacing slickwater with CO_2 or CH_4-foam fracturing fluid (≤ 10 vol% water) were evaluated; total impacts change <8%, and relative impacts related to water use decrease to 3-15% of total impacts. Hence, switching to a foam-based fracturing fluid does not appear to have a large effect on total impacts or relative water-related impacts. Changes in lateral well length, produced to fresh-water ratios, fracturing fluid composition, and LCA control volume do not change these findings. More benefits could potentially be realized by considering water versus foam-related impacts of ecological health and energy production.

INTRODUCTION

U.S. natural gas production from shale gas and tight oil plays increased from approximately 9.3 to 18.8 trillion cubic feet from 2009 to 2016, and is predicted to account for nearly two-thirds of domestic natural gas production by 2040[1]. This rapid increase can be attributed to the combined methods of horizontal drilling with multistage hydraulic fracturing (HF). The most commonly used hydraulic fracturing fluids are water-based, containing approximately 90 wt% water, 9 wt% proppants, and the remainder a suite of chemical additives to modify the properties of the fluid in order to enhance fracturing and improve hydrocarbon recovery. A data survey of around 40,000 wells (oil and gas) in the United States found that hydraulic fracturing consumes an average of 2.5 million gallons of water per well[2]. Approximately 25,000 to 30,000 wells were fractured each year between 2011 and 2014[3], amounting to approximately 97 billion gallons of water consumed[2]. Despite the obvious benefits of increased energy production, hydraulic fracturing raises several concerns, including competition for water resources, negative ecological impacts, groundwater contamination, and induced seismicity[4]. All of these concerns are affected by the high water use associated with hydraulic fracturing, and using low-water or no-water based fracturing fluids may be an attractive alternative.

US freshwater consumption for hydraulic fracturing is less than 1% of total freshwater use and 3% of freshwater consumption in each state[3], but it can be high locally and compete with other needs. For example, water use for hydraulic fracturing in 2011 and 2012 was compared to total water use in 2010 for 401 US counties; in 26, hydraulic fracturing accounts for >10% of total water use, and in nine, >30% of total water use[3]. High local water withdrawals from surface water or groundwater resources can have negative ecological impacts such as erosion and sedimentation[5], habitat fragmentation[6], and reduction of available surface and hyporheic water volumes. In Michigan, some streams with sensitive fisheries are at risk from neighboring high-volume hydraulic fracturing operations during drought and low-flow periods[7].

The large volumes of hydraulic fracturing and wastewater fluids handled at each well pad are associated with water contamination risks. Of particular concern is groundwater contamination by chemical amendments used in hydraulic fracturing fluids, as well as natural gas and oil. Pathways for water contamination related to shale gas development include surface spills, well casing leaks, migration through fractured rock, and wastewater disposal[8,9]. The EPA identified 457 spills that occurred on or near the well pad in the United States between January 2006 and April of 2012[3]. 151 of these occurred during chemical mixing of hydraulic fracturing fluid, and 225 occurred during handling of produced water; spill volumes for releases during mixing of hydraulic fracturing fluid ranged from 5 to 19,320 gal, with a median value of 420 gal[3].

The impact of spills and leaks on water resources has been documented in a number of studies[10]. The Department of Environmental Protection (DEP) in Pennsylvania issued 161 "positive determination letters" (PDLs) between 2008 and 2012 regarding water supply contamination, or diminishment of quantity due to oil/gas activities. 56% of these PDLs are due to natural gas migration, with the remainder due to release of brine salts or other engineering components (e.g. hydraulic fracturing, flowback, and produced water)[11]. A study in a Pavillion, Wyoming field reported detection of organic chemicals used in hydraulic fracturing fluids, and also identified the migration (including upward) of hydraulic fracturing fluid components to groundwater[12].

The large volumes of water and proppants used at each well pad are typically transported by trucks. Each truck can only hold a relatively small volume of water or proppant relative to the total volumes required. Large volumes of injected water also result in large volumes of flow back from wells, which is essentially wastewater. Wastewater from hydraulic fracturing operations is often disposed of in Class

II injection wells, and this too must be transported from a well pad to a disposal well. Water and wastewater transportation result in high transportation costs, high fuel consumption, excessive road wear, and increased traffic fatalities. The injection of wastewater has also been shown to induce seismic events with associated structural damage to buildings in some areas[13].

The objectives of this study are to quantify the relative energy and environmental life cycle impacts of water use for typical hydraulic fracturing operations in shale gas recovery, and to test the hypothesis that using low or no-water based fracturing fluids (e.g., foams) would significantly decrease these impacts. Prior life cycle assessment studies of hydraulic fracturing have evaluated various environmental impacts (e.g., greenhouse gas emissions, energy consumption, freshwater consumption, eutrophication) for unconventional oil and gas plays[14], and in some cases compared results to those for unconventional shale oil with flare gas recovery (Laurenzi et al., 2016), or for conventional energy sources[15–17]. In one study, the greenhouse gas and water impacts of replacing freshwater in fracturing fluid with CO_2 was evaluated for the Marcellus shale[18], but well construction impacts, as well as wastewater disposal in Class II injection wells, were not considered. Replacement of water in fracturing fluids with CO_2 and other nonaqueous fluids is being explored by a number of researchers and companies, both to reduce water use, and in some cases to enhance hydrocarbon recovery[19–22].

APPROACH

System Boundary. Processes required for hydraulic fracturing operations in shale gas plays are illustrated in Figure 1, and the life cycle system boundary considers only those within the red dash-dot-dash line. Gas production, processing, and transmission, as well as well plugging and closure, are outside the system boundary. The potential impacts of these processes on the final life cycle results are considered in the Discussion section.

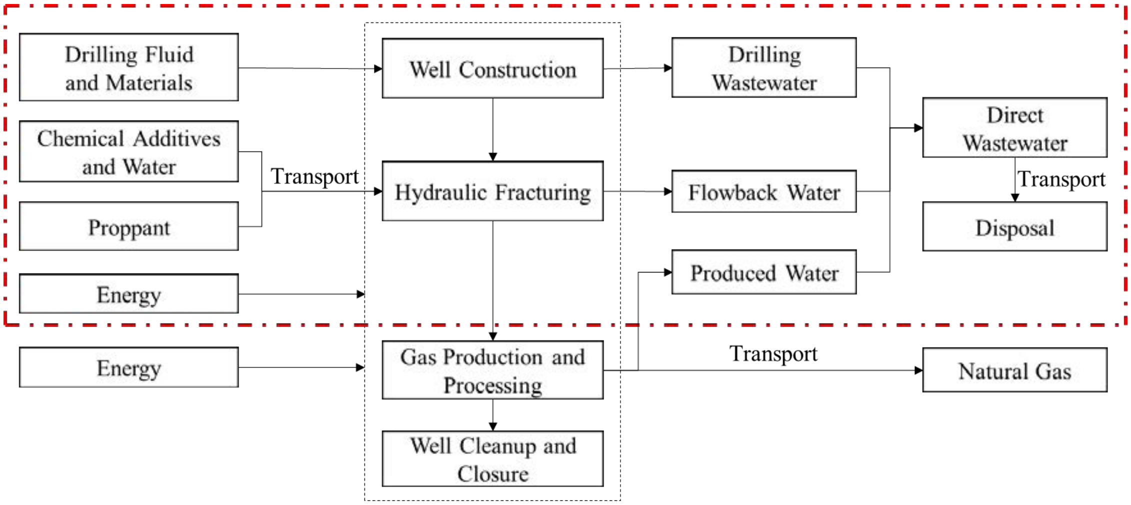

Figure 1: LCA system boundary, as indicated by the red dot-dashed-line

(Grey dotted line indicates the shale gas production main processes)

Functional Unit. The functional unit of the life cycle assessment is hydraulic fracturing operations for a single well in the Barnett shale gas-producing region. All energy and environmental impacts are presented on a per well basis.

Life Cycle Inventories and Assessment Tools. The Life Cycle Assessment was performed using SimaPro 8 software (by PRé Consultant), following the framework established by the International Organization of Standardization (ISO). Representative chemicals and processes to model the actual fracturing processes were selected from the Ecoinvent 3 Database of the LCA software. Tool for the Reduction and Assessment of Chemical and other environmental Impacts (TRACI) 2.1(Version 1.01) was used as the assessment method, with the following environmental impact categories: ozone depletion (kg CFC-11-equivalent), global warming (kg CO_2-eq.), smog formation (g NO_x-eq.), acidification (kg SO_2-eq.), eutrophication (kg N-eq.), carcinogenics (Comparative Toxic Unit for human, CTUh), noncarcinogenics (CTUh), respiratory effects (kg PM 2.5-eq), ecotoxicity (CTUe) and fossil fuel depletion (MJ surplus).

Water-Based Fracturing Fluid. The most common fracturing fluids are composed of mainly water (about 90 wt%) and proppant (about 9 wt%), plus minor fractions of various chemicals. The proppant is usually sand, and becomes lodged in fractures to keep them open. The chemical additives serve various functions, such as modifying the fluid viscosity to enhance proppant carrying capacity, protecting pipes from corrosion, and inhibiting microbial growth[23].

A representative hydraulic fracturing fluid for the Barnett shale play was determined from individual well records from the FracFocus Chemical Disclosure Registry[24]. First, the composition of fluid used in many individual wells was obtained from the FracFocus database, and the average mass fractions of dominant components were computed. Second, the masses of water and other representative components were computed using their weight ratios. Finally, substitutions of components not found in the Ecoinvent database were made. These steps are briefly described below, and more fully in the Supporting Information.

Raw Data Retrieval and Reduction. Records for 324 wells installed in 2012 or 2013 in the Barnett shale were obtained from the FracFocus Registry for five counties, all located in gas producing areas (see Table S1, Figure S1). This was reduced to 35 by eliminating duplicate/similar records.

Hydraulic Fracturing Fluid Composition. The hydraulic fracturing fluid components in the 35 unique well records were classified into 21 different categories (e.g., biocide, scale inhibitor, corrosion inhibitor, friction reducer). The components occurring with the highest frequency in a category, or in more than one fifth of the records for that category, were selected as representative. An exception is gelling agent; this category appeared in only 10 of 35 records (29%), but were not considered because slickwater was the dominant fluid[25]. The potential change in LCA results when using a gelling agent based fluid is addressed in the Discussion.

Among all components, eight were not categorized and are accounted for in a separate “other” category; i.e., ethanol, methanol, isopropanol, ethylene glycol, diethylene glycol, hydrotreated light distillate, sodium chloride and ammonium chloride. These chemicals generally act as solvents, carriers, or stabilizers for other components.

The mass fractions of the selected components within a category were scaled proportionally such that their sum added up to the new mass fractions for each category. Finally, the masses of each individual component in the representative fluid were then re-calculated by multiplying the final mass fractions by the total slickwater mass.

Hydraulic Fracturing Fluid Mass or Volume. The volume of water used per well depends on the lateral length of a horizontal well. This length has increased over time, and with it the volume of water. For example, in the Barnett shale, Nicot[26] reports that water use increased from ~3 million gallons per well in 2005 to ~5 million gallons per well in 2011. Based on the 35 selected records, an average water use per well of 4,400,000 gallons was determined. This value is close to that from Ceres[2]. The amounts of other components were computed based on mass fraction ratios.

The freshwater used in hydraulic fracturing comes from a mix of groundwater and surface water, and published data indicate the fraction of groundwater used has varied from 0.2 to more than 0.5 in the Barnett shale play[26 27]. The primary effect of this fraction on life cycle assessment results is from greater energy requirements for pumping groundwater. We calculated this energy in gallons of diesel fuel required for groundwater pumping per hydraulic fracturing well, and found it to be negligible compared to energy requirements for well completion, hydraulic fracturing, or wastewater disposal. Details are in the Supporting Information. Therefore, no distinction was made between groundwater and surface water in this study. Other potential impacts from this fraction are water scarcity and ecosystem degradation. The former is considered in the results; the latter was not considered due to lack of available information.

Substitutions for Chemicals in Database. The Ecoinvent database does not contain all selected components in the slickwater, so substitutions were made using a two-tiered approach; progression to the second tier only occurred if the first tier approach was unsuccessful. In the first tier, alternative chemicals with similar functionality and structure were used as substitutes if available in the Ecoinvent database. In the second tier, feedstock chemicals used to synthesize the chemical of interest or a similar chemical were identified, and these were used as available in the Ecoinvent database. The energy and ancillary materials required to synthesize a chemical from its feedstock chemicals were not considered, and implications of this are discussed in the Discussion.

Foam-Based Fracturing Fluid. Two foam-based fracturing fluids were considered for comparison to the base case assessment using slickwater, one containing 90% v CO_2 and 10% v H_2O (i.e., 90% v/v CO_2-foam), and the other containing 90% v/v natural gas (CH_4)-foam. These compositions have approximately the minimum water content possible for foams[28], and represent potentially favorable scenarios with respect to reducing impacts associated with freshwater use in hydraulic fracturing.

Transportation. During all processes, transportation of only freshwater for hydraulic fracturing fluid, proppant, and returned wastewater (including flowback and produced water) was considered. The impacts of transportation of materials for well construction were ignored, because their masses are generally less than 2% of the freshwater used for hydraulic fracturing fluid[29]. Also, the transportation of chemicals in the hydraulic fracturing fluid from their supply sources to the fracturing sites were not considered, because their masses are very small (<0.1% of freshwater). All the returned wastewater from the hydraulic fracturing site was disposed in a Class II injection well[26].

An average distance of 5 miles was assumed for transportation between a fresh water source and the hydraulic fracturing site, and 10 miles for transportation between the hydraulic fracturing site and a Class II injection well, both based on a report from Argonne National Laboratory[29]. For comparison, a recent analysis of the average transportation distance between a freshwater source and the hydraulic fracturing site in the Marcelus Shale is 10.5 miles, based on a detailed Graphical Information System analysis of optimal transportation routes[30]. No distinction was made between transportation distances for surface and groundwater sources due to lack of available data. Water reuse was not considered, because it is minimally applied (~5.5%) in the Barnet shale play[26].

The amount of water transported from a source to a well pad site equals that used to hydraulically fracture a single well. Freshwater is generally transported in tractor trailer trucks, and fuel use and environmental impacts were determined by selecting 32 metric ton trucks for transport (EURO 5) in the SimaPro software. The empty truck weight is 34,000 lbs[31], and gross weight of a loaded truck is ~80,000 lbs, identical to the maximum truck gross weight limit specified in U.S. Federal Regulations (23 US Code § 127). In some cases, temporary pipelines are installed for fluid transportation in order to eliminate road-based transportation[32], but no data was available to consider this option.

Round trips between well pads and either a freshwater source or a Class II disposal well were divided into loaded trips and unloaded trips, where the ratio of wastewater (i.e., flowback + produced water) to freshwater used for hydraulic fracturing was assumed to be 1.9, based on the mean value of ~1,400 Class II well records for the Barnett shale spanning 2001 to 2012[26]. This value is relatively large compared to values reported for other shale plays (e.g., 0.2 for Marcellus shale and 0.25 for Fayetteville shale[29]). This may be due to the extension of fractures into, and/or fluid migration upward from, the underlying water-bearing Ellenberger and Viola/Simpson formations. We note that in another literature source a value of 2.75 was identified[29], based on personal communication with an operator. Given the likely importance of this parameter on life cycle assessment results, we evaluate a range of possible values in the Discussion section.

The number of truck trips needed was calculated using the mass of water or wastewater transported and truck capacity. Thus, the total payload-distance for a round trip is calculated as follows.

$$\textit{Total payload-distance} = N * \textit{Distance} * (\textit{Empty Truck Weight} + \textit{Loaded Truck Weight}) \quad (1)$$

N is the number of round trips needed to transport the materials. *Distance* is the average between the water source and hydraulic fracturing site, or between the site and the disposal well, both from Clark et al.[29]. *Total payload-distance* has unit of tons-kilometers (TKM), and determines fuel use, road wear, and related environmental impacts in the SimaPro software.

Sand was the proppant in all well records, and its transportation distances were calculated by assuming the average transportation distance is from the centroid of each county to the nearest fracturing sand supplier, as detailed in Supporting Information. The total payload-distance in TKM for all round trips was calculated using equation 1.

Well Construction. Well construction requires drilling, mud circulation, casing, and perforation, and is considered separate from the hydraulic fracturing process. The materials and energy used in well construction are from the Argonne report[29], and energy used is expressed as diesel fuel consumed. Some materials used for well construction were not available in the Ecoinvent database, and were substituted using the aforementioned two-tiered method. Water used for drilling and mud circulation is only 6% of water used for hydraulic fracturing, and water used for steel casing and cementing is less than 1%[33,34]; therefore, these water uses were ignored.

The energy for well construction obtained from the Argonne report[29] was independently compared to that calculated with the GHGfrack model[35]. This model considers energy consumption for rotating the drilling string and maintaining drilling fluid circulation. Model inputs include well characteristics, drilling speed, and mud properties. Well characteristics were modeled after those in the Barnett shale. Briefly, the horizontal well consisted of three sections of length 6500, 1000, and 3800 feet, with 0, 45, and 90 degrees inclination angles to vertical, respectively. Other parameters remained as default (i.e., Table S8).

Energy Input for Hydraulic Fracturing. The energy used to hydraulically fracture shale was determined with GHGfrack[35]. Hydraulic fracturing fluid properties and well characteristics were required inputs, and the output was energy in terms of diesel fuel consumed (i.e., Table S9). We note that the energy required to compress gas used for foam-based fracturing fluids was not considered in the life cycle assessment. We calculated this energy independently (see Supporting Information), and it is negligible compared to the energy required for well completion, hydraulic fracturing, or wastewater injection.

Deep Well Disposal. The energy used for disposal of flow back and produced water in a Class II injection well was obtained from the Argonne report[29]. The energy output was in the form of electricity consumption, and is assumed proportional to the volume of wastewater injected.

RESULTS

Hydraulic Fracturing Fluid Composition. The representative composition of slickwater determined from the 35 unique well records is presented in Figure 2, with details in Table S2. The values are in mass fractions of total slickwater. Water and proppant (sand) comprise more than 99% of the slickwater mass, while the remainder is 22 chemical additives that fall into 15 categories. Most chemicals listed are common components in a representative hydraulic fracturing fluid reported by EPA and others[36,37]. Also, the slickwater composition is similar to that in an EPA report[3], i.e., the mass fractions of the water and proppant are similar. For other additives, the representative categories vary, but the mass fraction differences of the same category are within one order of magnitude. Ten out of the 22 chemicals did not appear in the EcoInvent database and required substitutions. Three of these were substituted using similar chemicals (tier 1), and seven were substituted using chemical feedstocks (tier 2). Details are in Table S3.

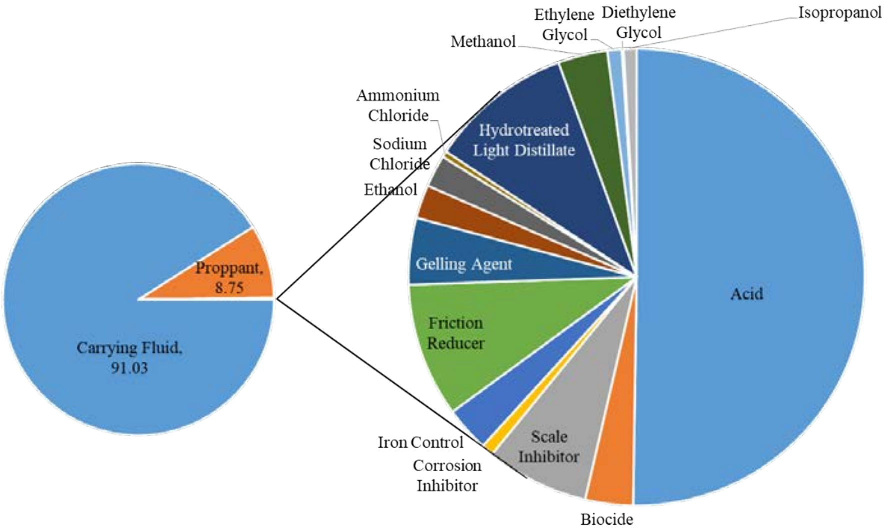

Figure 2: Mass fractions (wt%) of all categories in slickwater.

Transportation. Average transport distances between fresh water sources and hydraulic fracturing well pads, between well pads and Class II injection wells, and between sand vendor locations and county centroids are in Table S5, along with total fluid or sand mass transported, number of tractor-trailer truck round trips, and total payload-distance calculated. The locations of county centroids and sand vendors are shown in Figure S2, and their geographical coordinates are listed in Table S4. The key parameter in Table S5 is total payload-distance, expressed in units of ton-kilometers (TKM). The TKM for fresh water transportation (when using slickwater) is more than three times larger than that of sand transportation, even though the average transportation distance for freshwater is ~1/3 of that for sand. This is because about ten times more trips are required for the freshwater. The largest TKM is for wastewater, primarily due to the relatively large volume that must be transported from the well pad to a Class II well. It totals 1,260,000 TKM, approximately four times that for freshwater transportation.

Well Construction Materials and Energy. Well construction materials and their masses are listed in Table S6, and are from the Argonne report[29]. Substitutions for materials not found in Ecoinvent were identified and justified, and were determined using the same two-tiered approach described previously. The GHGfrack model was used to calculate the energy required for drilling and mud circulation, to compare with the diesel fuel requirement from the Argonne report[29]. The calculated diesel volumes required for drilling and mud circulation are 5,230 and 50,600 gallons (for a 3,800 feet lateral length well, Table S8), respectively. This totals ~55,800 gallons of diesel, which is only about 10% lower than the diesel fuel from Argonne (~62,000)[29]. Details of GHGfrack model inputs and outputs for drilling and mud circulation are in Table S8.

Energy for Hydraulic Fracturing and Wastewater Disposal. The total energy required to hydraulically fracture a characteristic well in the Barnett shale is 307,000 kWh, as computed by GHGfrack (3,800 ft lateral length well, Table S9). In comparison, the total energy required to inject wastewater into a Class II disposal well is 95,400 kWh (Table S10). This is ~31% of the energy required for hydraulic fracturing, even though there is 1.9 times as much wastewater as the fracturing fluid. This is because more energy is required for hydraulic fracturing to exceed the overburden pressure and induce fracturing.

Environmental Impacts of Hydraulic Fracturing Fluid Components. The life cycle assessment results for the hydraulic fracturing fluid components are summarized in Figure 3. Water and sand are natural resources; their production is not considered by SimaPro, so their impacts were not calculated. Components grouped into "Other" are ethanol, methanol, isopropanol, ethylene glycol, diethylene glycol, hydrotreated light distillate, sodium chloride and ammonium chloride. Results in each category are normalized to one, so only relative comparisons between categories are possible. Absolute comparisons have little value because the units of each category are different. For example, ozone depletion impact has units of kg CFC-11-equivalent, while global warming impact is expressed as kg CO_2-equivalent.

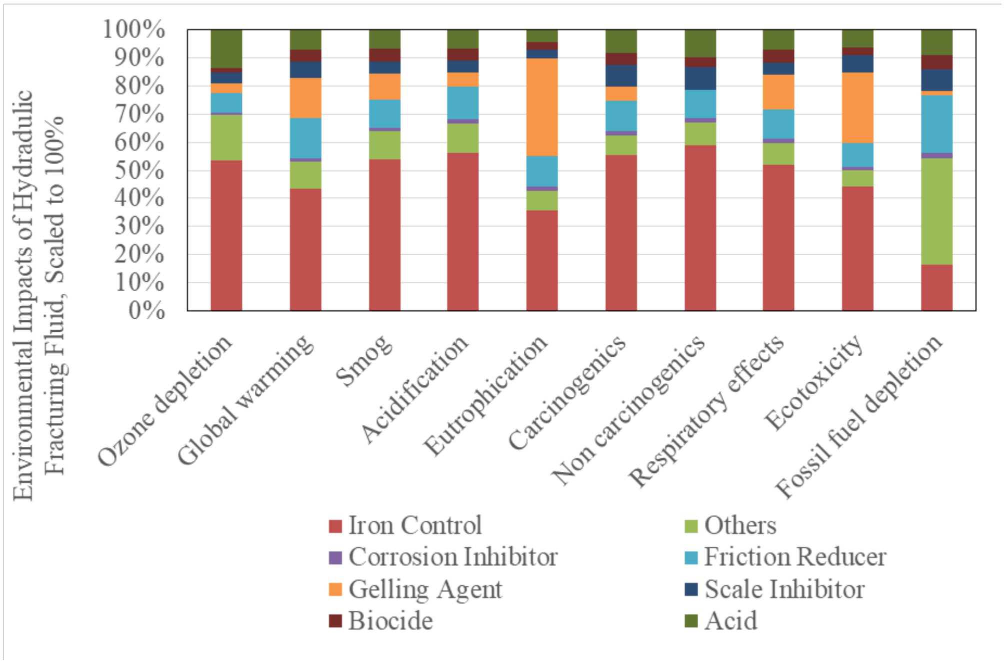

Figure 3: Environmental impacts of slickwater components.

Iron control agents have the largest life cycle impacts (more than 50%), except in the category of fossil fuel depletion (16%). The iron control agents are citric acid and acetic acid, and citric acid dominates the environmental impacts even though it makes up only 0.0053% of the mass of the hydraulic fracturing fluid. Its large impact stems from its multistep synthesis, which involves heating and then fermentation of carbohydrates into citric acid, followed by purification with ion exchange and carbon treatment, and finally evaporation, crystallization, drying, sieving, and packaging.

The “Other” fluid components contribute <15% of the total in any category except fossil fuel depletion, and in that category the impact is ~38%. The largest impacts for fossil fuel depletion in “Other” come from hydrotreated light distillates, comprising 24.2% of the total impact. This is because the production of these distillates requires direct consumption of fossil fuel; the amount is still large, even though the distillates make up only 0.0226% of the mass of hydraulic fracturing fluid.

Environmental Impacts of Well Construction. The life cycle impacts of individual components that are used in well construction are shown in Figure 4. The major contributions are from diesel fuel consumption (~62,000 gallons per well) and reinforced steel (163 metric tons per well). Diesel fuel dominates all environmental impacts except for carcinogenics, because of emissions of greenhouse gases, acidic gases, fine particulates, and other polluting gases. For comparison, the diesel fuel contribution to global warming is approximately 0.79x10^9 gCO_2e per well, similar to the value of 0.69x10^9 gCO_2e determined for a well with similar depth and length by Jiang et al.[16].

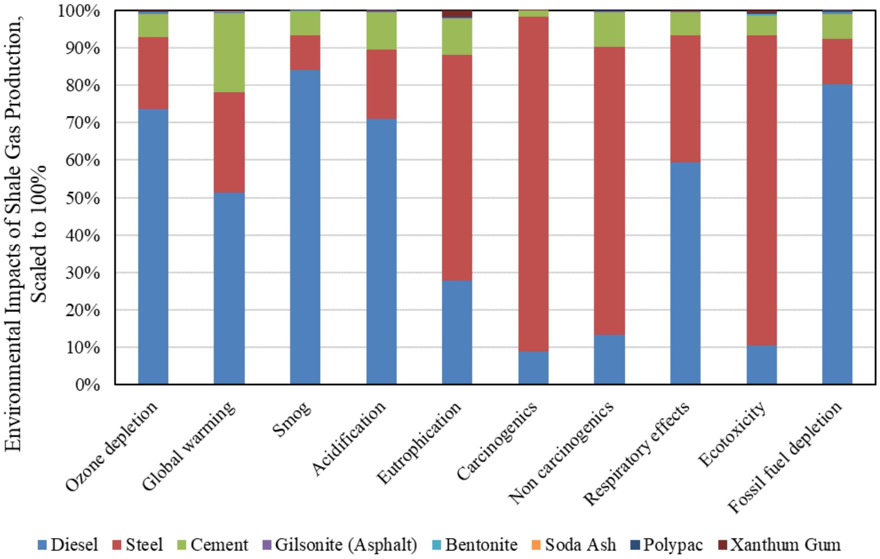

Figure 4: Environmental impacts of well construction components

Reinforced steel has larger environmental impacts to eutrophication, carcinogenic, non-carcinogenic and ecotoxicity effects, because of emissions of metal-containing fine particulates, PAHs, NO_x, etc. during production[38]. The material with the next largest environmental impact is cement, and 267 metric tons are used per well to stabilize the steel casing and form a protective seal between the well casing and formation. Again for comparison, the total well construction contribution to global warming is approximately 1.54x10^9 gCO_2e per well, smaller but similar in magnitude to the value of 2.5x10^9

gCO$_2$e determined by Laurenzi et al. (Laurenzi et al., 2016), who considered process-based material and energy needs for a similar length well. We note that environmental impacts associated with gas flaring during well completion were not considered in this study, and these are highly variable and in some cases substantial[16]. This likely accounts for much of the difference between total well construction contributions to global warming from this study and that from Laurenzi et al. (Laurenzi et al., 2016).

Total Impact and Component Comparison. The life cycle impacts for the entire hydraulic fracturing process with slickwater considered in the system boundary (i.e., base case) are shown in Figure 5, with details in Table S12. This includes well construction, transportation, fracturing fluid production, energy for fracturing, and energy for wastewater disposal. The results in each category of Figure 5 are normalized to 1. The well construction process has the largest environmental impacts, contributing more than 63% (and more than 73% in 8 out of 10 categories) of total impacts in any category. Well construction impacts also dominate greenhouse gas emissions and energy consumption in another study[15]. Next are contributions from the energy used for hydraulic fracturing, and then transportation of freshwater, sand and wastewater.

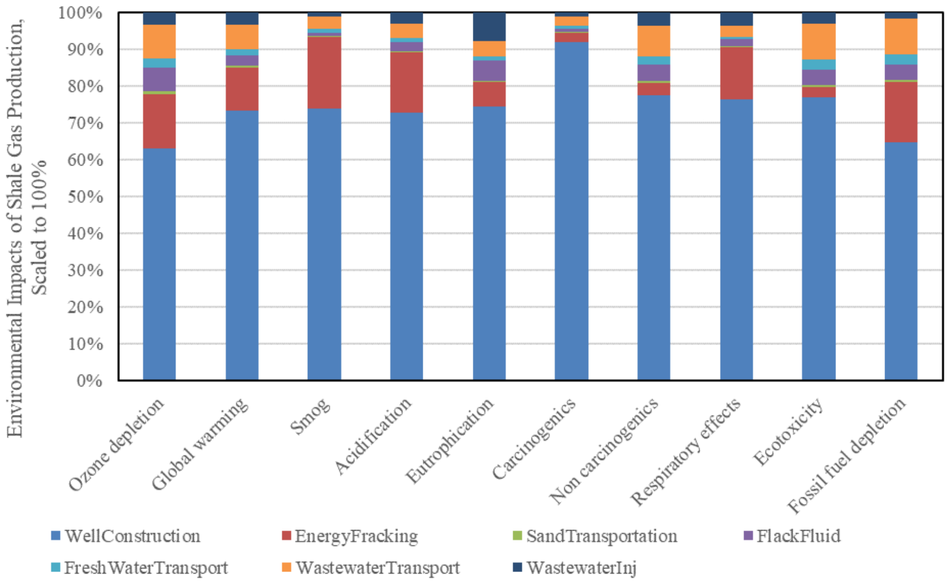

Figure 5: Environmental Impacts of Shale Gas Production Components

The energy used for hydraulic fracturing contributes <20% in any category, with most contributions in smog, fossil fuel depletion, respiratory effects, and ozone depletion due to the large amount of diesel fuel combusted. The contribution of this energy to global warming is approximately $0.25\text{x}10^9$ g CO2e per well, which is only ~25% of that from Jiang et al.[16]. Reasons for this discrepancy are not clear (wells have similar depth and length). However, GHGfrack was used to compute energy requirements for hydraulic fracturing in this study, and there is good agreement between this model and the Argonne report[29] for drilling energy during well construction.

The hydraulic fracturing fluid components contribute <7% in any category due to the very small masses of chemicals used relative to other materials. Freshwater and wastewater transportation contribute <3% and <10% in any category respectively, while sand transportation contributes <1%. Deep well injection of the wastewater contributes <8% in any category. The total impact to global warming per well is approximately $2.11\text{x}10^6$ kg CO_2e, and is similar to the value of $2.2\text{x}10^6$ kg CO_2e computed for the Marcelus shale by Dale et al. despite some differences in processes considered[15].

Summarizing, the life cycle impacts are mainly from materials and energy input for well construction. The processes directly affected by high water volume are slickwater chemical components, water and wastewater transportation, and energy for wastewater injection, whose relative environmental impacts are <22% in any category, and <15% in five out of 10 categories.

Sensitivity Analysis. A sensitivity analysis was performed by identifying reasonable lower and upper values of life cycle input parameters from the literature and our own calculations, and performing life cycle assessments with each parameter varied separately from the base case parameters that resulted in Figure 5. Base case parameters, along with lower and upper values, are listed in Table S19, along with descriptions of how lower and upper values were selected. Results from each model run are listed in

Tables S20 through S37, and minimum and maximum values of impacts in each category (e.g., global warming) from all model runs for are shown in Figure S3, both for the entire hydraulic fracturing process considered in the system boundary and for only water related processes. The range of values for any impact category of the former (i.e., entire hydraulic fracturing process) do not overlap the range of values for any impact category of the latter (only water related processes). Also, the minimum and maximum values for all impact categories of the latter range from 0.03-0.34 (compared to 0.05- 0.22 for the base case), and for any one impact category are within 65% of the base case value.

Freshwater Consumption Impact. Life cycle impacts of freshwater withdrawals from surface and groundwater are not considered in SimaPro. Freshwater is clearly a valuable resource, and in water-stressed areas environmental impacts related to, for example, groundwater drawdown and pumping energy, decreased stream or estuarine habitats for aquatic species, and increased turbidity must be more broadly considered outside of the life cycle software.

The five counties considered in this work are located in the Brazos River Basin (BRB) and Trinity River Basin (TRB). Ten lakes and reservoirs are located in the five counties, and the water storage totaled 648,384 acre-ft in 2013. The freshwater needs for hydraulic fracturing in the five counties is only 0.6% of the water in the lakes/reservoirs (see Table S11 for details), suggesting that water use for shale gas production has a relatively low impact. However, more local-scale impacts are still possible and require further investigation.

DISCUSSION

The largest environmental impacts of the hydraulic fracturing life cycle process come from well construction, mainly from the large amount of energy, steel and cement consumption. They are greater than 63% in all life cycle impact categories. Well construction requires very little water compared to hydraulic fracturing, and switching to a low or no-water based hydraulic fracturing fluid would not affect the environmental impacts from this process.

The materials and processes that would be most affected by using a low or no-water based fracturing fluid are hydraulic fracturing fluid chemical components, fresh water transportation, wastewater transportation, and wastewater disposal; the relative environmental impacts of these combined processes in any of the ten categories are <22%. Information regarding the types and amounts of chemical components used in low or no-water based hydraulic fracturing fluid is lacking. However, the small LCA impact of these chemicals (i.e., <7% in any category) indicates consideration of this decrease when switching to a low or no-water based fracturing fluid would have only marginal effects. A best case scenario is that chemical use for fracturing fluid would decrease by 90% for a 90% v/v CO_2-foam. This would decrease LCA impacts of chemical amendments to <1% in any category, and the LCA impacts of water-based processes to <21% in any category.

Freshwater transportation impacts would scale directly with freshwater volume used, but the reduction in freshwater transportation impacts could be at least partially offset by transportation impacts of an alternative fluid. For example, if a CO_2-foam were used, then CO_2 transportation by truck and/or pipeline would need to be considered[39]. Assuming a 90% v/v CO_2-foam, water use would decrease by 90%, resulting in only 10% of the fresh water transportation required for a water-based fluid. Assuming equal volumes (~4.4 million gallons) of water and CO_2-foam (supercritical CO_2+water) are needed under fracturing conditions, approximately 0.68 kg of CO_2 would be needed for every kg of water (see Table S7). Because CO_2 sources or pipelines are less densely located than freshwater sources, transportation impacts from overland trucking could easily match or exceed those from the same volume of freshwater. Alternatively, a natural gas-foam could be used (Plummer & Johnson, 1976; Zhang et al., 2000). While use of this gas (CH_4) as a foam has not generated much interest lately, it represents the most favorable selection to reduce water related impacts because it is produced onsite, or very nearby, and transportation impacts can be practically eliminated; as a result, the payload-distance for fluid transportation would be only 10% of that for slickwater. An unintended consequence of using either CO_2 or CH_4 would be greater energy required for gas compression and hydraulic fracturing. Assuming the overall energy conversion efficiency is 75%, approximately 430 gallons of diesel fuel would be required to compress these gases; this is insignificant compared to diesel fuel requirements for well completion, hydraulic fracturing, or wastewater disposal. Another consequence would be extra energy required to inject a lower density CO_2 or CH_4-foam, due to the decrease of in-well hydrostatic head compared to slickwater. For example, it was estimated using GHGfrack that approximately 46% more diesel fuel (i.e., ~9000 more gallons) would be required for hydraulic fracturing in the Barnett shale using a CO_2-foam compared to slickwater (Table S9).

Wastewater transportation and disposal impacts would decrease with the use of low or no-water based fracturing fluids. It was assumed that the volume of wastewater is 1.9 times the volume of slickwater used in this study, based on data from Nicot et al[26] . The best case scenario is that all injected water is recovered as flowback. Therefore, if a 90% v/v foam is used instead of slickwater, the volume of wastewater produced would be equal to the volume of slickwater (0.1 for injected/flow back water and 0.9 for produced water). This results in a payload-distance for wastewater transportation that is 53% of that for slickwater. Combining the most favorable freshwater and wastewater transportation savings, the payload-distance would decrease by ~900,000 TKM (56%). Also, the energy required for wastewater injection would decrease by ~45,000 kWh (33%, Table S10).

Considering the materials and processes that would be markedly affected by switching to a 90% v/v CO_2-foam (i.e., fresh water transportation, wastewater transportation, wastewater disposal, energy for hydraulic fracturing), and ignoring CO_2 transportation requirements, the environmental impacts of the processes directly affected by the change in water use (i.e., fracking fluid chemicals, fresh water transportation, wastewater transportation, wastewater disposal) in any of the ten categories are <14%, down from <22% with slickwater (see Table S16). Also, the total environmental impacts in seven of ten categories decrease by up to 7% with the switch to CO_2-foam from slickwater. In three categories (i.e., smog, acidification, respiratory effects) there is an increase in total environmental impacts due to the additional diesel fuel combusted during hydraulic fracturing, but the increases are small (2-6%). Correspondingly, the relative environmental impacts of energy required for fracking increase from 2-20% with slickwater to 4-27% with CO_2-foam (with values >20% in five categories). Instead of CO_2-foam, a CH_4-foam could be used, and it is more reasonable to ignore CH_4 transportation requirements because natural gas is produced in the formation at adjacent wells. The environmental impacts for a CH_4-foam in all ten categories are slightly less but within 6% of those for the CO_2-foam (see Table S17). They are also less but within 8% of those for slickwater. Hence, the CH_4-foam appears to be a slightly better choice than CO_2-foam or slickwater, provided energy recovery is not negatively impacted. However, the changes in any environmental impact category that result from switching to a CO_2- or CH_4-based foam are all within the minimum and maximum range of values determined from the sensitivity analysis. We note that the marginal changes in global warming impacts that result when switching from slickwater to these foams are not consistent with the large change in greenhouse gas impacts estimated by Wilkins et al.[18]. This is primarily because well construction impacts are considered in this work, and they are dominant.

In this study, it was assumed that 4.4 million gallons of freshwater are required per well when using slickwater, and the lateral well length is 3,800 feet. Water use per well and lateral well lengths are increasing[40]. Therefore, an additional LCA analysis was performed for a well with a lateral length of 6,000 ft, corresponding to 7.03 million gallons of freshwater required for slickwater fracturing (1,200 gallons freshwater increase per feet[26]). This increase in well length corresponds to 172 metric tons of steel, 272 metric tons of cement, and 100,000 gallons of diesel fuel for well construction, and 38,600 gallons of diesel fuel for hydraulic fracturing. For the greater lateral well length, the total environmental impacts increase by 15% to 60% compared to the base case (i.e., 3800 ft lateral well length). The relative environmental impacts associated with well construction (i.e., compared to total impacts) only marginally decrease, and are 59-88% in all categories. The impacts associated with water increase by 60% compared to the base case, but the relative contribution compared to total impacts only marginally increase and are <26% in all categories (compared to <22% for the base case). Details of LCA results are in Table S13.

Also in this study, it was assumed that the volume ratio of wastewater to freshwater is 1.9. This represents the mean value, and also the 70th percentile value, from Nicot et al.[26]. The 30th percentile value from this same literature source is 0.7, and a value of 2.75 was cited in the Argonne report[29]. Therefore, life cycle assessment was performed with the base case parameters, except with 1.9 replaced with either 0.7 or 2.75 to explore the sensitivity of results to this ratio. Results are in Table S14 and S15. Total life cycle impacts decrease or increase with this ratio, but are within 8% of those when the ratio of 1.9 is used. Water related impacts also decrease or increase with this ratio; they are either <15% or <26 % of total impacts for a wastewater to freshwater ratio of 0.7 or 2.75, respectively (compared to <22% for the base case). These changes are all within the minimum and maximum range of values determined from the sensitivity analysis.

Several additional assumptions were made in this study that require further examination. First, the life cycle impacts of gas production, processing, and transportation were ignored, and this includes fugitive emissions of natural gas that occur during production. Considering these processes would certainly increase the overall life cycle impacts of the hydraulic fracturing process; however; they would have no clear impact on the life cycle impacts related to using low or no-water based fracturing fluids, so the relative life cycle impacts related to water use would only decrease. Second, the energy and ancillary materials required to synthesize chemicals from feedstock chemicals was not considered when chemical substitutions were required in SimaPro. Because the environmental impacts of chemicals used in hydraulic fracturing fluids are relatively small (<7%), considering these would only marginally change the results. Third, only slickwater which contains a friction reducer was considered, and not polymer-based hydraulic fracturing fluids that contain gelling agents. Gelling agents used in hydraulic fracturing can increase fluid viscosity and enhance proppant carrying capacity. An additional LCA analysis was performed by adding a gelling agent (i.e., represented by carboxymethyl hydroxyethyl cellulose) to the representative hydraulic fracturing fluid. The LCA results are in Table S18; life cycle impacts of this chemical are very small and do not appreciably change the results from those of slickwater in nine of ten impact categories (<0.1%), and by ~3% for smog impact.

The results of this study do not support our initial hypothesis that the large volumes of water used, recovered, and disposed of during typical hydraulic fracturing operations dominate energy and environmental life cycle impacts. Instead, life cycle impacts related to freshwater use in slickwater are <22% of total impacts in any category, and well construction impacts are dominant. Hence, changes in well construction methods could yield the largest environmental benefits, e.g., using recycled steel. The most favorable option considered for reducing total and relative water-related environmental impacts is switching to a 90% v/v CH_4-foam, but the gains fall within the bounds of the sensitivity analysis performed with reasonable lower and upper bounds of life cycle input parameters. For example, total environmental impacts decrease slightly for a switch from slickwater to CH_4-foam (up to 8%), despite the higher impacts associated with greater fuel use for fracturing with a less dense fluid, and relative water-related environmental impacts reduce from <22% to <15% in any category. Another consideration is water consumption and its impacts on local water resources and ecology, especially in water-stressed areas. Given the large water storage volumes in the five counties considered in this effort, such impacts do not appear to be a concern. However, this may not be the case on a more local scale, or in other counties or shale plays where water stress is greater. This, as well as changed in hydrocarbon recovery, must be considered to fully assess the impact of switching to low or no water based fracturing fluid.

REFERENCE

(1) Energy, U. D. of. *Annual Energy Outlook 2017*; 2017.

(2) Freyman, M. Hydraulic Fracturing & Water Stress : Water Demand by the Numbers. *Ceres* **2014**, No. February, 85.

(3) US Environmental Protection Agency - US EPA. Hydraulic Fracturing for Oil and Gas: Impacts from the Hydraulic Fracturing Water Cycle on Drinking Water Resources in the United States (Main Report - EPA/600/R-16/236fa). **2016**, No. December, 666.

(4) Spellman, F. *Environmental Impacts of Hydraulic Fracturing*; 2012.

(5) Williams, H. F. L.; Havens, D. L.; Banks, K. E.; Wachal, D. J. Field-Based Monitoring of Sediment Runoff from Natural Gas Well Sites in Denton County, Texas, USA. *Environ. Geol.* **2008**, *55* (7), 1463–1471.

(6) Drohan, P. J.; Brittingham, M.; Bishop, J.; Yoder, K. Early Trends in Landcover Change and Forest Fragmentation Due to Shale-Gas Development in Pennsylvania: A Potential Outcome for the Northcentral Appalachians. *Environ. Manage.* **2012**, *49* (5), 1061–1075.

(7) Burton, G. A.; Basu, N.; Ellis, B. R.; Kapo, K. E.; Entrekin, S.; Nadelhoffer, K. Hydraulic "Fracking": Are Surface Water Impacts an Ecological Concern? *Environ. Toxicol. Chem.* **2014**, *33* (8), 1679–1689.

(8) Gross, S. A.; Avens, H. J.; Banducci, A. M.; Sahmel, J.; Panko, J. M.; Tvermoes, B. E. Analysis of BTEX Groundwater Concentrations from Surface Spills Associated with Hydraulic Fracturing Operations. *J. Air Waste Manage. Assoc.* **2013**, *63* (4), 424–432.

(9) Rozell, D. J.; Reaven, S. J. Water Pollution Risk Associated with Natural Gas Extraction from the Marcellus Shale. *Risk Anal.* **2012**, *32* (8), 1382–1393.

(10) Vengosh, A.; Jackson, R. B.; Warner, N.; Darrah, T. H.; Kondash, A. A Critical Review of the Risks to Water Resources from Shale Gas Development and Hydraulic Fracturing in the United States. *Environ. Sci. Technol.* **2014**, *16* (4), 6838.

(11) Brantley, S. L.; Yoxtheimer, D.; Arjmand, S.; Grieve, P.; Vidic, R.; Pollak, J.; Llewellyn, G. T.; Abad, J.; Simon, C. Water Resource Impacts during Unconventional Shale Gas Development: The Pennsylvania Experience. *Int. J. Coal Geol.* **2014**, *126*, 140–156.

(12) DiGiulio, D. C.; Jackson, R. B. Impact to Underground Sources of Drinking Water and Domestic Wells from Production Well Stimulation and Completion Practices in the Pavillion, Wyoming, Field. *Environ. Sci. Technol.* **2016**, *50* (8), 4524–4536.

(13) Ellsworth, W. L. Injection-Induced Earthquakes. *Science (80-.).* **2013**, *341* (6142), 1225942.

(14) Jiang, M.; Hendrickson, C. T.; VanBriesen, J. M. Life Cycle Water Consumption and Wastewater Generation Impacts of a Marcellus Shale Gas Well. *Environ. Sci. Technol.* **2014**, *48* (3), 1911–1920.

(15) Dale, A. T.; Khanna, V.; Vidic, R. D.; Bilec, M. M. Process Based Life-Cycle Assessment of Natural Gas from the Marcellus Shale. *Environ. Sci. Technol.* **2013**, *47* (10), 5459–5466.

(16) Jiang, M.; Griffin, W. M.; Hendrickson, C.; Jaramillo, P.; VanBriesen, J.; Venkatesh, A. Life Cycle Greenhouse Gas Emissions of Marcellus Shale Gas. *Environ. Res. Lett.* **2011**, *6* (3), 34014.

(17) Weber, C. L.; Clavin, C. Life Cycle Carbon Footprint of Shale Gas: Review of Evidence and Implications. *Environ. Sci. Technol.* **2012**, *46* (11), 5688–5695.

(18) Wilkins, R.; Menefee, A. H.; Clarens, A. F. Environmental Life Cycle Analysis of Water and CO2-Based Fracturing Fluids Used in Unconventional Gas Production. *Environ. Sci. Technol.* **2016**, *50* (23), 13134–13141.

(19) Garbis, S. J.; Taylor III, J. L.; others. The Utility of CO2 as an Energizing Component for Fracturing Fluids. *SPE Prod. Eng.* **1986**, *1* (05), 351–358.

(20) Barati, R.; Liang, J.-T. A Review of Fracturing Fluid Systems Used for Hydraulic Fracturing of Oil and Gas Wells. *J. Appl. Polym. Sci.* **2014**, *131* (16).

(21) Middleton, R.; Viswanathan, H.; Currier, R.; Gupta, R. CO2 as a Fracturing Fluid: Potential for Commercial-Scale Shale Gas Production and CO2 Sequestration. *Energy Procedia* **2014**, *63*, 7780–7784.

(22) Middleton, R. S.; Carey, J. W.; Currier, R. P.; Hyman, J. D.; Kang, Q.; Karra, S.; Jiménez-Mart\'\inez, J.; Porter, M. L.; Viswanathan, H. S. Shale Gas and Non-Aqueous Fracturing Fluids: Opportunities and Challenges for Supercritical CO 2. *Appl. Energy* **2015**, *147*, 500–509.

(23) Holloway, M. D.; Rudd, O. *Fracking: The Operations and Environmental Consequences of Hydraulic Fracturing*; John Wiley & Sons, 2013.

(24) FracFocus Chemical Disclosure Registry https://fracfocus.org/ (accessed Dec 2, 2017).

(25) Fink, J. K. *Hydraulic Fracturing Chemicals and Fluids Technology*; 2013.

(26) Nicot, J.-P.; Scanlon, B. R.; Reedy, R. C.; Costley, R. A. Source and Fate of Hydraulic Fracturing Water in the Barnett Shale: A Historical Perspective. *Environ. Sci. Technol.* **2014**, *48* (4), 2464–2471.

(27) Nicot, J.-P.; Scanlon, B. R. Water Use for Shale-Gas Production in Texas, US. *Environ. Sci. Technol.* **2012**, *46* (6), 3580–3586.

(28) Hutchins, R. D.; Miller, M. J.; others. A Circulating Foam Loop for Evaluating Foam at Conditions of Use. *SPE Prod. Facil.* **2005**, *20* (04), 286–294.

(29) Clark, C. E.; Han, J.; Burnham, A.; Dunn, J. B.; Wang, M. *Life-Cycle Analysis of Shale Gas and Natural Gas.*; 2012.

(30) Gilmore, K. R.; Hupp, R. L.; Glathar, J. Transport of Hydraulic Fracturing Water and Wastes in the Susquehanna River Basin, Pennsylvania. *J. Environ. Eng.* **2013**, *140* (5), B4013002.

(31) Ghosn, M. Development of Truck Weight Regulations Using Bridge Reliability Model. *J. Bridg. Eng.* **2000**, *5* (4), 293–303.

(32) Kargbo, D. M.; Wilhelm, R. G.; Campbell, D. J. Natural Gas Plays in the Marcellus Shale: Challenges and Potential Opportunities. ACS Publications 2010.

(33) Laurenzi, I. J.; Jersey, G. R. Life Cycle Greenhouse Gas Emissions and Freshwater Consumption of Marcellus Shale Gas. *Environ. Sci. Technol.* **2013**, *47* (9), 4896–4903.

(34) Clark, C. E.; Horner, R. M.; Harto, C. B. Life Cycle Water Consumption for Shale Gas and Conventional Natural Gas. *Environ. Sci. Technol.* **2013**, *47* (20), 11829–11836.

(35) Vafi, K.; Brandt, A. GHGfrack: An Open-Source Model for Estimating Greenhouse Gas Emissions from Combustion of Fuel during Drilling and Hydraulic Fracturing. *Environ. Sci. Technol.* **2016**, *50* (14), 7913–7920.

(36) Waxman, H. A.; Markey, E. J.; DeGette, D. *Chemicals Used In Hydraulic Fracturing. United States House of Representatives, Committee on Energy and Commerce*; 2011.

(37) Stringfellow, W. T.; Domen, J. K.; Camarillo, M. K.; Sandelin, W. L.; Borglin, S. Physical, Chemical, and Biological Characteristics of Compounds Used in Hydraulic Fracturing. *J. Hazard. Mater.* **2014**, *275*, 37–54.

(38) Burchart-Korol, D. Life Cycle Assessment of Steel Production in Poland: A Case Study. *J. Clean. Prod.* **2013**, *54*, 235–243.

(39) Munkejord, S. T.; Hammer, M.; Løvseth, S. W. CO 2 Transport: Data and Models--A Review. *Appl. Energy* **2016**, *169*, 499–523.

(40) Gallegos, T. J.; Varela, B. A. *Trends in Hydraulic Fracturing Distributions and Treatment Fluids, Additives, Proppants, and Water Volumes Applied to Wells Drilled in the United States from 1947 through 2010: Data Analysis and Comparison to the Literature*; 2015.

Supporting Information

Environmental Impacts of Replacing Slickwater with Low/No-Water Fracturing Fluids for Shale Gas Recovery

Table of Contents

Lists of Tables

Lists of Figures

Hydraulic Fracturing Fluid Composition

Raw data retrieval and reduction

Individual well records were obtained from the FracFocus Chemical Disclosure Registry[1] for five counties in the Barnett shale play, i.e., Johnson, Hood, Tarrant, Parker, and Sommervell counties. All five counties are located in gas producing areas of the Barnett Shale play and are shown in Figure S1. In the first four counties, only records from 2013 were considered. No records are available for this period from Sommervell county, so all records from 2012 were considered.

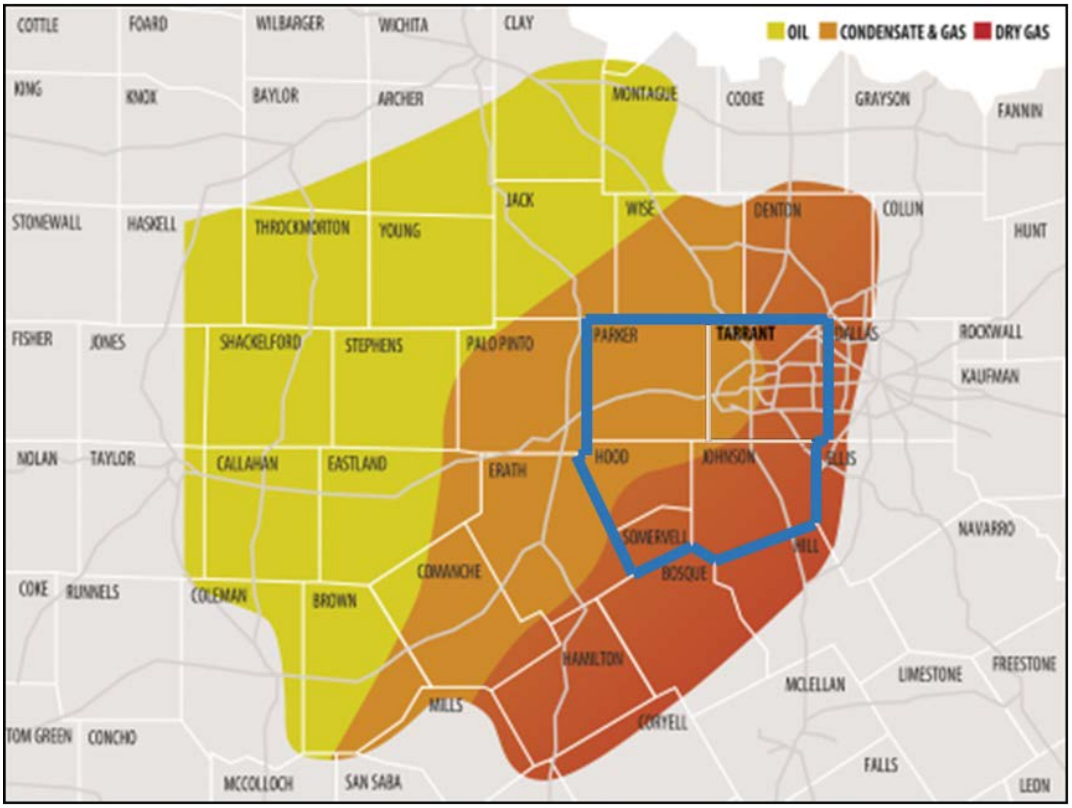

Figure S6. Barnett shale and Texas county geography (modified from a figure on Oilshalegas.com[2])

The number of records retrieved from the FracFocus database for each county and operator are listed in Table S1. A total of 324 records for hydraulic fracturing wells were retrieved from Johnson, Hood, Tarrant, and Parker counties in 2013, and Somervell county in 2012. The table lists operators in order of decreasing total number of records.

Table S1. Number of records retrieved for the study, with operator and county information.

Operator	Johnson	Hood	Somervell	Tarrant	Parker	Total
Chesapeake Operating Inc.	19	2		87		108

XTO Energy/ExxonMobil	4	6		69	4	83
EnerVest Ltd.	3			9	29	41
Devon Energy Production Company L. P.	11			10	19	40
Newark EP Operating LLC				11		11
EagleRidge Energy LLC				9		9
Aruba Petroleum Inc.					8	8
Atlas Energy L.P.	4	3				7
Quicksilver Resources Inc.			3	3		6
Vantage Fort Worth Energy LLC				3		3
EOG Resources Inc.	2					2
Edge Barnett Operating Company LLC				2		2
Sauder Management Company					2	2
Western Production Co.	1					1
Tamarack Petroleum Company Inc.					1	1
Total	44	11	3	203	63	324

There is considerable overlap in fracturing fluid composition among wells for the same operator, and also among some operators. Therefore, the number of hydraulic fracturing records was reduced by eliminating duplicate records with the same fluid components and similar amounts, regardless of the operator or county. This reduced the total number of records considered from 324 to 35 for all five counties. These records were used to determine the composition of a representative hydraulic fracturing fluid.

Hydraulic Fracturing Fluid Composition

All hydraulic fracturing fluid components listed in each of the 35 unique well records were classified into different categories. Based on the actual FracFocus Chemical Disclosure records, these categories are water, acid, proppant (including resin coated proppant), biocide (including antibiotics), scale inhibitor, corrosion inhibitor, iron control agent, pH adjusting agent, friction reducer, gelling agent, crosslinker, breaker, water foaming agent, surfactant, conductivity enhancer, solvent, non-emulsifier, oxygen scavenger, ball sealer, water-emulsion copolymer, and concentrate. Some components listed in individual well records could not be easily categorized, and were put into one of the aforementioned categories based on their physiochemical properties and potential use identified in the literature, or (in some cases) treated as their own separate category.

The mass and mass fraction of each component of the hydraulic fracturing fluid are listed in each well record. However, because of small errors in accuracy, or incomplete records, the mass fractions of all components do not add up to 1. Therefore, new mass fractions were calculated for all components in a record from the ratio of the original mass fraction of a component to the sum of all mass fractions. The sum of all new mass fractions for components in a well record then totaled one, as did the sum of new mass fractions for all categories.

The number of times a component appeared in each category was identified, and then summed for all 35 well records. Components occurring with the highest frequency in a category, or in more than one fifth of the records for that category, were selected as representative components. The remaining components of a category were not further considered with two exceptions. The first exception is corrosion inhibitors; proprietary products appeared in more than one fifth of the records, and their compositions were unknown. Therefore, only non-proprietary components were used. The second exception is gelling agents, which appeared in 10 of the 35 records (29%) but were not considered. Instead, friction reducers were included, which are common slickwater components, to increase fluid viscosity[3]. For the 35 records, there are 15 that have friction reducers, while only 3 among these 15 also have gelling agents. The potential change in LCA results for using a gelling agent based fluid is addressed in the Discussion section of the main manuscript.

Among all components, eight were not categorized and accounted for separately; these are ethanol, methanol, isopropanol, ethylene glycol, diethylene glycol, hydrotreated light distillate, sodium chloride and ammonium chloride. In general, these chemicals act as solvents, carriers, and/or stabilizers for other components in the hydraulic fracturing fluid.

The mass fractions of the selected components within a category were then scaled proportionally such that their sum added up to the new mass fractions for each category identified above. We note that several categories (cross linker, breaker, water foaming agent, surfactant, conductivity enhancer, non-emulsifier, oxygen scavenger and sealer) had no components selected, so the mass fractions were rescaled proportionally such that the sum of the remaining categories added to one, as did the sum of all remaining components.

Finally, the masses of each individual component in a well record were then re-calculated by multiplying the final mass fractions by the total hydraulic fracturing fluid mass.

Hydraulic Fracturing Fluid Mass or Volume

The volume of water used per well depends on the lateral length of a horizontal well. This length has increased over time, and with it the volume of water used. For example, in the Barnett shale, Nicot[4] reports that water use increased from ~3 million gallons per well in 2005 to ~5 million gallons per well in 2011[4]. Based on the 35 selected records from the Fracfocus database, we obtained an average water use per well of 4,400,000 gallons. This value is also close to that reported by Ceres[5]. This volume was converted to mass assuming the density of water is 1.0 g/mL. The masses of other components were computed based on mass fraction ratios.

The freshwater used in hydraulic fracturing comes from both groundwater and surface water, and ratios of groundwater to total freshwater used reported in the literature for the Barnett shale vary from 0.2 to more than 0.5, depending on the time period[4]. However, the distinction of the freshwater source does not significantly impact life cycle assessment results for three reasons, and is not further considered. The first and primary reason is that the energy needs for pumping groundwater or surface water are negligible compared to energy needs for well completion, hydraulic fracturing, or wastewater disposal, and this is the primary input variable to the life cycle software that would affect environmental impacts. An explanation for the pumping calculation is at the end of this paragraph. The second reason is that we determine in the manuscript that water scarcity (at the county level) is not a concern for the amount of water being used in hydraulic fracturing. The third and last reason is that our life cycle assessment does not consider ecosystem degradation related to water withdrawals from groundwater or surface water. Such an assessment is not included in the life cycle software, we were unable to identify relevant prior studies, and a detailed assessment of this impact is outside the scope of our effort.

We used the following equation to calculate the energy required for pumping groundwater[6]:

$$whp = \frac{gpm \times TDH}{3{,}960 \times \eta}$$

$$Amount\ of\ Diesel = whp \times \frac{1\ gal}{12.5\ whp \cdot hrs} \times (pumping\ time)$$

The whp is water horsepower (horsepower), gpm is water pumping rate (gallon per minute), TDH is total dynamic head (feet), η is pump efficiency. The TDH is the sum of static head, friction loss, operating pressure, and elevation change. We set the static head equal to the approximate depth of the potable groundwater aquifer in the Barnett Shale play (300 ft). We set the friction loss equal to that expected for a 300 ft long x 4 inch inner diameter steel pipe (104 ft) at a pumping rate of 825 gpm. We set the operating pressure equal to 28.5 ft, based on look up information for a typical pump. We set the elevation change equal to zero, assuming the water was pumped directly to a truck at the point of extraction. This resulted in a TDH equal to 432.5 ft. With the pumping rate (825 gpm), we assumed a reasonable pump efficiency (75%), and calculated a requirement of 40.04 horsepower. Last, we calculated that 2,700 minutes (~2 days) is needed to pump 2.2 Mgal of water at 825 gpm (50% groundwater for a single well), and determined that 439 gallons of diesel fuel are needed. We note that more than 60,000 gallons of diesel fuel are needed for drilling and mud circulation, 19,500 gallons of diesel fuel are needed for hydraulic fracturing, and 95,400 gallons of diesel fuel are needed for wastewater disposal. Hence, the 439 gallons are negligible.

The full list of hydraulic fracturing fluid components are in Table S2, along with categories and mass fractions. The frequency column gives the number of occurrences of the components in the 35 hydraulic fracturing fluid records.

Table S2. Full list & occurrences of components in FracFocus hydraulic fracturing fluid records.

Category	**Component (CAS Number)**	**Frequency**	**Mass Fraction of Component in the Fluid (%)**	**Mass of Component in the Fluid (kg)**
Carrying Fluid	Water 7732-18-5	35	91.0	16,700,000
Acid	Hydrochloric acid 7647-01-0	33	0.11	20,300
Proppant	Crystalline silica 14808-60-7	34	8.75	1,600,000
Biocide	Quartenary ammonium compounds (alkyl (c12-16) dimethylbenzylammonium chloride) 68424-85-1	14	0.0010	174
Biocide	Glutaraldehyde 111-30-8	23	0.0061	1,110
Biocide	Didecyl dimethyl ammonium chloride 7173-51-5	9	0.0005	91
Scale Inhibitor	Polyacrylate (proprietary)	8	0.016	2,947
Corrosion Inhibitor	(Modified) thiourea polymer 68527-49-1	14	0.00060	112
Corrosion Inhibitor	Propargyl alcohol 107-19-7	23	0.00040	75
Corrosion Inhibitor	Dimethyl formamide 68-12-2	8	0.00090	162
Iron Control	Acetic acid 64-19-7	14	0.0018	323

Iron Control	Citric acid 77-92-9	23	0.0053	967
Friction Reducer	Copolymer of acrylamide and sodium acrylate 25987-30-8	11	0.017	3,130
Friction Reducer	Sorbitan monooleate 1338-43-8	15	0.0021	381
Friction Reducer	Alcohols (c12-c16), ethoxylated 68551-12-2	8	0.0018	332
Gelling Agent	Guar gum 9000-30-0	10	0.011	1,910
	Ethanol in biocide, surfactant, water foaming agent 64-17-5	25	0.0052	957
	Sodium chloride unknown, in scale inhibitor, riction reducer 7647-14-5	21	0.0051	923
	Ammonium chloride in friction reducer, scale inhibitor 12125-02-9	11	0.00090	172
	Hydrotreated light distillate as carrier in the friction reducer 64742-47-8	32	0.0230	4,120
	Methanol in nonemulsifier, corrosion, scale, iron control, water foaming agent, solvent, resin coated sand, surfactant, conductivity enhancer 67-56-1	31	0.0078	1,420
	Ethylene glycol in scale inhibitor 107-21-1	16	0.0023	412
	Diethylene glycol in scale inhibitor 111-46-6	10	0.00030	51
	Isopropanol in corrosion inhibitor 67-63-0	14	0.0020	371

Substitutions for Chemicals in Database

The Ecoinvent database does not contain all selected components in the hydraulic fracturing fluid, so substitutions were made using a two-tiered approach, where progression from the first to the second tier only occurred if the first tier approach was unsuccessful. In the first tier, alternative chemicals with similar functionality and structure were identified and used as substitutes if available in the Ecoinvent database. For example, polyacrylate, categorized as a scale inhibitor, was substituted for polycarboxylate, in which polyacrylate is a group. Also, polycarboxylate has been documented as a scale inhibitor[7].

In the second tier, feedstock chemicals used to synthesize the chemical of interest were identified in the literature, and these were used as available in the Ecoinvent database. For example, the environmental impacts of propargyl alcohol were based on the stoichiometric amounts of acetylene and formaldehyde used in its synthesis. The energy and ancillary materials required to synthesize a chemical from its feedstock chemicals were not considered, and implications of this are addressed in the Discussion section of the main manuscript. All chemicals fit into either the tier one or tier two approach.

Among 24 chemicals, substitutes were required for 10 chemicals. 3 of these were tier 1, and 7 were tier 2. All substitutions are listed in Table S3.

Table S3. Hydraulic fracturing fluid component substitutions.

Category	**Component**	**Mass of Component (kg)**	**Description/Justification**
Carrying Fluid	Water	16,600,000	No substitution needed. The fresh water sources include surface water and groundwater source.
Substitution	Surface Water	6,650,000	40% of total water use[8]
	Groundwater	9,980,000	60% of total water use[8]
Acid	Hydrochloric Acid	20,300	No substitution needed.
Proppant	Crystalline Silica	1,600,000	No substitution needed.
Biocide	Quartenary Ammonium Compounds (Alkyl (C12-16) Dimethylbenzylammonium Chloride)	174	Tier 2 substitution. One mole of alkyl (C12-16) dimethylbenzyl ammonium chloride is represented by one mole of benzyl dimethyl ammonium chloride due to structural similarly. The latter is produced by the alkylation of one mole each of trimethylamine and benzyl chloride[9].
Substitution	Benzyl Chloride	65	
	Trimethylamine	30	
Biocide	Glutaraldehyde	1,110	Tier 2 substitution. One mole of glutaraldehyde can be synthesized by the Diels-Alder reaction of one mole each of acrolein and ethyl vinyl ether followed by hydrolysis that produces one mole of ethanol[10]. One mole of ethyl vinyl ether can be made by reaction of one mole each of acetylene and ethanol in presence of a base[11].
Substitution	Acrolein	620	
	Acetylene	288	
Biocide	Didecyl Dimethyl Ammonium Chloride	91	Tier 2 substitution. One mole of didecyl dimethyl ammonium chloride is represented by one mole of tetramethylammonium chloride based on structural similarity. One mole of tetramethylammonium chloride is synthesized by 1 mole of ammonium chloride, 4 moles of methanol, and 2 moles of phosgene[10].
Substitution	Ammonium Chloride	13	
	Methanol	32	
	Phosgene	50	
Scale Inhibitor	Polyacrylate	2,950	Tier 1 substitution. Polyacrylate is a subset of, and was substituted with the same mass of, polycarboxylate[12].
Substitution	Polycarboxylates, 40% Active Substance	2,950	
Corrosion Inhibitor	(Modified) Thiourea Polymer	112	Tier 2 substitution. The thiourea polymer is prepared from three monomers in equal molar amounts: thiourea,

			formaldehyde, 1-phenylethanone. Thiourea and 1-phenylethanone require multistep substitutions. One mole of thiourea is produced by one mole of calcium cyanamide, two moles of water, one mole of sulfide hydrogen, and one mole of byproduct calcium hydroxide is produced[13]. One mole of calcium cyanamide is prepared from one mole of calcium carbide and one mole of nitrogen gas with byproduct carbon[14]. Each mole of acetophenone is prepared as a byproduct of oxidation of one mole of ethylbenzene to ethylbenzene hydroperoxide[15]. One mole of ethylbenzene is produced by combining one mole of benzene and one mole of ethylene[9]. Byproduct impacts were not considered.
Substitution	Formaldehyde	15	
	Hydrogen Sulfide	17	
	Nitrogen	14	
	Oxygen	16	
	Calcium Carbide	32	
	Benzene	39	
	Ethylene	14	
Corrosion Inhibitor	Propargyl Alcohol	75	Tier 2 substitution. One mole of propargyl alcohol is produced by the copper-catalyzed addition of one mole of formaldehyde to one mole of acetylene[10].
Substitution	Acetylene	35	
	Formaldehyde	40	
Corrosion Inhibitor	Dimethyl Formamide	162	No substitution needed.
Iron Control	Acetic Acid	323	No substitution needed.
Iron Control	Citric Acid	967	No substitution needed.
Friction Reducer	Copolymer of Acrylamide and Sodium Acrylate	3,130	Tier 2 substitution. The copolymer is assumed to be synthesized from a 1:1 molar ratio of acrylamide and sodium acrylate. One mole of acrylamide is produced by hydrolysis of one mole of acrylonitrile with nitrile hydratase present[16]. One mole of sodium acrylate is produced by one mole each of acrylic acid and sodium hydroxide[10].
Substitution	Acrylonitrile	1,010	
	Acrylic Acid	1,370	
	Sodium Hydroxide	759	
Friction Reducer	Sorbitan Monooleate	381	Tier 1 substitution. A common sorbitan monooleate is called Span 80, which has MW=428.6 g/mol, but is not found in SimaPro. Alcohols (C12-C16) are also a common friction reducer[7], and were used as substitute, with an approximate molecular weight 346 g/mol[17].
Substitution	Alcohols (C12-C16), Ethoxylated	308	

Friction Reducer	Alcohols (C12-C16), Ethoxylated	332	
Other	Ethanol	957	No substitution needed.
Other	Sodium Chloride	923	No substitution needed.
Other	Ammonium Chloride	172	No substitution needed.
Other	Hydrotreated Light Distillate	4,120	Tier 1 Substitution. Hydrotreated Light Distillate may be also called kerosene, which is more common in the U.S.
Substitution	Kerosene	4,120	
Other	Methanol	1,420	No substitution needed.
Other	Ethylene Glycol	412	No substitution needed.
Other	Diethylene Glycol	51	No substitution needed.
Other	Isopropanol	371	No substitution needed.

Sand Transportation

The five county (Johnson, Hood, Somervell, Tarrant, Parker) centroids are shown in Figure S2, along with the sand vendors. Although seven sand vendors were found in Texas, only five are shown for better resolution. The other two vendors are further away (not shown in Figure S2) and were not considered. The geographical coordinates of the county centroids and vendors are listed in Table S4.

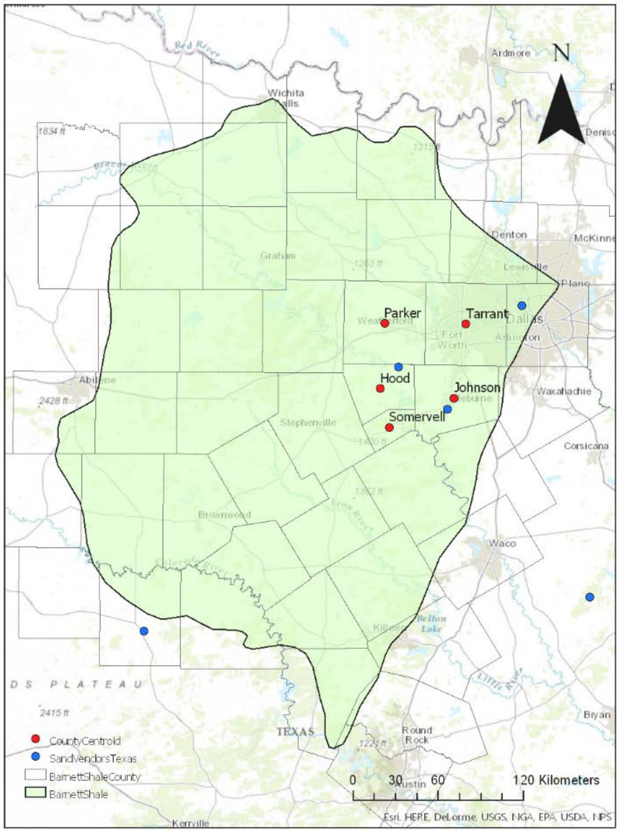

Figure S7. County centroids and sand vendors geographic locations
(modified from map provided by U.S. EIA, 2016)

Table S4. County centroid locations and closest sand vendor locations.

County	Latitude (°)	Longitude (°)	Smallest Distance (km)	Vendor Latitude (°)	Vendor Longitude (°)
Johnson	32.3790	-97.3663	7.81	32.3183	97.4081
Hood	32.4299	-97.8323	16.43	32.5425	97.7188
Tarrant	32.7716	-97.2912	41.36	32.8704	96.9396
Somervell	32.2223	-97.7743	35.99	32.5425	97.7188
Parker	32.7776	-97.8051	27.36	32.5425	97.7188

Transportation Requirement for Water-based Fluid and Foam-based Fluid

The total transportation considered in the system includes sand transportation from source to fracturing sites, fresh water transportation from source to fracturing sites, and wastewater transportation from fracturing sites to disposal wells. The transportation of well materials was not considered, as it is small compared to fresh water and sand transportation. The results are listed in Table S5.

Table S5. Transportation requirements for water-based fluid and foam-based fluid, with different lateral well lengths.

	Trip*	Average Distance (km)	Mass Transported (metric tonnes)	Number of Round Trips	Total payload-distance (TKM)
Sand, 3,800ft lateral	Sand Transportation from Sources to Sites	26	1,600	77	102,000
Sand, 6,000ft lateral	Sand Transportation from Sources to Sites	26	2,560	123	164,000
Water-based Fluid,	Fresh Water Transportation from Sources to Sites	8	16,600	800	332,000

3,800ft lateral	Wastewater Transportation from Fracturing Sites to Disposal Wells	16	31,600	1,520	1,260,000
Water-Based Fluid, 6,000 ft lateral	Fresh Water Transportation from Sources to Sites	8	26,600	1,280	531,000
	Wastewater Transportation from Fracturing Sites to Disposal Wells	16	50,600	2,430	2,020,000
Foam-based Fluid, 3800ft lateral	Fresh Water Transportation from Sources to Sites	8	1,660	80	33,200
	Wastewater Transportation from Fracturing Sites to Disposal Wells	16	16,630	800	664,072

* The return trips when trucks are empty were considered and are included in the table.

Well Construction Materials

The materials for well construction are listed in Table S6, with needed substitutions following the two-tiered substitution approach described above.

Table S6. Well construction materials and substitutions.

Material	Mass of Materials Needed (Metric Tons) (Or volume if specified) in 3800 ft lateral length wells	Mass of Materials Needed (Metric Tons) (Or volume if specified) in 6000 ft lateral length wells	Substitution	Description/Justification
Steel	163	172	Reinforced steel	Replaced with reinforced steel.
Portland Cement	267	272	No substitution needed	
Gilsonite (Asphalt)	9	9	Mastic asphalt	Replaced with mastic asphalt.
Bentonite	61.4	61.4	No substitution needed	
Soda Ash	1.06	1.06	Limestone	Replaced with limestone.
Gelex	0.04	0.04	No substitution needed	Absorbed into polypac, impact ignored.
Polypac	1.6	1.6	Bitumen seal	Polypac is a compact seal which is mainly made of rubber. So,

				polyethylene seal was used to model the polypac seal.
Xanthum Gum	0.81	0.81	Guar gum	Replaced with guar gum.
Water	270,000 (gallon)	270,000 (gallon)	No substitution needed	

Foam-Based Hydraulic Fracturing Fluid

Mass of CO_2 or CH_4 in the foam fluid

A 90% v/v foam was used as a substitute for slickwater in the hydraulic fracturing process, with either CO_2 or CH_4 as the substitute fluid. To create the same amount of fracture volume, the total volume of the gas and liquid for a foam fluid is assumed to equal the volume of water for a water-based fluid (4.39 million gallons in the 3800 ft lateral length case, 7.03 million gallons in the 6,000 ft lateral length case), both under reservoir conditions. The water required in the foam fluid is one-tenth the volume of that in the slickwater, and the remaining volume is occupied by supercritical CO_2 or CH_4. The mass of CO_2 or CH_4 was calculated using the Van der Waals equation of state:

$$\left(p + a\frac{n^2}{V^2}\right)(V - nb) = nRT$$

The parameter p is the pressure of the Barnett shale during hydraulic fracturing, set at 4,500 psi (pressure gradient times the average depth, equals 310.2641 bar). n is the molar amount of gas. V is the volume of the gas. R is gas constant (0.08314 L bar/(mol K)). T is the temperature (assume 150 Fahrenheit degrees under hydraulic fracturing conditions, which equals 338.7 Kelvin). Furthermore, for CO_2 or CH_4:

$a = 3.640\ L^2\ bar/mol^2$ (CO_2); a = 2.300 L2 bar/mol2 (CH_4)

$b = 0.04267\ L/mol$ (CO_2); b = 0.04301 L/mol (CH_4)

Therefore, for CO_2 and the 3800 ft. lateral length case:

$$\left(310.2641 + 3.640\frac{n^2}{14965905.61^2}\right)(14965905.61 - 0.04267n) = 28.1595n$$

For CO_2 and the 6000 ft. lateral length case:

$$\left(310.2641 + 3.640\frac{n^2}{23950289.07^2}\right)(23950289.07 - 0.04267n) = 28.1595n$$

Here, n is in the unit of mol.

Based on these calculations, the compositions of the foam fluid for both lateral well lengths are listed in Table S7.

Table S7. Compositions of 90% foam-based fluid.

	3,800ft lateral length well
Water volume (million gallons)	0.439
CO_2 or CH_4 volume under fracturing conditions (million gallons)	3.95
CO_2/CH_4 amount (million mol)	218 / 165
CO_2/CH_4 masses (kg)	9,590,000 / 2,640,000
Total mass CO_2/CH_4 –foam (kg)	11,200,000 / 4,300,000
Apparent density under fracturing conditions CO_2/CH_4–foam (kg/L)	0.677 / 0.259
Apparent density under fracturing condit. CO_2/CH_4 – foam(lbm/gal)	5.65 / 2.16

Viscosity of Foam Fluid Under Fracturing Conditions

The apparent viscosity of the foam fluid was calculated based on Tong et al.[18]. Given well characteristics and hydraulic fracturing conditions, a 70% CO_2-foam has an apparent viscosity as 20 centipoise (cp) while an 80% CO_2-foam has an apparent viscosity of 30 cp. A linear extrapolation was applied to estimate the viscosity of 90% v/v CO_2-foam fluid, resulting in 40 cp. The same viscosity was assumed for 90% v/v CH_4-foam fluid.

Greater Lateral Length Analysis

Due to drilling and completion advancements, lateral lengths of shale gas wells are increasing. In some plays, lateral lengths increase to as much as 10,000 feet[19]. Although this value is dependent on shale play and can be variable in each play, an LCA was conducted assuming a well with a longer lateral length of 6,000 ft, identical to the average value in Eagle Ford shale in 2014[19].

Based on ISO/API specification (ISO 11960:2011), the production casing used has an outside diameter 4.5 inches and a thickness 0.205 inches, while cement outside the production casing has a 5 inch outside diameter, and thickness of 0.25 inches. Bulk density of steel is 8050 kg/m^3, while that of cement is 3150 kg/m^3. Therefore, the increase in lateral length will result in an increase of steel use by 4.38 kg/ft, and of cement use by 2.31 kg/ft.

Only the increase in steel and cement use were considered for the longer well, because they dominate environmental impacts. Assuming the steel and cement amounts used in outer layers of steel casing and cementing are small compared to the production casing layer, a well with 6,000 ft lateral length and aforementioned configurations will need about 172 metric tons of steel and 272 metric tons of cement. Based on GHGfrack model[20] calculations, the energy needed for well drilling and mud circulation (not including hydraulic fracturing) totals 90,800 gallons of diesel fuel. The energy for constructing the 3,800 ft lateral length well was obtained from the Argonne report[21], and is only 110% of the value determined from GHGfrack. Therefore, the energy required to construct the 6,000 ft lateral length well was determined by multiplying the 90,800 gallons by the ratio of Argonne to GHGfrack diesel fuel values for the 3,800 ft lateral length well. This came out to approximately 100,000 gallons of diesel fuel.

Water use per well in hydraulic fracturing fluid will also increase with the lateral length by 1,200 gallon/ft [4]. Water use in 2013 is 4.39 million gallons, based on FracFocus records and ~3,800 ft[4] of lateral length. Therefore, a well with a 6000 ft lateral length will require 7.03 million gallons of water. Other hydraulic fracturing fluid components, and the produced water volume, are assumed to scale with the water volume.

With the above input changes, a well with 6,000 ft lateral length requires total transportation of about 2.71 million TKM (increase by 1.02 million TKM compared to 3800 ft lateral length well, details in Table S5). Energy for well construction will increase to 100,000 gallons of diesel fuel (increase by 38,200 gallons of diesel fuel, see Table S10). Also, energy used for hydraulic fracturing will increase to 38,600 gallons of diesel fuel (increase by 19,100 gallons, see Table S10), and energy use for wastewater injection will become 153,000 kWh per well (increase by 57,600 kWh). These changes will result in increasing environmental impacts, detailed in Table S13.

Well Construction and Hydraulic Fracturing Energy Consumption

Table S8 lists the inputs and outputs of the drilling module for the GHGfrack model. The well is modeled with 3 sections, i.e., vertical, inclined and horizontal. The lengths of each section were determined based on the Barnett shale geology, where the shale formation average depth is 7,500 feet [22], and the average length of the horizontal section in the Barnett shale is about 3,800 feet[4]. We assumed an intermediate section with 1,000 feet length and a 45 degrees inclined angle. Thus, the vertical section length is set to be 700 feet shorter than the average depth of the shale formation, and the total length of the well is 11,600 feet.

Table S9 lists the inputs and outputs of the hydraulic fracturing module for the GHGfrack model. Most input parameters are identical to the default values in the GHGfrack model. The only exceptions are the well geometry, hydraulic fracturing fluid volume, fracture gradient, and hydraulic fracturing injection time. The injection times for each hydraulic fracturing stage are assumed to be two hours, for either slickwater fracturing or foam fluid fracturing. The number of fracturing stages were calculated by the well lateral length (3800 feet or 6000 ft), and the length for each fracturing stage (300 feet/stage). Also, the gravitational head of slickwater was assumed to be 0.468 psi/ft (with density 9 lbm/gal), and that of foam fluid 0.291 psi/ft (with density 5.6 lbm/gal).

The fracture gradient in Barnett shale differs between stages, but in the model an average value of 0.6 psi/ft was used based on Speight[23]. For comparison, the Woodford shale has an initial stage fracture gradient of 0.71 psi/ft [24]. Also, the Barnett shale has an overpressure gradient of 0.52 psi/ft [25].

We note that the energy required to compress gases used in foams was not considered, because it is negligibly small compared to the energy required for well completion, hydraulic fracturing, or wastewater disposal. We determined this energy using the following equation[26]:

$$W = P_1 V_1 \frac{\kappa}{1-\kappa}\left[\left(\frac{P_2}{P_1}\right)^{(\kappa-1)/\kappa} - 1\right]\frac{Z_1 + Z_2}{2Z_1}$$

where Z_1 and Z_2 are compressibility factors, P_1 and P_2 are pressures, and V_1 and V_2 are volumes, each at conditions 1 (ambient) and 2 (downhole), respectively. κ is the isentropic expansion factor (or heat capacity ratio). We calculated the energy needed to compress CH_4 is 47.8 million kJ, which is equivalent to 434.7 gallons of diesel fuel if 75% efficiency is assumed. The energy for CO_2 compression is of the same order. We note that more than 60,000 gallons of diesel fuel are needed for drilling and mud circulation, 19,500 gallons of diesel fuel are needed for hydraulic fracturing, and 95,400 gallons of diesel fuel are needed for wastewater disposal.

Table S8. Inputs and outputs of the drilling module for the GHGfrack model.

Bulk Data Drilling Inputs
Drilling

Well Section Number	Section 1	Section 2	Section 3	Section 3
Well Section Length (ft)	6,800	1,000	3,800	6,000
Inclination Angle (w.r.t. vertical) (degree)	0	45	90	90
Torque Value (ft-lbf)	9,000	11,000	11,000	11,000
Rate of penetration of drill bit (ROP) (ft/min)	2.5	1.25	0.22	0.22
Rotational Speed (rpm)	60 rpm	60 rpm	60 rpm	60 rpm
Mechanical power transmission efficiency (%)	45%	45%	45%	45%
Mud Circulation				
Mud fluid type	Bingham Plastic	Bingham Plastic	Bingham Plastic	Bingham Plastic
Mud plastic viscosity (cp)	25	25	25	25
Consistency index K (power law fluid)	0.066	0.066	0.066	0.066
Power law index n	0.29	0.29	0.29	0.29
Yield Stress (lbf/100 ft^2)	15	15	15	15
Mud density (lbm/gal)	12	12	12	12
Drill cuttings sieve diameter (in)	0.5	0.5	0.5	0.5
Drill cuttings density (lbm/gal)	25	25	25	25
Length of drill collar (ft)	700	700	700	700
Hole diameter	12.30	8.75	8.75	8.75
Drill pipe Outside Diameter (ft)	6.63	5	5	5
Drill pipe Inside Diameter (ft)	6 ft	4	4	4

Drill collar Outside Diameter (ft)	9.5	6.75	6.75	6.75
Drill collar Inside Diameter (ft)	4.43	3.25	3.25	3.25
Number of segments of the drilling section	100	100	100	100
Drill pipe roughness (inch)	0.00008			
Mud pump efficiency (%)	65			
Drill Bit				
Number of Nozzles	5			
Size of Nozzles (inch)	0.50			
Nozzle discharge coefficient Cd	0.95			
Pressure drop across downhole motor (psi)	500	700	700	700
Downhole motor type	Turbine			
Downhole motor rpm (rpm)	100			
Other pressure drop source (psi)	0			
Bulk Data Drilling Outputs				
Drilling				
Drilling time (hour, including mud circulation)	45.3	13.3	288	455
Drilling energy required (MMbtu)	26.3	9.5	204	323
Fuel efficiency (Btu/hp.h)	7,140	7,120	7,120	7,120
Diesel fuel used (gallon)	575	206	4,450	7,030
Mud Circulation				
Mud flow rate (gpm)	610	296	821	821

Total pressure drop (max) (psi)	1,240	1,200	5,160	5,790
Energy consumption by mud pump (MMBtu)	70.0	10.5	2490	4210
Fuel efficiency (Btu/hp.h)	6,940	7,100	6,420	6320
Diesel fuel used (gallon)	1,490	228	48,900	81,300

Table S9. Inputs and outputs of the hydraulic fracturing module for the GHGfrack model.

Input	Slickwater fracturing – 3,800 ft	Slickwater fracturing – 6,000 ft	90% CO_2 Foam fracturing – 3,800 ft	90% CH_4 Foam fracturing – 3,800 ft
Volume of Fluid (million gallons)	4.39	7.03	4.39	4.39
Fluid density (lbm/gal)	9.0	9.0	5.650	2.16
Viscosity (cp)	1	1	40	40
Fracture gradient	0.6	0.6	0.6	0.6
Pipe roughness (inch)	0.00008	0.00008	0.00008	0.00008
Length of fracking stage (ft)	300	300	300	300
Pump Efficiency	65%	65%	65%	65%
Injection time (hr)	25.2	40	25.2	25.2
Outputs				
Flow rate (gpm)	2,900	2,930	2,900	2900
Pressure drop due friction in non-horizontal section (psi)	3,370	2,530	4,460	2,170
Hydrostatic pressure (psi)	3,510	3,510	2,200	842

Pressure drop due hydraulic fracturing (psi)	4,500	4,500	4,500	4,500
Pump energy consumption (MMBtu)	1,050	2,050	1,530	1,170
Fuel efficiency (Btu LHV Diesel/hp.hr)	6,060	6,150	6,090	6,120
Fuel consumption (gallon)	19,500	38,600	28,600	21,900

Energy Consumption Summary

The energy requirements for well construction and wastewater injection are shown in Table S10.

Table S10. Summary of energy consumption in well construction and hydraulic fracturing.

Analysis	Slickwater fracturing – 3,800 ft	Slickwater fracturing – 6,000 ft	90% CO_2 Foam fracturing – 3,800 ft	90% CH_4 Foam fracturing – 3,800 ft
Well Construction (gallons of diesel)	61,800	100,000	61,800	61,800
Hydraulic fracturing energy consumption (gallons of diesel)	19,500	38,600	28,600	21,900
Energy for wastewater deep well injection (kWh of electricity)	95,400	153,000	50,200	50,200

Water impact calculations

The average amount of water stored in the nearby reservoirs for the five counties in 2013 are listed in Table S16.

Table S11: Average storage of reservoirs in 2013.

Basin Name	Brazos				Trinity					
Name	Squaw Creek	Granbury	Mineral Wells	Pat Cleburne	Weatherford	Eagle Mountain	Benbrook	Worth	Arlington	Grapevine
Type	Reservoir	Lake	Lake	Lake	Lake	Reservoir	Lake	Lake	Lake	Lake
Reservoir Storage (acre-ft)	152,000	84,000	4,580	17,700	11,800	136,000	66,700	23,700	32,100	121,000

Linear Fluid LCA Analysis

Linear gels are alternatives of slickwater for hydraulic fracturing. A commonly used gelling agent is carboxymethyl hydroxyethyl cellulose (CMHEC)[7]. The LCA of a linear fluid containing CMHEC was conducted, and the mass of gelling agent was calculated based on FracFocus records. It is 0.0008% of total fluid mass and is substituted with carboxymethyl cellulose (Tier 1 substitution) in the Ecoinvent database. Although fluid composition changes, the fluid characteristics that will affect energy consumption, etc. for hydraulic fracturing were assumed the same. Results of the LCA are shown in Table S16.

Comparison of Different LCA Scenarios

(1) Slickwater fracturing fluid.

Table S12: Base Case: LCA result with 3,800 ft lateral length and slickwater fracturing fluid.

Impact category	Unit	Well Construct-ion	Energy Fracking	Sand Transp-ortation	Flack Fluid	Fresh Water Transport	Waste-water Trans-port	Waste-water Injection
Ozone depletion	kg CFC-11 eq	0.0926	0.0215	0.0011	0.0096	0.0035	0.0133	0.0050
Global warming	kg CO2 eq	1,540,000	249,000	11,500	54,700	37,200	142,000	68,900

Smog	kg O3 eq	267,000	70,700	1,020	3,160	3,310	12600	3,930
Acidification	kg SO2 eq	10,100	2,260	44.5	339	145	550	423
Eutrophication	kg N eq	2,410	211	11.0	178	35.7	136	254
Carcinogenics	CTUh	0.212	0.0059	0.0005	0.0022	0.00155	0.0059	0.0027
Non carcinogenics	CTUh	0.247	0.0105	0.0021	0.0142	0.00695	0.0264	0.0115
Respiratory effects	kg PM2.5eq	1,660	311	5	40	1	63	80
Ecotoxicity	CTUe	6,650,000	221,000	68,000	360,000	221,000	841,000	269,000
Fossil fuel depletion	MJ surplus	1,940,000	491,000	23,600	125,000	76,700	292,000	53,400

Table S13: LCA result with 6,000 ft lateral length and slickwater fracturing fluid.

Impact category	Unit	Well Construct-ion	Energy Fracking	Sand Transp-ortation	Frack Fluid	Fresh Water Transport	Waste-water Trans-port	Waste-water Injection
Ozone depletion	kg CFC-11 eq	0.136	0.0426	0.0017	0.0154	0.0056	0.0213	0.0080
Global warming	kg CO2 eq	2,070,000	495,000	18,400	87,500	59,600	226,000	110,000
Smog	kg O3 eq	409,000	140,000	1,630	5,060	5,290	20,100	6,280
Acidification	kg SO2 eq	14,700	4,500	71	542	232	880	676
Eutrophication	kg N eq	2,920	419	18	285	57	217	406
Carcinogenics	CTUh	0.235	0.0118	0.0008	0.0035	0.0025	0.0094	0.0043
Non carcinogenics	CTUh	0.279	0.0208	0.0034	0.0228	0.0111	0.0423	0.0184
Respiratory effects	kg PM2.5eq	2,320	618	8	65	26	101	127
Ecotoxicity	CTUe	7,390,000	439,000	109,000	576,000	354,000	1,350,000	430,000
Fossil fuel depletion	MJ surplus	2,930,000	976,000	37,800	200,000	123,000	467,000	85,500

Table S14: LCA result with 3,800 ft lateral length and slickwater fracturing fluid, but with a wastewater to freshwater ratio of 0.7 used instead of the base case parameter of 1.9.

Impact category	Unit	Well Construct-ion	Energy Fracking	Sand Transp-ortation	Flack Fluid	Fresh Water Transport	Waste-water Trans-port	Waste-water Injection
Ozone depletion	kg CFC-11 eq	0.0926	0.0215	0.0011	0.0096	0.0035	0.0049	0.0018
Global warming	kg CO2 eq	1,540,000	249,000	11,500	54,700	37,200	52,100	25,400
Smog	kg O3 eq	267,000	70,700	1,020	3,160	3,310	4,630	1,450
Acidification	kg SO2 eq	10,100	2,260	44.5	339	145	203	156
Eutrophication	kg N eq	2,410	211	11.0	178	35.7	50	93
Carcinogenics	CTUh	0.212	0.0059	0.0005	0.0022	0.00155	0.0022	0.0010
Non carcinogenics	CTUh	0.247	0.0105	0.0021	0.0142	0.00695	0.0097	0.0042
Respiratory effects	kg PM2.5eq	1,660	311	5	40	1	23	29
Ecotoxicity	CTUe	6,650,000	221,000	68,000	360,000	221,000	310,000	99,000
Fossil fuel depletion	MJ surplus	1,940,000	491,000	23,600	125,000	76,700	107,000	20,000

Table S15: LCA result with 3,800 ft lateral length and slickwater fracturing fluid, but with a wastewater to freshwater ratio of 2.75 used instead of the base case parameter of 1.9.

Impact category	Unit	Well Construct-ion	Energy Fracking	Sand Transp-ortation	Flack Fluid	Fresh Water Transport	Waste-water Trans-port	Waste-water Injection
Ozone depletion	kg CFC-11 eq	0.0926	0.0215	0.0011	0.0096	0.0035	0.0192	0.0073
Global warming	kg CO2 eq	1,540,000	249,000	11,500	54,700	37,200	205,000	99,800

Smog	kg O3 eq	267,000	70,700	1,020	3,160	3,310	18,200	5,680
Acidification	kg SO2 eq	10,100	2,260	44.5	339	145	796	612
Eutrophication	kg N eq	2,410	211	11.0	178	35.7	196	367
Carcinogenics	CTUh	0.212	0.0059	0.0005	0.0022	0.00155	0.0085	0.0039
Non carcinogenics	CTUh	0.247	0.0105	0.0021	0.0142	0.00695	0.0382	0.0167
Respiratory effects	kg PM2.5eq	1,660	311	5	40	1	91	115
Ecotoxicity	CTUe	6,650,000	221,000	68,000	360,000	221,000	1,220,000	389,000
Fossil fuel depletion	MJ surplus	1,940,000	491,000	23,600	125,000	76,700	422,000	77,300

(2) Foam fracturing fluids

Table S16: LCA result with 3,800 ft lateral length and CO_2-foam fracturing fluid.

Impact category	Unit	Well Construc-tion	Energy Fracking	Sand Transp-ortation	Flack Fluid	Fresh Water Transport	Wastewater Transport	Waste-water Injection
Ozone depletion	kgCFC11eq	0.0926	0.0315	0.0011	0.0097	0.0003	0.0070	0.0026
Global warming	kg CO2 eq	1,540,000	366,000	11,500	55,300	3,720	74,500	36,300
Smog	kg O3 eq	267,000	104,000	1,020	3,200	331	6,610	2,070
Acidification	kg SO2 eq	10,100	3,330	45	342	14	290	222
Eutrophication	kg N eq	2,410	310	11	180	4	71	134
Carcinogenics	CTUh	0.212	0.0087	0.0005	0.0022	0.0002	0.0031	0.0014
Non carcinogenics	CTUh	0.247	0.0154	0.0021	0.0144	0.0007	0.0139	0.0061
Respiratory effects	kg PM2.5eq	1,660	457	5	41	2	33	42
Ecotoxicity	CTUe	6,640,000	325,000	68,200	364,000	22,100	443,000	141,000
Fossil fuel depletion	MJ surplus	1,940,000	722,000	23,600	126,000	7,670	153,000	28,100

Table S17: LCA result with 3,800 ft lateral length and CH_4-foam fracturing fluid.

Impact category	Unit	Well Construc-tion	Energy Fracking	Sand Transp-ortation	Flack Fluid	Fresh Water Transport	Wastewater Transport	Waste-water Injection
Ozone depletion	kgCFC11eq	0.0926	0.0241	0.0011	0.0097	0.0003	0.0070	0.0026
Global warming	kg CO2 eq	1,540,000	280,000	11,500	55,300	3,720	74,500	36,300
Smog	kg O3 eq	267,000	79,500	1,020	3,200	331	6,610	2,070
Acidification	kg SO2 eq	10,100	2,550	45	342	14	290	222

Eutrophication	kg N eq	2,410	237	11	180	4	71	134
Carcinogenics	CTUh	0.212	0.0067	0.0005	0.0022	0.0002	0.0031	0.0014
Non carcinogenics	CTUh	0.247	0.0118	0.0021	0.0144	0.0007	0.0139	0.0061
Respiratory effects	kg PM2.5eq	1,660	350	5	41	2	33	42
Ecotoxicity	CTUe	6,640,000	249,000	68,200	364,000	22,100	443,000	141,000
Fossil fuel depletion	MJ surplus	1,940,000	552,000	23,600	126,000	7,670	153,000	28,100

(3) Linear gel fracturing fluid

Table S18: LCA result with 3,800 ft lateral length and water-based linear gel fracturing fluid.

Impact category	Unit	Well Construction	Energy Fracking	Sand Transportation	Flack Fluid	Fresh Water Transport	Wastewater Transport	Wastewater Injection
Ozone depletion	kgCFC11eq	0.0926	0.0180	0.00107	0.00971	0.00350	0.0192	0.00725
Global warming	kg CO2 eq	1,540,000	209,000	11,400	55,300	37,200	204,000	99,700
Smog	kg O3 eq	267,000	59,200	1,020	3,200	3,310	18,100	5,680
Acidification	kg SO2 eq	10,100	1,900	44.5	342	145	794	611
Eutrophication	kg N eq	2,410	177	11.0	180	35.7	195	367
Carcinogenics	CTUh	0.212	0.00496	0.000476	0.00221	0.00155	0.00849	0.00389
Non carcinogenics	CTUh	0.247	0.00878	0.00214	0.0144	0.00695	0.0381	0.0167
Respiratory effects	kg PM2.5eq	1,660	261	5.08	40.8	16.5	90.6	115
Ecotoxicity	CTUe	6,650,000	185,000	68,000	364,000	221,000	1,210,000	388,000
Fossil fuel depletion	MJ surplus	1,940,000	412,000	23,600	126,000	76,700	421,000	77,300

Sensitivity Analysis

A sensitivity analysis on the variables listed in the Table S18 was conducted. Reasonable ranges of the variables were determined based on literature sources and our own calculations. We use the upper and lower values of each range to perform a sensitivity analysis, varying each parameter independently, and identify how uncertainty in each affects environmental impacts.

Table S19: Life cycle assessment software input parameters, with base case value for each parameter, along with upper and lower values used to perform the sensitivity analysis.

Parameter(s) of Interest	Range of Values	Comment

Freshwater transportation (TKM)	Base case value = 332,000 Lower Value = 166,000 Upper Value = 664,000	Base case value is determined from travel distances in the Argonne report[21]. Lower and upper values are half and double the base case value, and are determined using approximately the same relative range of freshwater travel distances assumed by Dale et al., 2013 in the Marcelus shale.
Wastewater transportation (TKM)	Base case value = 1,260,000 Lower value = 631,000 Upper value = 2,520,000	Base case value is determined from travel distances in the Argonne report[21]. Lower and upper values are half and double the base case value, and are approximately the same as the relative range of values determined for freshwater transportation.
Energy used to hydraulically fracture shale (Gallons diesel fuel)	Base case value = 19,500 Lower value = 17,500 Upper value = 21,400	Base case value is from the GHGfrack model simulation. Lower and upper values represent the same relative error used for the parameter in the next table row: i.e., Energy for well construction.
Energy for well construction (Gallons diesel fuel)	Base case value = 61,800 Lower value = 55,600 (-10%) Upper value = 67,900 (+10%)	Base case value is from the Argonne report[21]. Lower value is based on the energy for drilling and mud circulation from the GHGfrack model, which is 90% of the base case value. Upper

		value was selected with same percent difference.
Sand transportation (TKM)	Base case value = 102,000 Lower value =31,000 Upper value = 164,000	Base case value is the mean of five values for the five counties considered, based on closest sand vendor locations from county centroids. Lower and upper values are extreme values from the same data set.
Materials for well construction: Reinforced steel and cement dominate impacts (Metric tonnes)	Reinforced steel: Base case value = 163 Lower value = 121 Upper value = 205 Cement: Base case value = 267 Lower value = 199 Upper value = 335	Reinforced steel: Base case value is from the Argonne report[21]. Lower and upper values were obtained from an estimation of steel use assuming lower and upper wall thicknesses of possible production casing from API (API Specification 5CT / ISO 11960). Cement: Base case value is from the Argonne report[21]. Lower and upper values were obtained by using the same relative uncertainty obtained for reinforced steel.
Citric acid and acetic acid (iron control agents) Mass Fractions in Frac Fluid (kg)	Citric acid: Base case value = 968 Lower value = 0 Upper value = 3,110	Citric acid and acetic acid dominate the life cycle impacts of hydraulic fracturing chemicals (>50%) for various categories. Any other chemical has a much

	Acetic acid: Base case value = 329 Lower value = 0 Upper value = 1,080	smaller impact (<4%). The base case value is the mean from FracFocus well records. The lower value for both acids is 0, since more than half of the records don't have citric or acetic acid. The upper value represents one standard deviation from average, based on the FracFocus well records.

The maximum range of environmental impacts (i.e., sensitivities) from any upper and lower range of parameter values identified in Table S17 are shown in Figure S3, where the total and water related impacts are presented for each category, and the total impacts are scaled to 1, and the water related impacts are presented separately. The water related impacts come from hydraulic fracturing fluid components, freshwater and wastewater transportation, and wastewater disposal.

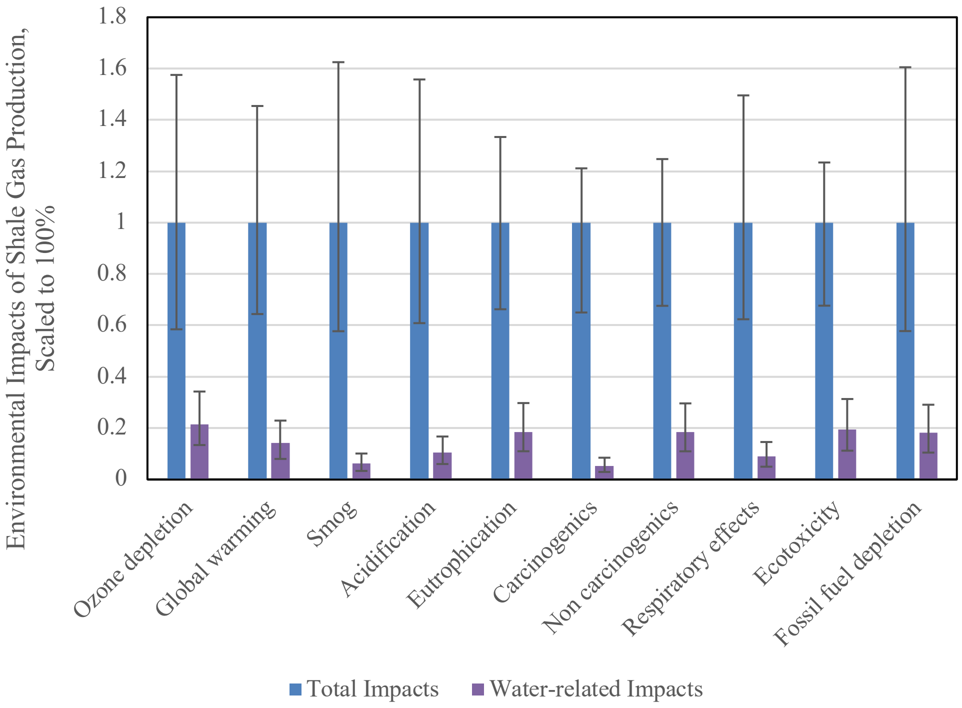

Figure S8. Maximum and minimum range of environmental impacts determined from a sensitivity analysis, where the upper and lower values of each parameter were separately evaluated in the life cycle assessment software.

Table S20: LCA result with base case parameters, except with lower freshwater transportation distance.

Impact category	Unit	Well Construc-tion	Energy Fracking	Sand Transportation	Flack Fluid	Fresh Water Transport	Wastewater Transport	Wastewater Injection
Ozone depletion	kgCFC11eq	0.0926	0.0215	0.0011	0.0096	0.0017	0.0133	0.0050
Global warming	kg CO2 eq	1,540,000	249,000	11,500	54,700	18,600	142,000	68,900
Smog	kg O3 eq	267,000	70,700	1,020	3,160	1,650	12600	3,930
Acidification	kg SO2 eq	10,100	2,260	44.5	339	72	550	423
Eutrophication	kg N eq	2,410	211	11.0	178	18	136	254
Carcinogenics	CTUh	0.212	0.0059	0.0005	0.0022	0.0008	0.0059	0.0027
Non carcinogenics	CTUh	0.247	0.0105	0.0021	0.0142	0.0035	0.0264	0.0115
Respiratory effects	kg PM2.5eq	1,660	311	5	40	8	63	80
Ecotoxicity	CTUe	6,640,000	221,000	68,000	360,000	111,000	841,000	269,000
Fossil fuel depletion	MJ surplus	1,940,000	491,000	23,600	125,000	38,400	292,000	53,400

Table S21: LCA result with base case parameters, except with upper freshwater transportation distance.

Impact category	Unit	Well Construc-tion	Energy Fracking	Sand Transportation	Flack Fluid	Fresh Water Transport	Wastewater Transport	Wastewater Injection

Ozone depletion	kgCFC11eq	0.0926	0.0215	0.0011	0.0096	0.0070	0.0133	0.0050
Global warming	kg CO2 eq	1,540,000	249,000	11,500	54,700	74,500	142,000	68,900
Smog	kg O3 eq	267,000	70,700	1,020	3,160	6,610	12600	3,930
Acidification	kg SO2 eq	10,100	2,260	44.5	339	290	550	423
Eutrophication	kg N eq	2,410	211	11.0	178	71	136	254
Carcinogenics	CTUh	0.212	0.0059	0.0005	0.0022	0.0031	0.0059	0.0027
Non carcinogenics	CTUh	0.247	0.0105	0.0021	0.0142	0.0139	0.0264	0.0115
Respiratory effects	kg PM2.5eq	1,660	311	5	40	33	63	80
Ecotoxicity	CTUe	6,640,000	221,000	68,000	360,000	443,000	841,000	269,000
Fossil fuel depletion	MJ surplus	1,940,000	491,000	23,600	125,000	153,000	292,000	53,400

Table S22: LCA result with base case parameters, except with lower wastewater transportation distance.

Impact category	Unit	Well Construc-tion	Energy Fracking	Sand Transp-ortation	Flack Fluid	Fresh Water Transport	Wastewater Transport	Waste-water Injection
Ozone depletion	kgCFC11eq	0.0926	0.0215	0.0011	0.0096	0.0035	0.0066	0.0050
Global warming	kg CO2 eq	1,540,000	249,000	11,500	54,700	37,200	70,800	68,900
Smog	kg O3 eq	267,000	70,700	1,020	3,160	3,310	6,280	3,930
Acidification	kg SO2 eq	10,100	2,260	44.5	339	145	275	423
Eutrophication	kg N eq	2,410	211	11.0	178	35.7	68	254
Carcinogenics	CTUh	0.212	0.0059	0.0005	0.0022	0.00155	0.0029	0.0027
Non carcinogenics	CTUh	0.247	0.0105	0.0021	0.0142	0.00695	0.0132	0.0115
Respiratory effects	kg PM2.5eq	1,660	311	5	40	1	31	80
Ecotoxicity	CTUe	6,640,000	221,000	68,000	360,000	221,000	421,000	269,000
Fossil fuel depletion	MJ surplus	1,940,000	491,000	23,600	125,000	76,700	146,000	53,400

Table S23: LCA result with base case parameters, except with upper wastewater transportation distance.

Impact category	Unit	Well Construc-tion	Energy Fracking	Sand Transp-ortation	Flack Fluid	Fresh Water Transport	Wastewater Transport	Waste-water Injection
Ozone depletion	kgCFC11eq	0.0926	0.0215	0.0011	0.0096	0.0035	0.0266	0.0050
Global warming	kg CO2 eq	1,540,000	249,000	11,500	54,700	37,200	283,000	68,900
Smog	kg O3 eq	267,000	70,700	1,020	3,160	3,310	25,100	3,930

Acidification	kg SO2 eq	10,100	2,260	44.5	339	145	1,100	423
Eutrophication	kg N eq	2,410	211	11.0	178	35.7	271	254
Carcinogenics	CTUh	0.212	0.0059	0.0005	0.0022	0.0155	0.0118	0.0027
Non carcinogenics	CTUh	0.247	0.0105	0.0021	0.0142	0.00695	0.0528	0.0115
Respiratory effects	kg PM2.5eq	1,660	311	5	40	1	126	80
Ecotoxicity	CTUe	6,640,000	221,000	68,000	360,000	221,000	1,680,000	269,000
Fossil fuel depletion	MJ surplus	1,940,000	491,000	23,600	125,000	76,700	583,000	53,400

Table S24: LCA result with base case parameters, except with lower energy for hydraulic fracturing.

Impact category	Unit	Well Construc-tion	Energy Fracking	Sand Transp-ortation	Flack Fluid	Fresh Water Transport	Wastewater Transport	Waste-water Injection
Ozone depletion	kgCFC11eq	0.0926	0.0193	0.0011	0.0096	0.0035	0.0133	0.0050
Global warming	kg CO2 eq	1,540,000	224,000	11,500	54,700	37,200	142,000	68,900
Smog	kg O3 eq	267,000	63,700	1,020	3,160	3,310	12600	3,930
Acidification	kg SO2 eq	10,100	2,040	44.5	339	145	550	423
Eutrophication	kg N eq	2,410	190	11.0	178	35.7	136	254
Carcinogenics	CTUh	0.212	0.0053	0.0005	0.0022	0.00155	0.0059	0.0027
Non carcinogenics	CTUh	0.247	0.0094	0.0021	0.0142	0.00695	0.0264	0.0115
Respiratory effects	kg PM2.5eq	1,660	280	5	40	1	63	80
Ecotoxicity	CTUe	6,640,000	199,000	68,000	360,000	221,000	841,000	269,000
Fossil fuel depletion	MJ surplus	1,940,000	442,000	23,600	125,000	76,700	292,000	53,400

Table S25: LCA result with base case parameters except with upper energy for hydraulic fracturing.

Impact category	Unit	Well Construc-tion	Energy Fracking	Sand Transp-ortation	Flack Fluid	Fresh Water Transport	Wastewater Transport	Waste-water Injection
Ozone depletion	kgCFC11eq	0.0926	0.0236	0.0011	0.0096	0.0035	0.0133	0.0050
Global warming	kg CO2 eq	1,540,000	274,000	11,500	54,700	37,200	142,000	68,900
Smog	kg O3 eq	267,000	77,800	1,020	3,160	3,310	12600	3,930
Acidification	kg SO2 eq	10,100	2,490	44.5	339	145	550	423

Eutrophication	kg N eq	2,410	232	11.0	178	35.7	136	254
Carcinogenics	CTUh	0.212	0.0065	0.0005	0.0022	0.00155	0.0059	0.0027
Non carcinogenics	CTUh	0.247	0.0115	0.0021	0.0142	0.00695	0.0264	0.0115
Respiratory effects	kg PM2.5eq	1,660	342	5	40	1	63	80
Ecotoxicity	CTUe	6,640,000	243,000	68,000	360,000	221,000	841,000	269,000
Fossil fuel depletion	MJ surplus	1,940,000	541,000	23,600	125,000	76,700	292,000	53,400

Table S26: LCA result with base case parameters, except with lower energy for well construction.

Impact category	Unit	Well Construc-tion	Energy Fracking	Sand Transp-ortation	Flack Fluid	Fresh Water Transport	Wastewater Transport	Waste-water Injection
Ozone depletion	kgCFC11eq	0.0858	0.0215	0.0011	0.0096	0.0035	0.0133	0.0050
Global warming	kg CO_2 eq	1,460,000	249,000	11,500	54,700	37,200	142,000	68,900
Smog	kg O_3 eq	245,000	70,700	1,020	3,160	3,310	12600	3,930
Acidification	kg SO_2 eq	9,410	2,260	44.5	339	145	550	423
Eutrophication	kg N eq	2,350	211	11.0	178	35.7	136	254
Carcinogenics	CTUh	0.2105	0.0059	0.0005	0.0022	0.00155	0.0059	0.0027
Non carcinogenics	CTUh	0.2437	0.0105	0.0021	0.0142	0.00695	0.0264	0.0115
Respiratory effects	kg PM2.5eq	1,570	311	5	40	1	63	80
Ecotoxicity	CTUe	6,570,000	221,000	68,000	360,000	221,000	841,000	269,000
Fossil fuel depletion	MJ surplus	1,780,000	491,000	23,600	125,000	76,700	292,000	53,400

Table S27: LCA result with base case parameters, except with upper energy for well construction.

Impact category	Unit	Well Construc-tion	Energy Fracking	Sand Transp-ortation	Flack Fluid	Fresh Water Transport	Wastewater Transport	Waste-water Injection
Ozone depletion	kgCFC11eq	0.0994	0.0215	0.0011	0.0096	0.0035	0.0133	0.0050
Global warming	kg CO_2 eq	1,620,000	249,000	11,500	54,700	37,200	142,000	68,900
Smog	kg O_3 eq	290,000	70,700	1,020	3,160	3,310	12600	3,930
Acidification	kg SO_2 eq	10,800	2,260	44.5	339	145	550	423

Eutrophication	kg N eq	2,480	211	11.0	178	35.7	136	254
Carcinogenics	CTUh	0.2142	0.0059	0.0005	0.0022	0.00155	0.0059	0.0027
Non carcinogenics	CTUh	0.2504	0.0105	0.0021	0.0142	0.00695	0.0264	0.0115
Respiratory effects	kg PM2.5eq	1,760	311	5	40	1	63	80
Ecotoxicity	CTUe	6,710,000	221,000	68,000	360,000	221,000	841,000	269,000
Fossil fuel depletion	MJ surplus	2,100,000	491,000	23,600	125,000	76,700	292,000	53,400

Table S28: LCA result with base case parameters, except with lower sand transportation distance.

Impact category	Unit	Well Construc-tion	Energy Fracking	Sand Transp-ortation	Flack Fluid	Fresh Water Transport	Wastewater Transport	Waste-water Injection
Ozone depletion	kgCFC11eq	0.0926	0.0215	0.0003	0.0096	0.0035	0.0133	0.0050
Global warming	kg CO2 eq	1,540,000	249,000	3,450	54,700	37,200	142,000	68,900
Smog	kg O3 eq	267,000	70,700	308	3,160	3,310	12600	3,930
Acidification	kg SO2 eq	10,100	2,260	14	339	145	550	423
Eutrophication	kg N eq	2,410	211	3	178	35.7	136	254
Carcinogenics	CTUh	0.212	0.0059	0.0001	0.0022	0.00155	0.0059	0.0027
Non carcinogenics	CTUh	0.247	0.0105	0.0006	0.0142	0.00695	0.0264	0.0115
Respiratory effects	kg PM2.5eq	1,660	311	2	40	1	63	80
Ecotoxicity	CTUe	6,640,000	221,000	20,700	360,000	221,000	841,000	269,000
Fossil fuel depletion	MJ surplus	1,940,000	491,000	7,160	125,000	76,700	292,000	53,400

Table S29: LCA result with base case parameters, except with upper sand transportation distance.

Impact category	Unit	Well Construc-tion	Energy Fracking	Sand Transp-ortation	Flack Fluid	Fresh Water Transport	Wastewater Transport	Waste-water Injection
Ozone depletion	kgCFC11eq	0.0926	0.0215	0.0017	0.0096	0.0035	0.0133	0.0050
Global warming	kg CO2 eq	1,540,000	249,000	18,400	54,700	37,200	142,000	68,900
Smog	kg O3 eq	267,000	70,700	1,630	3,160	3,310	12600	3,930
Acidification	kg SO2 eq	10,100	2,260	72	339	145	550	423

Eutrophication	kg N eq	2,410	211	18	178	35.7	136	254
Carcinogenics	CTUh	0.212	0.0059	0.0008	0.0022	0.0155	0.0059	0.0027
Non carcinogenics	CTUh	0.247	0.0105	0.0034	0.0142	0.0695	0.0264	0.0115
Respiratory effects	kg PM2.5eq	1,660	311	8	40	1	63	80
Ecotoxicity	CTUe	6,640,000	221,000	109,000	360,000	221,000	841,000	269,000
Fossil fuel depletion	MJ surplus	1,940,000	491,000	37,900	125,000	76,700	292,000	53,400

Table S30: LCA result with base case parameters, except with lower citric acid amount in hydraulic fracturing fluid.

Impact category	Unit	Well Construc-tion	Energy Fracking	Sand Transp-ortation	Flack Fluid	Fresh Water Transport	Wastewater Transport	Waste-water Injection
Ozone depletion	kgCFC11eq	0.0926	0.0215	0.0011	0.0043	0.0035	0.0133	0.0050
Global warming	kg CO2 eq	1,540,000	249,000	11,500	27,600	37,200	142,000	68,900
Smog	kg O3 eq	267,000	70,700	1,020	1,320	3,310	12600	3,930
Acidification	kg SO2 eq	10,100	2,260	44.5	142	145	550	423
Eutrophication	kg N eq	2,410	211	11.0	82	35.7	136	254
Carcinogenics	CTUh	0.212	0.0059	0.0005	0.0009	0.00155	0.0059	0.0027
Non carcinogenics	CTUh	0.247	0.0105	0.0021	0.0060	0.00695	0.0264	0.0115
Respiratory effects	kg PM2.5eq	1,660	311	5	17	1	63	80
Ecotoxicity	CTUe	6,640,000	221,000	68,000	152,000	221,000	841,000	269,000
Fossil fuel depletion	MJ surplus	1,940,000	491,000	23,600	106,000	76,700	292,000	53,400

Table S31: LCA result with base case parameters, except with upper citric acid amount in hydraulic fracturing fluid.

Impact category	Unit	Well Construc-tion	Energy Fracking	Sand Transp-ortation	Flack Fluid	Fresh Water Transport	Wastewater Transport	Waste-water Injection
Ozone depletion	kgCFC11eq	0.0926	0.0215	0.0011	0.0213	0.0035	0.0133	0.0050
Global warming	kg CO2 eq	1,540,000	249,000	11,500	115,000	37,200	142,000	68,900
Smog	kg O3 eq	267,000	70,700	1,020	7,230	3,310	12600	3,930

Acidification	kg SO2 eq	10,100	2,260	44.5	775	145	550	423
Eutrophication	kg N eq	2,410	211	11.0	390	35.7	136	254
Carcinogenics	CTUh	0.212	0.0059	0.0005	0.0049	0.00155	0.0059	0.0027
Non carcinogenics	CTUh	0.247	0.0105	0.0021	0.0325	0.00695	0.0264	0.0115
Respiratory effects	kg PM2.5eq	1,660	311	5	92	1	63	80
Ecotoxicity	CTUe	6,640,000	221,000	68,000	820,000	221,000	841,000	269,000
Fossil fuel depletion	MJ surplus	1,940,000	491,000	23,600	167,000	76,700	292,000	53,400

Table S32: LCA result with base case parameters, except with lower acetic acid amount in hydraulic fracturing fluid.

Impact category	Unit	Well Construc-tion	Energy Fracking	Sand Transp-ortation	Flack Fluid	Fresh Water Transport	Wastewater Transport	Waste-water Injection
Ozone depletion	kgCFC11eq	0.0926	0.0215	0.0011	0.0095	0.0035	0.0133	0.0050
Global warming	kg CO2 eq	1,540,000	249,000	11,500	54,100	37,200	142,000	68,900
Smog	kg O3 eq	267,000	70,700	1,020	3,130	3,310	12600	3,930
Acidification	kg SO2 eq	10,100	2,260	44.5	335	145	550	423
Eutrophication	kg N eq	2,410	211	11.0	176	35.7	136	254
Carcinogenics	CTUh	0.212	0.0059	0.0005	0.0022	0.00155	0.0059	0.0027
Non carcinogenics	CTUh	0.247	0.0105	0.0021	0.0141	0.00695	0.0264	0.0115
Respiratory effects	kg PM2.5eq	1,660	311	5	40	1	63	80
Ecotoxicity	CTUe	6,640,000	221,000	68,000	356,000	221,000	841,000	269,000
Fossil fuel depletion	MJ surplus	1,940,000	491,000	23,600	124,000	76,700	292,000	53,400

Table S33: LCA result with base case parameters, except with upper acetic acid amount in hydraulic fracturing fluid.

Impact category	Unit	Well Construc-tion	Energy Fracking	Sand Transp-ortation	Flack Fluid	Fresh Water Transport	Wastewater Transport	Waste-water Injection
Ozone depletion	kgCFC11eq	0.0926	0.0215	0.0011	0.0098	0.0035	0.0133	0.0050
Global warming	kg CO2 eq	1,540,000	249,000	11,500	56,000	37,200	142,000	68,900
Smog	kg O3 eq	267,000	70,700	1,020	3,230	3,310	12600	3,930

Acidification	kg SO2 eq	10,100	2,260	44.5	348	145	550	423
Eutrophication	kg N eq	2,410	211	11.0	182	35.7	136	254
Carcinogenics	CTUh	0.212	0.0059	0.0005	0.0022	0.00155	0.0059	0.0027
Non carcinogenics	CTUh	0.247	0.0105	0.0021	0.0146	0.00695	0.0264	0.0115
Respiratory effects	kg PM2.5eq	1,660	311	5	41	1	63	80
Ecotoxicity	CTUe	6,640,000	221,000	68,000	370,000	221,000	841,000	269,000
Fossil fuel depletion	MJ surplus	1,940,000	491,000	23,600	129,000	76,700	292,000	53,400

Table S34: LCA result with base case parameters, except with lower steel amount for well construction.

Impact category	Unit	Well Construc-tion	Energy Fracking	Sand Transp-ortation	Flack Fluid	Fresh Water Transport	Wastewater Transport	Waste-water Injection
Ozone depletion	kgCFC11eq	0.0880	0.0215	0.0011	0.0096	0.0035	0.0133	0.0050
Global warming	kg CO2 eq	1,440,000	249,000	11,500	54,700	37,200	142,000	68,900
Smog	kg O3 eq	261,000	70,700	1,020	3,160	3,310	12600	3,930
Acidification	kg SO2 eq	9,640	2,260	44.5	339	145	550	423
Eutrophication	kg N eq	2,040	211	11.0	178	35.7	136	254
Carcinogenics	CTUh	0.1634	0.0059	0.0005	0.0022	0.00155	0.0059	0.0027
Non carcinogenics	CTUh	0.1973	0.0105	0.0021	0.0142	0.00695	0.0264	0.0115
Respiratory effects	kg PM2.5eq	1,520	311	5	40	1	63	80
Ecotoxicity	CTUe	5,230,000	221,000	68,000	360,000	221,000	841,000	269,000
Fossil fuel depletion	MJ surplus	1,880,000	491,000	23,600	125,000	76,700	292,000	53,400

Table S35: LCA result with base case parameters, except with upper steel amount for well construction.

Impact category	Unit	Well Construc-tion	Energy Fracking	Sand Transp-ortation	Flack Fluid	Fresh Water Transport	Wastewater Transport	Waste-water Injection
Ozone depletion	kgCFC11eq	0.0972	0.0215	0.0011	0.0096	0.0035	0.0133	0.0050
Global warming	kg CO2 eq	1,650,000	249,000	11,500	54,700	37,200	142,000	68,900
Smog	kg O3 eq	274,000	70,700	1,020	3,160	3,310	12600	3,930

Acidification	kg SO2 eq	10,600	2,260	44.5	339	145	550	423
Eutrophication	kg N eq	2,790	211	11.0	178	35.7	136	254
Carcinogenics	CTUh	0.2613	0.0059	0.0005	0.0022	0.00155	0.0059	0.0027
Non carcinogenics	CTUh	0.2968	0.0105	0.0021	0.0142	0.00695	0.0264	0.0115
Respiratory effects	kg PM2.5eq	1,810	311	5	40	1	63	80
Ecotoxicity	CTUe	8,060,000	221,000	68,000	360,000	221,000	841,000	269,000
Fossil fuel depletion	MJ surplus	2,000,000	491,000	23,600	125,000	76,700	292,000	53,400

Table S36: LCA result with base case parameters, except with lower cement amount for well construction.

Impact category	Unit	Well Construc-tion	Energy Fracking	Sand Transp-ortation	Flack Fluid	Fresh Water Transport	Wastewater Transport	Waste-water Injection
Ozone depletion	kgCFC11eq	0.0911	0.0215	0.0011	0.0096	0.0035	0.0133	0.0050
Global warming	kg CO2 eq	1,460,000	249,000	11,500	54,700	37,200	142,000	68,900
Smog	kg O3 eq	263,000	70,700	1,020	3,160	3,310	12600	3,930
Acidification	kg SO2 eq	9,870	2,260	44.5	339	145	550	423
Eutrophication	kg N eq	2,350	211	11.0	178	35.7	136	254
Carcinogenics	CTUh	0.2115	0.0059	0.0005	0.0022	0.00155	0.0059	0.0027
Non carcinogenics	CTUh	0.2411	0.0105	0.0021	0.0142	0.00695	0.0264	0.0115
Respiratory effects	kg PM2.5eq	1,640	311	5	40	1	63	80
Ecotoxicity	CTUe	6,560,000	221,000	68,000	360,000	221,000	841,000	269,000
Fossil fuel depletion	MJ surplus	1,910,000	491,000	23,600	125,000	76,700	292,000	53,400

Table S37: LCA result with base case parameters, except with upper cement amount for well construction.

Impact category	Unit	Well Construc-tion	Energy Fracking	Sand Transp-ortation	Flack Fluid	Fresh Water Transport	Wastewater Transport	Waste-water Injection
Ozone depletion	kgCFC11eq	0.0941	0.0215	0.0011	0.0096	0.0035	0.0133	0.0050
Global warming	kg CO2 eq	1,630,000	249,000	11,500	54,700	37,200	142,000	68,900
Smog	kg O3 eq	271,000	70,700	1,020	3,160	3,310	12600	3,930

Acidification	kg SO2 eq	10,400	2,260	44.5	339	145	550	423
Eutrophication	kg N eq	2,470	211	11.0	178	35.7	136	254
Carcinogenics	CTUh	0.2132	0.0059	0.0005	0.0022	0.00155	0.0059	0.0027
Non carcinogenics	CTUh	0.2530	0.0105	0.0021	0.0142	0.00695	0.0264	0.0115
Respiratory effects	kg PM2.5eq	1,690	311	5	40	1	63	80
Ecotoxicity	CTUe	6,730,000	221,000	68,000	360,000	221,000	841,000	269,000
Fossil fuel depletion	MJ surplus	1,970,000	491,000	23,600	125,000	76,700	292,000	53,400

Reference

(1) FracFocus Chemical Disclosure Registry https://fracfocus.org/ (accessed Dec 2, 2017).

(2) Barnett Shale - Barnett Shale Oil & Gas Field - Texas Shale http://oilshalegas.com/barnettshale.html (accessed Dec 2, 2017).

(3) Fink, J. K. *Hydraulic Fracturing Chemicals and Fluids Technology*; 2013.

(4) Nicot, J.-P.; Scanlon, B. R.; Reedy, R. C.; Costley, R. A. Source and Fate of Hydraulic Fracturing Water in the Barnett Shale: A Historical Perspective. *Environ. Sci. Technol.* **2014**, *48* (4), 2464–2471.

(5) Freyman, M. Hydraulic Fracturing & Water Stress : Water Demand by the Numbers. *Ceres* **2014**, No. February, 85.

(6) Fipps, G. Calculating Horsepower Requirements and Sizing Irrigation Supply Pipelines. **1995**.

(7) Holloway, M. D.; Rudd, O. *Fracking: The Operations and Environmental Consequences of Hydraulic Fracturing*; John Wiley & Sons, 2013.

(8) Nicot, J.-P.; Scanlon, B. R. Water Use for Shale-Gas Production in Texas, US. *Environ. Sci. Technol.* **2012**, *46* (6), 3580–3586.

(9) Smith, M. B.; March, J. *March's Advanced Organic Chemistry: Reactions, Mechanisms, and Structure*; John Wiley & Sons, 2007.

(10) Elvers, B.; Hawkins, S.; Russey, W. *Ullmann's Encyclopedia of Industrial Chemistry*; Wiley Online Library, 1989.

(11) Schneider, H. J. One Step Synthesis of Vinyl Ethers and Vinyl Sulfides. Google Patents 1962.

(12) Billmeyer, F. W. Textbook of Polymer Science. **1971**.

(13) Kersten, H.; Meyer, G. Process for the Production of Thiourea. Google Patents 1974.

(14) Güthner, T.; Mertschenk, B. Cyanamides. In *Ullmann's Encyclopedia of Industrial Chemistry*; Wiley-VCH Verlag GmbH & Co. KGaA, 2000.

(15) Siegel, H.; Eggersdorfer, M. Ketones. *Ullmann's Encycl. Ind. Chem.* **2000**.

(16) Brazdil, J. F. Acrylonitrile. Ullmann's Encyclopedia of Industrial Chemistry. Weinheim: Wiley-VCH 2005.

(17) HERA, H. Environmental Risk Assessment on Ingredients of European Household Cleaning Products: Alcohol Ethoxylates. 2009.

(18) Tong, S.; Singh, R.; Mohanty, K. K. Proppant Transport in Fractures with Foam-Based Fracturing Fluids. *SPE Annu. Tech. Conf. Exhib.* **2017**, No. October, 9–11.

(19) Energy, U. department of. *Annual Energy Outlook 2016*; 2016.

(20) Vafi, K.; Brandt, A. GHGfrack: An Open-Source Model for Estimating Greenhouse Gas Emissions from Combustion of Fuel during Drilling and Hydraulic Fracturing. *Environ. Sci. Technol.* **2016**, *50* (14), 7913–7920.

(21) Clark, C. E.; Han, J.; Burnham, A.; Dunn, J. B.; Wang, M. *Life-Cycle Analysis of Shale Gas and Natural Gas.*; 2012.

(22) Hayden, J.; Pursell, D. The Barnett Shale: Visitors Guide to the Hottest Gas Play in the US. *Pick. Energy Partners* **2005**.

(23) James G. Speight. *Deep Shale Oil and GaS*; 2016.

(24) Travis Vulgamore, Steve Wolhart, Mike Mayerhofer, T. C. and C. P. Hydraulic Fracture Diagnostics Help Optimize Stimulations Of Woodford Shale Horizontals. *The American Oil & Gas Reporter*. 2008.

(25) Bowker, K. A. Barnett Shale Gas Production, Fort Worth Basin: Issues and Discussion. *Am. Assoc. Pet. Geol. Bull.* **2007**, *91* (4), 523–533.

(26) Avallone, E. A.; Baumeister, I. T.; Sadegh, A. *Marks' Standard Handbook for Mechanical*

Engineers. 10; New York: McGraw-Hill, 2006.

SECTION D: Presentation of major findings on the effects of surfactant adsorption on calcite dissolution at reservoir pressure and temperature

Effect of Sulfonate Group Surfactants on Dissolution of Calcite under Reservoir Conditions: A Combined Experimental and DFT Study

Abstract:

Direct injection of carbon dioxide (CO2) into deep geological reservoirs creates acidic brines near well bores that can promote dissolution of carbonate minerals, altering pore space geometry and geomechanical integrity. This is considered a major obstacle for successful geological carbon sequestration (GCS). In this study, the effects of an anionic surfactant (i.e., internal olefin sulfonate (IOS C15-18)) on calcite dissolution in simulated reservoir brine was investigated in a high pressure and temperature batch reactor, and complemented with density functional theory (DFT) calculations. The reservoir brine was either saturated with carbonic acid ($H_2CO_3^*$), adjusted to the same pH with HCl, or set at circumneutral pH. Results from batch experiments show that $H_2CO_3^*$ or H_2O driven dissolution is strongly inhibited by the presence IOS, while H+ driven dissolution is not. Examination of etch pit morphology using laser profilometry shows IOS preferentially inhibits dissolution of obtuse edges in etch pits for H+ and H2O driven dissolution, compared to acute edges. They also show that IOS more uniformly inhibits etch pit growth at all edge and kink sites for $H_2CO_3^*$ driven dissolution. DFT results indicate that the binding energies of IOS to calcite terrace, obtuse edge, and three calcium kink (i.e., acute-acute, obtuse-obtuse, acute-obtuse) sites are much more favorable than binding energies of $H_2CO_3^*$, H^+, or H_2O at these same locations, but less so at acute edge sites. This at least partially explains why the growth of calcite etch pits are preferentially inhibited by IOS along obtuse edge sites for H^+ or H_2O driven dissolution. DFT results also indicate that both IOS and $H_2CO_3^*$ preferentially bind to surface Ca, while H2O binds to both surface Ca and CO3 and H+ preferentially bind to surface CO3. This can explain why IOS

has little effect on H+ driven dissolution, and appears to completely inhibit $H_2CO_3^*$ driven dissolution. This study sheds light on calcite dissolution mechanisms, and suggests the role that additives can play in inhibiting carbonate mineral dissolution during GCS to mitigate pore space alteration and geomechanical integrity loss.

1. Introduction

The effects of anionic surfactant adsorption on calcite dissolution at ambient temperature and pressure was evaluated in our paper published in *Colloids and Surfaces A*, and presented in Section B. The surfactant was internal olefin sulfonate (IOS) C15-18. It was added to nanopure water amended with 0.4M KCl and adjusted with KOH to pH > 6. Both shale and calcite pieces were then placed in this brine solution to promote dissolution. Calcite was the primary component of shale that underwent dissolution, and experiments with pure calcite showed etch pits with acute and obtuse edges and terraces were formed (e.g., **Figure 1**). The primary findings were that weak IOS adsorption on flat calcite surfaces (i.e., terraces) disrupts water structure and enhances mass transfer of dissolution, while strong IOS adsorption on calcite pit edges displaces adsorbed water and inhibits further etch pit growth. The work in this section builds on these findings by exploring the mechanisms of calcite dissolution at reservoir temperature and pressure.

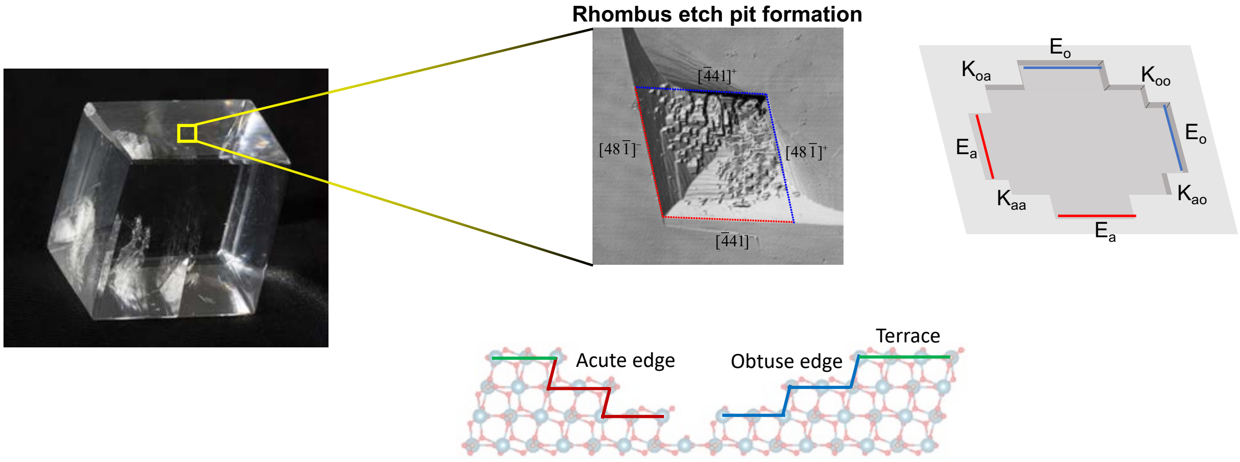

Figure 1. Image of calcite crystal and a corresponding dissolution etch pit that forms, along with simple and atomistic illustrations of different calcite binding sites in the etch pit (e.g., acute edge = E_a, obtuse edge = E_o, acute-acute vertex or kink = K_{aa}, obtuse-obtuse vertex or kink = K_{oo}, acute-obtuse vertex or kink = K_{ao}/K_{oa}).

Calcite dissolution kinetic has been successfully described by the following rate expression:

$$R = k_1 a_{H^+} + k_2 a_{H_2CO_3^*} + k_3 a_{H_2O} - k_4 a_{Ca^{2+}} a_{HCO_3^-} \qquad (1)$$

Here, k_1, k_2, and k_3 are rate constants of dissolution promoted by protons (H^+), carbonic acid ($H_2CO_3^*$), and water (H_2O), respectively, while k_4 is a rate constant of precipitation promoted by calcium (Ca^{2+}) and bicarbonate (HCO_3^-) ions. Values of a_i represent activities, which are equal to concentrations multiplied by activity coefficients. In our prior work at room temperature and pressure (Section B), and near circumneutral pH, calcite dissolution kinetics was controlled only by the activity of water (i.e., $k_3 a_{H_2O}$). It was not possible under these conditions to evaluate dissolution kinetics under the control of $H_2CO_3^*$, which can be a common condition when supercritical CO2 is being used for enhanced oil recovery or being stored in a geological reservoir.

The goal of work presented in this section is to determine the effects IOS adsorption on calcite dissolution kinetics controlled by each of the three dissolution terms individually at reservoir temperature and pressure. Calcite dissolution experiments without and with IOS were performed in brine either saturated with supercritical CO_2, saturated with N_2 but adjusted with HCl to reach the same acidity, or saturated with N_2 at circumneutral pH. These three conditions result in experiments with the calcite dissolution rate (R) dominated by $k_2 a_{H_2CO_3^*}$, $k_1 a_{H^+}$, or $k_3 a_{H_2O}$, respectively. Laser profilometry was used to evaluate etch pit formation in calcite samples after dissolution in the aforementioned brines without and with IOS present. Dislocation theory was used to compare interfacial energy barriers to dissolution. Density functional theory was used to calculate binding energies for IOS, $H_2CO_3^*$, H^+, and H_2O to different calcite surface binding sites, and the results are used to interpret the experiments.

2. Methods

2.1.Materials

KCl (99%, Aldrich®) was used to prepare a brine. HCl (1M, 99.99%, Aldrich®) was used to adjust the pH of the brine. HNO_3 (70%, TraceMetal grade, Fisher Scientific) was used to prepare samples for elemental analysis. Internal olefin sulfonate C15-18 (30.1%, Shell Oil Company), hereafter referred to as IOS, was used as a dissolution inhibitor. The structure of IOS C15 is shown in Figure 2. Ultrapure water with a resistivity of 18.2 MΩ·cm produced by Barnstead Nanopure (Model 7143, Thermo Scientific) was used to prepare all solutions. Optical quality calcite was purchased from Ward's Science.

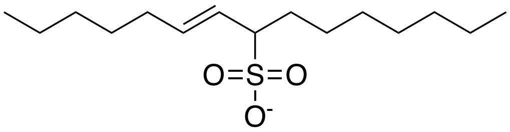

Figure 2. Representative structure of IOS (C15)

2.2.High-pressure high-temperature reactor setup

High-pressure and high-temperature experiments were carried out using a custom-built 20 mL cylindrical shape stainless steel reactor wrapped in heating tape and operated at 1300 psi and 50 °C. The pressure and temperature were controlled using the TELEDYNE ISCO D Series controller and the software package LabVIEW, respectively. The reactor has two sapphire windows (Figure 3) and is equipped with four ports for i) brine transfer ii) effluent sampling, iii) gas transfer to maintain pressure, and iv) a thermocouple. To avoid reactor corrosion induced by acidic brine with a high Cl- concentration, functionalized silica-like coating (Dursan®) was applied to all reactor parts made of stainless steel (i.e., reactor, connections, tubings) via chemical vapor deposition, and it was performed by the commercial company, SilcoTek®.

2.3.Experimental Conditions and dissolution experiments

Dissolution experiments were performed with either carbonic acid, protons, or water controlling dissolution, and without or with IOS (Table 1). To estimate the forward dissolution rate of each driving species, activities were calculated using a geochemical modeling program PHREEQC version 3 (Parkhurst & Appelo, 2013), and the kinetic constant for each species was calculated using reported values (Plummer et al., 1978). Detailed PHREEQC calculations are provided in a later section. When carbonic acid controls dissolution, brine was saturated with CO_2. When protons control dissolution, the brine is pH adjusted with HCl and pressurized with N_2 gas without CO_2. When water controls dissolution, the brine is initially pressurized with N_2 without CO_2 at circumneutral pH. Pressure and temperature were set to 1300 psi and 50 °C for all three cases, respectively. The concentration of IOS was 100 mg/L for all three cases, which was characterized as a critical micelle concentration (CMC) in our previous work(Kim et al., 2021; Zeng et al., 2020).

IOS solution was prepared with caution to prevent altering alkalinity when adding IOS. For all experiments, the IOS stock solution was freshly prepared and diluted to 15,000 mg/L. Subsequently, pH was reduced to 4.3 by adding an appropriate amount of HCl, and sonication and vacuum were applied to degas dissolved CO2 until no gas evolution was apparent. Lastly, the pH of the solution was adjusted to 7 by adding 0.1M KOH, and the volume of acid and base added was compensated. This dissolved carbonate species removal was essential in preparing IOS solutions because the IOS stock solution was kept at high pH (~14) for the stability of IOS molecules and contains very high alkalinity. Extra caution was taken to prevent any further confusion due to the addition of an unknown amount of carbonate species to experimental solutions.

Table 1. Calculated values of each term in Equation 1 using Phreeqc.

	pH	**Gas (Pressure/Temperature)**	$\mathbf{k_1a_{H+}}$	$\mathbf{k_2a_{H2CO3*}}$	$\mathbf{k_3a_{H2O}}$
$\mathbf{H_2CO_3^*}$	3.11	CO_2 (1300 psi/ 50 °C)	5.18E-05	1.27E-04	3.23E-07
$\mathbf{H^+}$	3.11	N_2 (1300 psi/ 50 °C)	5.18E-05	0.00E+00	3.28E-07
$\mathbf{H_2O}$	7	N_2 (1300 psi/ 50 °C)	6.65E-09	0.00E+00	3.28E-07

For each experiment, a freshly cleaved calcite slab sample was first placed in the reactor without brine. The reactor will then be pressurized with CO_2 or N_2 at 1300 psi and heated to 50 ˚C. Brine with or without IOS was pre-heated and pre-saturated with either CO_2 or N_2 for 3 days in the pre-saturation vessel at the experimental pressure and temperature, and then transferred to the reactor. Just before starting experiments, the pressure of the pre-saturation vessel was slightly increased to 1325 psi to induce a pressure difference between the pre-saturation vessel and the custom reactor. The saturated brine was then transferred to the reactor vessel by opening a valve, and this initiated experiments. The purpose of using the pre-saturation vessel is to avoid inconsistent results associated with fluid preparation, because the formation of carbonic acid is reported to be very slow and sensitive to temperature. In addition, this approach enables us to initiate dissolution at a constant temperature of 50 ˚C. All experiments were performed in duplicate for assessment of accuracy and precision.

Approximately 200 μL of brine samples were collected through a backpressure regulator during dissolution at 0.5, 1, 3, 6, 12, 24, 48 hrs. The dissolved Ca concentration in brine was measured to monitor calcite dissolution, and corresponding saturation state of each sample was calculated using PHREEQC. Elemental analysis was performed using a Varian 710-ES inductively coupled plasma optical emissions spectroscopy (ICP-OES) instrument. Approximately 100 μL out of 200 µL of each collected brine sample was diluted into 9.9 mL of ultra-pure water mixed with 200 µL of concentrated nitric acid and then analyzed for Ca. When the reaction was terminated, cleaved calcite samples were collected and dried by blowing ultrapure N_2 gas, and surface etch pits were evaluated using a laser profilometer.

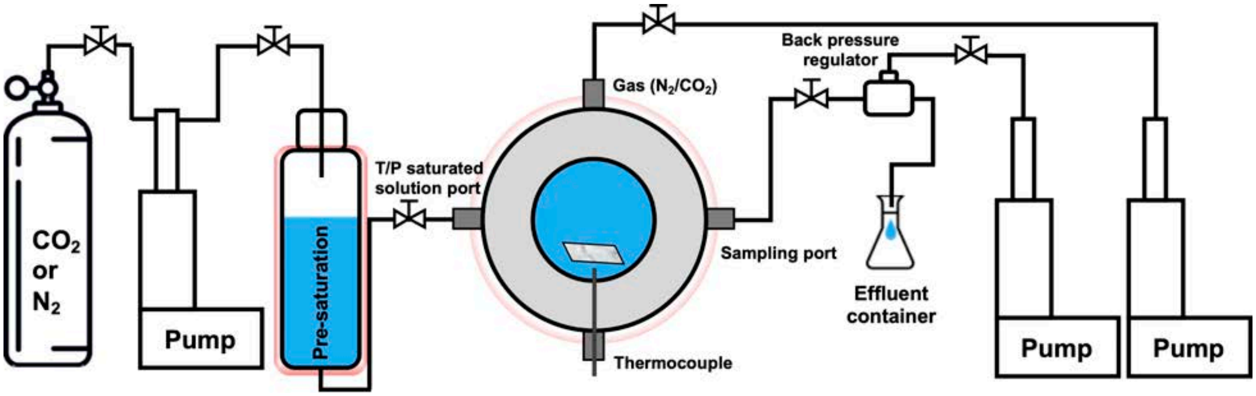

Figure 3. High-pressure high-temperature experimental setup

2.4.Laser profilometer

A laser scanning confocal microscope, Keyence VK-1100 laser profilometer, was used to investigate surface profile of samples after dissolution experiments. A 211×281 μm^2 was scanned for all samples using 50 x lens with a measuring resolution of 0.5 nm. Two acute edges were oriented toward lower left corner on the surface profile image for better comparison between samples. The depth and area of each pit were measured by referencing the nearby flat surface after the reference plain setting was completed with a relatively flat surface.

2.5.Density Functional Theory Calculations

Density Functional Theory (DFT) calculations based on the Generalized Gradient Approximation (GGA) were performed using the Vienna Ab initio Simulation Package (VASP). A plane wave basis set was used with an energy cutoff of 300 eV and a Gaussian smearing at the Fermi level with a width of 0.05 eV to improve convergence. The Perdew–Burke–Ernzerhof (PBE) functional was used to describe electron exchange and correlation (Perdew et al., 1996). The

Brillouin zone was sampled at the Γ-point. The plane-wave cutoff energy was set to 300 eV. The convergence criteria for electronic and geometric optimization were 10^{-6} eV and 0.01 eV/Å, respectively. To consider (implicit) solvent interactions, the VASPsol was used with a relative permittivity of 78.4 to mimic water.

A calcite$\{10\bar{1}4\}$ slab model of three molecular layers with a 10 Å thick vacuum layer was first prepared using a reference unit cell. An appropriate portion of Ca and CO_3 was removed from the top surface to build surfaces with defects including acute, obtuse edges, and acute-acute, acute-obtuse, and obtuse-obtuse kinks. Only Ca kink sites will be considered, because IOS is attracted by electrostatic force to positively charged Ca. All atoms in the bottom molecular calcite layer were fixed, and the top two molecular layers were allowed to relax during the adsorption reaction. Model IOS molecule had a total of 10 carbon atoms in the hydrocarbon chains, and a deprotonated form of IOS was used since sulfonic acid is a strong acid. IOS or one of the dissolution promotors (H^+, H_2O, and H_2CO_3) were then placed approximately 2~3 Å away from the defect sites and allowed to relax. The adsorption energies (E_{ad}) of each molecule were calculated based on the optimized structures using the following equation 2.

$$E_{ad} = E_{molecule-calcite} - E_{calcite} - E_{molecule} \quad (1)$$

Here, E_{ad} is the adsorption energy of an adsorbate on the calcite surface, $E_{molecule\text{-}calcite}$ is the total energy of the calcite model with adsorbate, $E_{calcite}$ and $E_{molecule}$ are the energy of the calcite model, and energy of the adsorbate (i.e., IOS, H^+, H_2O, and H_2CO_3), respectively.

2.6.Geochemical modeling

Geochemical modeling was performed using PHREEQC (Parkhurst & Appelo, 2013). The *pitzer.dat* database was used for thermodynamic data. PHREEQC can calculate the fugacity coefficient with the Peng-Robinson equation of state from the critical pressure and temperature providing a more reliable calculation under the condition we encounter under the reservoir (Anabaraonye et al., 2019). Activities of three dissolution promotors (i.e., H^+, H_2O, and $H_2CO_3^*$) corresponding to each experimental condition listed in section 2.3 are calculated first to determine dominating promotors in the solution.

3. Results and Discussion

3.1. Dissolution kinetics of calcite under different chemical environments

The effect of 100 mg/L (CMC) of IOS on calcite dissolution was evaluated under three different chemical environments listed in Table 1, and the results are shown in Figure 4. The brine solutions for each case are at far from equilibrium where no dissolved Ca exists, and cleaved calcite started to dissolve and released Ca. When dominated by $H_2CO_3^*$ with no IOS present, dissolved Ca concentration reached approximately 25 mM, whereas when dominated by H+ and H2O, dissolved Ca reached 1 mM and 0.5 mM, respectively. As calculated from PHREEQC, the equilibrium concentration of Ca for the $H_2CO_3^*$ dominating system is 28.5 mM due to higher pCO2 compared to H^+ and H_2O dominating conditions. In the open condition, the activity of $H_2CO_3^*$ is constant for all pH, and at elevated pCO_2, the lower equilibrium pH ~5 results in lower carbonate concentration when the solution is in equilibrium with respect to calcite. Thus, the contribution of Ca^{2+} to ion activity product is much higher compared to H^+ and H_2O dominating systems, where the estimated equilibrium pH is 8, and 9, respectively.

When IOS was added to brine at the CMC, effective inhibition was observed for $H_2CO_3^*$ and H_2O dominating conditions, whereas no significant inhibition was observed for H^+ dominating conditions. For $H_2CO_3^*$ driven dissolution with IOS, the rate of dissolution was significantly suppressed by IOS. After 48 hours, the dissolution rate decreased but had not reached apparent equilibrium for both cases. This selective inhibitory effect led us to conclude that IOS hinders the approach of $H_2CO_3^*$ and H_2O to calcite surfaces, and motivated us to further probe site-specific inhibitory effect of IOS to etch pit formation.

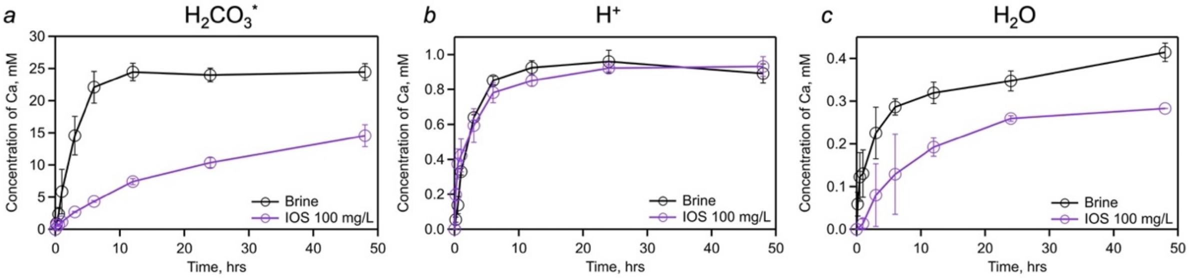

Figure 4. Dissolved Ca concentration with and without IOS as a function of reaction time when the rate of dissolution is promoted by a) $H_2CO_3^*$, b) H^+ and c) H_2O, respectively. Corresponding experimental conditions are summarized in Table 1. All experiments were run in duplicate, error bar represents the standard deviation.

3.2.Morphology of etch pits after the dissolution

The etch pit formation upon dissolution of calcite is a well-known phenomenon and the pit morphology is regarded and provided as the most direct evidence of site-specific inhibition of calcite dissolution by various additives (Arvidson et al., 2006; Kim et al., 2021; Lea et al., 2001; Lüttge & Conrad, 2004; Teng, 2004; Vinson et al., 2007; Vinson & Lüttge, 2005). Etch pit morphology formed after dissolution experiments was evaluated using a laser profilometer. For all the cases except H2CO3* promoted dissolution without IOS, surface profiles were obtained after 48 hours of dissolution; the surface morphology for H2CO3* promoted dissolution without IOS was taken after 10 min of dissolution because precipitation occurred in this sample at longer times when depressurizing/venting CO2. To minimize the precipitation from the remaining solutions, samples were rinsed with IOS immediately after collecting from the reactor and dried using N_2 gas. Disassembling reactor and rinsing tool about 1 min. The laser profilometry surface profiles are shown in Figure 5. To better compare etch pit morphology, the two acute edges of each sample are always placed toward the right bottom of the collected image. Since the mass of calcite dissolved from the cleaved sample varies between samples, we mostly focused on comparing the shape of etch pits, not on their size and depth.

When dissolution is primarily promoted by H_2O, etch pits formed during dissolution had classic rhombic shapes (the last column of Figure 5) as reported by various researchers (Anabaraonye et al., 2019; Britt & Hlady, 1997; Duckworth & Martin, 2004; Teng, 2004). The angle of each etch pit is smaller on the acute side of a rhombus, which is an indication of a faster step retrieving velocity of the acute edge compared to the obtuse edge. Although it has been reported that etch pit growth is faster on the obtuse edge, the step retrieving velocity varies with the solution composition in contact with calcite. Arvidson et al. also observed faster dissolution of acute edges in the presence of Mg^{2+} (Arvidson et al., 2006). When IOS is added, the obtuse edge dissolution is inhibited, resulting in a triangular etch pit led by the dissolution of acute edges (i.e., $[\bar{4}41]_-$ and $[48\bar{1}]_-$ faces).

The dissolution kinetics experiments (Figure 4) showed that during H^+ promoted dissolution, IOS did not measurably affect Ca release to solution. Hence, we expected no dramatic changes in etch pit morphology. Interestingly, during H+ promoted dissolution, rhombic etch pits were formed with brine with no IOS, while triangular etch pits were observed in the presence of IOS. Hence, it appears that there is at least some inhibition by IOS. An explanation for this inhibition will be addressed later with DFT results.

For $H_2CO_3^*$ promoted dissolution, an atypical etch pit shape was observed, even with no IOS present. Etch pit propagated towards the obtuse-obtuse kink, resulting in a triangular or arrow-like pentagon etch pit shape after 10 min of dissolution (Figure 5a). The resulting etch pit morphology indicates that dissolution primarily occurred at obtuse edges, and dissolution kinetics of the obtuse-

obtuse kink is faster than acute-obtuse kink. This anisotropic dissolution under high pCO2 conditions has not been reported before, and we still have no mechanistic explanation for this phenomenon. A similar etch pit shape also developed on the calcite surface in the presence of IOS. We note that the etch pit in Figure 5d was obtained after 48 hours of dissolution, and the size of etch pits are much smaller than the sample without IOS. This implies that adsorption of IOS inhibits dissolution uniformly at all sites within the etch pit in the presence of $H_2CO_3^*$.

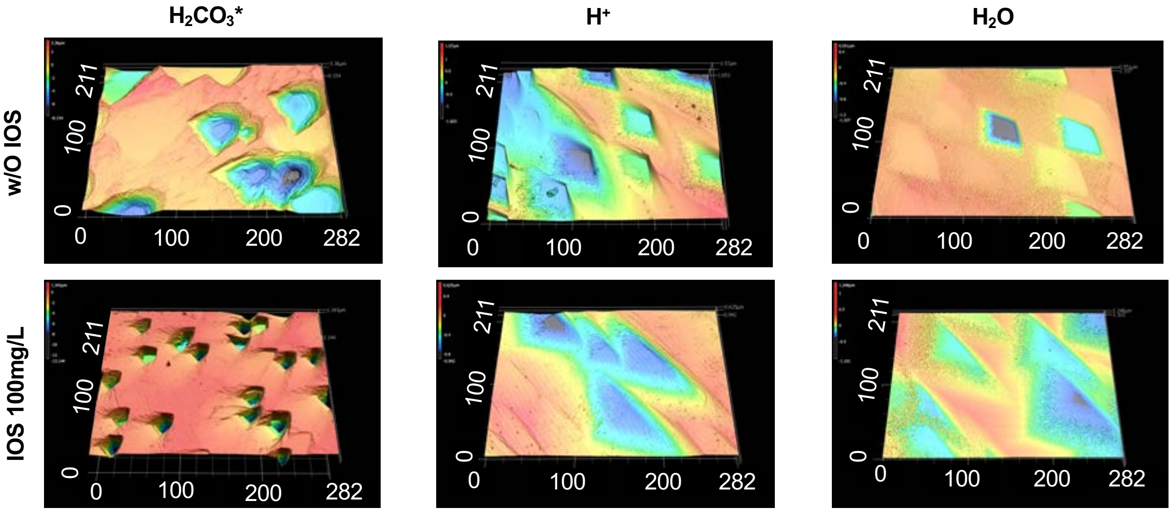

Figure 5. Etch pit morphology was measured by laser profilometer after the reaction brine without IOS, d-f) etch pit morphology in the presence of IOS, note that only surface profile of a) was taken after 10 min of reaction, and b-f) were taken after 48 hours of reaction. All the numbers shown in this figure are in μm.

3.3.DFT Calculations

The dissolution process can be broken down into seven sequential steps: 1) diffusion of reactants from solution to the solid surface, 2) Adsorption of reactants on the solid surface, 3) migration of reactants on the surface to dissolution active sites (e.g., step, kinks), 4) chemical reaction between the adsorbed reactants and solid (e.g., hydration of ions, bond breakage and formation), 5) migration of products away from the reaction site, 6) desorption of produces to the solution, 7) diffusion of products to the bulk solution (Morse & Arvidson, 2002). The second and third steps initiate dissolution, and the dissolution rate is dependent on the number of adsorbed promotors on reactive sites (Van Cappellen et al., 1993). In the presence of additives (e.g., IOS in this study), competitive interactions between the IOS and three promotors may result in different kinetics and etch pit morphology as observed in the dissolution experiments. To interpret our experimental results, we performed DFT calculations to probe site-specific inhibitory effects of IOS when dissolution is dominated by each driving species (i.e., H+, $H_2CO_3^*$, H2O).

3.3.1. Adsorption of IOS

Sulfonic acid is a strong acid, and thus exists as in deprotonated form and is negatively charged. The three oxygen atoms in sulfonate can potentially interact with surface Ca atoms and form three or fewer bonds. The binding configurations of IOS to calcite defect models were obtained (Figure 7 and Figure S1) and corresponding binding energies are shown in Figure 6 (purple bar). The binding energies vary for different sites, and this was expected given the varied arrangements of Ca atoms at acute and obtuse edges and three different kinks. When IOS was adsorbed at the acute edge, it was predicted to have the lowest binding energy (-0.98 eV). A simple comparison between adsorption figuration and energy on the acute edge (-0.98 eV) and obtuse edge (-1.26 eV) explains why IOS has the weakest binding energy at the acute edge. Binding energy has a strong relation to number of bonds between adsorbent and adsorbate. On the acute edge, O atoms of IOS form three bonds to one Ca atom on the upper slab and two on the lower slab, and bond distances are 2.51, 2.57, and 2.48 Å, respectively. Whereas on the obtuse edge, only two O atoms of IOS participated in forming bonds and were bonded to the Ca atoms on the upper and lower slabs, respectively. The bond distances are 2.38 and 2.40 Å, respectively. This indicates that although IOS forms more bonds to the acute edge, due to the longer bond distances (on average

2.52 Å) at the acute edge compared to the obtuse edge (on average 2.39 Å), it exhibits stronger adsorption energy to the obtuse edge. The correlation between binding energy and bond distance for adsorption on kinks appears to be the same as it is on edges. In all three cases, IOS formed three bonds to Ca kinks, two bonds to Ca atoms on the upper slab and one to lower slab. Binding energy of IOS is strongest at the obtuse-obtuse kink (-1.84 eV) followed by the acute-obtuse kink (-1.81 eV), and the acute-acute kink (-1.30 eV), and the average bond distance is shortest at the obtuse-obtuse kink (2.37 Å) followed by the acute-obtuse kink (2.39 Å), and the acute-acute kink (2.43 Å). (Table S1, Figure S1). In order for dissolution to occur, dissolution promotors are required to displace adsorbed IOS molecules, and it requires stronger or comparable adsorption energy to each defect site. The following sections address adsorption of the three promotors, and direct comparison of binding energies and conformations are in the discussion section.

3.3.2. Adsorption of H_2O

A water molecule was initially placed at the defect sites, and the structure was optimized. De Leeuw and Cooper showed that even though a hydrogen atom in the water molecule interacts with an oxygen atom in the surface carbonate, the interaction between water molecules is very little (De Leeuw & Cooper, 2004). Thus, we considered the adsorption energy of only one water molecule. To assure the most stable adsorption configuration, the H_2O molecule was placed at defect sites in a slightly different position and angle, and the geometry was optimized. The adsorption energies of H_2O to calcite surfaces were calculated using the most stable binding configuration and are presented in Figure 6 and Figure S2.

For adsorption to slab, the O atom of water strongly binds to the surface Ca atom, and one of the H atoms of water is oriented toward the protruding O atom of the surface CO_3 ion on the c-gliding plane [010] (Figure S2). This binding configuration has been identified as the most stable configuration by (Lardge et al., 2010) and the corresponding binding energy calculated in this study was -0.25 eV. Water adsorbs more strongly to acute and obtuse edges compared to the slab, and the acute edge was more preferred compared to the obtuse edge. The calculated binding energies of water to acute and obtuse edges were -0.58, and 0.40 eV, respectively. On the acute edge, the O atom of water formed two bonds with two Ca atoms that are located on the upper and lower slab respectively, and hence the H atom of the water molecule interacts with a neighboring surface carbonate in the lower slab. The bond distances to Ca atoms on the upper and lower slab were 2.51 and 2.5 Å, respectively. On the obtuse edge, the O atom of the water however formed one bond with a Ca atom on the upper slab with a bond length of 2.43 Å, and similarly, the H atom was oriented toward the adjacent carbonate ion on the upper slab. Although the bond distance between the O atom of water and the surface Ca atom on the obtuse edge is much shorter than the acute edge, the number of bonds resulted in stronger binding of the water molecule to the acute edge. The difference in binding conformation of the acute and obtuse edges is due to a steric effect. The distances between Ca on the upper and lower slab of the acute and obtuse edges are 4.14 and 5.17 Å, respectively. The calculated bond distances are summarized in Table S2. We initially postulated that the obtuse edge would exhibit stronger binding energy than the acute edge, since it has more space to accommodate water molecules. However, it turns out that the distance between two Ca atoms is too far to form two bonds with the O atom of water molecule. These binding conformations are in good agreement with (Lardge et al., 2010).

In order to investigate more detailed dissolution steps, the adsorption energies of a water molecule to kink sites were also calculated. Since the sulfonate head group of IOS interacts with surface Ca atoms, Ca-terminating kinks were evaluated. Our binding energy calculations indicate that the binding of water molecule is strongest at the acute-acute kink (-0.58 eV) followed by the acute-obtuse kink (-0.42 eV), and then the obtuse-obtuse kink (-0.31 eV). Similar to adsorption to the acute edge, when water molecule adsorbed to the acute-acute kink, it formed two bonds with two Ca atoms placed on the upper and lower slab with a distance of 2.47 and 2.49 Å, respectively. The H atom of the water molecule interacts with a neighboring surface CO_3 on the upper slab. Unlike the acute-acute kink, the O atom of water molecule forms only one bond to the Ca atom on the lower slab when it is adsorbed to acute-obtuse and obtuse-obtuse kinks. Hence, as reported by Lardge et al., dissociation of water molecule into a H^+ and OH^- was not found in all cases listed above (Lardge et al., 2010).

3.3.3. Adsorption of H^+

In order to better understand the experimental results of proton-promoted dissolution with and without IOS, the adsorption energy and binding conformation of the proton was also investigated using the same calcite models in section 3.3.1. Positively charged proton adsorbs to negatively charge surface carbonate, and spectroscopic evidence (i.e., X-ray photoelectron spectroscopy (XPS)) of protonated carbonate sites ($>CO_3H^0$) was provided by (Stipp & Hochella, 1991). Hence, prior efforts to understand the dissolution kinetics of calcite using surface complexation models (SCMs) showed that the proton-promoted dissolution rate of calcite is proportional to the second power of the concentration of protonated carbonate sites ($>CO_3H^0$) (Van Cappellen et al., 1993).

As expected, DFT calculations showed that the proton was adsorbed to surface carbonate ion, and the binding conformation is shown in Figure 7. Adsorption to carbonate on the slab and acute edge was found to be most stable compared to that on the obtuse edge, and kinks. However, comparing the adsorption energies of IOS and a proton does not provide a useful interpretation because, regardless of the strength of the binding, the active adsorption site of each is different. Meanwhile, the fact that the IOS and proton adsorb to different surface sites supports the results in which IOS showed little effect on proton-promoted dissolution. Since a thorough interpretation of the adsorption of water, protons, and IOS is necessary to understand the formation of triangular etch pits in the presence of IOS, it will be covered in detail in the discussion section that follows.

3.3.4. Adsorption of H_2CO_3

Carbonic acid adsorption is next considered in comparison to that for IOS. A noticeable finding is that when H_2CO_3 is adsorbed to calcite defect sites, dissociative adsorption is observed; in other words, one of the protons in the H_2CO_3 transferred to a neighboring O of surface carbonate, and the remaining bicarbonate formed two or three bonds with Ca atoms at defect sites except when it is adsorbed to the slab. The binding conformations for all 6 cases are shown in Figure S3. The calculated binding energies are shown in Figure 6, and the order is: acute-obtuse kink < slab < acute-acute kink < obtuse edge < obtuse-obtuse kink < acute edge. For adsorption to the slab, acute edge, and acute-obtuse kink, the H in bicarbonate weakly interacts with the three O atoms of surface carbonate, and the distances between these two atom types are 1.34, 1.57, and 1.41 Å. However, for obtuse edge, acute-acute kink, and obtuse-obtuse kink, distances from the H in bicarbonate to the surface carbonate are far enough that there is no bonding.

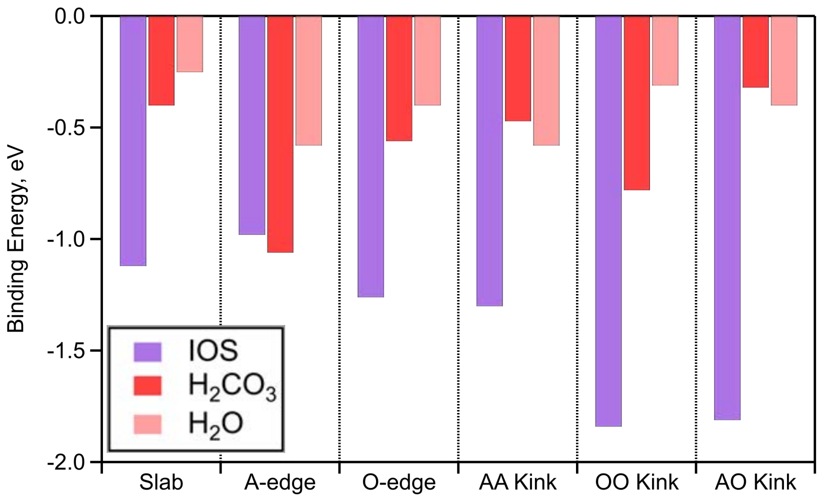

Figure 6. Adsorption energy IOS and dissolution promotors to calcite slab and defect models.

4. Discussion

4.1. Inhibition of H_2O promoted obtuse edge dissolution

Results from this study show site specific inhibitory effect of IOS to water promoted calcite dissolution under 1300 psi, and 50 ˚C condition. When IOS present, the dissolution rate is significantly slowed (Figure 4C), and obtuse edge growth is truncated (Figure 5, third column). To investigate the mechanisms behind site-specific inhibition, we compare adsorption energies of H_2O and IOS to various defect sites. At pH greater than 5, H_2O dominated carbonate mineral dissolution and surface complexation model successfully described that the rate of carbonate dissolution is proportional to the surface concentration of hydrated metal surface sites ($>MeOH_2^+$) as shown in Equation 3.

$$R_{H_2O} = k_{Me}\{> MeOH_2^+\}^n \quad (2)$$

Here, k_{Me} is a kinetic constant, and n is the reaction order. Equation 1 suggests that dissolution occurs when n number of surface metal atoms surrounding a carbonate site are hydrated, and Pokrovsky and Schott reported that n for calcite is 1(Pokrovsky & Schott, 2002).

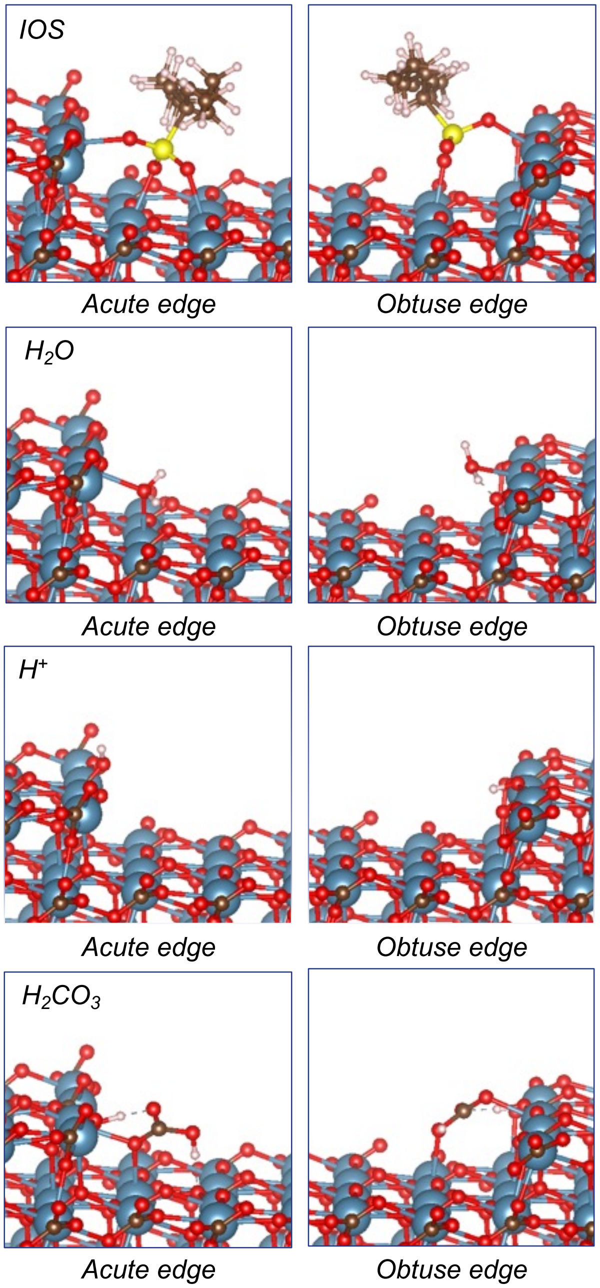

Figure 7. Binding conformations of IOS, H_2O, H^+ and H_2CO_3 at acute and obtuse edges.

In this study, we calculated the adsorption energy of only one H_2O molecule. For all 6 cases, adsorption energies of IOS are greater than H2O. Direct comparison of adsorption energies of IOS with water does partially explain macroscopic inhibition of calcite dissolution (Figure 3c), but not at obtuse edge sites. To explain this inhibition, we consider that the number of bonds formed by

IOS and H_2O to surface Ca atoms are different. For example, at acute edge sites, IOS forms three bonds whereas water forms two bonds: IOS and H_2O both forms bonds to Ca atoms on the upper and lower slab, while IOS forms one additional bond on the lower slab. To account for this, it is required to add adsorption energies of water to acute edge and slab sites, assuming the additional Ca site on the lower slab is similar to a slab on a terrace site. This additive approach is reasonable since it is reported that even though adsorbed water molecules form a structured layer on the calcite surface via interaction of surface Ca atom through their O atom, and surface O atom through their H atoms, adsorbed water molecules do not significantly interact with each other. Hence, the presence of steps does not affect the adsorption pattern on a terrace (De Leeuw & Cooper, 2004). If we adapt this method, the adsorption energy of IOS to the acute edge is -0.98 eV, whereas the sum of adsorption energies of water to the acute edge and a slab is -0.58 eV (acute) -0.25 eV (slab) = -0.83 eV. Now the adsorption energies of IOS and (two) water molecules are comparable and becomes more likely. On the other hand, for obtuse edge, IOS forms two bonds, whereas water forms one bond. Similar to the acute edge, an additional water molecule needs to be considered, and the resulting binding energy of two water molecules adsorbing to two Ca atoms on obtuse edge is -0.65 eV (-0.40 eV - 0.25 eV): this is much weaker binding energy compared to IOS (-1.31 eV). Thus, an additional -0.66 eV is required to displace an adsorbed IOS molecule and initiate dissolution at obtuse edges. For the kinks, IOS exhibits stronger binding energies thus it requires more energy to be displaced by water.

4.2.Inhibition of H+ promoted obtuse edge dissolution

The macroscopic dissolution results and the profilometer results in this work showed two apparently different effects of the IOS on calcite dissolution. Ca released from the calcite was barely affected when was IOS added, whereas obtuse edge dissolution is truncated like H_2O

promoted dissolution. It is well known that surface Ca and carbonate exhibit opposite charges. Thus, H+ electrostatically adsorb to surface carbonate. However, IOS adsorbs and forms two or three bonds with surface Ca sites, so H^+ and IOS do not compete each other and H^+ promoted dissolution is minimally affected by IOS. However, there remains a question why the obtuse edge is truncated in the presence of IOS. To understand this, it is necessary to understand H^+ promoted dissolution. Van Cappellen et al. reported a second order dependence of H^+ promoted dissolution rate on the concentration of $>CO_3H^0$. Following the same logic as H_2O promoted dissolution, their findings suggest that dissolution occurs when two of surface carbonate sites surrounding a hydrate Ca site are protonated (Van Cappellen et al., 1993). The protonation of surface carbonate results in weaking of oxygen bridges that bind surface carbonate and surface calcium, thereby releasing Ca ions from the calcite lattice to the solution. Hence, calcite dissolution cannot be initiated by protonation of carbonate, but requires hydrated surface Ca sites ($>CaOH_2^+$). As noted in section 4.1, water molecules can barely displace adsorbed IOS molecules on the obtuse edge. In other words, surface $>CaOH_2^+$ barely exists on the obtuse edge, so proton promoted dissolution is inhibited, and this results in obtuse edge truncation and triangular etch pits.

4.3.Inhibition of carbonic acid promoted dissolution

There is a lack of understanding on carbonic acid promoted dissolution and only phenomenological observations have been reported (Pokrovsky et al., 2005; Pokrovsky et al., 2009; Xu et al., 2012). One observation is that the calcite dissolution rate increases as pCO_2 increases from 1 atm to 25 atm and is independent from pCO_2 greater than 25 atm (Pokrovsky et al., 2005). Subhas et al. also reported that the presence of higher concentrations of carbonic anhydrase, which corresponds to a greater availability of H_2CO_3 on the surface, decreases the energy barrier to etch pit nucleation at near equilibrium (Subhas et al., 2017). The same group also reported that carbonic anhydrase enhanced calcite dissolution is possibly due to the transfer of a proton from the carbonic anhydrase catalytic center to the calcite surface during CO_2 hydration(Dong et al., 2020). Our DFT results provide a more detailed insight into carbonic acid promoted dissolution. They show that the dissociative adsorption occurs when carbonic acid adsorbs to defect sites. Dissociated proton may then exhibit an identical effect to proton promoted dissolution discussed in section 4.2. A remaining question is what is the effect of adsorbed bicarbonate after donating a proton to the calcite surface. Numerous surface complexation model works have reported that bicarbonate and carbonates are dissolution inhibitors of carbonate minerals because hydrated surface species (i.e., $>CaOH_2^+$, and $>CO_3H^0$) decrease with increasing surface concentration of $>CaHCO_3^0$, and $>CaCO_3^-$ (Pokrovsky et al., 2005; Pokrovsky et al., 2009; Pokrovsky & Schott, 2002). However, Van Cappellen et al. suggest a different view, where the adsorbed surface bicarbonate ($>CaHCO_3^0$) has similar effect to ligand promoted dissolution of oxide and silicate minerals (Van Cappellen et al., 1993).

Interestingly, we observe that acute edge dissolution is truncated both in the presence and absence of IOS. This is maybe due to relatively greater adsorption energy of H_2CO_3 to acute edge. The dissociative adsorption of H_2CO_3 may have two opposite effects to calcite dissolution. The dissociated proton may serve as a promotor, whereas the remaining bicarbonate may serve as an inhibitor. In order for dissolution to take place, the remaining bicarbonate is required to be displaced by H_2O molecules. As it is shown in figure 6, binding energy difference between carbonic acid and water are greater for adsorption to acute edge sites. This implies that displacement of the bicarbonate by water molecule is thermodynamically unfavorable.

The H_2CO_3 promoted dissolution resulted in a similar arrow like etch pit morphology with and without IOS. Note that etch pit morphology shown in Figure 5 without IOS was obtained after 10 min of dissolution, whereas with IOS was obtained after 48 hours. Considering the reaction times and slope of etch pits, addition of IOS inhibited growth of etch pit upon dissolution. DFT results partially explains the inhibition of overall etch pit propagation. The calculated adsorption energies of H_2CO_3 to calcite surfaces are weaker than those of IOS except for acute edge. The relative adsorption energy of H_2CO_3 and IOS is not a significant factor since both IOS and H_2CO_3 exhibits inhibitory effect to acute edges.

5. Conclusions

In summary, results from batch experiments show that $H_2CO_3^*$ or H_2O driven dissolution is strongly inhibited by the presence IOS, while H+ driven dissolution is not. Examination of etch pit morphology using laser profilometry shows IOS preferentially inhibits dissolution of obtuse edges in etch pits for H+ and H2O driven dissolution, compared to acute edges. They also show that IOS more uniformly inhibits etch pit growth at all edge and kink sites for $H_2CO_3^*$ driven dissolution. DFT results indicate that the binding energies of IOS to calcite terrace, obtuse edge, and three calcium kink (i.e., acute-acute, obtuse-obtuse, acute-obtuse) sites are much more favorable than binding energies of $H_2CO_3^*$, H^+, or H_2O at these same locations, but less so at acute edge sites. This at least partially explains why the growth of calcite etch pits are preferentially inhibited by IOS along obtuse edge sites for H^+ or H_2O driven dissolution. DFT results also indicate that both IOS and $H_2CO_3^*$ preferentially bind to surface Ca, while H2O binds to both surface Ca and CO3 and H+ preferentially bind to surface CO3. This can explain why IOS has little effect on H+ driven dissolution, and appears to completely inhibit $H_2CO_3^*$ driven dissolution. This study sheds light on calcite dissolution mechanisms, and suggests the role that additives can play in inhibiting carbonate mineral dissolution during GCS to mitigate pore space alteration and geomechanical integrity loss.

References

- Anabaraonye, B. U., Crawshaw, J. P., & Trusler, J. P. M. (2019). Brine chemistry effects in calcite dissolution kinetics at reservoir conditions. *Chemical Geology*, *509*, 92-102. https://doi.org/10.1016/j.chemgeo.2019.01.014
- Arvidson, R. S., Collier, M., Davis, K. J., Vinson, M. D., Amonette, J. E., & Luttge, A. (2006). Magnesium inhibition of calcite dissolution kinetics. *Geochimica et Cosmochimica Acta*, *70*(3), 583-594. https://doi.org/10.1016/j.gca.2005.10.005
- Britt, D. W., & Hlady, V. (1997). In-situ atomic force microscope imaging of calcite etch pit morphology changes in undersaturated and 1-hydroxyethylidene-1, 1-diphosphonic acid poisoned solutions. *Langmuir*, *13*(7), 1873-1876.
- De Leeuw, N. H. (2002). Molecular Dynamics Simulations of the Growth Inhibiting Effect of Fe²⁺, Mg²⁺, Cd²⁺, and Sr²⁺ on Calcite Crystal Growth. *The Journal of Physical Chemistry B*, *106*(20), 5241-5249. https://doi.org/10.1021/jp014488h
- De Leeuw, N. H., & Cooper, T. G. (2004). A Computer Modeling Study of the Inhibiting Effect of Organic Adsorbates on Calcite Crystal Growth. *Crystal growth & design*, *4*(1), 123-133. https://doi.org/10.1021/cg0341003
- De Leeuw, N. H., & Parker, S. C. (1997). Atomistic simulation of the effect of molecular adsorption of water on the surface structure and energies of calcite surfaces. *Journal of the Chemical Society, Faraday Transactions*, *93*(3), 467-475. https://doi.org/10.1039/a606573b
- De Leeuw, N. H., Parker, S. C., & Harding, J. H. (1999). Molecular dynamics simulation of crystal dissolution from calcite steps. *Physical Review B*, *60*(19), 13792-13799. https://doi.org/10.1103/physrevb.60.13792
- De Leeuw, N. H., Parker, S. C., & Rao, K. H. (1998). Modeling the Competitive Adsorption of Water and Methanoic Acid on Calcite and Fluorite Surfaces. *Langmuir*, *14*(20), 5900-5906. https://doi.org/10.1021/la980269k
- Dong, S., Berelson, W. M., Teng, H. H., Rollins, N. E., Pirbadian, S., El-Naggar, M. Y., & Adkins, J. F. (2020). A Mechanistic Study of Carbonic Anhydrase-Enhanced Calcite Dissolution. *Geophysical Research Letters*, *47*(19). https://doi.org/10.1029/2020gl089244
- Duckworth, O. W., & Martin, S. T. (2004). Dissolution rates and pit morphologies of rhombohedral carbonate minerals. *American Mineralogist*, *89*(4), 554-563.
- Elhadj, S., Salter, E., Wierzbicki, A., De Yoreo, J., Han, N., & Dove, P. (2006). Peptide controls on calcite mineralization: Polyaspartate chain length affects growth kinetics and acts as a stereochemical switch on morphology. *Crystal growth & design*, *6*(1), 197-201.
- Kim, K. T., Jagannath, M. S. P., Su, G. M., Freychet, G., Zeng, T., Mohanty, K. K., Henkelman, G., Katz, L. E., & Werth, C. J. (2021). Surfactant inhibition mechanisms of carbonate mineral dissolution in shale. *Colloids and Surfaces A: Physicochemical and Engineering Aspects*, *625*, 126857.
- Lardge, J. S., Duffy, D. M., Gillan, M. J., & Watkins, M. (2010). Ab Initio Simulations of the Interaction between Water and Defects on the Calcite (101¯4) Surface. *The Journal of Physical Chemistry C*, *114*(6), 2664-2668. https://doi.org/10.1021/jp909593p
- Lea, A. S., Amonette, J. E., Baer, D. R., Liang, Y., & Colton, N. G. (2001). Microscopic effects of carbonate, manganese, and strontium ions on calcite dissolution. *Geochimica et Cosmochimica Acta*, *65*(3), 369-379.

- Lüttge, A., & Conrad, P. G. (2004). Direct observation of microbial inhibition of calcite dissolution. *Applied and Environmental Microbiology*, *70*(3), 1627-1632.
- Morse, J. W., & Arvidson, R. S. (2002). The dissolution kinetics of major sedimentary carbonate minerals. *Earth-Science Reviews*, *58*(1-2), 51-84. https://doi.org/10.1016/s0012-8252(01)00083-6
- Parkhurst, D. L., & Appelo, C. (2013). Description of input and examples for PHREEQC version 3—a computer program for speciation, batch-reaction, one-dimensional transport, and inverse geochemical calculations. *US geological survey techniques and methods*, *6*(A43), 497.
- Perdew, J. P., Burke, K., & Ernzerhof, M. (1996). Generalized Gradient Approximation Made Simple. *Physical Review Letters*, *77*(18), 3865-3868. https://doi.org/10.1103/physrevlett.77.3865
- Plummer, L. N., Wigley, T. M. L., & Parkhurst, D. L. (1978). The kinetics of calcite dissolution in CO 2 -water systems at 5 degrees to 60 degrees C and 0.0 to 1.0 atm CO 2. *American Journal of Science*, *278*(2), 179-216. https://doi.org/10.2475/ajs.278.2.179
- Pokrovsky, O. S., Golubev, S. V., & Schott, J. (2005). Dissolution kinetics of calcite, dolomite and magnesite at 25 C and 0 to 50 atm pCO2. *Chemical Geology*, *217*(3-4), 239-255.
- Pokrovsky, O. S., Golubev, S. V., Schott, J., & Castillo, A. (2009). Calcite, dolomite and magnesite dissolution kinetics in aqueous solutions at acid to circumneutral pH, 25 to 150 C and 1 to 55 atm pCO2: New constraints on CO2 sequestration in sedimentary basins. *Chemical Geology*, *265*(1-2), 20-32.
- Pokrovsky, O. S., & Schott, J. (2002). Surface Chemistry and Dissolution Kinetics of Divalent Metal Carbonates. *Environmental Science & Technology*, *36*(3), 426-432. https://doi.org/10.1021/es010925u
- Stipp, S. L., & Hochella, M. F. (1991). Structure and bonding environments at the calcite surface as observed with X-ray photoelectron spectroscopy (XPS) and low energy electron diffraction (LEED). *Geochimica et Cosmochimica Acta*, *55*(6), 1723-1736. https://doi.org/10.1016/0016-7037(91)90142-r
- Subhas, A. V., Adkins, J. F., Rollins, N. E., Naviaux, J., Erez, J., & Berelson, W. M. (2017). Catalysis and chemical mechanisms of calcite dissolution in seawater. *Proceedings of the National Academy of Sciences*, *114*(31), 8175-8180.
- Teng, H. H. (2004). Controls by saturation state on etch pit formation during calcite dissolution. *Geochimica et Cosmochimica Acta*, *68*(2), 253-262. https://doi.org/10.1016/s0016-7037(03)00423-x
- Teng, H. H., & Dove, P. M. (1997). Surface site-specific interactions of aspartate with calcite during dissolution: Implications for biomineralization. *American Mineralogist*, *82*(9-10), 878-887.
- Van Cappellen, P., Charlet, L., Stumm, W., & Wersin, P. (1993). A surface complexation model of the carbonate mineral-aqueous solution interface. *Geochimica et Cosmochimica Acta*, *57*(15), 3505-3518. https://doi.org/10.1016/0016-7037(93)90135-j
- Vinson, M. D., Arvidson, R. S., & Luttge, A. (2007). Kinetic inhibition of calcite (104) dissolution by aqueous manganese(II). *Journal of Crystal Growth*, *307*(1), 116-125. https://doi.org/10.1016/j.jcrysgro.2007.05.059

- Vinson, M. D., & Lüttge, A. (2005). Multiple length-scale kinetics: an integrated study of calcite dissolution rates and strontium inhibition. *American Journal of Science*, *305*(2), 119-146.
- Xu, J., Fan, C., & Teng, H. H. (2012). Calcite dissolution kinetics in view of Gibbs free energy, dislocation density, and pCO2. *Chemical Geology*, *322*, 11-18.
- Xu, M., & Higgins, S. R. (2011). Effects of magnesium ions on near-equilibrium calcite dissolution: Step kinetics and morphology. *Geochimica et Cosmochimica Acta*, *75*(3), 719-733. https://doi.org/10.1016/j.gca.2010.10.018
- Zeng, T., Kim, K. T., Werth, C. J., Katz, L. E., & Mohanty, K. K. (2020). Surfactant Adsorption on Shale Samples: Experiments and an Additive Model. *Energy & Fuels*, *34*(5), 5436-5443. https://doi.org/10.1021/acs.energyfuels.9b04016

SUPPORTING INFORMATION

Table S1. Bonds distances formed by interaction between O atoms of IOS and Ca atoms on the calcite defect models. O1 represents a O atom interacts with Ca atom on the upper slab and O2 and O3 represent those interact with Ca atoms on the lower slab.

	Number of bonds	Distance (Å)				Binding Energy (eV)
		O1-Ca	O2-Ca	O3-Ca	Average (O-Ca)	
Slab	1	2.39	-	-	2.39	-1.12
Ea	3	2.51	2.57	2.48	2.52	-0.98
Eo	2	2.38	2.40	-	2.39	-1.26
Kaa	3	2.40	2.41	2.48	2.43	-1.30
Koo	3	2.28	2.42	2.40	2.37	-1.84
Kao	3	2.34	2.40	2.42	2.39	-1.81

Table S2. Bonds distances formed by interaction between O atoms of H2O and Ca atoms on the calcite defect models, and H atom of H2O between O of surface Carbonate. O1 represents a O atom interacts with Ca atom on the upper slab and O2 represents that interacts with Ca atoms on the lower slab.

	Number of bonds	Distance (Å)			Binding Energy (eV)
		O1-Ca	O2-Ca	H-O	
Slab	1+(1)	2.52	-	1.81	-0.25
Ea	2+(1)	2.51	2.50	1.63	-0.58
Eo	1+(1)	2.43	-	1.60	-0.40
Kaa	2+(1)	2.47	2.49	1.53	-0.58
Koo	1+(1)	-	2.42	1.74	-0.31
Kao	1+(1)	-	2.45	1.65	-0.42

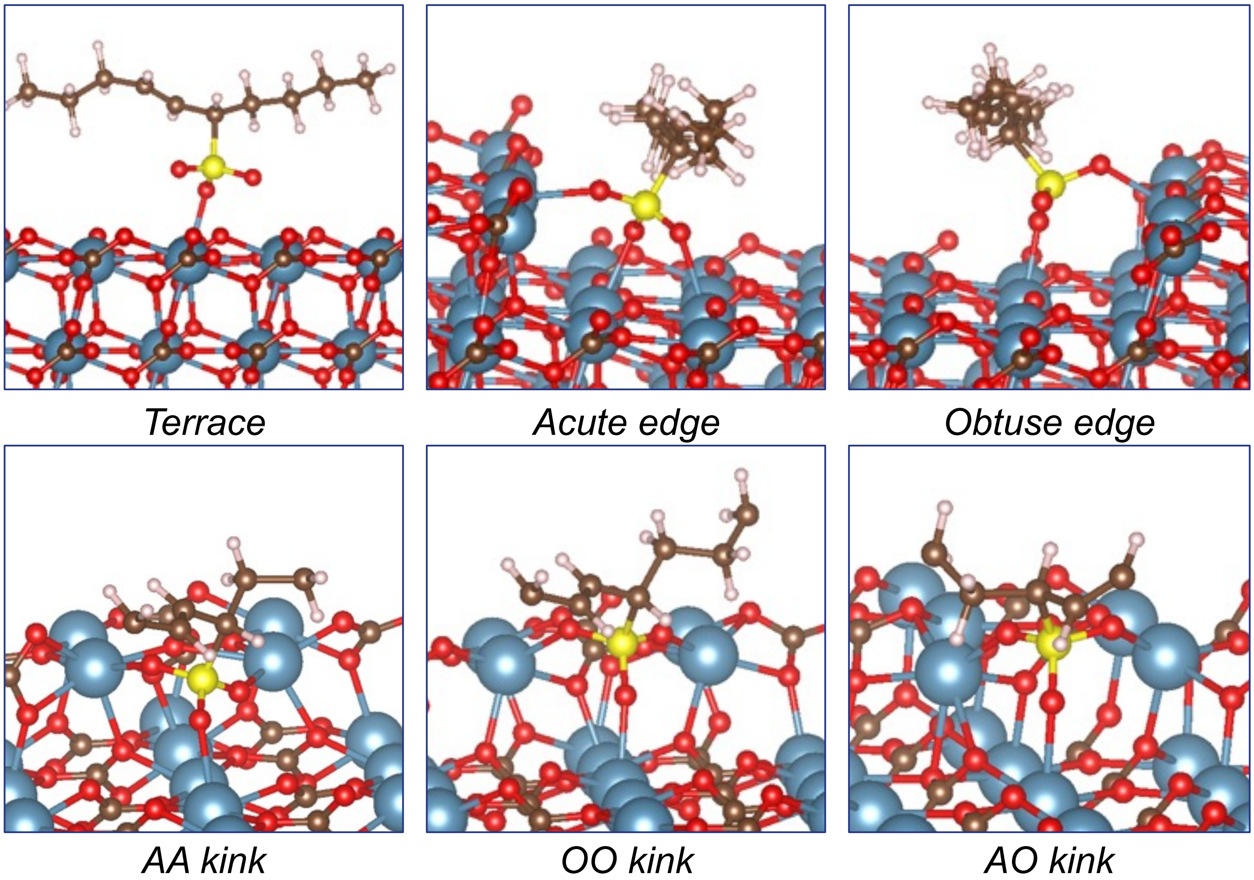

Figure S3. Binding conformation of IOS to calcite defect models. Some portions of calcite lattice and hydrocarbon tails are hidden for better graphical representation.

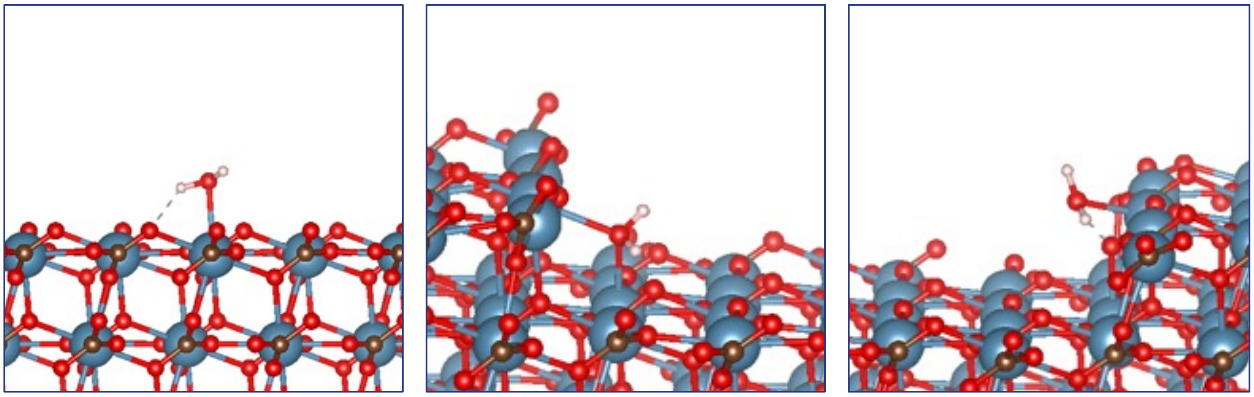

Terrace *Acute edge* *Obtuse edge*

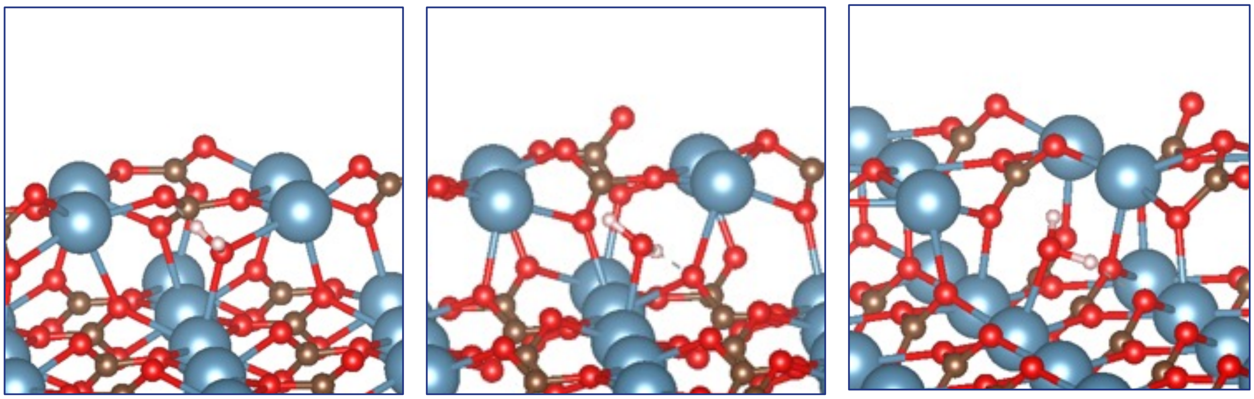

AA kink *OO kink* *AO kink*

Figure S1. Binding conformation of H_2O to calcite defect models. Some portions of calcite lattice and hydrocarbon tails are hidden for a better graphical representation.

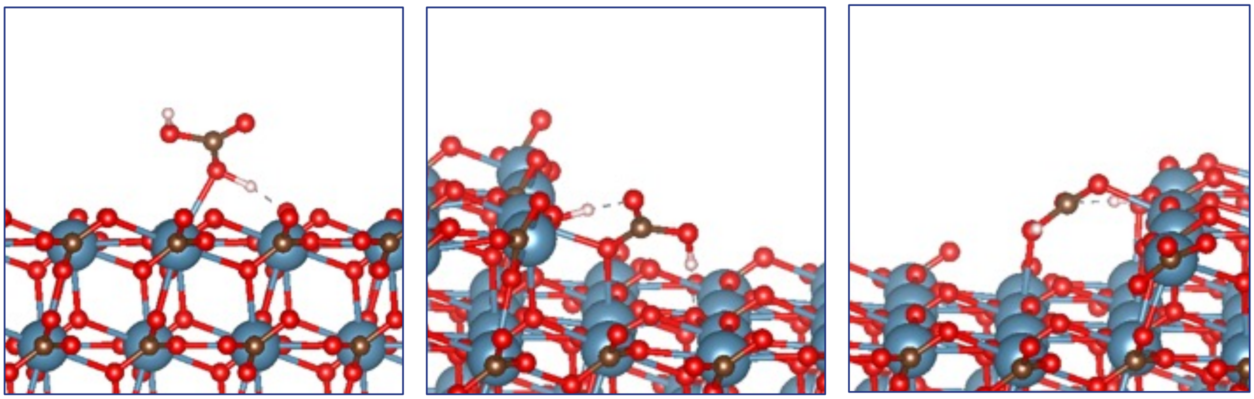

Terrace *Acute edge* *Obtuse edge*

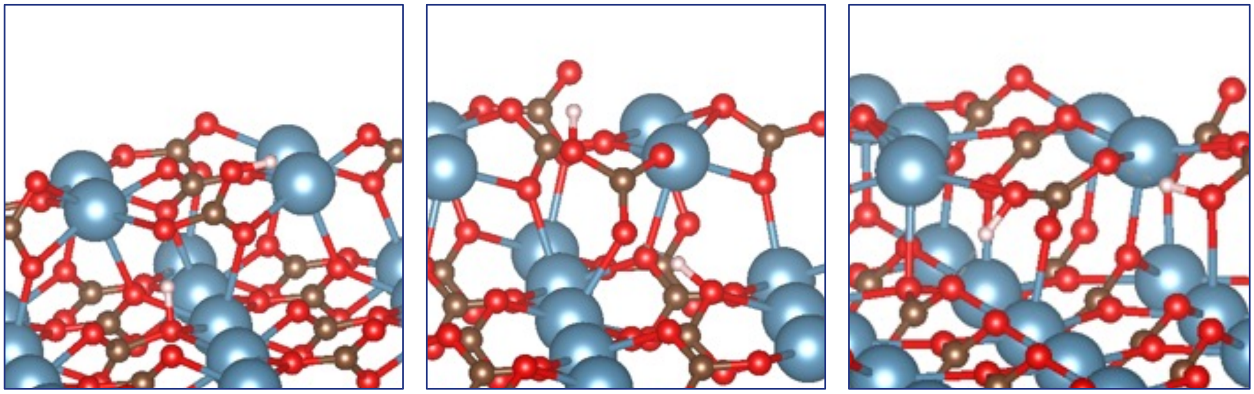

AA kink *OO kink* *AO kink*

Figure S2. Binding conformation of H_2CO_3 to calcite defect models. Some portions of calcite lattice and hydrocarbon tails are hidden for a better graphical representation.

SECTION E: Presentation of major findings on mechanisms of reaction of simulated reservoir brine with shale components, and effects on shear slip at reservoir pressure

Impacts of acidified brine reaction with artificially fractured shale under differential stress

Abstract

The efficacy of geological carbon sequestration is reliant on the integrity of the caprock and its resistance to physical and chemical alteration. Caprocks with high abundance of reactive carbonates like calcite are susceptible to acid-promoted dissolution and can result in structural weakening, conditions that can be promoted by dissolution of injected CO_2 into pore water. This work investigates the effect of acidified brine flow through an artificially fractured, high-carbonate (30% by XRD) shale under differential compressive stress. Cylindrical samples were cut in half vertically and milled to create an artificial fracture with alternating regions of interlocking asperities and open channels. Samples were sheared with a single step applied stress in a custom flow cell housed within an industrial CT scanner. Either acidic (pH 4) or reservoir-simulated (pH 9.5) brine was flowed through the artificial fracture for 7-8 days under reservoir pressure and room temperature. CT images indicate that after the initial shear-step, no further slip occurred. Model simulations indicate flow mainly occurred in open channels, with some flow between overlapping asperities. Mean apertures and transmissivity values were lower in channels exposed to pH 4 versus pH 9.5 brine, possibly due to clay swelling at low pH. Analysis of fracture surfaces by optical microscopy, scanning electron microscopy, and optical profilometry generally indicate increased surface alteration and/or roughness after exposure to pH 4 versus pH 9.5 brine, and this effect is greater in areas that receive the highest brine flows. Similarly, analysis of these surfaces by scratch testing shows fracture toughness decreases more after exposure to acidic versus reservoir simulated brine (1.261 ± 0.036 MPa $m^{1/2}$ initially to 0.462 ± 0.074 MPa $m^{1/2}$ and 0.871 ± 0.089 MPa $m^{1/2}$ respectively); also, this decrease is greater in areas that receive the highest acidic brine flows. Overall, the results indicate that acidified brine can result in significant physical and geomechanical alteration of fracture surfaces in shale caprock, and in heterogeneous fractures the effects are greatest in preferential flow regions.

1. Introduction

Geological Carbon Sequestration (GCS) involves capturing CO_2 emissions at a point source and injecting it into a subsurface formation to mitigate anthropogenic climate change. Relevant subsurface formations include deep saline aquifers and depleted oil and gas reservoirs, with storage capacities in the United States of approximately 1610 and 120 Gt of CO_2, respectively (Wright et al. 2013). These formations are typically hydraulically capped by overlying low permeability and high capillary pressure shales or mudstones. These caprocks prevent buoyant CO_2 from migrating out of the formation, and promotes GCS via capillary trapping, stratigraphic trapping, mineral precipitation, and dissolution into brine formation water. Dissolved CO_2 forms carbonic acid and reduces the brine pH to almost 4 (Wigand et al. 2008), thereby promoting geochemical reactions with the reservoir material and caprock. A general concern is that the acidified brine will cause mineral dissolution along pre-existing fractures, weakening the caprock matrix at the fracture surface and promoting slip (Zoback and Gorelick 2012). Slip events can open fractures and promote preferential flow of CO_2 or acidified brine into overlying stratigraphic units that contain potable groundwater (Harvey et al. 2013). These scenarios motivate the need to determine the subsurface environmental conditions under which acidified brines compromise the geomechanical integrity of fracture surfaces in caprock, and to what extent.

Several studies have examined the geochemical reaction of acidified brine and minerals within caprock material. The most ubiquitous, reactive minerals in shales and mudstones are carbonates, and these readily dissolve under GCS conditions (Black, Carroll, and Haese 2015; Peng et al. 2015; Guo et al. 2017). A carbonate-rich (18wt%) Mancos shale exposed to $scCO_2$-saturated brine at 2500 psi and 90°C for 8 weeks resulted in complete dissolution of calcite and partial dissolution of dolomite according to XRD results (Ilgen et al. 2018). A brine-wet, carbonate-rich Utica shale exposed to dissolved CO_2 under supercritical conditions developed surface pitting associated with carbonate dissolution (Goodman et al. 2019). Outside of carbonate, dissolution and reprecipitation of feldspars, iron oxides, and phyllosilicate minerals have been observed at GCS conditions (Garcia et al. 2012; Liu et al. 2012; Rathnaweera et al. 2015; Yang et al. 2022). Often, complex mineralogical composition results in simultaneous dissolution and precipitation of different minerals, with the distribution of reactive species, the heterogeneity of the lamination, and the pore structure determining the extent of geochemical alterations in shales. For example, in batch experiments of Eau Claire Shale with $scCO_2$-saturated brine at 200°C and 300 bar, results indicated dissolution of K-feldspar and anhydrite, and precipitation of illite/smectite and siderite (Liu et al. 2012). However, in another series of batch studies, $scCO_2$ saturated with water at increasing pressures (10 to 24 MPa) at 70°C resulted in increasing dissolution of clays and precipitation of quartz (Fatah et al. 2022). The relative extent of varying reactions depends on the availability of reactants and saturation limits. Batch reactor experiments usually involve much larger volume ratios of water/CO_2 to minerals than in-reservoir conditions.

The geochemical alteration of shale has a significant effect on its geomechanical properties and integrity as caprock for GCS. In several studies, exposure to acidified brines has promoted mineral dissolution and a reduction in geomechanical integrity (Shukla et al. 2010; Aman et al. 2018; Akono et al. 2019). After exposure to $scCO_2$ saturated brine, clay-rich shale was significantly deteriorated, with observed surface dissolution and roughening, and a more than 30% reduction in compressive strength (Choi, Kim, and Song 2021). When a carbonate-rich shale was exposed to $scCO_2$-saturated brine for 15 days at 15 MPa and 60°C, a 6% decrease in carbonate content and a 20% decrease in compressive strength was measured (Yang et al. 2022). These mechanical alterations are highly dependent on mineralogy and heterogeneity of the shale. For example, after exposure to a $scCO_2$-saturated brine, the scratch toughness of dolomite-clay-rich layers of Mancos shale were reduced up to 50 ± 20%, but quartz-calcite-rich layers experienced no measurable reduction (Ilgen et al. 2018). In contrast, the precipitation of secondary minerals such as carbonates have been shown to increase rock stiffness over geological time scales (Espinoza et al. 2018; Major et al. 2018). Finally, an increase in subcritical fracture growth due to geochemical reactions is also a concern for both increased flow paths for reactive brine and the potential creation of larger fractures that could compromise the sealing capacity of the caprock (Major et al. 2018).

The flow of acidified brine in caprock significantly shapes the type and extent of geochemical and geomechanical alteration. Shales have relatively low permeability, and this can limit the extent of geochemical reactions to only exposed surfaces near injection zones and along existing flow paths. Over time, these reactions can open preferential flow paths and restrict others, such as dissolution of carbonate creating deeper channels (Deng et al. 2015), or precipitation of carbonate sealing pores and fractures (Matter and Kelemen 2009; Fang et al. 2018). In the Marine Shale sealing the Tuscaloosa sandstone, laboratory experiments with $scCO_2$ and brine under reservoir conditions indicated dissolution along preferential flow paths, causing existing fractures to open and connect, greatly increasing permeability (Soong et al. 2018). In a similar study with Tuscaloosa shale exposed to $scCO_2$ and brine under reservoir conditions, results show a significant porosity increase from dissolution of both carbonate and silicate materials including pores >1 μm in size (Mouzakis et al. 2016). In the same study, a carbonate mudstone Gothic Shale was exposed to the same conditions, and both porosity and pore connectivity increased, though pore size was limited to 200 nm (Mouzakis et al. 2016). Overall, the primary concerns for caprock integrity are mineralogical reactions with acidified reservoir fluid along preferential flow paths causing mechanical weakening, particularly under high temperature and pressure.

The objective of this study is to evaluate the effects of variably-distributed acidified brine flow through a fractured shale under compression and shear stress. An artificially fractured Marcellus shale core with variable aperature width was placed into a custom triaxial flow cell, subjected to shear, and then flushed with either acidic (pH 4) or reservoir-simulated brine (pH 9.5) for approximately one week. Samples were monitored using X-ray Computed Tomography (CT) to evaluate changes in strain and fracture morphology. CT images were used to determine changes in fracture aperture depths, and flow was simulated using a modified 2D Stokes model (NETL-Ap-Map Flow) to determine changes in fracture transmissivities. Samples were analyzed before and after experimentation with optical microscopy and energy dispersive spectroscopy to evaluate changes in mineralogy, scanning electron microscopy (SEM) and optical profilometry to evaluate changes in surface morphology and roughness, and scratch testing to evaluate changes in geomechanical integrity. These experiments tested the hypothesis that acidic dissolution of matrix carbonates preferentially occurs along primary flow paths on fracture surfaces in shale caprock, resulting in a decrease in shale surface integrity which leads to slip. This is relevant to the field of GCS because many storage reservoirs are overlain by shale caprock, and these caprocks are expected to have heterogeneous fracture networks that might be exposed to acidified brines and reactivated during GCS.

2. Materials and Methods

2.i. Materials

Rock samples from the Marcellus Formation, commonly referred to as Marcellus Shale, were obtained from Kocurek Industries with a reported mineral composition of 45.9% quartz, 26.6% calcite, 4.0% dolomite, 15.3% muscovite, 1.2% kaolinite, 1.4% K-feldspar, 2.8% Na-feldspar, and 2.8% pyrite by X-Ray Diffraction (XRD). Synthetic brine was created by adding potassium iodide (Sigma-Aldrich, ≥99.0%) to ultrapure, deionized water (resistivity 18 MΩ·cm) for a 0.5 M solution (8.3wt%). The brine was amended with nitric acid (Sigma-Aldrich, 70%) to reach a pH of 4. This approach was used to replicate the pH and high salinity of a deep saline aquifer following CO_2 injection (Wigand et al. 2008), with iodide specifically chosen to produce high CT imagery contrast (Nakashima and Nakano 2014). Nitric acid was used instead of CO_2 (g) due to a lack of temperature control to reach supercritical conditions. Nitric acid was used instead of other acids because it was shown to have limited corrosion potential for the experimental steel components ("Stainless Steel Chemical Compatibility Chart" 2021). Reservoir-simulated brine was obtained by grinding 30g of Marcellus shale and equilibrating it with 0.5 M KI brine for 7 days while sparging with N_2 (Airgas, industrial grade) to ensure anoxic conditions, followed by filtering the solution. The resulting pH of this brine was 9.5.

2.ii. Sample Preparation

Samples of Marcellus shale were cut into 38.1 mm (1.5 in) long and 33.02 mm (1.3 in) diameter cylinders and cut vertically down the length of the sample to create an artificial fracture. The fracture surfaces were milled to create uniform, artificial asperities consisting of 0.1 mm raised squares; these asperities interlocked when put together in order to resist sliding (Figure 1). Four open flow channels were created, clear of asperities, to allow for transport rather than diffusion-based reaction, as reported in previous work (Fuchs et al. 2021).

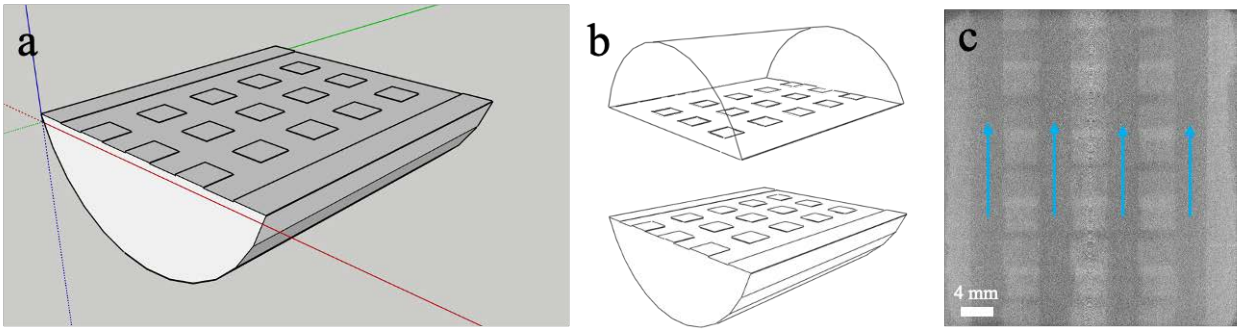

Figure 1: a) Pattern for surface milling of 4 mm wide, 0.1 mm deep artificial asperities created using SketchUp, b) Diagram of top and bottom milling patterns showing interlock and continuous edge guide to prevent bypassing, c) Radiograph across central slice of milled shale fracture indicating where flow is preferred along channels.

The milled fracture pattern was chosen due to the large variability in fracture morphology in natural or lab-created fractures by hammer impaction. This selected milling pattern does not equate to a natural fracture, but provides a controlled, reproducible set of asperities that serve as an analogue of natural fracture contact points.

Thin sections from were produced by Wagner Petrographic. Shale fracture surfaces before and after reaction were cut from the center of milled samples to obtain 20 x 33 mm pieces, which were cut and polished to make standard 30 µm deep thin sections. The thin-section surface was collected within 0.5 mm from the flat, milled surface of the channels. Blue epoxy was used for impregnation for identification of pore space and microfractures.

2.iii. Flow Experiments under Differential Stress

Each sample was placed in a custom shearing core holder which uses threaded end caps to apply shear displacement of a cylindrical sample fractured in half (Figure 2), as described in Moore et al. 2018 and employed in our previous work (Fuchs et al. 2021). For each experiment, the system was saturated with either acidic (pH 4) or reservoir-simulated (pH 9.5) brine and brought to a confining pressure of 2000 psi (13.79 MPa) and pore pressure of 100 psi (0.69 MPa). To induce shear slip, one end cap was turned to a known displacement of 0.794 mm (1/32 inch), forcing the fractured sample to shear.

Brine flow, confining pressure, and pore pressure were controlled by a set of Teledyne ISCO 500HP pumps, with inlet pump set to 0.5 mL/min of constant flow and outlet pump set to 100 psi. The triaxial core holder and ISCO pumps were placed in a shielded room with a Northstar Imaging Inc. M-5000 Industrial Computed Tomography (CT) System, using a source voltage of 174kV and a current of 300 μA. (Figure S1). CT scans captured three-dimensional data of the brine-saturated sample to identify fracture morphology pre-shear, immediately post-shear (called *Initial*), and on experimental days 1, 2, 3, 4, and either 7 or 8. CT scans were obtained with North-Star Imaging Inc. software with spatial resolution at 15.8 μm^3 per voxel. Each scan took 150 minutes to acquire. All experiments were run at room temperature. After each experiment, samples were removed from the core holder and Buna-N sleeve and allowed to dry in the RTV (room temperature vulcanizing) silicone jacket for 6 hours before silicone removal. Sample halves were then separated and dried in a vacuum oven for 24 hours at 40°C before analysis. Each experiment was performed twice for comparison.

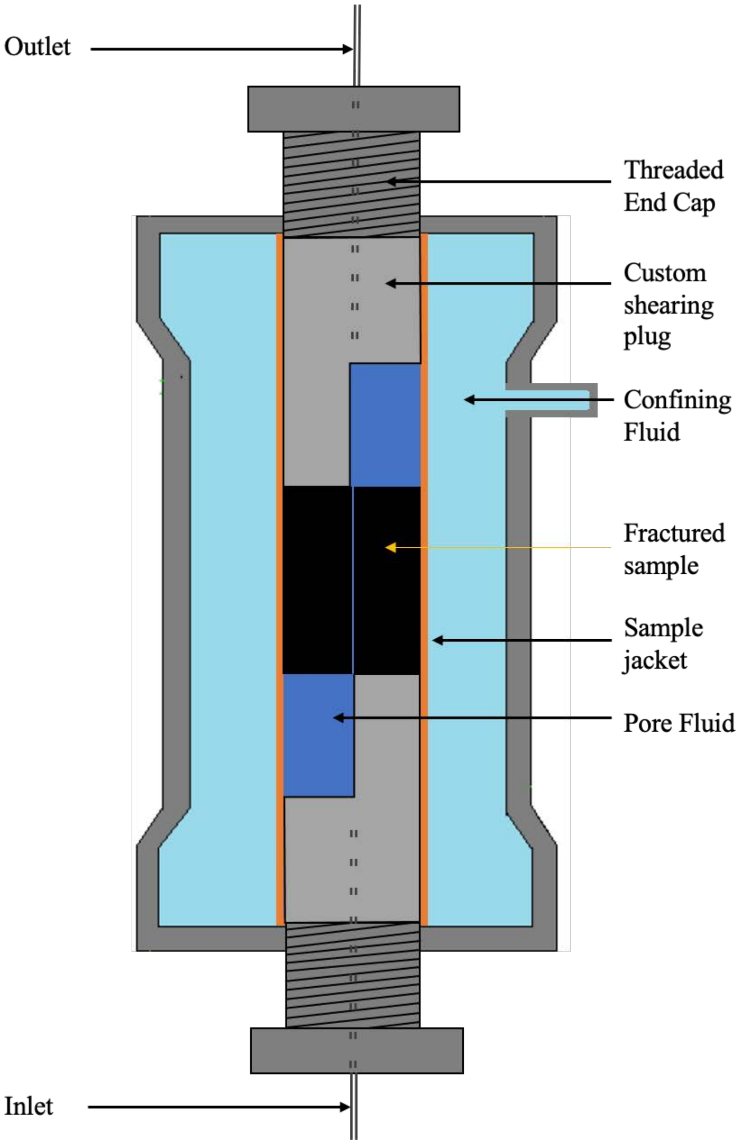

Figure 2: Modified core holder with shearing end caps for reactive flow experiments based on Moore et al. 2018. Threaded end caps are not fully seated and allow for application of stress by displacement of plugs. Pore fluid and confining fluid are separated by the sample jacket, consisting of shrink-wrap Teflon, then aluminum side shields, and then a Buna-N rubber membrane. Aluminum side shields prevent collapse of the rubber membrane under differential pressure. Figure is not drawn to scale.

2.iv. 3D Fracture Imagery and Modeling

Radiographs were reconstructed into 3D volumes by North-Star Imaging eFX© at a resolution of 15.8 μm/pixel. Volumes were analyzed using the NIH-supported digital image processing software, ImageJ, in three-dimensional (3D) tiff stacks. To measure shear slip, each volume was resliced perpendicular to the fracture to show a cross-section of each sample half. Pre-shear, initial, and subsequent day scans were compared using the Image Calculator function to identify changes in lengths of each cylinder half. Figure 3 illustrates the measurement method of shear slip.

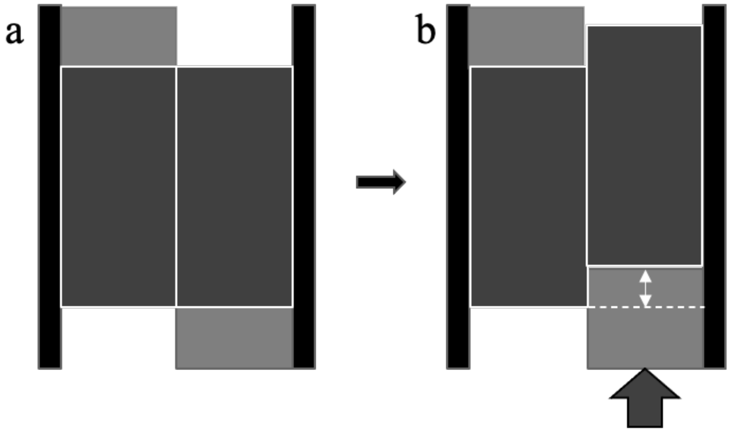

Figure 3: Shear slip measurement diagram of fractured core of a) pre-shear position and b) displacement after applied stress.

The data were input into the image analysis software, Ilastik, for segmentation to identify the central artificial fracture (Berg et al. 2019). Ilastik was set to pixel characterization and identified the central fracture and any equivalently sized secondary fractures by applying filters of Gaussian Smoothing (σ = 0.3-3.5), Laplacian of Gaussian (σ = 3.5-5.0), Gaussian Gradient Magnitude (σ = 3.5-5.0), and Difference of Gaussians (σ = 3.5-5.0). The segmented dataset was exported to create a 2D fracture aperture map with fluid flow simulated using a modified Navier-Stokes 2D flow model (NETL-Ap-Map-Flow) to calculate flow paths, transmissivity, and mean aperture as described elsewhere (M. Stadelman 2017), and in the Supporting Information (SI.i). The model was based on constant flow at the inlet and outlet set at 0.05 mL/min with no body forces.

2.v. Scratch Testing

Fracture toughness was evaluated using microscopic scratch testing as described in Akono 2021. In this test, a hard probe is pushed across a sample surface with a linearly increasing load. Scratch tests were conducted using an Anton Paar (Ashland, VA) microscope with a Rockwell C diamond probe, with a half-apex angle of 60° and a tip radius of 200 µm. Each test employed a maximum vertical force of 5.5 N over a length of 3 mm at a speed of 6 mm/min. Vertical and horizontal forces were recorded with load sensors with a resolution of 0.1 mN, and scratch depth was measured using a linear variable differential transformer (LVDT) system with a resolution of 0.3 nm. A nonlinear fracture mechanics models was used to calculate fracture toughness, K_c, in units of MPa $m^{1/2}$:

$$K_c = \frac{F_T}{\sqrt{2pA}}$$

In this equation, F_T is the measured transverse force, p is the perimeter of the probe, and A is the projected contact area of the probe with the surface. $2pA$ is a shape function that varies with the recorded depth and is calibrated to the probe's geometry.

Identified areas of interest for scratch testing are illustrated in Figure 4, which correspond to fracture surfaces in locations with different aperture depths. Area 1 corresponds to surfaces in channels between interlocking asperities (see Figure 1c) where the greatest flow velocity is anticipated. Area 2 corresponds to surfaces on raised asperities upflow from regions of contact with asperities from the opposing surface. Area 3 corresponds to surfaces opposite the asperities from the opposing surface. Area 4 corresponds to surfaces in the region of overlap between the interlocking asperities where the lowest flow velocity is anticipated. A total of 6-11 scratch tests were conducted for these areas of interest for unreacted Marcellus Shale and each sample experimental condition, except for Area 4, for reasons described in the results.

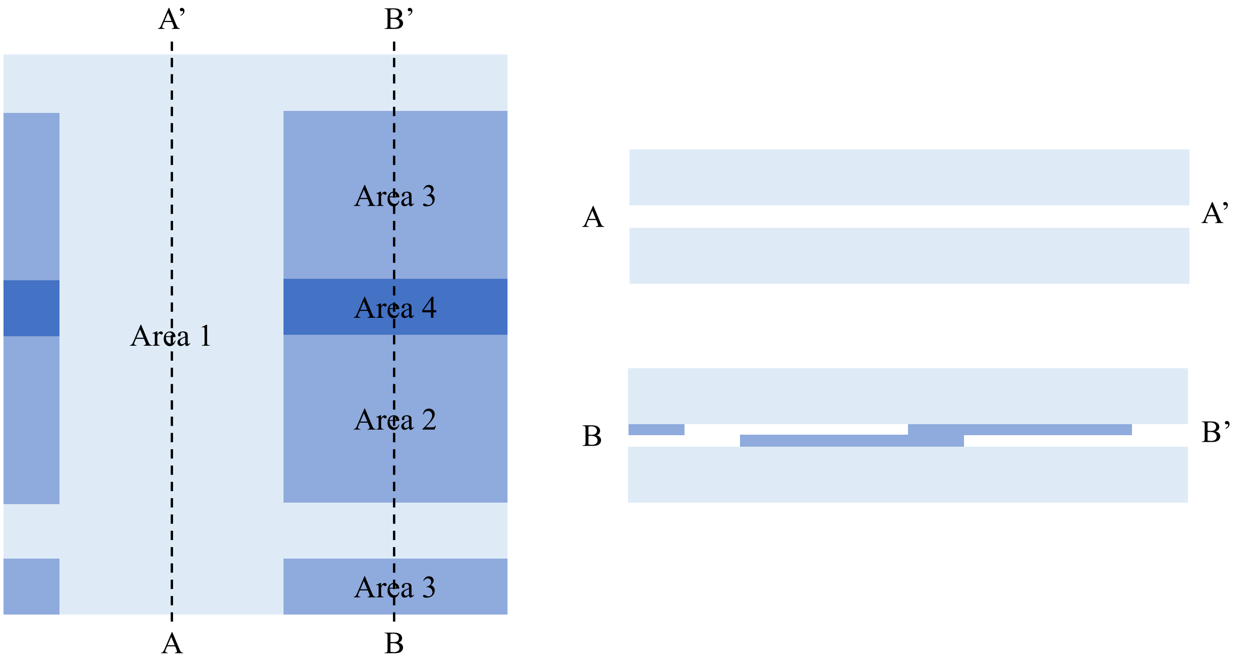

Figure 4: Plan and side view conceptual images of fracture aperture following shear. Flow is bottom to top. Each asperity is milled to be 0.1 mm high. Area 1: surfaces in channels between interlocking asperities. Area 2: surfaces on raised asperities upflow from regions of contact with asperities from the opposing surface. Area 3: surfaces on raised asperities downflow from regions of contact. Area 4: surfaces in the region of overlap between the interlocking asperities.

2.vi. Spectroscopic Methods

A summary of the experimental IDs and analyses performed is given in Table 1. A Leica DM 2500 compound light microscope with a Nikon camera was used to image the surface of samples in brightfield mode as well as thin sections of samples in brightfield and polarized light mode. A Wyko NT 9100 Optical Profilometer was used to quantify the surface roughness, Ra, (DeGarmo, Black, and Kohser 2003) determined by the arithmetic deviation from the mean height of the surface (SI.iii, Equation 3) using Vision Software. The data was collected using a 5X lens and a 0.55X field of view for a horizontal resolution of 3.67 µm/pixel across a vertical scan range of 200 µm at 1 µm resolution. A JEOL-JSM6490 Scanning Electron Microscope with Electron Dispersive Spectroscopy (SEM-EDS) was used to evaluate surface morphology and elemental composition of samples and thin sections. Samples were made conductive using a 20 nm carbon coat.

Table 1. Sample identities, experimental conditions, and techniques performed. MR represents Marcellus Shale, and 1 and 2 represent replicate experiments.

Sample ID	Flow Condition	CT Scan	SEM-EDS, Optical Microscopy	Profilometry, Scratch Test, Thin Section Petrology
MR1-pH4	pH 4	Initial, Day 0, 1, 2, 3, 4, and 8	Analyzed Pre- and Post- Reaction	Analyzed Pre- and Post-Reaction
MR2-pH4	pH 4			
MR1-pH9.5	pH 9.5	Initial, Day 0, 1, 2, 3, 4, and 7		
MR2-pH9.5	pH 9.5			

3. Results

3.i. Thin Section Mineralogy and Petrology

The primary reactive species in the Marcellus shale is calcite, followed by dolomite, feldspars, and clays (Black, Carroll, and Haese 2015). The spatial distribution of these species was evaluated before and after exposure to acidic and reservoir simulated brine using petrographic thin sections obtained near the fracture surface, coupled with optical microscopy and SEM-EDS. An example petrographic thin section of untreated Marcellus shale is shown in Figure 5; the thin section is imaged with an optical microscope under plane-polarized light (5a) and cross-polarized light (5b), and SEM (5c), with mineralogical assignments supported by elemental compositions from EDS. The overall matrix is comprised of fine, light quartz and calcite grains embedded in a darker matrix, broken up by irregular microfractures filled with calcite. There are off-vertical bedding planes with small calcite-filled microfractures parallel to the planes. Quartz and calcite represent the majority of the shale matrix along with significant clay coatings, along with spots of pyrite and organic carbon. Quartz and calcite are translucent under plane-polarized light, but calcite is iridescent under cross-polarized light. The larger calcite grains and clays make up the majority of the light-gray matrix of the shale in the SEM image, with darker quartz grains and the dark, organic carbon fractures becoming more prominent due to lower deflection of electrons from Si compared to Ca. Also, pyrite becomes distinguishable in the SEM image due to the high deflection of electrons from Fe, resulting in bright white grains as opposed to dark, non-reflective spots of organic carbon.

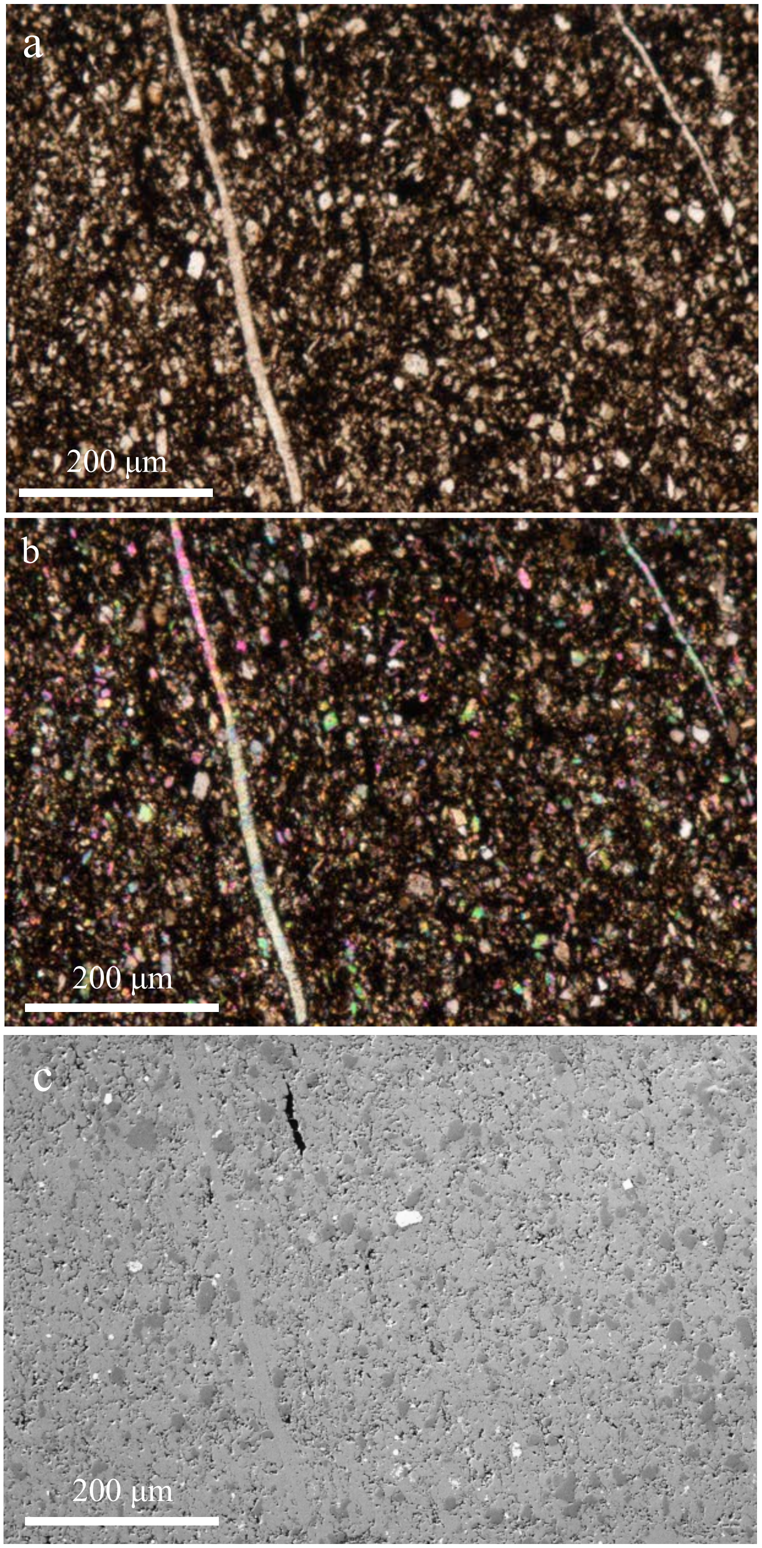

Figure 5: Images of unreacted Marcellus Shale thin section by a) plane-polarized light, b) cross-polarized light, and c) SEM. Calcite is (a) translucent, (b) iridescent, and (c) light gray.

Images of thin sections taken from shale samples after exposure to acidic or reservoir simulated brine are in the supporting information (Figure S2) and show no appreciable difference from the untreated sample. Thin sections were collected within 0.5 mm from the flat, milled surface of the channels. The lack of differences before and after exposure to the acidified brine is likely due to the low permeability of the Marcellus shale, which did not allow acid to penetrate to 0.5 mm below the channel surface.

3.ii Fractures Aperture and Flow Alteration

Sample fractures were identified by segmentation of the 3D CT scans using iLastik software. This data was used to create two-dimensional (2D) aperture maps of the fractures for the pre-shear and initial scans recorded on Day 0, plus each successive day of experimentation; these aperture maps were then input into a Stokes 2D flow model to identify flow paths and determine petrophysical flow parameters (Details in SI.ii). The aperture and flow maps are presented in Figure 6, with flow from bottom to top. All samples were initially expected to have four relatively large-aperture channels (oriented vertically in the figure) located between regions with interlocking asperities, with short segments of relatively large aperture connections (oriented horizontally in the figure) located between channels and interlocking asperities. This was initially the case for three of four samples, but with MR1-pH4 the apertures of the outer two channels and the horizontal connections were relatively smaller. In some cases, apertures of the outer two channels decreased later, but not in a consistent manner across duplicates. These effects are likely due to the confining stress around the cylinder, causing differential compression on the outside. Also, limited flow occurred upgradient and downgradient of overlapping aperatures (i.e., Area 4,

Figure 4), with higher flow upgradient (i.e., Area 2) than downgradient (i.e., Area 3). Overall, general differences or trends in aperture width for samples exposed to acidic versus reservoir simulated brine were not apparent.

Larger apertures corresponded to greater simulated flow rates in Figure 6, and most flow was in the center two channels. In some cases, flow became more concentrated in the center two channels over time, but not in a consistent manner across samples. Very little flow was apparent perpendicular to and between channels. Overall, general differences or trends in simulated flow were not apparent for acidic versus reservoir simulated brine.

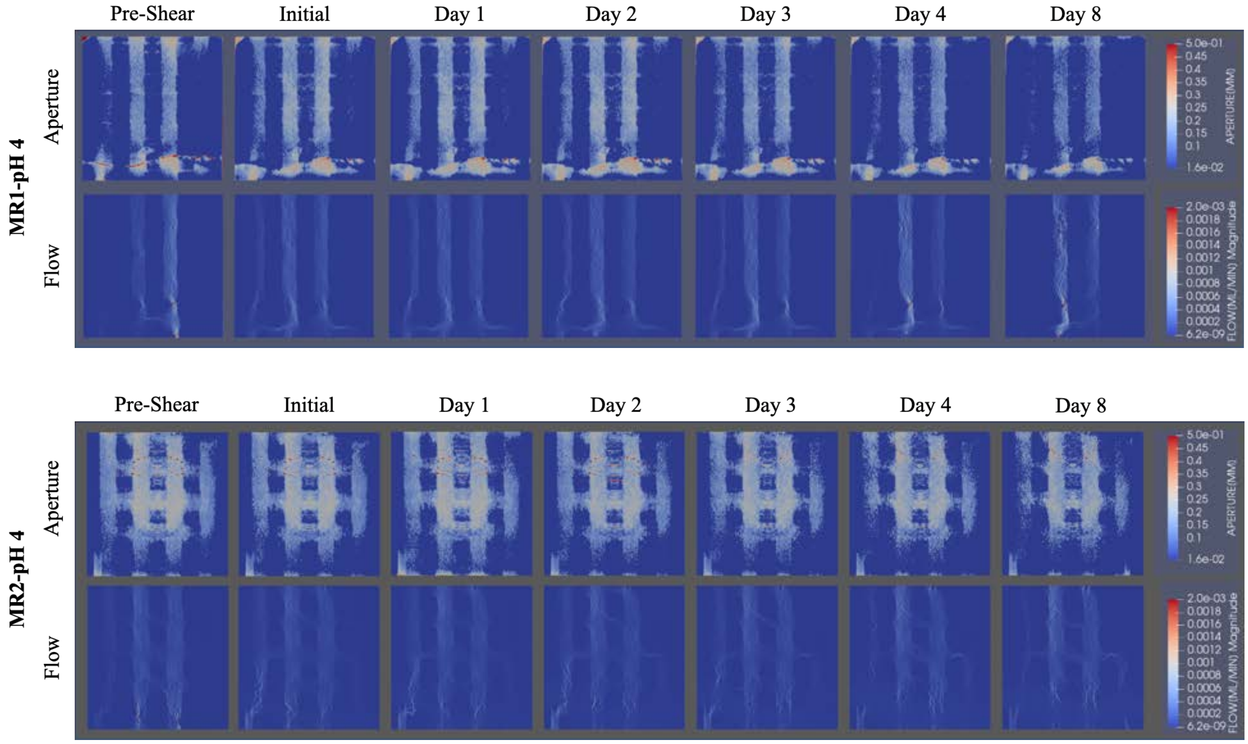

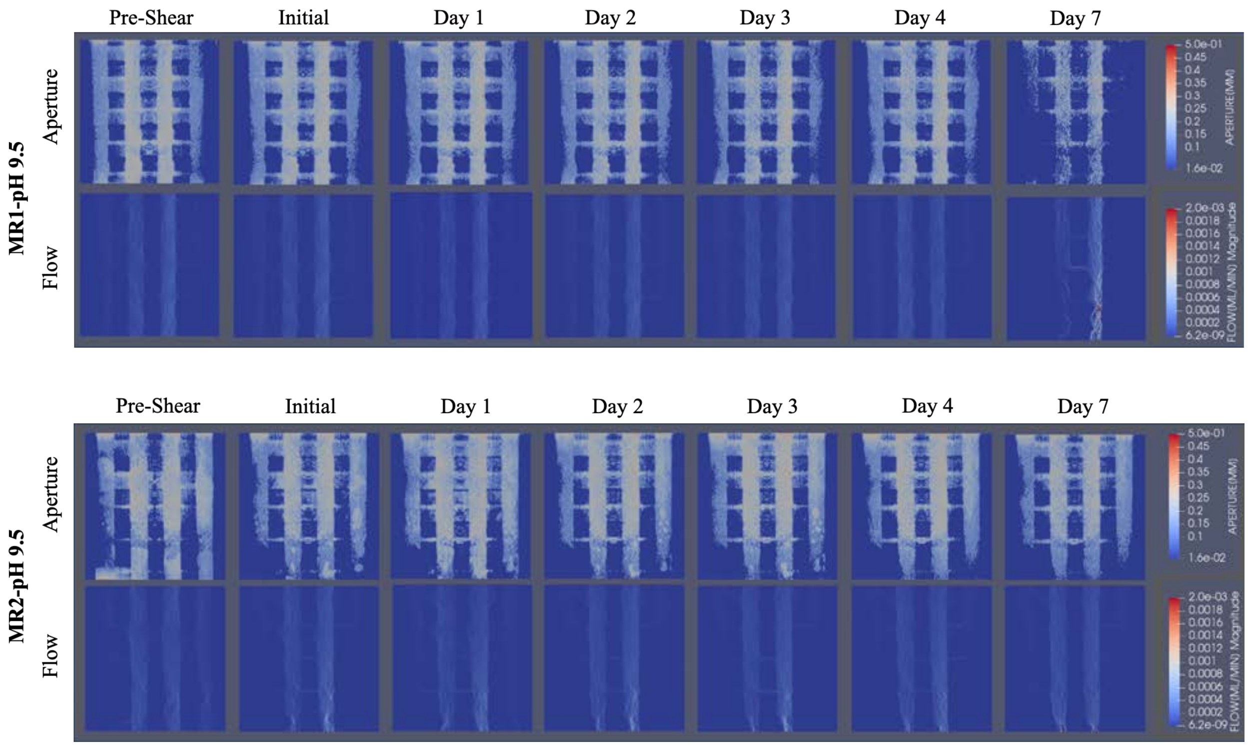

Figure 6: Aperture and flow maps for all experimental conditions.

Mean aperture and transmissivity values were calculated for all fractures across time, and results are presented in Figure 7. Generally, aperture and transmissivity values decrease over time for all cases, likely due (at least in part) to compression around each cylindrical sample. The samples prepared with acidified brine have lower mean aperture and lower transmissivity values compared to those prepared with reservoir simulated brine. This is the case for all time points, including Pre-Sheared conditions, suggesting either small differences in machine milling, sample clay swelling at the lower pH, or fast dissolution of surface calcite as the reason. The latter reason is supported by studies showing significant mechanical weakening can occur because of limited dissolution of carbonate cement at grain-to-grain contacts (Marbler et al. 2013; Rathnaweera et al. 2018; Fuchs et al. 2021).

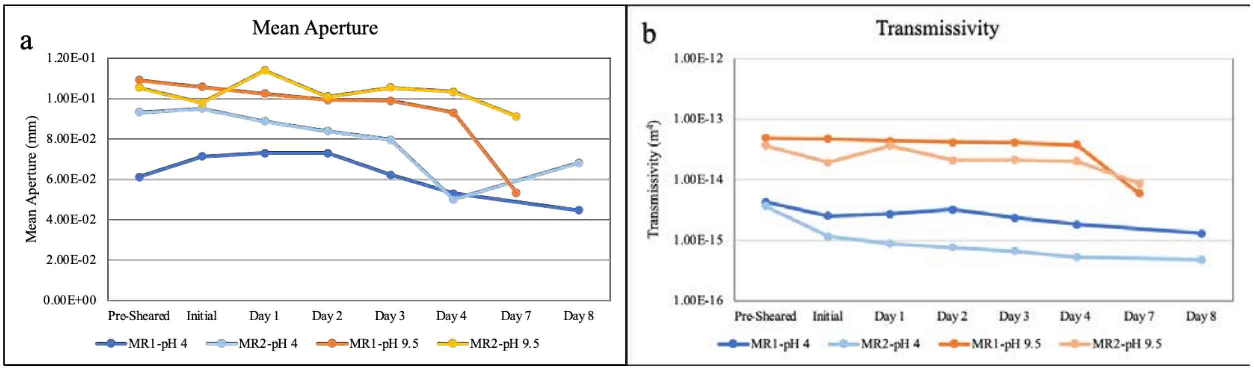

Figure 7: a) Mean Aperture and b) Transmissivity for all experiments at acidic (pH 4) and reservoir-simulated (pH 9.5) brine flow.

3.iii. Fracture Surface Morphology

Fracture surfaces from the core halves before and after exposure to acidic and reservoir simulate brine were evaluated by optical microscopy, SEM, and laser profilometry to analyze the effects of both chemical reaction and physical alteration from shearing. Optical images of the fracture surfaces are shown in Figure 8. In some locations material was lost from one side of the fracture surface and adhered to the opposite side, so the analysis focuses on areas where this delamination did not occur. The shale surface when unreacted were initially blue-gray, with clearly delineated milled asperities. After reaction, both aged samples were tinted reddish-brown due to oxidation of adsorbed iodine from the brine, which occurred after removal from the flow cell. The aged samples show darker rectangular “overlaps” on top of the asperities, which is a result of contact with the other side of the sample half’s asperities after applied shear. These overlaps were further analyzed by SEM. Several spots showed a white precipitate which was determined to be KCl and KI salt crystals (by SEM-EDS) precipitating on the scraped surfaced during the drying process, rather than geochemical reaction during the flow experiments. Images of replicates are provided in the SI (Figure S3).

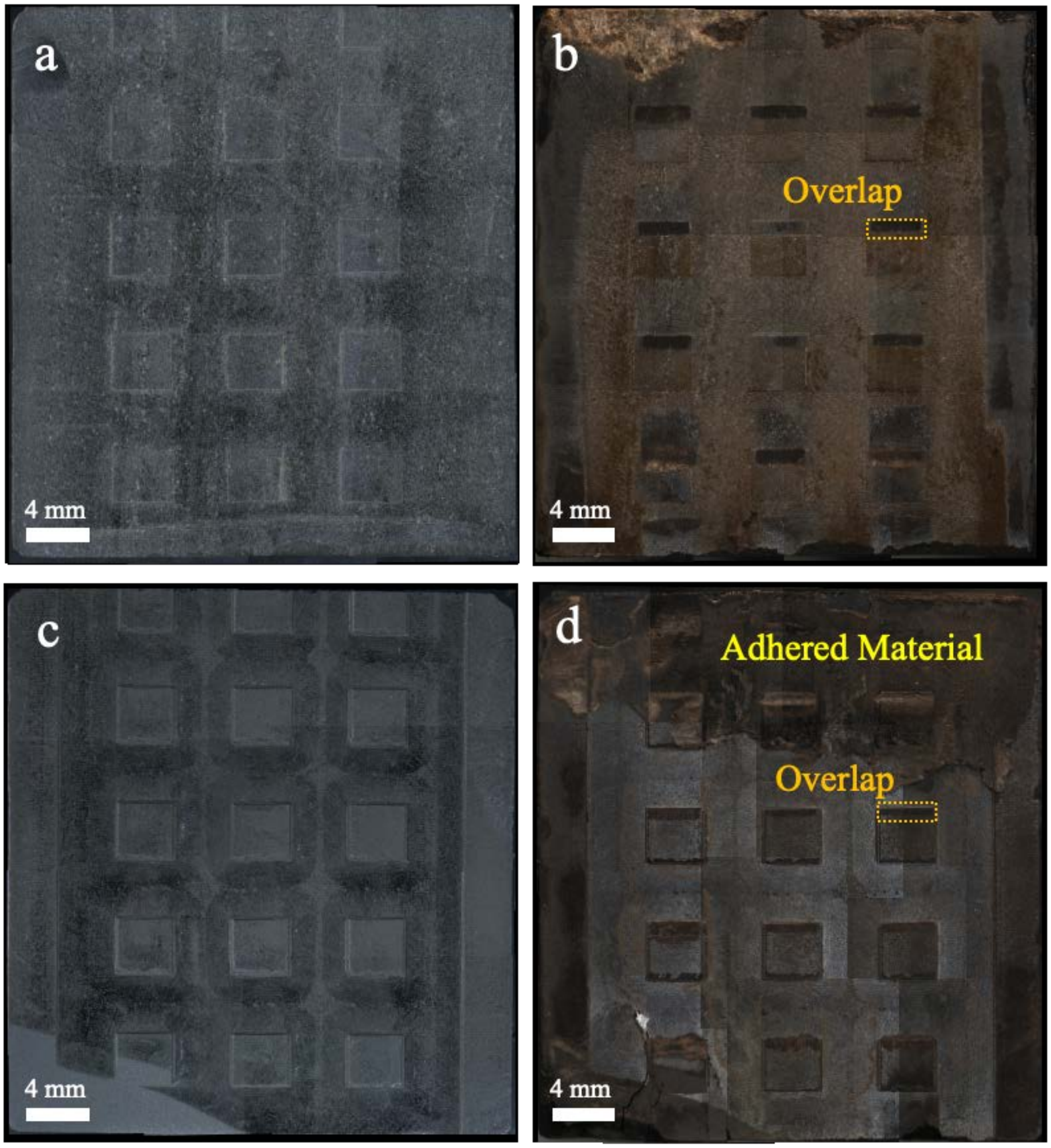

Figure 8: Optical Microscope images of a) unreacted MR2-pH 4, b) aged MR2-pH 4, c) unreacted MR2-pH 9.5, and d) aged MR2-pH 9.5. Dashed box and 'Overlap' give an example of where asperities were in contact with opposite half of reacted, fractured shale. 'Adhered material' describes a delamination of shale from the opposite half that has stuck.

SEM images of fracture asperity surfaces before and after brine exposure are shown in Figure 9. The unreacted sample images show milled, delineated surfaces, as expected from the optical images, and then varied alteration after each experiment (Figure 8). There were two observed types of physical change at each asperity overlap, where the samples were sheared together: sliding and scraping. In the cases of sliding, exposure to acidified brine resulted in a compressed, irregular edge that was smeared upwards with contact, in the opposite direction of shearing motion (Figure 9b). Exposure to reservoir-simulated brine resulted in an intact edge with vertical striations in the overlap area, following the direction of sliding by contact with the asperity from the opposite sample half (Figure 9d). In the cases of scraping, both acidified brine and reservoir-simulated brine resulted in the asperity edges catching on each other and breaking portions of the material (Figure 9f, h). Approximately equal numbers of asperities on samples exposed to reservoir-simulated brine showed evidence of sliding vs. shearing, likely due to the corresponding asperity on the opposite sample half. However, the majority of asperities exposed to acidified brine (~75%) showed sliding, with the samples that did exhibit scraping resulting in significantly smaller quantities of scraped material compared to the reservoir-simulated brine. These morphological results suggest that the matrix of the asperities, after initial reaction, was sufficiently weakened under pH 4 to be more compressed and smeared than under pH 9.5. This compression corresponds to the smaller mean aperture values (Figure 7).

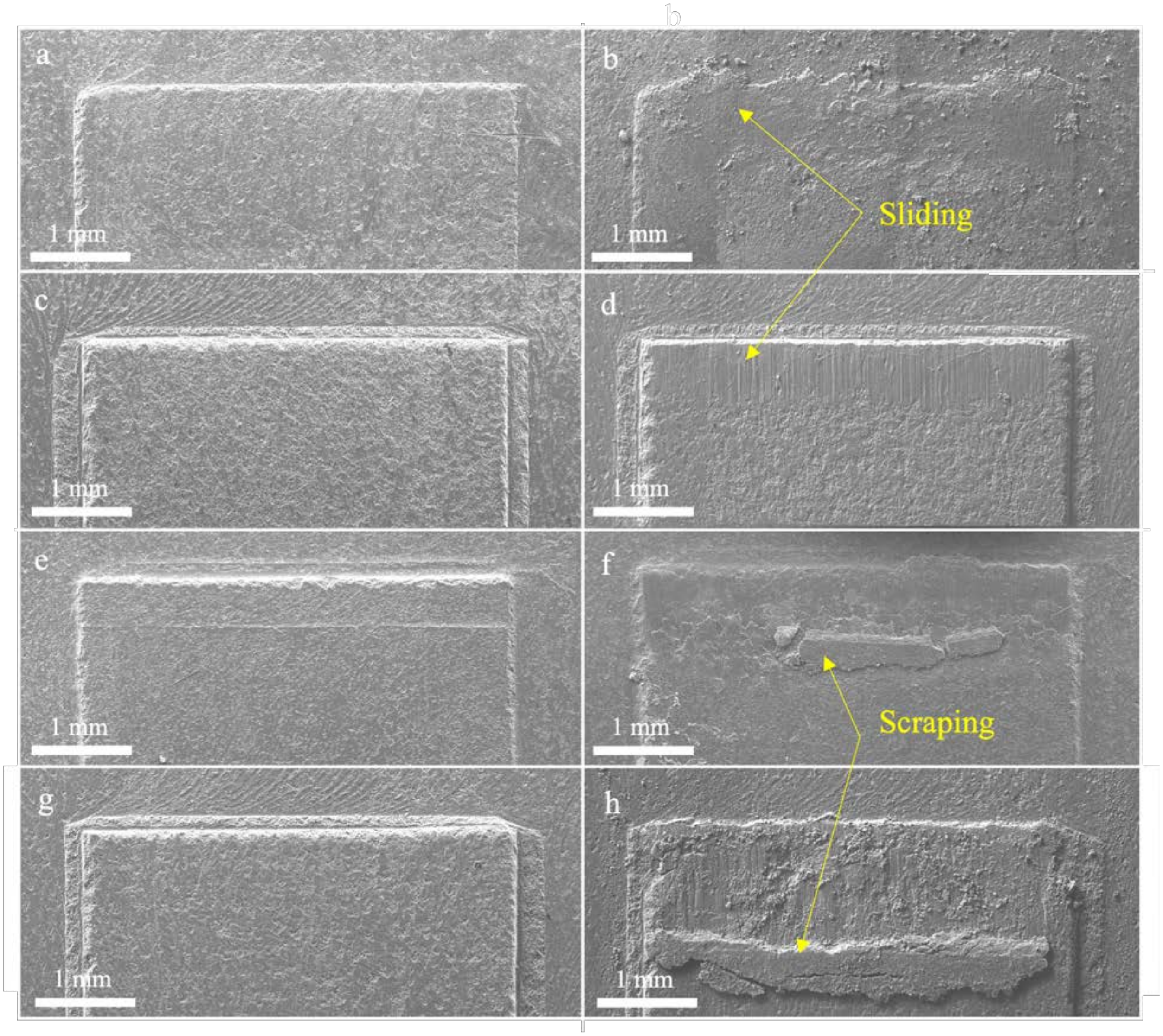

Figure 9: SEM Images of a) unreacted MR2-pH 4, b) reacted MR2-pH 4 exhibiting sliding and compression, c) unreacted MR1-pH 9.5, d) reacted MR1-pH 9.5 exhibiting sliding and vertical striations, e) unreacted MR2-pH 4, f) reacted MR2-pH 4 exhibiting scraping and compression, g) unreacted MR1-pH 9.5, and h) reacted MR1-pH 9.5 exhibiting scraping with a large amount of moved material. In (f), the scraped material does not appear to be a stuck layer from the opposite half of the sample due to the milling artifact line present in (e) appearing on the surface of the asperity in (f).

Higher magnification images from flow channels between asperities were taken by SEM and are shown in Figure 10. The milled surfaces of both unreacted samples have some irregular dips, possibly due to grain plucking during milling, and are not completely smooth. However, after reaction, the acidified brine reacted sample has a much rougher, discontinuous surface than the reservoir-simulated brine. The acidified brine sample no longer has recognizable divots despite being in the same area, whereas the reservoir-simulated brine surface is still similar to the original, with matched pits.

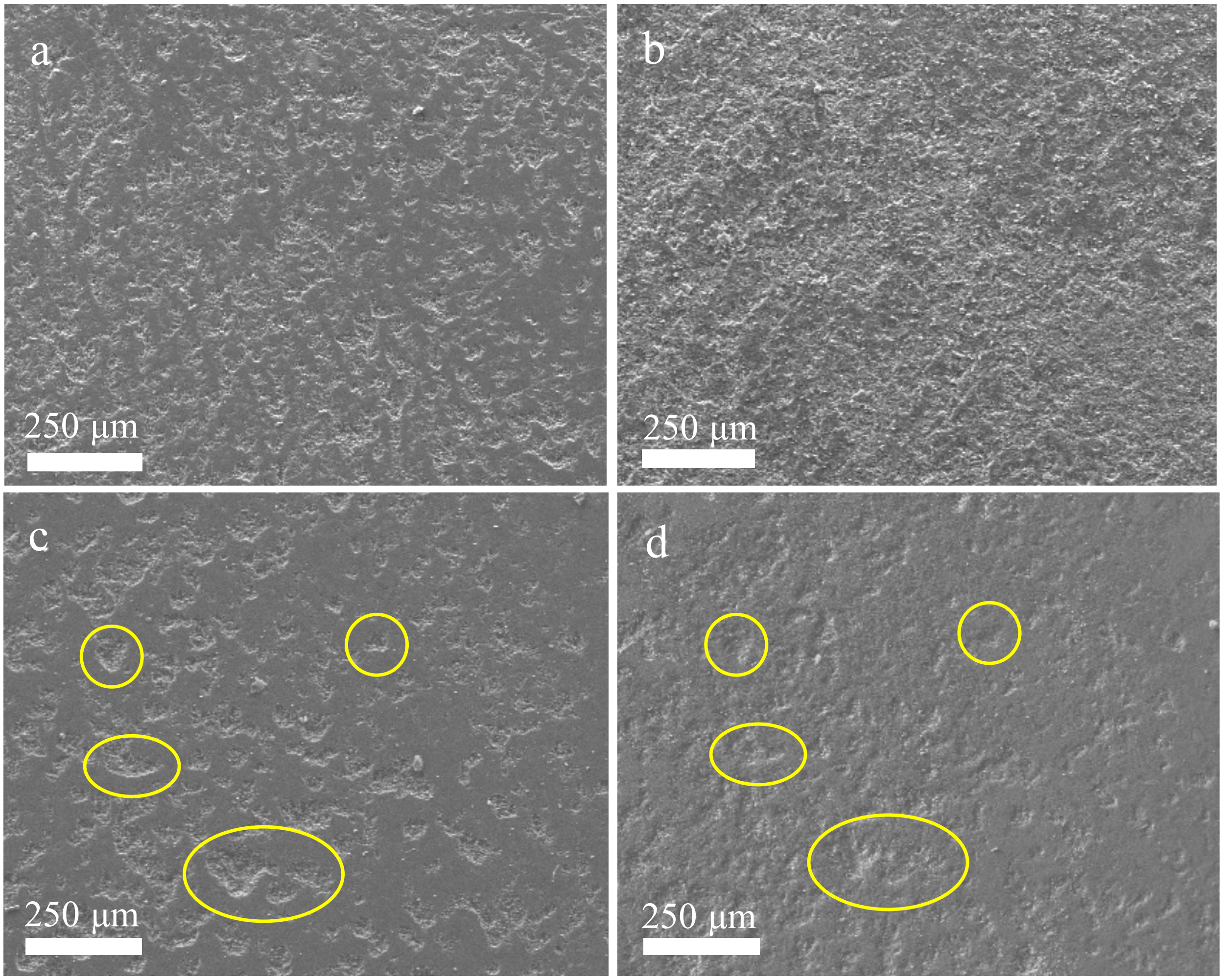

Figure 10: SEM Images of channel surfaces of a) unreacted MR1-pH 4, b) reacted MR1-pH 4, c) unreacted MR2-pH 9.5, and d) reacted MR2-pH 9.5. Pits in unreacted MR2-pH9.5 remain after reaction without significant loss (examples given in yellow circles), but surface is more greatly altered for MR1-pH4.

An optical profilometer was used to measure surface height as well as roughness of the unreacted and reacted samples. Images showing example asperity and channel regions for each condition are presented in Figure 11. The asperity height on the shearing edge was reduced in the acidified brine case from 100 μm to ~50 μm, but not in the reservoir-simulated brine case, which remained at ~100 μm. This corresponds to the compression and smearing qualitatively observed in the SEM imagery.

Roughness analysis was conducted both in channels between asperities and on top of asperities where contact occurred. This was done to differentiate geochemical alteration that could occur solely due to geochemical reaction from unobstructed flow and alteration that could be due to both physical shearing and limited flow. The roughness analysis of the asperities excluded the edges due to the sharp discontinuity of the surface. All values are reported in Figure 12. In the flow channels, the roughness was initially 1.198 ± 0.541 μm, which increased significantly after shearing experiments; roughness was 3.055 ± 2.491 μm after reaction with acidified brine and 1.578 ± 0.711 μm after reaction with reservoir-simulated brine. Both the acidic and reservoir-simulated channels were significantly rougher than the initial (two-tailed test for results compated to the original were $p = 0.00166$ and $p = 0.0346$ respectively) but most importantly, the roughness after acidic reaction was significantly higher than the reservoir-simulated control ($p = 0.00491$). On the center of the raised asperities, but not at the leading edge where smearing or scraping was observed, the surface roughness increased for all reacted shale samples. The roughness increased from the initial 2.433 ± 0.266 μm to 6.121 ± 1.840 μm for acidic conditions and 5.675 ± 0.941 μm reservoir-simulated conditions. The acidic and reservoir-simulated cases were significantly different compared to the initial case ($p = 2.323 \times 10^{-4}$ and $p = 4.394 \times 10^{-7}$ respectively), but they were not different compared to each other ($p = 0.4673$). The asperity surface roughness is significantly higher after reaction with either pH compared to the channel surface roughness, indicating that the physical alteration due to shearing has a greater effect on surface roughness than chemical reaction alone.

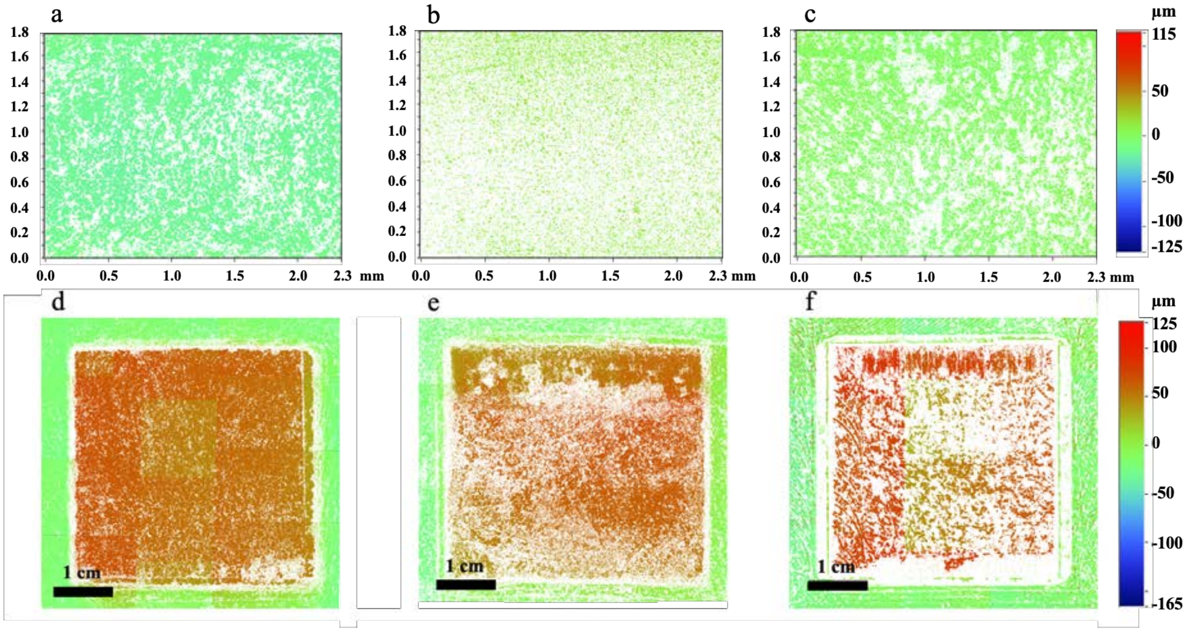

Figure 11: Optical Profilometry images showing surface height for (a-c) channels and (d-f) asperities for a,d) unreacted, milled Marcellus Shale, b,e) MR1-pH4 after reaction, and c,f) MR2-pH9.5 after reaction. Note, these images are comprised of 16 individually stitched together maps with relative "0" resetting occurring in the center of the asperities without reference to the channel; this reset the color scale, particularly noted in (d) and (f).

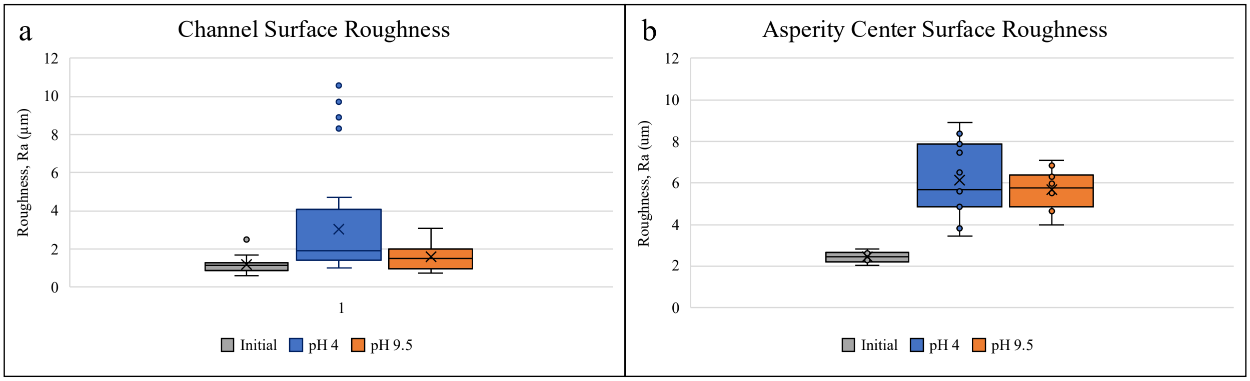

Figure 12: Surface Roughness, Ra, measured from optical profilometry images of a) surface channels and b) asperity centers.

3.iv. Fracture Toughness

The fracture toughness of Marcellus shale surfaces after exposure to the acidic and reservoir simulated brine were analyzed by micro-scratch testing to assess the extent of alteration during the week-long experiments. This method probes the first ~0.5 mm of the surface. Results are plotted in Figure 13 and provided in Table 2, with statistical analysis provided in Table 3. Scratch tests were performed on three different surface areas of interest, chosen for their differences in aperture width and access to flow. These correspond to Areas 1-3 in Figure 4; Area 4 was not evaluated because the surface was too irregular.

After reaction with brine, both acidic and reservoir-simulated conditions resulted in significantly decreased fracture toughness compared to the initial values, with the acidified brine resulting in the greatest decrease overall. In the open channels, fracture toughness decreased from 1.261 ± 0.036 MPa $m^{1/2}$ initially, to 0.462 ± 0.074 MPa $m^{1/2}$ after reaction with acidified brine, to 0.871 ± 0.089 MPa $m^{1/2}$ after reaction with reservoir-simulated brine. Interestingly, there are opposing and statistically significant trends for the samples exposed to acidic versus reservoir simulated brine. In the former, fracture toughness increases from Area 1, to 2, and finally 3, while for the reservoir simulated brine the opposite trend occurs. Area 1 corresponds to the main flow channels and receives the most flow. Area 2 is downflow from the larger aperture horizonal segments, and upflow from the region of aperture overlap (Area 4). It receives more flow than Area 3, which is downflow from Area 4. Overall, access to fresh brine increases from Area 1, to 2, and finally 3. Therefore, the fracture toughness decreases for areas exposed to more acidified brine, as expected. However, the fracture toughness increases for areas exposed to more reservoir-simulated brine; potential reasons for this non-intuitive behavior are discussed in a later section.

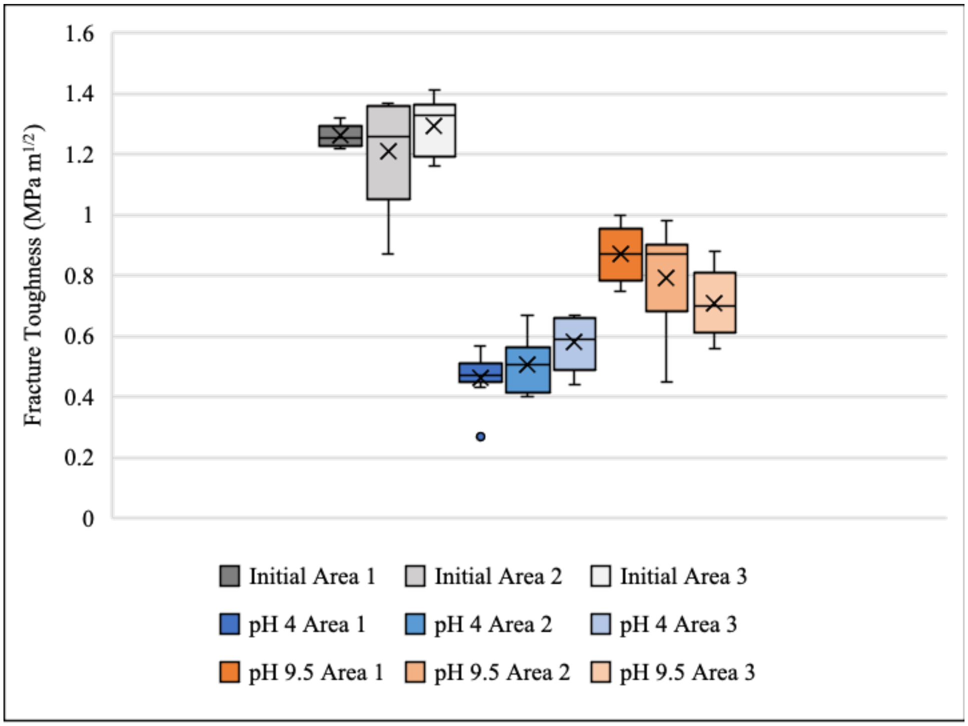

Figure 13: Fracture Toughness measured along channel surface of Marcellus shale initially, after exposure to acidified brine, and after exposure to reservoir-simulated brine according to areas of interest.

Table 2: Scratch test results for Marcellus shale samples before and after experiments according to areas of interest.

	Initial			pH 4			pH 9.5		
	Area 1	Area 2	Area 3	Area 1	Area 2	Area 3	Area 1	Area 2	Area 3
verage Fractur oughness MPa $m^{1/2}$]	1.261	1.211	1.295	0.462	0.505	0.581	0.871	0.792	0.709
Standard Deviation	0.036	0.180	0.093	0.074	0.096	0.082	0.089	0.162	0.109

Table 3: P values from calculated T-tests (Two-Sample Assuming Equal Variances) for fracture toughness measurements in specific Areas of interest. Initial Marcellus shale samples were not statistically different to each other depending on Area. Corresponding Areas for the Initial sample were used to compare to the Area of either pH 4 or pH 9.5 samples for analysis. Data are considered to be significantly different for $p<0.05$ and bolded to identify.

		Initial	pH 4			pH 9.5		
		*	Area 1	Area 2	Area 3	Area 1	Area 2	Area 3
Initial	*		**1.08E-17**	**8.25E-07**	**6.29E-13**	**1.68E-10**	**5.32E-05**	**5.87E-10**
pH 4	Area 1			3.18E-01	**1.96E-03**	**5.46E-10**	**7.26E-06**	**6.47E-03**
	Area 2				1.07E-01	**2.05E-06**	**1.57E-03**	**2.05E-03**
	Area 3					**2.64E-07**	**1.16E-03**	**6.47E-03**
pH 9.5	Area 1						1.93E-01	**1.86E-03**
	Area 2							1.96E-01
	Area 3							

3.v. Shear Slip

The shear slip following a single applied stress in the milled, artificial fractures with flow by either acidic (pH 4) or reservoir-simulated (pH 9.5) brine was not significantly different for all samples, and equal to 0.068 ± 0.63 mm (Figure S4). Additionally, a volume-averaged compressive strain was measured for the change in length of the shale due to the applied stress and resulting shear stress of the fracture asperities, and values were not significantly different (Figure S4). We note that the volume-averaged compressive strain is not true strain, as the strain-field in the sample is non-homogenous. Although the samples held limited strain following the initial applied stress, no further slip or strain release occurred for any sample over the course of brine flow through the fractures over the week-long experiments. This is predicted to be because the ratio of shear to effective normal stress was too low, and asperity crushing would occur over shear slip. A remaining question is under what conditions, such as higher shear stress to effective normal stress, extended time, or lower pH, would slip occur.

3.vi. Mineralogical Analysis

Mineralogical analysis for the Marcellus shale reacted with either acidified brine or reservoir-simulated brine was inconclusive. Analysis by SEM-EDS did not show significant differences in the surface compositions of sample fractures following reaction with either pH 4 or pH 9.5 brine. Brine results were collected at the outlet, but samples showed no significant difference following experimentation in the compositions of Al, Ca, Fe, K, I, Mg, Na, S, and Si (Figure S5). It is likely that dissolution reactions are occurring, based on SEM imagery and surface roughness increase, but dissolution of calcite or other cements are not apparent from bulk effluent brine analysis. The initial concentrations of K^+ and I^- were significantly lower than input concentration for all experiments, likely due to sorption of iodide to stainless steel (with potassium due to electroneutrality), as has been demonstrated in the literature (Azim, Muralidharan, and Venkatakrishna Iyer 1995; Jeyaprabha, Sathiyanarayanan, and Venkatachari 2006; Khadom, Abd, and Ahmed 2018; Garcia-Ochoa et al. 2020) and in our previous work (Fuchs et al. 2021). The only difference noted between experimental conditions was that the acidified brine experiments resulted in saturation of KI sorption by the end of 8 days, but the reservoir-simulated brine experiments had not; this could indicate that potassium is being sorbed or exchanged with other ions in clays to a greater extent in the reservoir-simulated case.

4.i. Discussion and Conclusions

In this work, we uniquely probe how acidic versus reservoir simulated brine flow affects the physical, chemical, and geomechanical integrity of shale surfaces in a variable-aperature artificial fracture following a single shear event in a shearing triaxial core holder. In agreement with our initial hypothesis, we find that acidified brine promotes greater pitting, enhanced surface roughness, and decreasing fracture toughness in primary flow channels, with less alteration occurring in areas of smaller fracture apertures. However, in contrast to our initial hypothesis, this alteration following 8 days of reaction under acidified brine did not result in fracture slip as measured by CT scanning in the shearing apparatus. We note that our approach is unique because more commonly destructive shear tests are performed, such as triaxial compression and direct shear for measurements of permeability, strength and stiffness (Marbler et al. 2013; Zhang et al. 2020; Delle Piane and Sarout 2016), and the effects of heterogeneous flow paths are not considered. Geochemistry is also not typically a focus of shear slip experiments, with many studies focusing on CO_2 injection pressure (Jiang et al. 2018) and hydrodynamic effects with stress-induced fracturing (M. A. Stadelman 2017; Frash et al. 2016, 2018). In the discussion that follows, the main results of this work are explored in more detail and compared to the literature.

The differences in fracture aperture before and after reaction were evaluated by 3D CT scanning. Aperture maps provide evidence of fracture closing from the outside channels in, but this was not uniform among sample replicates; also, acidic cases show the smallest mean aperture values, possibly due to clay mineral swelling under these conditions. Flow model results show that flows were inversely related to aperature widths, with greater flow occurring in large aperature channels between regions of interlocking raised asperities. Detailed surface inspection was conducted on fracture surfaces after exposure to brine flow using visual microscopy, optical profilometry and SEM. Visual observation showed the shearing of the fracture halves resulted in either sliding or scraping of the contact zone between asperities, with the acidified brine causing greater instances of sliding, with the asperities compressed and smeared with contact. This was reinforced by reduced height observed in the profilometer images for acidified brine reacted samples. Additionally, SEM and profilometry noted increased roughness of the open channels and asperity surfaces. The channels are expected to only be altered due to chemical reaction, while the asperities are expected to experience both chemical and physical alteration due to contact from shearing. The morphological change at the surface, particularly in the high brine flow channels, indicates that dissolution reactions are occurring.

The surface pitting and roughness increase we observed on the Marcellus shale fracture surface upon exposure to acidic brine is consistent with observations by others. For example, significant surface etching and pitting was observed for Utica shale exposed to $scCO_2$, and this was attributed to the dissolution of calcite (Goodman et al. 2019). Pitting and increased surface roughness upon exposure of shales to acidic brine has also been observed in other studies, and shown to increase with increasing carbonate content (Guo et al. 2017). Prior studies have also shown greater reaction in areas of preferential flow. For example, CT scanning was used to show calcite dissolution and increased channelization in fractured carbonate rock along preferential flow paths exposed to low pH brine, with positive feedback between flow and reaction (Deng et al. 2013, 2015). Also, a reactive transport model was used to simulate experiments with acidic flow through a carbonate rich-shale fracture, and initial calcite dissolution created a porous, altered surface before flow channeling eroded the weakened porous layer (Deng et al. 2017).

The extent of the impact of geochemical reactions on fracture toughness was quantified by scratch testing. Overall, both acidic and reservoir-simulated conditions resulted in significantly decreased fracture toughness compared to the initial values, with the acidified brine resulting in the greatest decrease in every measured area of interest on the fracture surface. The lowered fracture toughness in the reservoir-simulated brine is likely due to the pressurized hydration of the shale clays, which has been found to reduce fracture toughness in shale (Lyu et al. 2017; Xiong et al. 2019). The lower fracture toughness in acidic conditions indicates additional chemical reactions are taking place, which are weakening the shale matrix, such as dissolution of calcite. The decreasing fracture toughness observed for the Marcellus shale after exposure to acidified brine is also consistent with results from similar studies in the literature. For example, in a stratified, carbonate-rich Mancos shale exposed to $scCO_2$-saturated brine at 2500 psi and 90°C, calcite-dolomite-clay-rich layers showed a reduction of scratch toughness of 50 ± 20% (Ilgen et al. 2018). A clay-rich shale exposed to $scCO_2$ saturated brine was significantly deteriorated after 63 days, with observed surface dissolution and roughening with a more than 30% reduction in compressive strength (Choi, Kim, and Song 2021).

Unique to our results is the coupling between preferential brine flow and geomechanical alteration in fractures. For example, the fracture toughness is lower for high flow channels versus low flow asperities after exposure to acidified brine. Hence, the decrease in fracture toughness corresponds to greater availability of H_3O^+ for dissolution of calcite, the primary cementing phase in the Marcellus shale. By contrast, fracture toughness decreases with decreasing flow after exposure to reservoir-simulated brine. The reservoir-simulated brine was made by pre-equilibrating 0.5 M KI with crushed Marcellus shale. It's possible this brine is promoting secondary precipitation at the fracture surface, which could cause the shale surface to be more brittle in areas of greater flow. Overall, the most significant finding is that acidified brine flow results in decreased fracture toughness, with the greatest reduction occurring in areas of high flow rate.

We could not directly attribute fracture toughness reduction to dissolution of calcite or other minerals. The composition of the Marcellus shale studied in this paper was 45.9% quartz, 26.6% calcite, 4.0% dolomite, 15.3% muscovite, 1.2% kaolinite, 1.4% K-feldspar, 2.8% Na-feldspar, and 2.8% pyrite by X-Ray Diffraction (XRD). The primary reactive species within our shale under acidic conditions is calcite, and then dolomite, feldspars, and lastly clays (Black, Carroll, and Haese 2015). Our petrographic thin sections and EDS data confirmed that there is significant calcite, and it is distributed throughout the shale and present in filled microfractures, providing structural support as a cement to the matrix. We were unable to detect mineralogical changes of each sample pre- and post-reaction due to several reasons. First, XRD analysis requires 5 g of powder for analysis of clays, which requires the top 1.5 mm of the shale fracture surface to be collected per sample; this is likely much more shale than was altered during flow due to the low permeability of shale and limited penetration into the pore space. A thinner surface collection across multiple samples was not attempted because of the destructive nature of powder XRD and the need to preserve some samples for thin section petrology. Second, the thin sections that were created did not include material directly at the shale fracture surface, but 0.5 mm below, where again acidified brine may not have reached due to the low permeability of the shale. Finally, the SEM-EDS was used to view the surface directly after reaction with either acidic or reservoir-simulated brine; surficial alteration was noted with SEM, but elemental analysis with EDS indicated similar concentrations of Ca and other elements due to fine grain sizes in the shale matrix. Limited dissolution at grain-to-grain contacts would not be apparent. Other studies have successfully demonstrated carbonate dissolution resulting in similar mechanical weakening as in our study. In one case, a brine-wet, carbonate-rich Utica shale exposed to $scCO_2$ observed surface pitting and corresponding dissolution of carbonate, similar to our SEM and profilometer imagery (Goodman et al. 2019). In another study, carbonate-rich shale exposed to $scCO_2$-saturated brine for 15 days at 15 MPa and 60°C resulted in a 20% decrease in compressive strength with a 6% decrease in carbonate content (Yang et al. 2022). A small loss of calcite cementation could still result in a significant loss of fracture toughness, as significant mechanical weakening can occur because of limited dissolution at grain-to-grain contacts (Marbler et al. 2013; Rathnaweera et al. 2018; Fuchs et al. 2021)

Despite the decrease in fracture toughness that we observed after exposure to acidified brine, our experiments did not indicate further slip following the initially applied stress. This is likely because the shear stress was too low relative to effective normal stress. Unfortunately, shear stress could not be measured directly with the current experimental set up and would require refinement to confirm. This apparatus did allow for geochemical alteration to occur with different pH brine flow and further experimentation with measurable shear stress could allow for shear slip observation. Other studies have observed mineralogical links between frictional strength or shear fracturing and the carbonate and phyllosilicate or tectosilicate content in shale (Fang et al. 2018). Others have also observed a decline in tensile strength and surface friction coefficient upon exposure of a carbonate-bearing shale to supercritical-CO_2-saturated brine, and this coincided with the dissolution of calcite, dolomite, K-feldspar, and albite (Zou et al. 2018). In our previous work, we observed increased shear slip during exposure to acidified brine flow that was attributed to dissolution of carbonate cements and subsequent reductions in fracture toughness in a dolomite-cemented sandstone (Fuchs et al. 2021). SEM results from our work indicate asperities experience more wear under acidic versus reservoir-simulated brine flow, indicating further shear slip may occur in Marcellus shale subject to acidified brine flow for longer times, but this remains to be verified. The coupled effects of geochemical reaction and hydrological flow paths on geomechanical properties warrants further study to resolve this gap in knowledge.

This study introduced a novel method of analysis of shear slip in artificially fractured shale and localized geochemical and geomechanical alteration. While this study covered a limited timescale and did not demonstrate slip, it provided insights into the effects of geochemical alteration on fracture surface topology and toughness as a function of access to flow with acidified brine. In future work, other factors such as higher shear stress, variable fracture geometry, brine composition, and experimental duration should be changed to extend results from our work, and to probe relationships with shear slip. Such results will provide new insights for predicting the stability of shale surfaces and fractures to guide selection of the most appropriate sites for GCS.

SI: Supporting Information

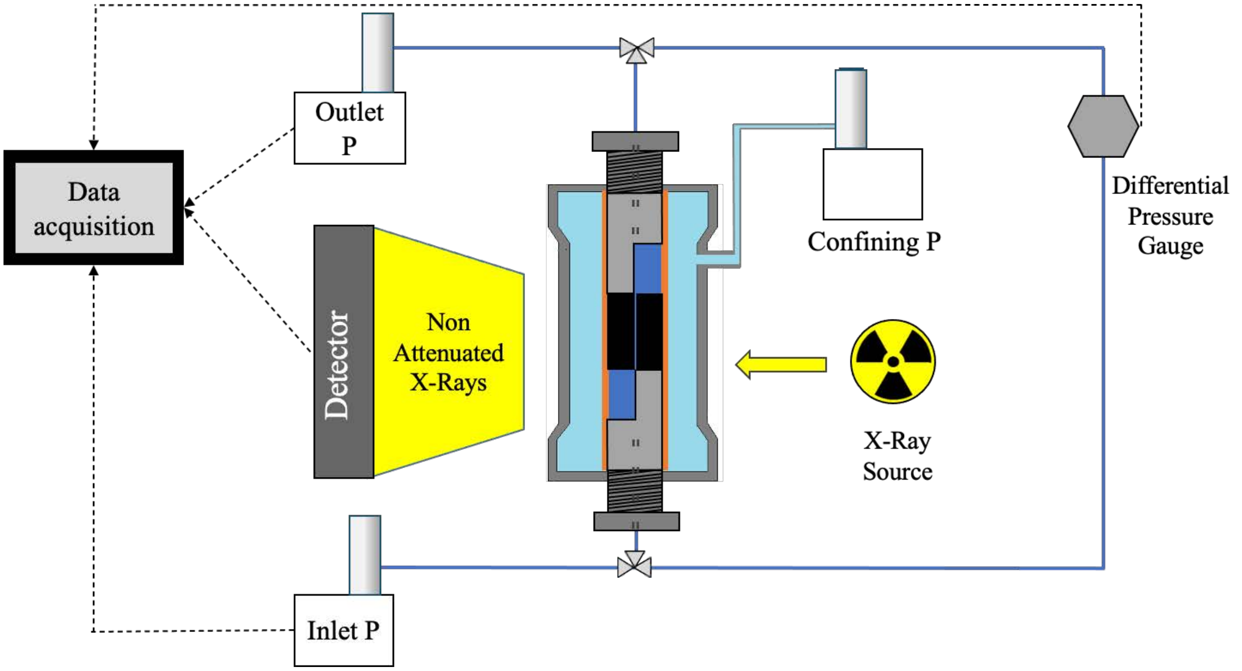

Figure S1: Industrial CT Scanner Experimental set up within shielded room, showing core holder, ISCO pumps, X-Ray source, detector, and data acquisition. Modified from Fuchs et al. 2021.

SI.i NETL-Ap-Map-Flow Model

The Stokes Flow 2D model, NETL-Ap-Map-Flow, takes an input binary image of a discrete fracture to create and aperture map through which it runs a flow model. The flow is solved as a finite volume problem according to the backwards time-centered space method (M. Stadelman 2017). Flow is assumed to be laminar and viscous-dominated, assumptions that equate the flow through narrowly spaced parallel plates from Navier-Stokes equations of continuity to Darcy’s law for flow through porous media. This can be described mathematically as:

$$Q = T_{local}\ \Delta P/L \qquad \text{(Equation 1)}$$

where T_{local} is the transmissivity and ΔP is the 2D pressure gradient across the length, L. Local transmissivity accounts for physical characteristics of the boundary between two grid points in the aperture map according to change in aperture size and permeability. Transmissivity can also account for viscosity, but viscosity was set constant for these models.

SI.ii Surface Roughness

Surface roughness is calculated using parameter Ra, which describes the arithmetic difference to the mean surface profile, or average height. Roughness is calculated according to Equation 2, with l_r describing the length of the surface being evaluated.

$$Ra = \frac{1}{l_r}\int_0^{l_r} |z(x)|\, dx \qquad \text{(Equation 2)}$$

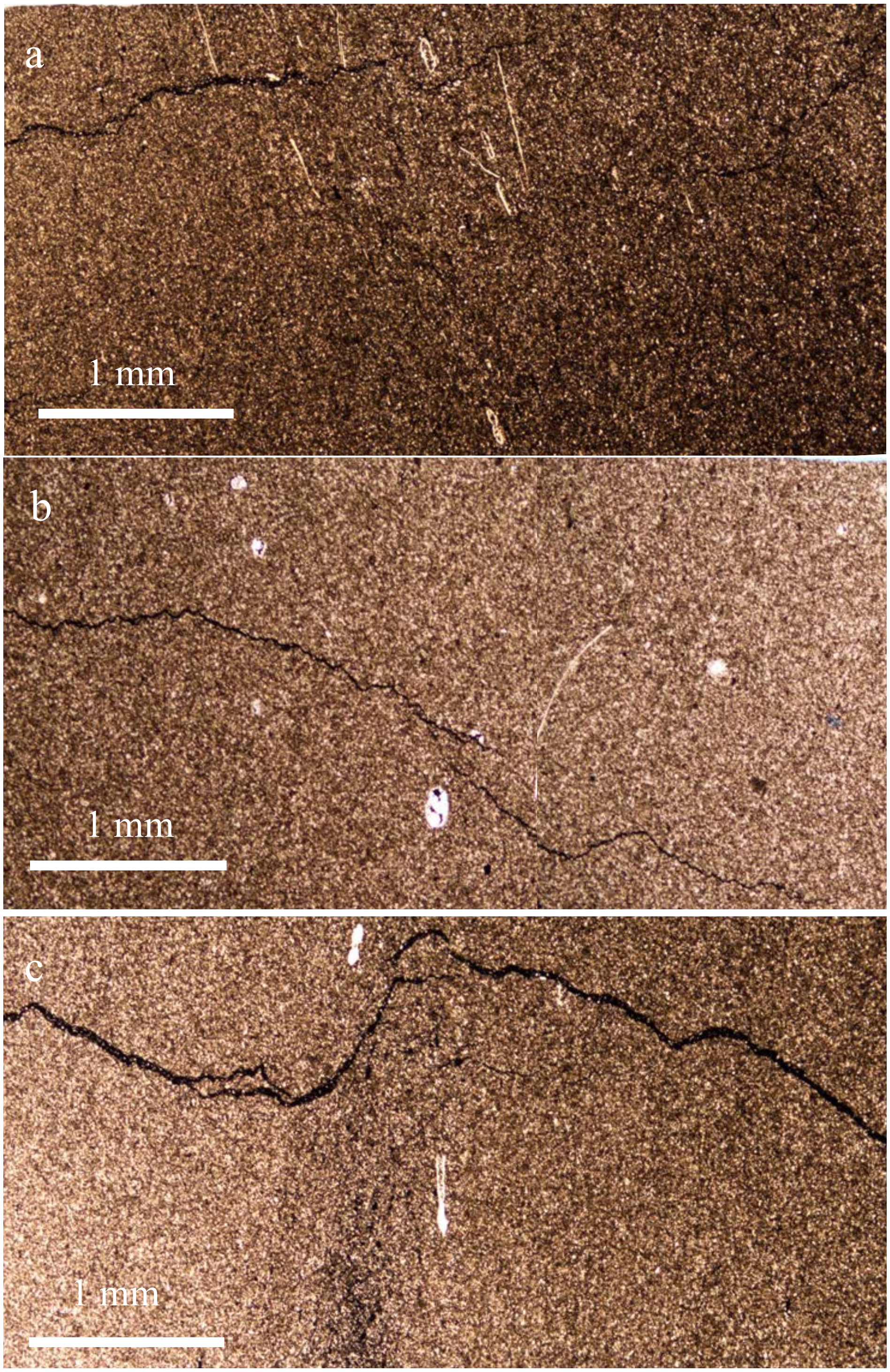
a
1 mm
b
1 mm
c
1 mm

Figure S2: Optical images of a) unreacted Marcellus Shale, b) MR1-pH4, and c) MR1-pH 8.3 thin sections within 0.5 mm of the channel-surface level of the samples. White inclusions are calcite and jagged, irregular dark lines are filled, pre-existing microfractures.

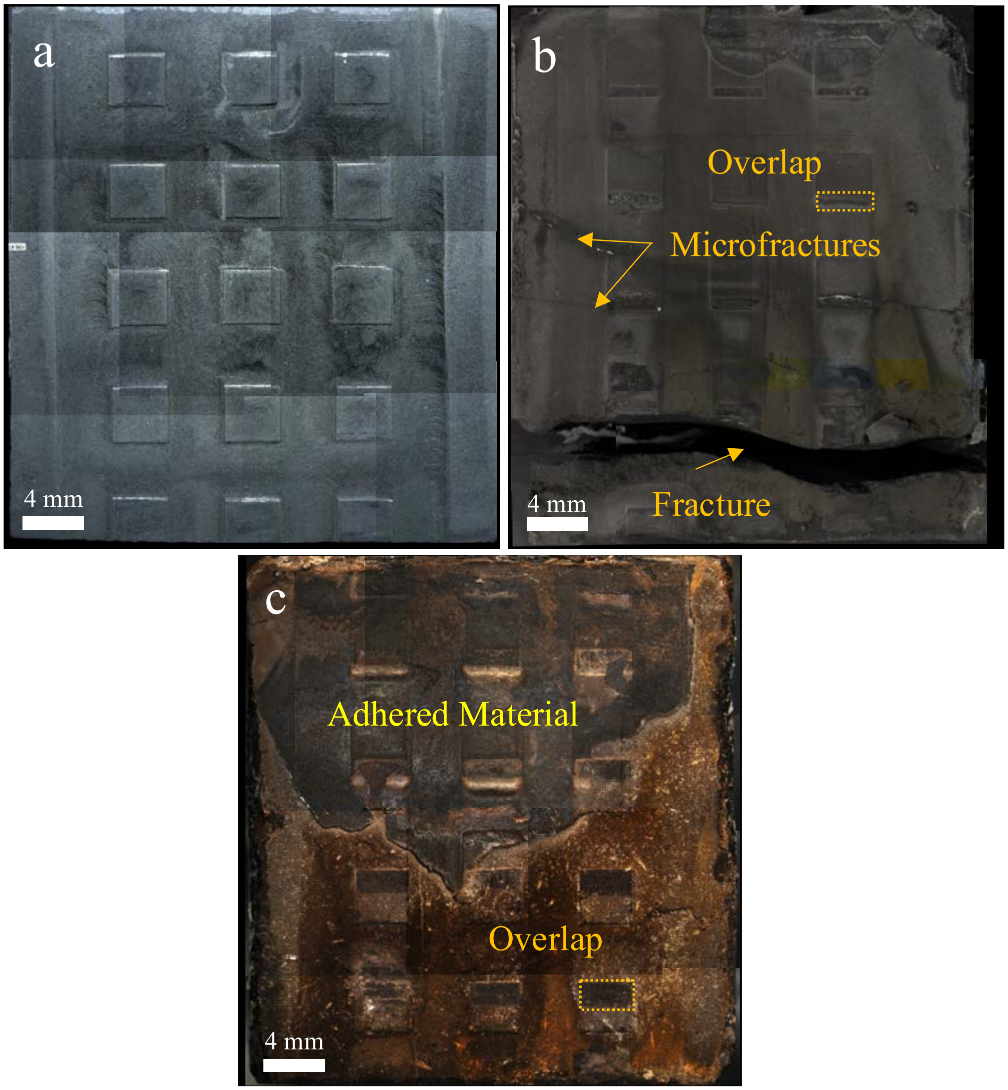

Figure S3: a) unreacted MR1-pH 4, b) aged MR1-pH 4, and c) aged MR1-pH 9.5. No unreacted image of MR1-pH9.5 was taken due to temporary instrument failure. ‘Microfractures’ and ‘Fracture’ indicate multiple induced fractures. The large fracture on MR1-pH4 was visible on CT scans from initial pressurization, not created by geochemical alteration, but the microfractures have an unknown origin. Dashed box and ‘Overlap’ give an example of where asperities were in contact with opposite half of reacted, fractured shale. ‘Adhered material’ describes a lamina of shale from the opposite half that has stuck.

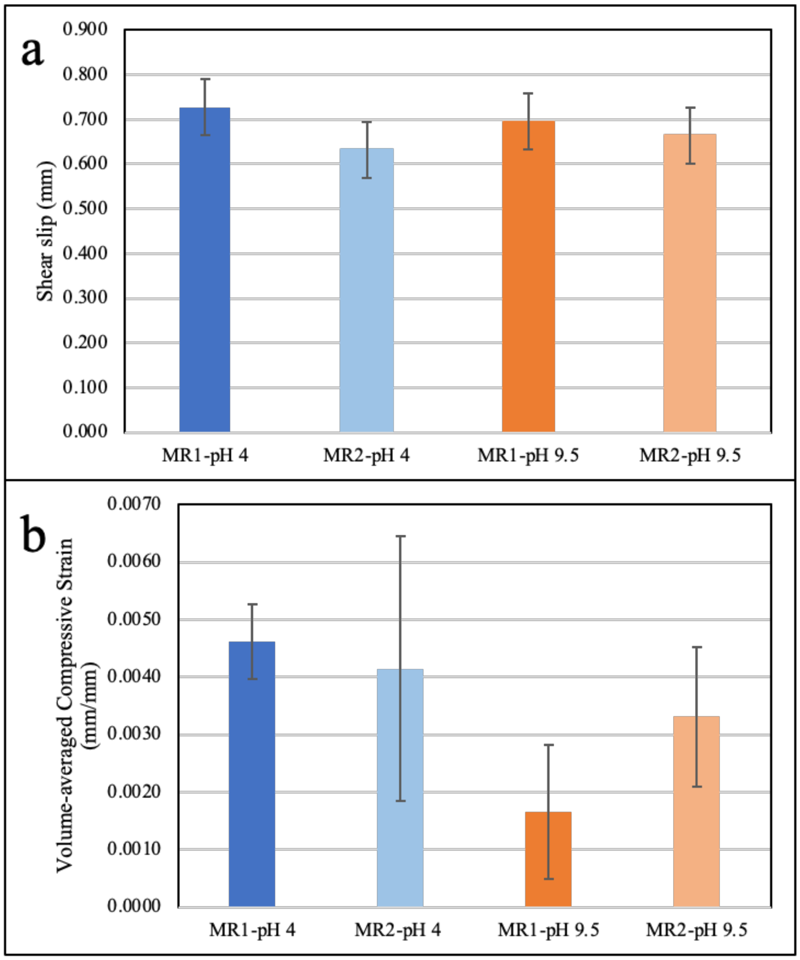

Figure S4: a) Shear slip and b) Volume-averaged compressive strain for each sample following initial applied stress. Induced shear is consistent for each sample within the margin of error. Measurements were made by DIC at a resolution of 15.8 µm.

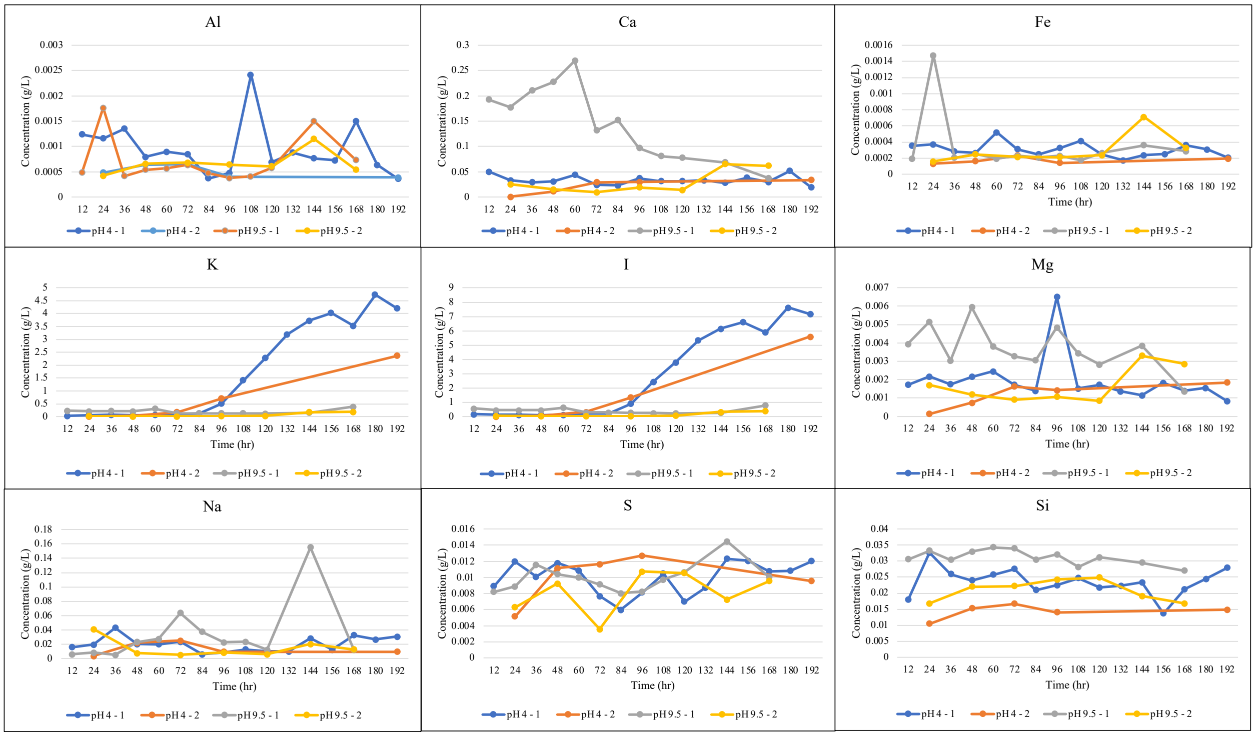

Figure S5: Effluent Brine elemental composition measured by ICP-OES. KI brine initial composition is 0.5 M, which sorbs to stainless steel piping until saturation.

References

Akono, Ange-Therese. 2021. “Fracture Toughness of One- and Two-Dimensional Nanoreinforced Cement via Scratch Testing.” *Philosophical Transactions of the Royal Society A: Mathematical, Physical and Engineering Sciences* 379 (2203): 20200288. https://doi.org/10.1098/rsta.2020.0288.

Akono, Ange-Therese, Pooyan Kabir, Zhuofan Shi, Samantha Fuchs, Theodore T. Tsotsis, Kristian Jessen, and Charles J. Werth. 2019. “Modeling CO2-Induced Alterations in Mt. Simon Sandstone via Nanomechanics.” *Rock Mechanics and Rock Engineering* 52 (5): 1353–75. https://doi.org/10.1007/s00603-018-1655-2.

Aman, Michael, D. Nicolas Espinoza, Anastasia G. Ilgen, Jonathan R. Major, Peter Eichhubl, and Thomas A. Dewers. 2018. “CO2-Induced Chemo-Mechanical Alteration in Reservoir Rocks Assessed via Batch Reaction Experiments and Scratch Testing.” *Greenhouse Gases: Science and Technology* 8 (1): 133–49. https://doi.org/10.1002/ghg.1726.

Azim, S. Syed, S. Muralidharan, and S. Venkatakrishna Iyer. 1995. “Studies on the Influence of Iodide Ions on the Synergistic Inhibition of the Corrosion of Mild Steel in an Acidic Solution.” *Journal of Applied Electrochemistry*. Vol. 25. https://link-springer-com.ezproxy.lib.utexas.edu/content/pdf/10.1007/BF00260694.pdf.

Berg, Stuart, Dominik Kutra, Thorben Kroeger, Christoph N. Straehle, Bernhard X. Kausler, Carsten Haubold, Martin Schiegg, et al. 2019. “Ilastik: Interactive Machine Learning for (Bio)Image Analysis.” *Nature Methods* 16 (12): 1226–32. https://doi.org/10.1038/s41592-019-0582-9.

Black, Jay R, Susan A Carroll, and Ralf R Haese. 2015. “Rates of Mineral Dissolution under CO

2 Storage Conditions." *Chemical Geology* 399: 134–44. https://doi.org/10.1016/j.chemgeo.2014.09.020.

Choi, Chae-Soon, Jineon Kim, and Jae-Joon Song. 2021. "Analysis of Shale Property Changes after Geochemical Interaction under CO2 Sequestration Conditions." *Energy* 214 (January): 118933. https://doi.org/10.1016/J.ENERGY.2020.118933.

Crandall, Dustin, Johnathan Moore, Magdalena Gill, and Matthew Stadelman. 2017. "CT Scanning and Flow Measurements of Shale Fractures after Multiple Shearing Events." *International Journal of Rock Mechanics and Mining Sciences* 100 (December): 177–87. https://doi.org/10.1016/J.IJRMMS.2017.10.016.

DeGarmo, E. Paul, J. T. Black, and Ronald Kohser. 2003. *Materials and Processes in Manufacturing*. 9th ed. Wiley.

Delle Piane, Claudio, and Joel Sarout. 2016. "Effects of Water and Supercritical CO 2 on the Mechanical and Elastic Properties of Berea Sandstone." *International Journal of Greenhouse Gas Control* 55: 209–20. https://doi.org/10.1016/j.ijggc.2016.06.001.

Deng, Hang, Brian R. Ellis, Catherine A. Peters, Jeffrey P. Fitts, Dustin Crandall, and Grant S. Bromhal. 2013. "Modifications of Carbonate Fracture Hydrodynamic Properties by CO2 - Acidified Brine Flow." *Energy & Fuels* 27 (8): 4221–31. https://doi.org/10.1021/ef302041s.

Deng, Hang, Jeffrey P. Fitts, Dustin Crandall, Dustin McIntyre, and Catherine A. Peters. 2015. "Alterations of Fractures in Carbonate Rocks by CO2-Acidified Brines." *Environmental Science & Technology* 49 (16): 10226–34. https://doi.org/10.1021/acs.est.5b01980.

Deng, Hang, Marco Voltolini, Sergi Molins, Carl Steefel, Donald DePaolo, Jonathan Ajo-Franklin, and Li Yang. 2017. "Alteration and Erosion of Rock Matrix Bordering a Carbonate-Rich Shale Fracture." *Environmental Science & Technology* 51 (15): 8861–68.

https://doi.org/10.1021/acs.est.7b02063.

Espinoza, D. Nicolas, Hojung Jung, Jonathan R. Major, Zhuang Sun, Matthew J. Ramos, Peter Eichhubl, Matthew T. Balhoff, R. Charles Choens, and Thomas A. Dewers. 2018. "CO2 Charged Brines Changed Rock Strength and Stiffness at Crystal Geyser, Utah: Implications for Leaking Subsurface CO2 Storage Reservoirs." *International Journal of Greenhouse Gas Control*, 16–28. https://doi.org/10.1016/j.ijggc.2018.03.017.

Fang, Yi, Derek Elsworth, Chaoyi Wang, and Yunzhong Jia. 2018. "Mineralogical Controls on Frictional Strength, Stability, and Shear Permeability Evolution of Fractures." *Journal of Geophysical Research: Solid Earth* 123 (5): 3549–63. https://doi.org/10.1029/2017JB015338.

Fatah, Ahmed, Hisham Ben Mahmud, Ziad Bennour, Raoof Gholami, and Md Mofazzal Hossain. 2022. "Geochemical and Physical Alteration of Clay-Rich Shales under Supercritical CO2 Conditions." *Applied Geochemistry* 140 (May): 105291. https://doi.org/10.1016/J.APGEOCHEM.2022.105291.

Frash, Luke, J William Carey, Zhou Lei, Esteban Rougier, Timothy Ickes, and Hari S Viswanathan. 2016. "High-Stress Traiaxial Direct-Shear Fracturing of Utica Shale and in Situ X-Ray Microtomography with Permeability Measurement." *Journal of Geophysical Research: Solid Earth*, 5493–5508. https://doi.org/10.1002/2016JB012850.Received.

Frash, Luke, James William Carey, Timothy Lee Ickes, Mark L Porter, and Hari S. Viswanathan. 2018. "Permeability of Fractures Created by Triaxial Direct Shear and Simultaneous X-Ray Imaging." In *51st US Rock Mechanics/Geomechanics Symposium*. Vol. 28. San Francisco, CA.

Fuchs, Samantha J., Dustin Crandall, Johnathan E. Moore, Mayandi Sivaguru, Bruce W. Fouke,

D. Nicolas Espinoza, Ange-Therese Akono, and Charles J. Werth. 2021. “Geochemically Induced Shear Slip in Artificially Fractured Dolomite- and Clay-Cemented Sandstone.” *International Journal of Greenhouse Gas Control* 111 (October): 103448. https://doi.org/10.1016/J.IJGGC.2021.103448.

Garcia-Ochoa, Esteban, Pablo Maldonado, | Francisco Corvo, Agustin Melgar, and San Francisco. 2020. “Nonlinear Dynamics of Potassium Iodide Adsorption on the Interface of Carbon Steel in Acidic Medium.” *Materials and Corrosion*, 1–8. https://doi.org/10.1002/maco.201911325.

Garcia, Daniel J., Hongbo Shao, Yandi Hu, Jessica R. Ray, and Young-Shin Jun. 2012. “Supercritical CO2–Brine Induced Dissolution, Swelling, and Secondary Mineral Formation on Phlogopite Surfaces at 75–95 °C and 75 Atm.” *Energy & Environmental Science* 5 (2): 5758. https://doi.org/10.1039/c2ee02026b.

Goodman, Angela, Sean Sanguinito, Mary Tkach, Sittichai Natesakhawat, Barbara Kutchko, Jim Fazio, and Patricia Cvetic. 2019. “Investigating the Role of Water on CO 2-Utica Shale Interactions for Carbon Storage and Shale Gas Extraction Activities-Evidence for Pore Scale Alterations.” *Fuel* 242: 744–55. https://doi.org/10.1016/j.fuel.2019.01.091.

Guo, Tiankui, Yanchao Li, Yong Ding, Zhanqing Qu, Naicheng Gai, and Zhenhua Rui. 2017. “Evaluation of Acid Fracturing Treatments in Shale Formation.” *Energy & Fuels* 31 (10): 10479–89. https://doi.org/10.1021/acs.energyfuels.7b01398.

Harvey, Omar R., Nikolla P. Qafoku, Kirk J. Cantrell, Giehyeon Lee, James E. Amonette, and Christopher F. Brown. 2013. “Geochemical Implications of Gas Leakage Associated with Geologic CO $_2$ Storage—A Qualitative Review.” *Environmental Science & Technology* 47 (1): 23–36. https://doi.org/10.1021/es3029457.

Ilgen, A.G., M. Aman, D. N. Espinoza, M. A. Rodriguez, J. M. Griego, T. A. Dewers, J. D.

Feldman, T. A. Stewart, R. C. Choens, and J. Wilson. 2018. “Shale-Brine-CO 2 Interactions and the Long-Term Stability of Carbonate-Rich Shale Caprock.” *International Journal of Greenhouse Gas Control* 78: 244–53. https://doi.org/10.1016/j.ijggc.2018.07.002.

Jeyaprabha, C, S Sathiyanarayanan, and G Venkatachari. 2006. “Influence of Halide Ions on the Adsorption of Diphenylamine on Iron in 0.5 M H 2 SO 4 Solutions.” *Electrochimica Acta* 51: 4080–88. https://doi.org/10.1016/j.electacta.2005.11.026.

Jiang, Yongdong, Chao Qin, Zhipeng Kang, Junping Zhou, Ye Li, Hui Liu, and Xiao Song. 2018. “Experimental Study of Supercritical CO 2 Fracturing on Initiation Pressure and Fracture Propagation in Shale under Different Triaxial Stress Conditions.” https://doi.org/10.1016/j.jngse.2018.04.022.

Khadom, Anees A., Ahmed N. Abd, and Nagham Arif Ahmed. 2018. “Potassium Iodide as a Corrosion Inhibitor of Mild Steel in Hydrochloric Acid: Kinetics and Mathematical Studies.” *Journal of Bio- and Tribo-Corrosion* 4 (2): 17. https://doi.org/10.1007/s40735-018-0133-4.

Liu, Faye, Peng Lu, Craig Griffith, Sheila W Hedges, Yee Soong, Helge Hellevang, and Chen Zhu. 2012. “CO 2-Brine-Caprock Interaction: Reactivity Experiments on Eau Claire Shale and a Review of Relevant Literature.” *International Journal of Greenhouse Gas Control* 7: 153–67. https://doi.org/10.1016/j.ijggc.2012.01.012.

Lyu, Qiao, Xinping Long, P G Ranjith, Jingqiang Tan, and Yong Kang. 2017. “Experimental Investigation on the Mechanical Behaviours of a Low-Clay Shale under Water-Based Fluids.” https://doi.org/10.1016/j.enggeo.2017.12.002.

Major, Jonathan R., Peter Eichhubl, Thomas A. Dewers, and Jon E. Olson. 2018. “Effect of CO2–Brine–Rock Interaction on Fracture Mechanical Properties of CO2 Reservoirs and Seals.” *Earth and Planetary Science Letters* 499: 37–47. https://doi.org/10.1016/j.epsl.2018.07.013.

Marbler, Herwig, Kirsten P. Erickson, Michael Schmidt, Christof Lempp, and Herbert Pöllmann. 2013. “Geomechanical and Geochemical Effects on Sandstones Caused by the Reaction with Supercritical CO2: An Experimental Approach to in Situ Conditions in Deep Geological Reservoirs.” *Environmental Earth Sciences* 69 (6): 1981–98. https://doi.org/10.1007/s12665-012-2033-0.

Matter, Jürg M., and Peter B. Kelemen. 2009. “Permanent Storage of Carbon Dioxide in Geological Reservoirs by Mineral Carbonation.” *Nature Geoscience* 2 (12): 837–41. https://doi.org/10.1038/ngeo683.

Moore, Johnathan, Dustin Crandall, Magdalena Gill, Sarah Brown, and Bryan Tennant. 2018. “Design and Implementation of a Shearing Apparatus for the Experimental Study of Shear Displacement in Rocks.” *Review of Scientific Instruments* 89 (4): 045107. https://doi.org/10.1063/1.5018419.

Mouzakis, Katherine M., Alexis K. Navarre-Sitchler, Gernot Rother, José Leobardo Bañuelos, Xiuyu Wang, John P. Kaszuba, Jason E. Heath, Quin R.S. Miller, Vladimir Alvarado, and John E. McCray. 2016. “Experimental Study of Porosity Changes in Shale Caprocks Exposed to CO2-Saturated Brines I: Evolution of Mineralogy, Pore Connectivity, Pore Size Distribution, and Surface Area.” *Environmental Engineering Science* 33 (10): 725–35. https://doi.org/10.1089/ees.2015.0588.

Nakashima, Yoshito, and Tsukasa Nakano. 2014. “Optimizing Contrast Agents with Respect to Reducing Beam Hardening in Nonmedical X-Ray Computed Tomography Experiments.” *Journal of X-Ray Science and Technology* 22 (1): 91–103. https://doi.org/10.3233/XST-130411.

Peng, Cheng, John P. Crawshaw, Geoffrey C. Maitland, and J.P. Martin Trusler. 2015. “Kinetics of Calcite Dissolution in CO2-Saturated Water at Temperatures between (323 and 373) K and Pressures up to 13.8 MPa." *Chemical Geology* 403 (May): 74–85. https://doi.org/10.1016/J.CHEMGEO.2015.03.012.

Rathnaweera, T.D., P.G. Ranjith, M.S.A. Perera, A. Haque, A. Lashin, N. Al Arifi, D Chandrasekharam, et al. 2015. "CO2-Induced Mechanical Behaviour of Hawkesbury Sandstone in the Gosford Basin: An Experimental Study." *Materials Science and Engineering: A* 641 (August): 123–37. https://doi.org/10.1016/J.MSEA.2015.05.029.

Rathnaweera, T.D., P.G. Ranjith, M.S.A. Perera, W.A.M. Wanniarachchi, and K.M.A.S. Bandara. 2018. "Stress State and Stress Path Evaluation to Address Uncertainties in Reservoir Rock Failure in CO2 Sequestration in Deep Saline Aquifers: An Experimental Study of the Hawkesbury Sandstone Formation." *Journal of CO2 Utilization* 26 (July): 184–201. https://doi.org/10.1016/J.JCOU.2018.05.008.

Shukla, Richa, Pathegama Ranjith, Asadul Haque, and Xavier Choi. 2010. "A Review of Studies on CO 2 Sequestration and Caprock Integrity." https://doi.org/10.1016/j.fuel.2010.05.012.

Soong, Yee, Dustin Crandall, Bret H. Howard, Igor Haljasmaa, Laura E. Dalton, Liwei Zhang, Ronghong Lin, et al. 2018. "Permeability and Mineral Composition Evolution of Primary Seal and Reservoir Rocks in Geologic Carbon Storage Conditions." *Environmental Engineering Science* 35 (5): 391–400. https://doi.org/10.1089/ees.2017.0197.

Stadelman, Matthew. 2017. "Netl-Ap-Map-Flow." GitHub. 2017. https://github.com/stadelmanma/netl-ap-map-flow.

Stadelman, Matthew A. 2017. "Comparing the Hydrodynamic Response of Fracture Shearing in Marcellus and Eau Claire Shales." West Virginia University.

"Stainless Steel Chemical Compatibility Chart." 2021. CP Lab Safety. 2021.

https://www.calpaclab.com/stainless-steel-chemical-compatibility-chart/.

Wigand, M., J.W. Carey, H. Schütt, E. Spangenberg, and J. Erzinger. 2008. "Geochemical Effects of CO2 Sequestration in Sandstones under Simulated in Situ Conditions of Deep Saline Aquifers." *Applied Geochemistry* 23 (9): 2735–45. https://doi.org/10.1016/j.apgeochem.2008.06.006.

Wright, Robert, Frank Mourits, Leonardo Beltran Rodríguez, and Dávila Serrano. 2013. "The First North American Carbon Storage Atlas Selection and/or Peer-Review under Responsibility of GHGT." *Energy Procedia* 37: 5280–89. https://doi.org/10.1016/j.egypro.2013.06.445.

Xiong, Jian, Kaiyuan Liu, Lixi Liang, Xiangjun Liu, and Chongyang Zhang. 2019. "Investigation of Influence Factors of the Fracture Toughness of Shale: A Case Study of the Longmaxi Formation Shale in Sichuan Basin, China." *Geotechnical and Geological Engineering* 37 (4): 2927–34. https://doi.org/10.1007/s10706-019-00809-0.

Yang, Kang, Junping Zhou, Xuefu Xian, Lei Zhou, Chengpeng Zhang, Shifeng Tian, Zhaohui Lu, and Fengshou Zhang. 2022. "Chemical-Mechanical Coupling Effects on the Permeability of Shale Subjected to Supercritical CO2-Water Exposure." *Energy* 248 (June): 123591. https://doi.org/10.1016/J.ENERGY.2022.123591.

Zhang, Guangqing, Dawei Zhou, Pu Wang, Kuangsheng Zhang, and Meirong Tang. 2020. "Influence of Supercritical CO2-Water on the Micromechanical Properties of Sandstone." *International Journal of Greenhouse Gas Control* 97 (June): 103040. https://doi.org/10.1016/J.IJGGC.2020.103040.

Zoback, Mark D, and Steven M Gorelick. 2012. "Earthquake Triggering and Large-Scale Geologic Storage of Carbon Dioxide." *Proceedings of the National Academy of Sciences of the United States of America* 109 (26): 10164–68. https://doi.org/10.1073/pnas.1202473109.

Zou, Yushi, Sihai Li, Xinfang Ma, Shicheng Zhang, Ning Li, and Ming Chen. 2018. “Effects of CO2–Brine–Rock Interaction on Porosity/Permeability and Mechanical Properties during Supercritical-CO2 Fracturing in Shale Reservoirs.” *Journal of Natural Gas Science and Engineering* 49 (January): 157–68. https://doi.org/10.1016/J.JNGSE.2017.11.004.